

Laser cooling and trapping of strontium atoms for experiments towards precision measurements and frequency metrology

A thesis

Submitted in partial fulfillment of the requirements of the degree of

Doctor of Philosophy

by:

Chetan Kumar Vishwakarma

Registration ID 20122035



Department of Physics


INDIAN INSTITUTE OF SCIENCE EDUCATION AND RESEARCH

PUNE - 411008, India

Certificate

Certified that the work incorporated in the thesis entitled “**Laser cooling and trapping of strontium atoms for experiments towards precision measurements and frequency metrology**” submitted by **Chetan Kumar Vishwakarma** was carried out by the candidate, under my supervision. The work presented here or any part of it has not been included in any other thesis submitted previously for the award of any degree or diploma from any other university or institution.

Date: December 17, 2020


(Supervisor)

Declaration

I hereby certify that the work which is being presented in the thesis entitled “**Laser cooling and trapping of strontium atoms for experiments towards precision measurements and frequency metrology**” in partial fulfillment of the requirements for the award of the Degree of **Doctor of Philosophy** and submitted in the Department of Physics of the Indian Institute of Science Education and Research, Pune is an authentic record of my own work carried out during a period from August, 2014 to June, 2020 under the supervision of Dr. Umakant D. Rapol, Associate Professor, Department of Physics, Indian Institute of Science Education and Research, Pune. The matter presented in the thesis has not been submitted by me for the award of any other degree of this or any other institute.



Date: December 17, 2020

(Chetan Kumar Vishwakarma)

Abstract

Measurement of physical parameters is the foundation of physical science. The improvement in precision of measurements has led to the discovery and validation of fundamental laws of physics. Development of measurement techniques in the field of atomic molecular and optical physics has opened the path to various discoveries such as the constancy of the speed of light, the early verification of quantum electrodynamics by performing the microwave spectroscopy for the fine structure of hydrogen atoms and the measurement of magnetic moment anomaly of the electron.

Among all the base units, ‘time’ is the most important and the most accurately measured quantity. It forms the basis for the definition of other base units in the SI system. Precision measurement of time is thus one of the most crucial fields of research in science, called the frequency metrology. Currently, the unit of time, the ‘SI second’, is defined as the duration of 9,192,631,770 periods of the radiation corresponding to the transition between two hyperfine levels of the ground state of ^{133}Cs atom. This transition frequency lies in the microwave regime of the electromagnetic spectrum. It has been shown that by switching to an optical transition with high Q value, one can increase the precision of measurement. These clocks with optical frequencies have been shown to be operated at the fractional uncertainty of the range of 10^{-18} . With such precision and accuracy, it holds the promise to revolutionize global timekeeping and tests of fundamental theories through the measurement of stability of fundamental constants of nature.

This thesis describes the design and construction of an experimental setup for the generation of cold strontium (Sr) atoms in a magneto-optical trap (MOT) with the ultimate aim of making an optical atomic clock operating on the singlet to triplet intercombination line. Special efforts have been put to simplify and make the entire system robust. The whole setup is built on a $1.5\text{ m} \times 3\text{ m}$ optical table. This table consists of both the optical setup for lasers as well as the vacuum assembly for generation, slowing, and trapping of the most abundant even isotope of Sr atoms. The MOT is loaded from an intense beam of Sr atoms generated by an oven and slowed by a zero-field crossing Zeeman slower. The oven is designed in such a way that it removes the complications of thermal isolation of the vacuum chamber from the high-temperature oven region. The

laser for the first stage of cooling is stabilized to the atomic transition by performing an atomic beam spectroscopy employing a novel design of the spectroscopy cell with an inbuilt titanium sublimation pump (TSP). The experimental setup is capable of producing an ensemble of cold ^{88}Sr with the atom number of $\sim 1 \times 10^7$ at a temperature of ~ 3 mK.

The atomic transition used as a reference for the clock frequency is affected by several external factors. The total uncertainty budget of the clock transition is an addition of all the uncertainties caused by various factors e.g., AC stark shift, Zeeman shift, black body radiation shift, background gas collision induced shift, etc. Systematic evaluation of these sources of uncertainties is one of the vital steps towards realizing the full potential of the ultra-narrow clock transition. Among the factors mentioned above, the collision induced shift and broadening of the clock transition is of the order of $\sim 10^{-19}$ (e.g., for H_2 it is 6×10^{-19}). For the current generation of clocks, this shift is not yet the limiting factor; however for next-generation clocks, it is necessary to consider the effects of this small yet important effect. In this thesis, we also focus on the study of loss induced by the background N_2 molecules and use this to measure the collision cross section between $^{88}\text{Sr}-\text{N}_2$ in MOT. We employed the measured collision cross section for the determination of C_6 of the ground state of Sr atoms. This quantity along with C_6 of the excited state is useful in determination of collision-induced shift and broadening. One of the focus of the present work is the study of the dynamics of atoms inside the MOT. We present a model for considering the various loss mechanism in MOT and evaluate their contributions. We experimentally determine the losses due to the decay of atoms in the long-lived state 3P_0 and due to the escape of atoms out of the MOT capture region. It occurs due to the branching of atoms into the state, which are not responsive to the first stage cooling laser. We further verify the experimentally measured loss rates with the calculated one in the presence of two different repumping schemes. We show that the contribution due to the latter can be the dominant loss channel. This loss channel is proportional to the atomic cloud temperature.

To my **Family**

Publications from the thesis work

- A simple atomic beam oven with a metal thermal break; **Chetan Vishwakarma**, Jay Mangaonkar, Kushal Patel, Gunjan Verma, Sumit Sarkar and Umakant D. Rapol, *Review of Scientific Instruments*, **90**, 053106 (2019)
- A compact atomic beam based system for Doppler free laser spectroscopy for strontium atoms; Gunjan Verma*, **Chetan Vishwakarma***, C. V. Dharmadhikari and Umakant D. Rapol, *Review of Scientific Instruments*, **88**, 033103 (2017)

* Both the authors have contributed equally to the work.

List of other publications

- Effects of finite momentum width on the reversal dynamics in a BEC based atom optics δ -kicked rotor; Jay Mangaonkar, **Chetan Vishwakarma**, S. Sagar Maurya, Sumit Sarkar, Jamie L. MacLennan, Pranab Dutta and Umakant D. Rapol, *Journal of Physics B: Atomic, Molecular and Optical Physics*, **53**, 235502 (2020)
- Nonmonotonic diffusion rates in atom-optics Lèvy kicked rotor; Sanku Paul, Sumit Sarkar, **Chetan Vishwakarma**, Jay Mangaonkar, M. S. Santhanam and Umakant D. Rapol, *Physical Review E*, **100**, 060201(R) (2019)
- Diffraction of a CW atom laser in Raman-Nath Regime; Sumit Sarkar, Jay Mangaonkar, **Chetan Vishwakarma** and Umakant D. Rapol, *Physical Review A*, **98**, 043625 (2018)
- Non-exponential decoherence and subdiffusion in atom-optics kicked rotor; Sumit Sarkar, Sanku Paul, **Chetan Vishwakarma**, Sunil Kumar, Gunjan Verma, M. Sainath, Umakant D. Rapol and M. S. Santhanam, *Physical Review Letters*, **118**, 174101 (2017)
- Bose-Einstein condensation in an electro-pneumatically transformed quadrupole-Ioffe magnetic trap; Sunil Kumar, Sumit Sarkar, Gunjan Verma, **Chetan Vishwakarma**, Md Noaman, and Umakant Rapol, *New Journal of Physics*, **17**(2), 023062 (2015)

Manuscripts under preparation

- Study of loss dynamics of strontium in magneto-optical trap; **Chetan Vishwakarma**, Kushal Patel, Jay Mangaonkar, Jamie L. MacLennan, Korak Biswas and Umakant D. Rapol, *arXiv:1905.03202* (2019)
- Design, fabrication and characterization of nanoplasmonic lattice for trapping of ultracold atoms; Sunil Kumar, Manav Shah, Ajith P. Ravishankar, **Chetan Vishwakarma**, Arindam Dasgupta, Jay Mangaonkar, Venu Gopal Achanta and Umakant D. Rapol, *arXiv:1810.10385* (2018)

Acknowledgments

I have always been interested in experiments and wanted to pursue a Ph.D. in experimental physics. The first week in IISER was confusing when it came to choosing a guide for the MS projects. Fortunately, the confusion didn't last long, and I decided to join the Atomic Physics and Quantum Optics Laboratory immediately after visiting the lab for the first time. During that visit, I was surprised to know that almost half of the lab was supposed to be for a single experiment and really wanted to learn how to build something like that by myself. Today, after more than seven years, I feel that I could not have taken any better decision. The time spent in this lab and IISER had been adventurous.

Building an experimental setup for laser cooling and trapping was not an easy task. I was fortunate enough to be surrounded by the people who have helped me at every stage. First of all, I would like to thank my supervisor Dr. Umakant Rapol for showing trust and assigning the ambitious project to me. He has always been full of enthusiasm and ready to consider some of the radical ideas. He has never been hesitant in doing any work when it comes to experiment. I have seen him performing experiments with his superior technical skills continuously for hours. He has been a true leader and a constant source of inspiration to all of us.

I want to acknowledge my research advisory committee (RAC) members, Dr. G. V. Pavan Kumar, and Dr. Shivprasad Patil, for their valuable feedback and insightful suggestions. Their yearly feedback helped me to align my research in the right direction. I would especially like to thank Pavan Sir for his words of encouragement during the challenging time of my Ph.D.

My labmates further smoothed the process of learning. I was continuously guided by Sumit Sarkar and Sunil Kumar. They were like my second teacher when it comes to lab training. I always felt free to consult them even with some silly doubts. I am especially thankful to Sunil Bhaiya; he is like an elder brother and helped in all walks of life. I would also like to thank my other labmates Gunjan Verma, Jay Mangaonkar, Pranab Dutta, Korak Biswas, Kushal Patel, Shivsagar Maurya, Harinee Natrajan, Jamie L. MacLennan, M. Sainath, Jithin K, Md. Noaman for the pleasant discussions and scientific interactions. I started working on the strontium setup along with Gunjan Verma.

We struggled together during the initial days of the experiment. It was a nice experience working with her. Although Jay didn't work directly on the strontium setup, he was always available for the discussion during the troubleshooting process. I was always happy to see his scientific approach towards any problems in hand. I am glad that the strontium setup is now in the safe hands of Kushal and Korak. I am grateful to Jay and Harinee for reading my thesis and giving me the feedbacks.

The inspiration and support which I received from some of my friends can not be acknowledged. Yet, I would like to express my gratitude to my close friends Sukrut Kamerkar, Mukul Rawat, Rahi Masoom Reja, and Anjusha VS for their company and for the quality time spent with them. In the first two years, I had shared my room with Rahi. We had a great time in two years during our MS. I guess we were the only roommates of the 2012 batch who survived in IISER till the end of our Ph.D. I am especially thankful to Anjusha for her endless help, support, and inspiration. She has always been there with me during my good and bad times. The time spent together during our random tea/coffee and the compulsory late night tea and delightful discussions on each and every topic will forever be missed. These people have been my second family.

I would also like to thank my batchmates and friends Mainak, Tomin, Sreejith, Amogh, Jerrin, Hridya, Aditi, Sneha, Abhishek, Prachi, Dipti, and Charu.

Building the experimental setup would not have been possible without the support from technical officer Mr. Nilesh Dumbre and other technical staff Prashant Kale, Sudhir Lone, and Santosh Khilare. I would like to thank Prabhakar Anagare and Dhanashree Sheth for efficiently handling all the official works. I also wish to thank Mr. Suresh K. Nair who helped us during the design and construction of a spectroscopy cell for strontium atoms with his glass blowing skill.

I acknowledge IISER Pune for providing a pleasant environment for working and funding my fellowship during MS and Ph.D. I would also like to thank the Council of Scientific and Industrial Research (CSIR) for providing me the scholarship during the last year of my Ph.D. under the direct-SRF scheme. I would also like to thank Indo-French Centre for the Promotion of Advanced Research (CEFIPRA) for providing me the opportunity to attend the European School on Nanoscience and Nanotechnology (ESONN)- 2016, Grenoble, France. During the final year of my Ph.D., I got a chance to

visit laboratories at Strathclyde University and the University of Sheffield, UK. I would like to convey my sincere thank to Newton-Bhabha Fund for sponsoring my trip to UK.

Last but not least, a wholehearted thanks to my family for their constant love and encouragement and making all of this possible. I would not be here without their enormous support and love.

Date: December 17, 2020

(Chetan Kumar Vishwakarma)

Contents

Declaration	v
Abstract	vii
Publications from the thesis work	xi
List of other publications	xiii
Manuscripts under preparation	xv
Acknowledgments	xvii
List of figures	xxv
List of tables	xxxv
1 Introduction	1
1.1 Setting the stage	1
1.2 Cold atoms and precision measurements	5
1.2.1 Interferometric measurement	6
1.2.2 Population based measurement	7
1.2.3 Frequency metrology	8
1.3 Measurement of time	9
1.3.1 Atomic frequency reference	12

1.3.2	The Cesium standard	13
1.4	The optical frequency standard	14
1.4.1	Measurement of optical frequency	15
1.4.2	Clock performance	17
1.5	Candidates for optical atomic clock	18
1.5.1	Neutral atom based platform	19
1.5.2	Ion based optical clocks	21
1.5.3	Nuclear transition for time measurement	21
1.6	Applications of optical clocks	23
1.7	Objective of the thesis	26
2	Theoretical background	29
2.1	Importance of cooling and trapping	29
2.2	The strontium atom	32
2.2.1	Cooling transitions	35
2.2.2	Repumping transitions	35
2.2.3	The clock transition	38
2.3	Laser cooling and trapping	38
2.3.1	Light atom interaction	38
2.3.2	Doppler cooling of atoms	40
2.4	Magneto optical trap	43
2.5	Determination of number of atoms	48
2.6	Magnetic trap	49
2.6.1	Majorana loss in magnetic trap	51
2.7	Temperature measurement of atoms	53
2.8	Rate equation	54
3	Experimental apparatus and methods - I : Vacuum assembly	57
3.1	The vacuum system	58
3.2	Atomic oven for strontium atoms	60
3.2.1	Design and Construction	61
3.2.2	Heating of strontium reservoir	63

3.2.3	Comsol simulation of the oven	65
3.2.4	Modification of oven design	67
3.2.5	Characterization of the oven	71
3.3	Zeeman slower	72
3.4	MOT capture region	75
3.5	Assembly of vacuum system	76
3.6	Magnetic field generating coils	80
3.6.1	Quadrupole coils	80
3.6.2	Shim coils	82
4	Experimental apparatus and methods - II : Laser systems	83
4.1	Generation of blue light for first stage cooling	83
4.1.1	Theory of nonlinear interaction	84
4.1.2	Theory and analysis of a ring resonator for a Gaussian beam	90
4.1.3	Cavity parameters	98
4.1.4	Master laser	101
4.1.5	Length stabilization of optical cavity	107
4.2	Doppler free spectroscopy of the Sr atoms	108
4.2.1	Design and construction	111
4.2.2	Baking of the spectroscopy cell	114
4.2.3	Characterization of spectroscopy cell	116
4.3	Frequency stabilization of laser systems	119
4.3.1	Frequency stabilization of seed laser	119
4.3.2	Frequency stabilization of repumping lasers	121
4.3.3	Frequency control of laser	122
4.4	Optical layout	124
4.5	Loading and characterization of MOT	126
4.5.1	MOT alignment procedure	129
4.5.2	Temperature measurement	130
4.6	Computer control	131

5	Study of loss dynamics of strontium in a magneto-optical trap	135
5.1	Definition of the problem	135
5.2	Theoretical background	138
5.3	Experimental Details	143
5.4	Results and Discussion	145
5.4.1	Determination of collision cross section	146
5.4.2	Determination of C_6 of the ground state	147
5.4.3	Determination of power and temperature-dependent loss rates	149
5.5	Conclusion	152
6	Conclusion and Outlook	153
6.1	Summary	153
6.2	Future work	155
6.2.1	Second stage cooling: Red MOT	155
6.2.2	Trapping of atoms in magic wavelength optical dipole trap	156
6.2.3	Magnetic field-induced spectroscopy of the clock transition	157
A	Appendix	159
A.1	Fast photodiode amplifier circuit	159
A.2	Lock box circuit diagram	160
A.3	High voltage amplifier circuit	161
A.4	Photo-multiplier tube controller	162
A.5	Crystal holder design	163
A.6	Frequency doubler mechanical drawing	164

List of Figures

1.1	The SI system of units: The seven base units in the SI system. Diagram shows the inter-dependence among the various base quantities. It should be noted that almost all the base units depend on the definition of second.	3
1.2	Clock schematic: Any clock consists of two parts: (a) The oscillator and (b) The counter	9
1.3	Evolution of the clock: (a) Sundial, (b) Pendulum clock, (c) The mechanical clock, (d) Quartz clock. Source: Wikipedia.	11
1.4	Atomic clock architecture: The atomic clock consists of an external radiation source which is stabilized with respect to an atomic transition. The frequency of this stabilized laser is counted by an appropriate counter.	13
1.5	Schematic view of an optical clock: Top: The cavity stabilized clock laser is used to interrogate the atomic transition and is stabilized with respect to it by electronic feedback loop. The atomic transition is an extremely narrow linewidth transition that allows for precise measurement. Bottom: The frequency of the clock laser is converted to an electronically measurable microwave frequency. This is done by beating the clock laser with one of the teeth of the frequency comb.	16
2.1	Schematic Grotrian diagram for strontium transitions: The low lying electronic energy levels of atomic strontium. The clock transition $^1S_0 \rightarrow ^3P_0$ and the transitions for laser cooling and repumping are indicated with their wavelength, linewidth and scattering rates.	36

2.2	Doppler force: The force experienced by an atom in a counter-propagating laser beam as a function of atomic velocity. The parameters are taken to be $I/I_{sat} = 0.1$ and $\Delta = -\Gamma$. The dashed lines show the forces due to the individual laser beams, and the solid line represents the net force experienced by the atom. Note that this plot is true only for the broad transition used for the first stage cooling of Sr atoms. For the second stage of cooling, the situation becomes complicated due to the narrow linewidth of the transition.	42
2.3	MOT Operation: Illustration of working of MOT in 1-dimension for an atomic system with $J = 0$ to $J = 1$ transition. Magnetic field along with the circularly polarized light provides the spatial confinement of the atoms.	45
2.4	Magneto-Optical Trap: Illustration of working of MOT in 3-dimension. Magnetic field along with the circularly polarized light provides the spatial confinement of the atoms.	46
2.5	Atoms number measurement: Schematic to collect the fluorescence emitted by a cloud of atoms in MOT. A lens of focal length ‘f’ is used to image the atomic cloud onto the calibrated photodiode.	48
2.6	Quadrupole field: The field profile generated by the anti-Helmholtz coil along one direction (Red dotted curve) and the corresponding potential seen by the atom (Green solid line).	50
3.1	Vacuum chamber: Side view of the vacuum chamber used for the production of cold strontium atoms. The oven region is shown within the dashed rectangle.	59
3.2	Strontium atomic beam source design: (a) Isometric view of the oven assembly; (b) Schematic diagram of Sr reservoir. All the dimensions are in mm; (c) Image of the needle holder carrying ~ 60 hypodermic needles.	62
3.3	Thermal isolation of heating elements: Aluminum enclosure filled with glass wool is used for minimizing the heat loss to the environment.	63

3.4	Power consumption of the Sr oven: Estimated electrical power as a function of the set temperature. Symbols represent the experimentally measured data point. The dashed line is a guide to eye. The error bars represent the uncertainty in the estimation of power due to an error in the measurement of the duty cycle.	64
3.5	FEM analysis of the temperature profile: Numerically simulated thermal profile of the oven including a CF35 6-way cross, a 55 l/sec ion pump (bottom) and an atomic beam shutter (right). The reservoir is maintained at the constant temperature of 800 K. The temperature is monitored at the region connected to 6-way cross, shown by point ‘P’ .	66
3.6	Thermal profile along the axis of oven: (a) cross-sectional view of the current design of the oven, including the assembly that holds the microcapillaries. Points ‘A’ and ‘B’ represent the two ends of the needle holder, and ‘C’ represents the point on the reservoir. The arrow at point ‘A’ shows the direction of the atomic beam, (b) temperature distribution along the length of the oven. The points under consideration are marked as ‘A,’ ‘B,’ and ‘C.’ The error bars represent the deviation of the simulated values considering uncertainty in the emissivity around 1 %. The dashed line is a guide to the eye.	67
3.7	Effect of the geometry of the constriction on thermal isolation: The numerically simulated temperature difference as a function of oven temperature (a) without any constriction (diamond symbols), (b) with the current design of constriction (circular symbols), (c) with proposed design (triangular symbols). Inset shows a comparison between the numerically simulated (circular symbols) and experimentally measured (square symbols) temperature difference as a function of the oven temperature. Error bars represent the uncertainty in the values of the temperature difference between point ‘P’ and the reservoir as represented in figure 3.3.	68

3.8	Contour plot of thermal profile: Contour plot of the difference in temperature as a function of oven temperature and thickness of the constriction (length of the constriction = 13.5 mm).	69
3.9	Cross section of Fig. 3.8: Variation of temperature difference as a function of thickness of the constriction for fixed oven temperature at 800 K (Cross section of the contour, shown in figure 3.8, along the dotted line). Dashed line is a guide to eye.	70
3.10	Stress profile: FEM simulations of the stress profile for the proposed design of oven. The maximum stress experienced is orders of magnitude smaller than the ultimate tensile strength of the material (~ 550 MPa).	71
3.11	Zeeman slower: The Zeeman slower used in the experiment. The spatially modulated magnetic field is generated using layers of solenoids with different number of turns.	73
3.12	Quartz cell: The quartz cell provides the optical access for cooling and trapping laser beams.	75
3.13	Strontium ampule: The ampule is broken inside a glove box and dendrite pieces are filled in the oven reservoir shown in Fig. 3.2(b).	77
3.14	Bakeout: Vacuum chamber during the baking process.	79
3.15	Quadrupole coil assembly: Pictures show the quadrupole coil assembly used in the experiment. (a) coil winding, (b) the coil mount, (c) profile of magnetic field generated by the coils at two different currents.	81
3.16	Shim coil assembly: Assembly of coils in Helmholtz configuration is used for the cancellation of stray magnetic field. The frames are made using a 3D printer.	82
4.1	Phase matching of fundamental and second harmonic wave: (a) The upper wave is the fundamental wave, and lower waves are the second harmonic waves emitted by different atoms in a nonlinear medium. When the refractive indices for the two waves are same, constructive interference occurs as mentioned in the text, (b) When the refractive indices of the two waves are different, they tend get out of phase and interfere destructively.	87

4.2	Critical phase matching: The variation of refractive index with the angle of propagation of light with respect to the crystal axis is used for achieving the phase matching condition. n^e and n^o represents the refractive index for extraordinary and ordinary ray respectively.	89
4.3	Periodically poled crystal: In quasi-phase-matching, a periodic variation in the crystalline axis of symmetry is produced by poling the non-linear medium with the application of a high voltage. This periodically resets the phase relation between the fundamental and the second harmonic waves. Thus, on average they remain roughly in phase and interfere constructively.	89
4.4	Example of ray matrix of method: An equivalent matrix is written corresponding to all the optical elements encountered by the ray from one reference plane to the final reference plane.	94
4.5	Cavity schematic: The ray diagram of the path traveled by the light inside the cavity.	96
4.6	Cavity mirrors data from manufacturer: Transmission of the cavity mirror as a function of wavelength. In ideal condition, the reflectivity at 922 nm should be maximum and transmittivity at 461 nm should be maximum. However, in practice, it is extremely difficult to achieve. Source: <i>CVI Melles Griot</i>	100
4.7	Seed laser for the generation of 922 nm light: (a) Schematic and (b) isometric view of ECDL in Littrow configuration for the generation of laser at 922 nm.	102
4.8	BoosTA output power as a function of TA chip current: The TA is seeded with a laser at 922 nm wavelength at the power of 22 mW.	103
4.9	BoosTA output beam profile: BoosTA profile as a function of TA chip current.	104
4.10	Crystal holder: The crystal is kept in a specially designed mount to maintain the fixed operating temperature. The crystal holder is fixed with the help of Newport 12.7 mm mirror mount (Part No.: U50-A) for achieving the freedom of fine alignment of light through the crystal.	105

4.11	Temperature optimization of the nonlinear crystal: Frequency doubling efficiency of PPKTP crystal as a function of crystal temperature	106
4.12	PDH module: Block diagram of the PDH module used for the length stabilization of the optical cavity. Standard RF components from Mini-Circuits have been used for making the module.	108
4.13	Optical cavity resonance: Cavity resonance (red curve) and the corresponding error signal (blue curve). The error signal is generated using the PDH scheme.	109
4.14	Optical frequency doubler: Picture of frequency doubler in the locked position.	109
4.15	SHG output: SHG output as a function of input fundamental power. The crystal is maintained at the optimum temperature for the best harmonic conversion efficiency.	110
4.16	Schematic diagram of the spectroscopy cell: The atomic beam is generated by a Sr dispenser source at the bottom of the cell. The collimation provided by the tube of the cell is nearly 95 mrad. The crossed arms are used for excitation and collection of the fluorescence signal. TSP maintains the UHV inside the cell.	112
4.17	Top view of the spectroscopy cell: The fluorescence signal is collected along the transverse direction using a planoconvex lens of diameter 25.4 mm and focal length 75mm.	113
4.18	Sr dispenser: Sr dispenser is spot welded to the tungsten electrode. These electrodes provide the electrical connections for dispenser operation.	113
4.19	Baking of spectroscopy cell: A cage-like enclosure is used for baking. A heating coils are wrapped around the enclosure. The cell is baked by the convective and radiative heating mechanism.	115

4.20	Dispenser characterization: Most probable velocity of atoms (red filled circles) and the estimated temperature (filled blue squares) of the dispenser vs. the current through the dispenser: A laser beam crossing the atomic beam at an angle 4.7° is used to probe the velocity distribution of the atomic beam. The broken horizontal line indicates the melting point of Sr.	117
4.21	Strontium spectrum: Fluorescence spectrum of $5s^2\ ^1S_0 \rightarrow 5s\ 5p\ ^1P_1$ transition of Sr atoms. The spectrum is fitted with a sum of six voigt profiles for the individual isotopes of Sr.	118
4.22	Error signal generation for locking seed laser: The secondary output of the SHG cavity at 461 nm is frequency modulated using an AOM. This modulated light is used for probing the first stage cooling transition $5s^2\ ^1S_0 \rightarrow 5s\ 5p\ ^1P_1$	120
4.23	Sr spectrum: Spectrum of Sr atoms (pink curve) along with the corresponding error signal (green curve). The error signal is generated using standard lock-in detection.	120
4.24	AOM driver block diagram: Block diagram of the AOM controller. This is made using the standard RF components from Mini-Circuits. . .	123
4.25	AOM driver box: Dual channel AOM controller, for controlling the frequency shifts of the different laser beams, showing all the necessary RF components in it.	123
4.26	Laser frequency scheme for first stage cooling: The light coming out of optical frequency doubler is shifted by 168 MHz using acousto-optical modulator (AOM) in double pass configuration. All other beams are derived with respect this frequency-shifted laser beam.	124
4.27	Optical table layout: Schematic of optical table layout showing all the necessary optical components used in the experiment.	125
4.28	MOT loading: Loading curve of Sr atoms in blue MOT. The repumping laser operates at the wavelength of 707.2 nm.	127
4.29	Atoms in MOT: Fluorescence of atoms trapped in MOT. The cloud of atoms is shown within the yellow circle	128

4.30	MOT temperature measurement: Fraction of recaptured atoms as a function of release time. Error bars of $\pm 5\%$ is added to incorporate the uncertainty in the measurement of recaptured fraction of atoms.	130
4.31	Control system: Block diagram of the FPGA based control system. . .	131
4.32	Digital sequencer: Front panel of the digital sequencer used for the generation of TTL pulses for the experiment.	132
4.33	Analog voltage generator: Front panel of the FPGA based analog voltage generator.	133
5.1	Strontium energy level diagram: The relevant low-lying energy level diagram of strontium (^{88}Sr) atoms. The wavelength (λ) and the decay rate (A) has been shown along with the transition.	138
5.2	Representation of collisional process: Strontium atoms with velocities less than the capture velocity are trapped inside the MOT. Various gas species such as nitrogen (red circle), untrapped Sr (blue), and other species (green) remain in the background of the chamber. The collision between them and the trapped atoms limits the lifetime of the MOT. . .	140
5.3	MOT loading in presence of two repumping schemes: Normalized fluorescence of ^{88}Sr MOT in the presence of repumping laser operating at (a) 481.3 nm and (b) 707.2 nm for different trapping intensities, $I_1 = 46.4 \text{ mW/cm}^2$, $I_2 = 26.4 \text{ mW/cm}^2$, $I_3 = 96.8 \text{ mW/cm}^2$ and $I_4 = 31 \text{ mW/cm}^2$. All other parameters are kept constant. Note that the loading rates of the MOT for the two repumping schemes is significantly different.	144
5.4	Loss rate measurement: Loss rate of atoms in Sr MOT as a function of background N_2 density. The two curves show the loss rate observed in the presence of two repumping schemes. (a) in the presence of repumper laser operating at the wavelength 707.2 nm and (b) with a repumping laser at 481.3 nm.	146

5.5	Loss rate of atoms in Sr MOT as a function of trapping beam intensity: The data is taken for two different configurations of repumping laser, (a) in the presence of repumping laser operating at 707.2 nm, (b) with repumper operating at 481.3 nm. The detuning and axial field gradient for the MOT is kept at -33 MHz and 48 gauss/cm respectively. Inset (c) is the expanded view of (b).	150
A.1	Circuit diagram of fast photodiode amplifier.	159
A.2	Circuit diagram of lock box used for scanning and locking the seed laser: The circuit diagram is adopted from PhD Thesis, Umakant D. Rapol, IISc, Bangalore, with appropriate modifications.	160
A.3	Circuit diagram of high voltage amplifier: The gain of this amplifier is 15 and it produces the maximum output voltage of 150 V. The circuit diagram is adopted from PhD Thesis, Umakant D. Rapol, IISc, Bangalore.	161
A.4	Hamamatsu PMT (H9307-02) controller: The circuit diagram is taken from H9306/H9307 photosensor module datasheet.	162
A.5	Mechanical design of the crystal holder	163
A.6	Frequency doubler mount: Base plate	164
A.7	Frequency doubler mount: Top platform for fixing mirrors. The distance between mirrors and folding angle is given in table - 4.3.	165

List of Tables

1.1	Neutral atom based clock species: Species used for the realization of neutral atom based atomic clock. Wavelengths and the scheme are written alongwith.	20
1.2	Trapped ion based atomic clocks: Trapped ion optical clocks currently under development. The clock transition, their wavelengths and their natural linewidth is mentioned alongwith.	21
1.3	Secondary representation of second: Systematic fractional uncertainty of various optical clock species.	24
2.1	Physical properties of Sr atom	32
2.2	Isotopes of Sr atom: Naturally stable isotopes of Sr atom. Numbers are taken from NIST data.	33
2.3	Comparison of the two cooling transitions: Relevant parameters for laser cooling and trapping using the $^1S_0 \rightarrow ^1P_1$ and $^1S_0 \rightarrow ^3P_1$ in Sr atoms.	37
3.1	Zeeman slower solenoids: Details of number of turns in each layer of the Zeeman slower.	74
4.1	Frequency doubling crystal specifications: The specification of the PPKTP crystal used for the SHG. The poling periode is decided by calculating the coherence length for the material.	90

4.2	Ray matrices for paraxial optical elements: ABCD matrices for the optical elements used in the analysis of optical resonator.	95
4.3	Cavity parameters: Geometrical parameters of the optical resonator in stable operating condition.	98
4.4	Cavity mirrors specifications: Specification of the mirrors used in the cavity-enhanced optical frequency doubler. Side 1 of each mirror faces inside of the frequency doubling cavity.	99
5.1	Comparison with literature values: Comparison of literature values for collision cross sections and C_6 of N_2 with Rb and Sr. * indicates the values obtained for this work.	148
5.2	Summary of power dependent loss rate: Comparison of experimentally obtained values of α , α_0 and collision cross section between ^{88}Sr and N_2 in the presence of two different repumping schemes employing the lasers operating at 707.2 nm and 481.3 nm	151

Chapter 1

Introduction

1.1 Setting the stage

Measurement is an integral part of daily life. It is used in our daily activities, research work, industries, etc. The measurements help in quantitative description of the world around us. They help in discovering the physical laws governing various phenomena in nature and formulate elegant mathematical equations expressing them, such as Newton's law of gravitation, the law of electromagnetism, among others. With such profound importance, measurement is considered as the building block of the physical world. As we model the world around us, we express the fundamental properties of matter in terms of dimensions. Some dimensions are frequently encountered in our everyday lives, such as mass, length, and time. These quantities are sufficient to meet our daily requirements. However, the developments in the field of science and technologies led us to the introduction of many other quantities such as electric charge, amount of substance etc. These are accepted as fundamental quantities.

The utility of these quantities depends on how well they are defined. In other words, to make complete sense, each quantity should have a well-defined unit for measurement. There are many systems of units, e.g., MKS (Meter-Kilogram-Second), CGS (Centimeter-Gram-Second). Different fields of science have their own system of units according to their convenience, e.g., the CGS system is more frequently used in chemistry. The MKS system, earlier known as the metric system, along with the other units for different physical quantities, is the most frequently used and is called the

International System of Units (SI, abbreviated from the French *Système international (d'unités)*). The SI system utilizes seven fundamental units called the base units, and twenty-two derived units, which can be expressed using the base units. The SI base units are second (time), meter (length), kilogram (mass), ampere (electric current), kelvin (temperature), mole (amount of substance) and candela (luminous intensity) [1, 2].

The quantitative utility of the SI system depends on how well one can define each of the base units. From a practical point of view, this definition is provided by the primary standard. A standard is some kind of a physical exemplar, a master copy that is used for the definition of a dimensional unit. As the name suggests, a primary standard is usually a specimen with the most exceptional performance in terms of accuracy and stability and to which the secondary standard traces back. This can be understood by considering the example of the primary standard for the SI kilogram. It was defined by the International Prototype Kilogram (IPK). IPK is a piece of cylindrical shape platinum-iridium alloy maintained by the International Bureau of Weights and Measures (BIPM). Any other material is designated to have a mass of one kilogram when it has the same measurable mass as IPK. However, by comparing the IPK mass to similarly constructed replicas of IPK, it has been found that the IPK mass changes over time due to various factors such as contamination, cleaning processes, etc. [3].

While deciding the standard of the measurement, it is necessary to look into the stability, accuracy, and reproducibility of the unit. It is thus preferred to use the physical constants of nature for the definition, instead of relying on the artifacts. Until recently, among all the base units, the Kilogram was the only one that was not defined in terms of the constants of nature. This definition was later changed on 20th May 2019. The currently accepted definition of the kilogram is based on the Planck's constant. It is defined by setting the Planck's constant exactly to $6.62607015 \times 10^{-34}$ J.s, provided the definitions of the meter, and the second are given by the accepted definition in the SI system of units. This redefinition is done with the help of a Kibble balance (also known as the Watt balance). A Kibble balance is an electro-mechanical measuring instrument that is capable of measuring the weight of a test object precisely by the electric current and the voltage needed to produce the compensating force [4]. The current in the coil is measured using the accepted definition of Planck's constant. It has to be noted that, the

balance determines the weight of an object (in this case that of IPK) and thus requires the accurate measurement of local earth's gravity with a precise gravimeter for the exact determination of the mass.

The definition and redefinition of standards is a continuous process. With the improvements in the techniques of measurements and better control of the experimental parameters, one can make more accurate and precise measurements. During the evolution of the standards of measurements, some of the units which were considered to be the base units could later be defined in terms of other more accurately measured base units. For example, the unit of length 'the meter' was defined based on a prototype maintained by the International Committee for Weights and Measures (CIPM) and kept at melting ice temperature. This definition was later replaced by something more fundamental. In 1960, the meter was defined as 1650763.73 wavelengths in vacuum of the radiation corresponding to the transition between the $2p^{10}$ and $5d^5$ states of the *krypton-86* atom. Later, developments in the field of laser spectroscopy helped to increase the measurement precision of the unit second. It was then realized that defining length in terms of the 'second' would be more precise. Hence, the definition of the unit of length was again changed in 1983. Currently, the meter is defined as the distance traveled by light in a vacuum in $1/299,792,458$ second.

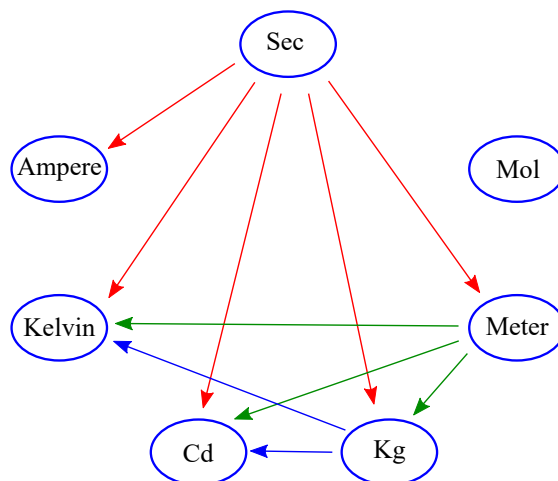


Figure 1.1: The SI system of units: The seven base units in the SI system. Diagram shows the inter-dependence among the various base quantities. It should be noted that almost all the base units depend on the definition of second.

The improvement in the precision of measurement not only allows us to define the units for various physical quantities in a superior way but also leads to the discoveries of many new phenomena. The field of atomic and molecular physics and optics is the one most benefited by this improvement and emerged as an ideal testbed for different theories such as the test of constancy of the speed of light [5], the early verification of quantum electrodynamics by performing microwave spectroscopy of the fine structure of hydrogen atom [6], etc.

Among all the base units, ‘second’ is the most important one. It is also one of the most accurately measured physical quantities and hence is used in the definitions of the other base units, as shown in Fig. 1.1. In order to have a universal time reference, which is immune to external influences, the definition of the SI second is based on a microwave transition between the hyperfine levels of the ground state of *Cesium-133* atoms. The combination of the technique of laser cooling and trapping with developments in the field of microwave electronics has improved the degree of precision to the level of 10^{-16} over the decades. In order to further increase the measurement accuracy to the level of 10^{-18} , a new generation of clocks is being tested. These clocks use the optical atomic frequency for achieving the finer division between any two time events.

This chapter describes the use of a laser-cooled sample of atoms for the application in precision measurements. After a brief discussion of the different techniques of precision measurements, we focus on the specific application of cold atoms for frequency metrology. It has been shown that an optical transition is far superior to the microwave one for metrology and is also a candidate for the redefinition of the SI unit of time. We discuss the development of clocks over the centuries and the accuracy associated with them. We look into the current definition of the SI second. We later focus on the possible candidates for the future redefinition of the second and list out the qualities that a device must possess to qualify as a clock. We briefly go through the measurement of optical frequency with the aid of an optical frequency comb. In the end, we list out the impact of such optical clocks in the field of science and technologies.

1.2 Cold atoms and precision measurements

The advancements in the field of laser cooling and trapping of atoms/ions have opened up a novel platform to study the interaction between atoms/molecules at very low and ultra-low temperatures. At extremely low temperatures, the motional degrees of freedom of particles under consideration tend to diminish. The effect of this reduced temperature is directly observable in the spectra of atoms/molecules, which is free from two significant sources of broadening viz. the Doppler broadening and the transit-time broadening.

Doppler broadening can be understood by considering an ensemble of atoms at room temperature. According to Maxwell-Boltzmann distribution, these atoms have different velocities – theoretically ranging from 0 to ∞ . The frequency of laser seen by such moving atoms is different from the frequency seen by a stationary observer in the laboratory frame of reference. This shift in frequency is called the Doppler shift, and the phenomenon is called the Doppler effect. These atoms, belonging to different velocity classes, emit light with their corresponding Doppler shifts, the cumulative effect of this is seen as the line broadening. This Doppler profile is broader than the natural linewidth of the transition under consideration and depends on the frequency of the spectral line, the mass of the emitting particle, and its temperature. Hence by reducing the temperature, this broadening can be reduced. On the other hand, the transit-time broadening can be understood by using the energy-time uncertainty principle. The finite velocity of atoms at room temperature limits the light-atom interaction time. For example, an atom moving with velocity ' v ' crosses a perpendicular probe laser beam of diameter ' d ' in the time τ . This leads to the transit time broadening of $\Delta_{tt} = 1/\tau$. This broadening can be larger than the natural linewidth of the transition and thus can limit the quality factor Q of the transition. Due to $1/\tau$ scaling of this factor, the broadening can be reduced by increasing the light-atom interaction time, which can be directly benefited by using laser-induced cooling techniques.

The progress in the field of laser cooling and trapping has improved the precision of the cesium based atomic clock. The inaccuracy of the clock performance has been improved from 10^{-9} to 10^{-16} since the first acceptance of its frequency for the time

standard. With the remarkable progress in the field of laser cooling, the field of precision measurements has flourished. The techniques for precision measurements using light-matter interaction can broadly be divided into three categories:

1.2.1 Interferometric measurement

Atom interferometry is one of the most popular techniques for precision measurements. It employs the wave-like nature of quantum particles [7]. Atoms, unlike light, are massive and are affected more by the gravitational field and thus it can be measured using atom based interferometers. The basic principle of the atom interferometer is similar to the light-based interferometer. In optical interferometry, light waves are recombined after passing through different paths. Depending upon the difference in the phase gathered along the two paths, the light may interfere constructively or destructively. In atom interferometry, the optical elements for the manipulation of atoms are generated using the laser beams. Many atom interferometers use three such optical elements: first to separate a group of atoms into two different divergent streams of atom waves, a second to bring the two streams back towards each other and third to make them interfere at the detection region. If one of the streams encounters different physical conditions than the other, it accumulates a phase proportional to its strength. The effect of this is seen as the shift in the fringe pattern.

Following are the advantages of atoms over light while performing interferometry:

a) The de-Broglie wavelength of atoms is orders of magnitude smaller than the wavelength of visible light (~ 100 's nm), making it more sensitive to small changes which are difficult to detect using conventional interferometer using photons

b) Atoms are sensitive to many physical parameters such as magnetic field, electric field, gravity etc. Thus it is possible to measure the phase gathered under the influence of the above-mentioned factors.

Over the time, this platform has proved its capability for use in fundamental and applied fields. Atom interferometry has been used for the measurements of rotations [8–10], the fine structure constant [11–13], atomic polarizability [14], the local gravitational field [15–19] and the gravity gradients [20, 21] etc. The high precision and accuracy of these interferometers can also be used for the gravitational wave detec-

tion [22, 23] in frequency bands (1 Hz to 10 Hz), currently inaccessible by the optical interferometers designed to detect gravitational waves from distance astrophysical sources in the frequency range of 10 Hz to 10 kHz.

1.2.2 Population based measurement

This measurement technique relies on tracking the population of trapped atoms. In principle, this can be done using atoms in a magneto-optical trap (MOT), magnetic trap (MT), or optical dipole trap. The loss of atoms from the trap is affected by factors such as the change of atomic spin state, decay of atoms into the metastable states, or the collisions with the untrapped background atoms/molecules. This loss rate of atoms from the trap can be used for the accurate determination of pressure inside a vacuum chamber in ultra-high vacuum (UHV) (10^{-7} to 10^{-12} mbar) and extreme-high vacuum (XHV) ($\leq 10^{-12}$ mbar) [24–26] regime. The contemporary technology relies on ion gauges for pressure measurement. However, ion gauges require recalibration after regular intervals of time. Also, the measurements based on ion gauge are not compatible with the efforts to base the SI unit on the fundamental and invariant constants of nature. A vacuum sensor based on atoms fulfills the above-mentioned criteria. The selection of atomic species for pressure sensing is one of the crucial factors which decides the sensitivity of the device. Traditionally, the alkali atoms such as rubidium, cesium, sodium have been used. However, it has been shown that the sensor based on lithium is more accurate for pressure measurements [26]. This is mainly due to the lower vapor pressure of lithium (10^{-17} Pa at room temperature) compared to other more popular species rubidium (2×10^{-5} Pa at room temperature). The lower vapor pressure limits the contamination of the vacuum chamber it is attempting to measure. Furthermore at a typical baking temperature (~ 150 °C), the saturated vapor pressure is approximately 10^{-9} Pa, low enough to allow the baking of vacuum chamber.

As the decay of atoms from the trap is induced by the collision with untrapped background atoms/molecules, the atomic loss rates can be used to measure collision cross section between various species of interest. It has been shown that the collision cross section determined using the loss rate measurement is more accurate than the conventional crossed beam technique [27]. There have been several experiments done

on the same spirit using cold rubidium [28–30], ytterbium [31], cesium [32], neon [27, 33] etc. With a slight modification in the experimental setup, the above-mentioned method can be used for the measurement of photo-ionization cross section [34, 35] and electron impact ionization [36].

1.2.3 Frequency metrology

Frequency metrology is the branch of science which deals with the methods of precise frequency measurements and its applications. The frequency of an atomic transition is affected by several factors such as the local gravitational potential, the external electric and magnetic fields, black-body radiation, inter- and intra-species collisions, etc. The utility of a particular atomic transition for frequency metrology is entirely dependent upon how accurately the frequency can be measured. Since the factors limiting the quality of measurements are the same, the use of optical frequency is preferred over microwave frequency for frequency metrology. In such a situation, it is desirable to have an optical transition with a high Q value. Considering the optical atomic transition with a narrow inter-combination line with the linewidth of the order of mHz, one can have a resonator with Q approaching 10^{18} . This is already a gain of the factor of 10^5 compared to the microwave atomic transitions.

Another advantage is that a narrow linewidth laser that is locked to such narrow optical transition can serve as a highly stable oscillator for an optical atomic clock. However, until recently, there was no proven clockwork mechanism that could count these optical frequencies with 100's of THz. Techniques using femtosecond-laser based frequency combs, developed within the past decades, have solved this problem [37, 38]. The gain in the ability to precisely and accurately count the *optical ticks* has opened an entirely new field of high precision optical spectroscopy and has led to the development of the optical atomic clock. The unprecedented sensitivity of these clock transitions can be used for answering some of the fundamental questions of physics, such as the time variation of the fine structure constant α . The variation in the value of α , if found, can raise some serious questions on the validity of the most successful model –the standard model in physics.

The narrow optical transition in atoms or ions can also be used for the precise mea-

surement of time. It holds the potential to replace the existing definition of SI second. In the following section, we briefly review the evolution of clocks over the centuries and compare their respective uncertainties.

1.3 Measurement of time

Among all the natural sciences, physics is the only one which uses the concept of time for various studies. In most of the modern and sophisticated physical models, time is considered a fundamental quantity and does not depend on anything else. According to the modern understanding of the universe, the time had a beginning, and it indeed came into being with the Big Bang. However, from a practical point of view, the concept of absolute time is absurd and is usually defined by its measurement; i.e., it is merely what a clock reads. The modern studies in physics require the measurement of time at an extreme level of precision. This led to the assumption that time is an infinitely divisible linear continuum and not quantized in nature.

The measurement of time has been crucial to humankind's everyday life. A clock is a device that does this by 'keeping time' in terms of the cycles of periodic events. In principle, any phenomenon which repeats itself at a certain period can be used for measuring the time interval by counting and keeping a record of the occurred number of cycles. Based on the above-presented logic, the clock is composed of two crucial subsystems: an oscillator and a counter, as shown in Fig. 1.2.

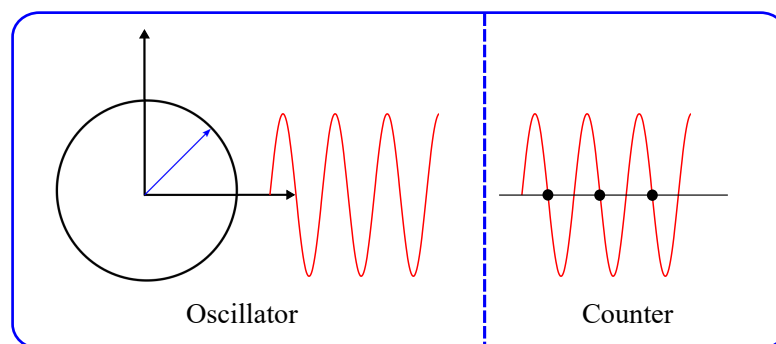


Figure 1.2: Clock schematic: Any clock consists of two parts: (a) The oscillator and (b) The counter

The first periodic phenomenon observed by humankind was the movement of heavenly bodies across the sky. Even without understanding its origin, people realized that

this could be used for the measurement of time. The periodic motion of the sun serves as an oscillator for the clock. To count the number of ticks, the position and length of the shadow of an object (e.g., a stick) were used. As the sun moves across the sky, the shadow changes its direction and length. However, it was soon realized that the lengths of days vary at a different time of the year. Also, it can not be used at night and cloudy weather. For the measurement at nights, the positions of constellations was used. One of the oldest recognized ones is the constellation of Orion. These phenomena could be used for synchronizing human activities on the time scale of months, days, or hours. However, the above-mentioned problems associated with the celestial clocks motivated to develop the first human-made clock. Initially, these clocks were based on the controlled flow of sand or water through a marked container to measure time. These were used for interpolation and keeping track of time between the marked astronomical events. However, with the increase in the complexity of human activities, it was soon realized that the time reference provided by the water clock was not sufficient. The fundamental idea to increase the resolution was increasing the frequency of the oscillator, i.e., to choose a periodic event with higher frequency. This led to the development of mechanical clocks. These clocks were good enough to keep time within the error of ~ 15 minutes a day but remained highly susceptible to external factors. The requirement was to have a device with high frequency and the period of which is independent of the external influences. In 17th century, Christian Huygens came up with a clock based on the Galileo pendulum. His clock was accurate within 10s of seconds a day [39], which was a drastic improvement over the earlier mechanical clocks. The pendulum clock was an outstanding piece of work with accuracy good enough for most of the human activities. However, with the development of the navigation across the oceans, it was realized that with all kinds of crazy rolling and pitching of the ships, these clocks were of little use. In particular, there was a crucial need to have a clock aboard ships showing the accurate time. These clocks were used to locate the position of the ship in the vast ocean. To overcome this problem, a different approach was required. In 1761 an English clockmaker, John Harrison, made and tested the first chronometer, based on the “balance-spring” mechanism. Due to inherent design limitations, these clocks could not be used as the absolute time reference due to its limited reproducibility. For exam-

ple, the period of oscillation of the pendulum clock depends on its length. Even with the universal agreement on a fixed-length, due to machining tolerances and mechanical and thermal expansion limits, there remained problems with the reproducibility of the timekeeping ability of a clock.

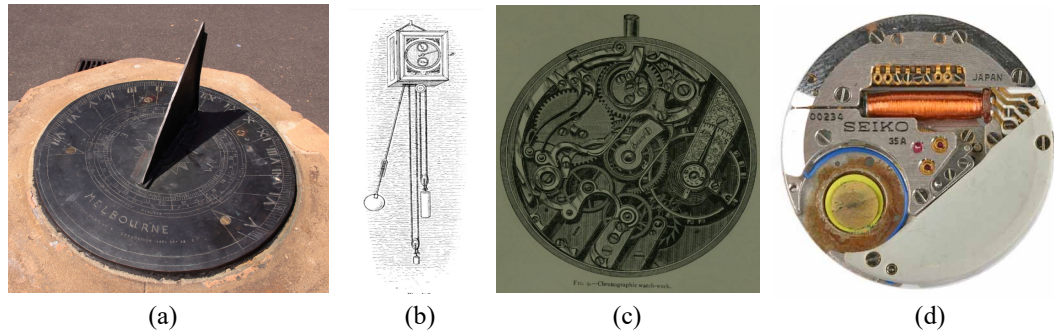


Figure 1.3: Evolution of the clock: (a) Sundial, (b) Pendulum clock, (c) The mechanical clock, (d) Quartz clock. Source: Wikipedia.

The next big revolution in the field of timekeeping came in 1929 with the discovery of a quartz clock. The operation of this new clock was based on the inherent piezoelectric quality factor of a quartz crystal that resonates with a frequency that depends on its physical dimensions, producing a voltage across a point on its surface. If it is placed in an oscillating electronic circuit that has nearly the same resonant frequency, the crystal vibrates at its natural frequency, and the oscillation frequency of the circuit becomes the same as that of crystal. Depending on the ‘cut’ of the crystal, its frequency of vibration can vary from 10s of kHz to 100s of kHz. The universally accepted frequency of vibration for the clock application is 32.768 kHz. This value of frequency is chosen such that it lies outside the audible range of the human ear and, at the same time, to be expressed in terms of 2^N . Here, the value of N is 15. This is done so that the chain of 15 flip-flops can effectively convert this high frequency to the movement of the second hand of the clock. The best crystal clocks can keep time within less than 1 ms per month. Currently, the quartz oscillators are being used in almost all electronic devices such as watches, mobile phones, computers, radios. However, since its resonance frequency depends on the size and shape of the crystal, no two crystals can be made precisely to have the same resonance frequency. Also, the frequency of the crystal varies gradually over time due to aging and can change more rapidly due to various environmental factors such as

temperature, pressure, and humidity. Thus, despite all the advantages offered, even the quartz crystal-based clocks are not qualified for a “universal time standard”.

The development of man-made clocks has seen significant improvements starting from the water clocks to pendulum clocks to the more recent quartz oscillator based clocks. Nevertheless, the fundamental limit remained with all the clocks is that they do not offer an absolute time. The quest for having a standard free from external factors and artifacts has led to the development of a new kind of clocks based on the atomic frequency reference. These clocks are called the “atomic clocks”.

1.3.1 Atomic frequency reference

The development of quantum mechanics in the beginning of the last century came to the rescue of the quest for the search of an absolute frequency reference. This allows having an oscillator that is more precise than any mechanical or astronomical reference realized earlier. These oscillators are based on atoms or molecules. According to the laws of quantum mechanics, atoms and molecules can have only well defined discrete energy levels. The transitions between these energy levels happen by emission or absorption of light having well defined and precise frequency ν such that:

$$\nu = \frac{|E_2 - E_1|}{h} \quad (1.1)$$

Here, h is the Planck’s constant. The idea of using the atomic transition as a frequency standard was put forward by James Clerk Maxwell [40]. In principle, the energy levels of atoms do get affected by external factors. There are many atomic systems where the energy levels are incredibly insensitive to external perturbations. Under a carefully isolated environment, these atomic systems can work as a natural frequency reference for an external oscillator. Based on the principle mentioned above, an atomic oscillator can be realized by a radiation source with a frequency ν , which can be compared and stabilized with a reliable atomic transition frequency ν_0 . With the incorporation of a counter that keeps track of the oscillations of the stabilized frequency, a complete atomic clock can be realized. The schematic of such an atomic clock is shown in Fig. 1.4.

The advantage of the above-mentioned scheme is that it removes all the external factors that affect the frequency of an oscillator. Every copy of a given atom is identical,

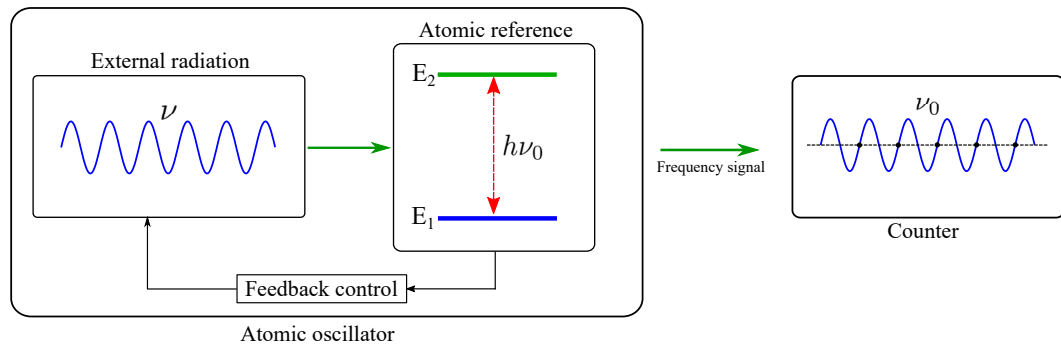


Figure 1.4: Atomic clock architecture: The atomic clock consists of an external radiation source which is stabilized with respect to an atomic transition. The frequency of this stabilized laser is counted by an appropriate counter.

independent of where the atom is placed or when the measurement is done. This means that once an agreement is made upon the choice of an atom and a particular atomic transition, one can replicate and use it as a “time standard” anywhere.

1.3.2 The Cesium standard

The first demonstration of a frequency reference using the atomic standard was done using the atomic transition of ammonia in 1949 [41, 42]. However, the boost to the development of an atomic frequency standard came with the progress in the field of microwave electronics during the second world war. This helped in the use of a microwave transition for the atomic clock reference. Cesium has many favorable properties that make it the right candidate for the primary standard of time. Cesium atoms are relatively heavy with atomic mass - 133; as a result, they move at a relatively slow speed (~ 130 m/s) at room temperature. The importance of high atomic mass can be understood by comparing the speed as mentioned above with the speed of hydrogen atoms at room temperature, which is ~ 1600 m/s. This enhances the interaction time with the interrogation radiation, resulting in a reduced transit time broadening. Another advantage is the existence of relatively high hyperfine splitting (9.2 GHz) of the ground state compared to other popular candidates, e.g., rubidium (6.8 GHz) and hydrogen (1.4 GHz). These frequencies can be directly measured using conventional microwave electronics.

The first demonstration of cesium (Cs) atomic clock using the technique of atomic beam magnetic resonance was done in the National Physical Laboratory (NPL) – United

Kingdom in 1955 [43]. The inaccuracy of this clock was $\sim 10^{-9}$. With excellent precision and accuracy, this microwave transition of the Cs atoms was accepted for the redefinition of SI second in 1967. The SI second was defined as “*the duration of 9,192,631,770 periods of the radiation corresponding to the transition between the two hyperfine levels of the ground state of the cesium-133 atoms*”. This definition of the second still holds. Advances in the field of laser cooling and trapping have affected the performance of Cs based clocks; currently, these clocks are based on atomic fountains instead of the atomic beams. The best achievable systematic uncertainty of such a clock has reached to $\sim 10^{-16}$.

Although Cs fountain clocks continue to be useful in many microwave-based time and frequency applications such as in navigation, communication, and synchronization of signals, etc., the fundamental limitation continues to exist. This arises due to the microwave frequency being relatively low in comparison to the optical one and the associated extended period of observation required for reaching the peak performance of $\sim 10^{-16}$.

1.4 The optical frequency standard

The performance of the frequency standard based on microwave transition of Cs-133 atoms has been outstanding, the development in laser technologies and a better understanding of light-matter interaction has pushed the limits on uncertainty to which it can be operated. They have now reached the limit beyond which it can not be further improved. The state-of-the-art Cs atomic clock’s uncertainty is limited by the collisional shifts and the microwave power [44]. Further improvements in the performance of the atomic clocks can only be achieved by increasing the operating frequency by moving away from microwave frequencies. Since the optical frequencies (10^{15}) are orders of magnitude larger than microwave frequencies (10^{10}), combined with narrow linewidth transitions of certain atoms, these optical clocks hold the potential to be orders of magnitude better in accuracy. The advantages of optical clocks due to their high Q value have been realized during the early days of the development of frequency standards. The use of optical transition for the frequency standard was first suggested by Dehmelt around the time when single ion traps and laser cooling were first developed [45]. Even after

the invention of coherent light source [46] for the interrogation of the atomic spectrum and the laser cooling techniques [47–49] to reduce the Doppler shifts in the frequency response of atoms and ions, the expected progress in the field of optical atomic clocks could not be achieved. The biggest hurdle in the development of this new superior time standard based on optical transition was the inability to measure the high frequencies associated with optical transitions with sufficient frequency resolution using conventional electronic devices. The fastest known electronic counter can measure the frequencies of upto 100s of GHz which is orders of magnitude less than the required counting speed.

The first plan to bridge this gap was based on chains of multiple doubling stages of a coherent microwave signal. This technique was highly complicated and inefficient. These frequency chains [50, 51] occupied the space of an entire room and required several skilled people for its operation. Due to the expensive and complicated setup of these frequency chains, only a few groups worldwide could pursue their research in this direction. The real revolution in optical frequency measurement came with the development of self-referenced optical synthesizers or the optical frequency comb [37, 38, 52–54]. This frequency comb technique provided the necessary clockwork mechanism to fill the gap between the optical and microwave domains of transition. More importantly, it maintains the high stability of the optical signals.

1.4.1 Measurement of optical frequency

As mentioned earlier, the measurement of optical frequency was simplified by the invention of the optical frequency comb. It consists of a mode-locked femtosecond (10^{15}) laser [55] where the pulses are separated in time by $1/f_{rep}$, determined by the repetition rate f_{rep} of the laser. Frequency spectrum of such a laser consists of evenly spaced frequency components that are separated by the pulse repetition rate f_{rep} . The frequency of the n^{th} mode of a comb can be written as:

$$f_n = n f_{rep} + f_0 \quad (1.2)$$

where, f_0 is the frequency offset. This offset is common to all the modes and arises due to the difference in group velocity and phase velocity inside the laser cavity. If the frequency of the comb covers the entire octave, then f_0 can be determined by frequency

doubling the infrared mode of the spectrum and beating with the existing mode in the visible region of the comb spectrum, i.e.

$$f_0 = 2(nf_{rep} + f_0) - (2nf_{rep} + f_0) \quad (1.3)$$

Typically, the repetition rate of such combs are of the order of 100s MHz to few GHz.

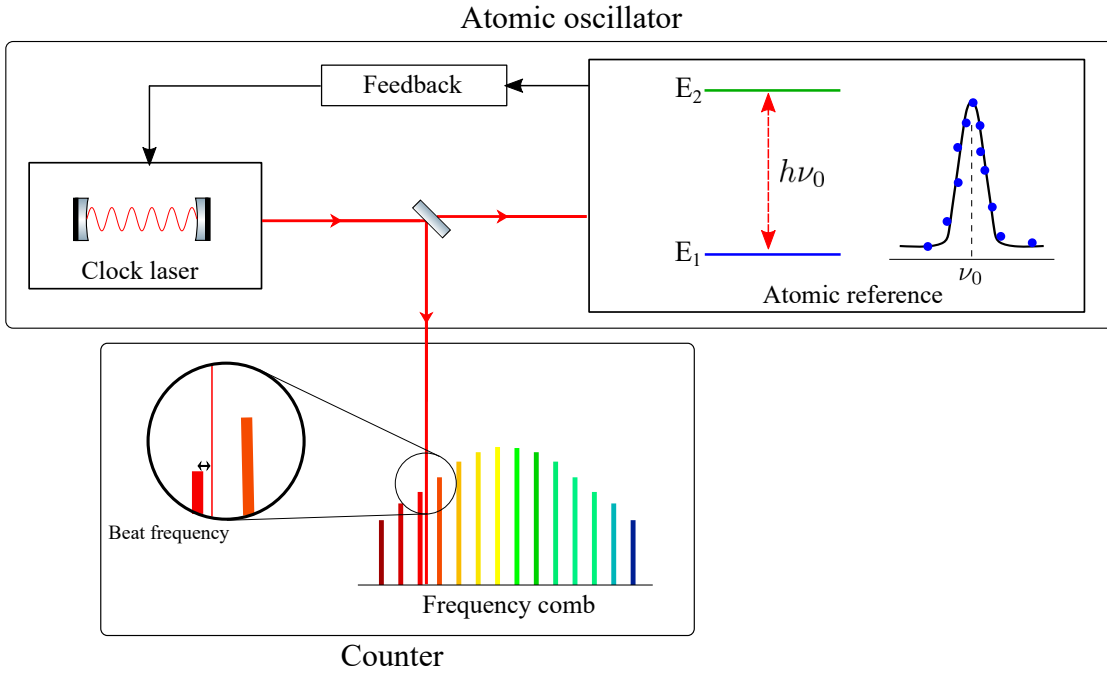


Figure 1.5: Schematic view of an optical clock: Top: The cavity stabilized clock laser is used to interrogate the atomic transition and is stabilized with respect to it by electronic feedback loop. The atomic transition is an extremely narrow linewidth transition that allows for precise measurement. Bottom: The frequency of the clock laser is converted to an electronically measurable microwave frequency. This is done by beating the clock laser with one of the teeth of the frequency comb.

The schematic of an optical clock is shown in Fig. 1.5. Here, a spectrally pure electromagnetic radiation is used for probing the narrow linewidth atomic transition with frequency ν_0 of atoms or ion. The laser then actively receives feedbacks from the control loop to keep its frequency at the center of the absorption resonance. This way, it acquires the stability of the atomic transition. This stabilized laser frequency is then sent to the optical comb. By beating the laser frequency with one of the teeth of the comb, it is possible to convert the frequency information from the optical frequency to

the microwave frequency. This microwave frequency can be measured easily by using an electronic counter. In this case, the optical frequency can be expressed as:

$$f_{opt} = n f_{rep} + f_0 + f_{beat} \quad (1.4)$$

Here, f_{beat} is the beat frequency of the interrogation laser with one of the comb's teeth. The value of n while determining the optical frequency is usually a very large integer. This can be determined using low-resolution measurement, e.g., by using a laboratory wave-meter.

1.4.2 Clock performance

Quantifying the performance of a frequency standard is an extremely important task. It is used to differentiate between a good clock and a bad clock. The figures of merit used to quantify the clock performance are described below:

Accuracy

Accuracy refers to the closeness of the measured value to the actual value. It is associated with systematic errors in the measurement. For an accurate atomic clock, the measured frequency matches with the natural atomic frequency. Accuracy depends on the selection of atomic species and the degree to which the atomic system can be isolated from the environmental effects (e.g., electric fields, magnetic fields, background blackbody radiation, etc.) during the interrogation of the clock state. Practically, it is almost impossible to isolate atoms from the external influences entirely, and thus, the clock can have significant systematic shifts. However, if these shifts are precisely known, they can be corrected accurately, resulting in a very accurate clock. On the other hand, a clock may have minimal but poorly understood systematic effects, which can lead to an inaccurate clock.

Stability

The stability of a clock represents the repeatability of the measured frequency over a given period of time. This is generally characterized by Allan deviation or modified Allan deviation. This can be defined by considering a discretely sampled time series

of frequency data y_i , with M samples, each averaged over a sample time τ for a total measurement time $T = M\tau$. In such case the Allan deviation can be written as:

$$\sigma_y(\tau) = \left[\frac{1}{2(M-1)} \sum_{i=1}^{M-1} (y_{i+1} - y_i)^2 \right]^{1/2} \quad (1.5)$$

The measurement of Allan deviation is essential for the clock operation as it carries information regarding the noise sources affecting it. By looking at the behavior of Allan deviation as a function of time scale, one can learn about the noise processes and their respective time scales [56, 57]. During the clock operation, the ultra-stable narrow linewidth laser used for the interrogation of atomic reference is stabilized using a feedback signal generated from the excitation information of a finite number of atoms. This leads to statistical fluctuation noise in the error signal. This source of noise is called the quantum projection noise since the statistical fluctuations are caused by the projection of the superposed quantum state of the atoms onto a measurement basis state [58]. The quantum projection noise is given by:

$$\sigma_y(\tau) = \frac{1}{\pi} \frac{\Delta\nu}{\nu} \frac{1}{SNR} \sqrt{\frac{1}{\tau}} \quad (1.6)$$

Here, ν is the clock operating frequency with the observed transition linewidth of $\Delta\nu$. SNR is the signal to noise ratio, and τ is the averaging time in second. The quantum projection noise sets a natural limit on the stability of a clock under consideration. For an optical lattice clock where the number of atoms can be of the order of 10^4 , the instability can be minimal.

1.5 Candidates for optical atomic clock

Two types of atomic species compete in the race to become the most precise and accurate clock viz. neutral atoms and ions. Both of them have their own advantages and disadvantages. In the next section, we briefly discuss these neutral atoms and ion based platforms. Apart from the conventional clocks, it has now been proposed to use a nuclear transition for the clock application. The frequency of operation of such clocks lies in the optical regime. There are several optical clock systems based on different species

that can achieve systematic frequency uncertainty lower than the Cs fountain clock. Few examples of ion-based architecture are $^{27}\text{Al}^+$, $^{199}\text{Hg}^+$, $^{171}\text{Yb}^+$ and $^{88}\text{Sr}^+$. On the other hand, some of the popular species for atoms in an optical lattice are ^{87}Sr , ^{199}Hg , and ^{171}Yb . The reported systematic uncertainties of such a systems lie in the range of 10^{-16} to 10^{-18} .

1.5.1 Neutral atom based platform

Due to a large number of atoms ($\sim 10^4$) for interrogation, the quantum projection noise for the neutral atom based optical lattice clocks is much smaller than the single ion-based clocks. One of the disadvantages of such a clock is the large Doppler shift in the reference frequency; this, however, can be countered by tightly confining the atoms in an optical lattice. This gives optical clocks the advantages of low Doppler shifts with the high number of atoms but potentially at the cost of larger influence of the environment [59]. It should be noted that the Doppler broadening can not be eliminated just by cooling the atoms. For example, at an extremely low temperature of the atomic cloud of the order of 1 nK, the atomic sample has a Doppler broadened linewidth at the kHz level due to weak dependence of Doppler width on temperature, which scales with the square root. Also, the recoil transfer from the clock laser can induce a shift in the order of a few kHz. These problems can be overcome by tightly confining the atoms in an optical lattice [60, 61]. The lattice is formed by a pair of counter-propagating laser beams at the atomic cloud. For the optical potential of depth much larger than the thermal energy of the atoms, most of the atoms populate the lowest vibrational ground state. In such a situation, the optical lattice's energy scale is larger than the photon recoil, and the atoms remain in the Lamb-Dicke regime. In this state, since the minimum energy scale is given by the lattice's vibrational state, the atoms are not allowed to take the photon recoil momentum of the clock laser. Instead, the momentum of the photon is taken up by the lattice potential. This allows the Doppler-free spectroscopy of the clock transition without inducing any shift in the transition frequency. In principle, any far detuned laser with enough intensity can generate the trapping potential for the atoms. However, for the clock operation, the selection of laser with the appropriate wavelength

is crucial. The energy levels of atoms in the presence of an external light field experience a shift called the AC stark shift. This would change the frequency of the clock transition due to uneven shifts in the energy levels. This problem can, however, be tackled by carefully selecting the wavelength of the lattice laser. The laser is selected in such a way that it compensates for the light shifts, i.e., the light shift of the ground and the excited states are the same in both magnitude and direction. The wavelength selected in such a way is called the “*magic wavelength*” [60]. The magic wavelength for the Sr clock transition is 813.428 nm. Apart from this, there are several other sources of broadening, such as collisional broadening. Since more than one atoms occupy each lattice site, the intra-atomic collision can shift and broaden the clock transition frequency. These factors have been extensively studied in the context of optical lattice clocks [62–66].

Among the possible candidates, alkaline earth (like) atoms are more popular due to favorable transitions for laser cooling and the existence of ultra-narrow linewidth transition that can be used as a clock. Sr is the most promising and the most studied candidate for the optical lattice clock. A large number of Sr optical lattice clocks [67] are currently under development worldwide with uncertainties of up to a few parts in 1×10^{-18} [57, 68, 69]. The most precise optical lattice clock is realized by the team at JILA using ^{87}Sr atoms in 3D optical lattice [70] with the measurement precision of the order of 5×10^{-19} in 1 hour of averaging time. The use of fermions instead of bosons reduces the collisional broadening due to reduced on-site atomic interaction. Following are the list of neutral atom based optical atomic clocks.

Atom	Clock Type	Clock λ nm	Lowest published systematic uncertainty
^{87}Sr	Lattice	698	2×10^{-18}
^{199}Hg	Lattice	266	7.2×10^{-17}
^{171}Yb	Lattice	578	3.4×10^{-16}
^1H	Cryogenic beam	243	4.2×10^{-15}

Table 1.1: Neutral atom based clock species: Species used for the realization of neutral atom based atomic clock. Wavelengths and the scheme are written alongwith.

1.5.2 Ion based optical clocks

The trapped ion-based optical frequency reference is another platform that promises to revolutionize global timekeeping. Since the number of ions inside a trap is very small, usually a single ion, the measurement stability can be small. However, the high trap stiffness enables repeated probing of the transition serially to average out the projection noise. Increasing the number of probes per clock cycle gives better information, lowers the statistical noise at the expense of longer acquisition time. Since the number of ions is minimal, they do not suffer from the collision-induced broadening. There are many candidates for ion-based frequency standard. Research is underway at several laboratories around the world to investigate the stability and accuracy of different trapped ion optical atomic clocks. Examples of these laser-cooled ions are Al^+ [71], Ca^+ [72–74], Hg^+ [75], Yb^+ [76,77], In^+ [78] and Sr^+ [79,80]. The reported systematic uncertainties of the above-mentioned system lie in the range of 10^{-16} to 10^{-18} [81].

Ion	Clock transition	Clock λ nm	$\Delta\nu_{nat}$ (Hz)
$^{27}\text{Al}^+$	$^1S_0 \longrightarrow ^3P_0$	267	8×10^{-3}
$^{40}\text{Ca}^+$	$^2S_{1/2} \longrightarrow ^2D_{5/2}$	729	0.14
$^{88}\text{Sr}^+$	$^2S_{1/2} \longrightarrow ^2D_{5/2}$	674	0.4
$^{115}\text{In}^+$	$^1S_0 \longrightarrow ^3P_0$	237	0.8
$^{171}\text{Yb}^+$	$^2S_{1/2} \longrightarrow ^2D_{3/2}$	436	3.1
$^{171}\text{Yb}^+$	$^2S_{1/2} \longrightarrow ^2F_{7/2}$	467	$\times 10^{-9}$
$^{199}\text{Hg}^+$	$^2S_{1/2} \longrightarrow ^2D_{5/2}$	282	1.8

Table 1.2: Trapped ion based atomic clocks: Trapped ion optical clocks currently under development. The clock transition, their wavelengths and their natural linewidth is mentioned alongwith.

1.5.3 Nuclear transition for time measurement

The hunt for a nuclear transition suitable for the clock started in 2003. Unlike the atomic clocks, the nuclear clock uses the transition between two states of an atomic nucleus. These clocks have not yet been realized, but it has the potential to outperform the existing timekeepers based on the atomic transitions and have applications in both fundamental and applied physics [82]. The most promising candidate in this category is

based on an excited nuclear state of *thorium-229*. Unlike the other known nuclei, this nucleus has an excited state (known as the isomeric state) only at a few eV above the ground state. With the advancement in laser technology, this state is now accessible. The hurdle is that the exact energy of this isomeric state is not known. However, there have been efforts towards understanding the exact character of *Th-229* transition [83,84]. The experiment, along with the simulations, shows that the *Th-229* nucleus can be excited by using a laser at a wavelength of around 150 nm. This clock is expected to be ten times more accurate than the best optical clock with an achievable accuracy approaching the 1×10^{-19} level [85].

Strontium optical lattice clock

Sr is one of the most popular species due to favorable level structures for laser cooling and trapping. The level structures are similar to Ca, another candidate for the atomic clock. Sr has two inter-combination transitions that can be used as a clock. These transitions are:

- $^1S_0 - ^3P_1$ transition. This transition is broader than similar transition in Ca. The linewidth of this transition is 7.4 kHz and is also used for the second stage of cooling. Due to favorable laser cooling, this transition is of interest as more and more atoms are available for interrogation, thus increasing the SNR. Also, the achievable cloud temperature is low. One can, therefore, expect the stability to be similar to that of the Ca system albeit with reduced sensitivity to Doppler shifts due to a slightly broader transition.
- *The doubly forbidden singlet to triplet transition: $^1S_0 - ^3P_0$ in ^{87}Sr .* The linewidth of this transition is ~ 1 mHz, and thus the achievable Q is only limited by technical issues such as laser noise and not by the transition itself. As mentioned earlier, this species is the most favorable due to the existence of transition that can be easily interrogated using the available lasers.

As mentioned in earlier section, the selection of laser with the appropriate wavelength is crucial for the reliable clock operation. The lattice laser must operate at the magic wavelength to compensate for uneven light shifts of the clock states. The wavelengths at

which the differential light shift is zero are ~ 915 nm and ~ 813 nm [86] for the above two transitions.

1.6 Applications of optical clocks

With its rapid development and excellent stability and accuracy, optical clocks have the potential to affect various fields in science and engineering. Some of them are the following:

Technological applications

The atomic clock is an integral part of the global navigation satellite system (GNSS). An atomic clock with an ultra-narrow optical transition can be used to improve navigational and timekeeping capabilities. Atomic clocks are fundamental tool in modern society and are present in satellites, primarily for navigation systems such as GPS. With the current microwave-based atomic clocks, the position can be determined within 20 meters on earth. The use of optical clock for navigation can potentially improve the position determination by 2-3 orders of magnitude.

Primary standard and worldwide coordination of atomic time

With the above-mentioned precision and accuracy of the optical atomic clocks, it is possible to redefine the SI second based on the optical transition. A comparison of reported uncertainty for various optical clocks is given in table- 1.3. These numbers are generated by utilizing measured or theoretically calculated sensitivities of the clock transition to external effects that shift the clock transition, e.g., Stark shifts, black-body radiation shifts, Zeeman shifts, background collision induced shifts, etc.

Atom/Ion	Clock Type	Clock λ nm	best published systematic uncertainty
^{87}Sr	Lattice	698	2×10^{-18}
$^{171}\text{Yb}^+$	Ion octopole	467	3.2×10^{-18}
$^{27}\text{Al}^+$	Ion, Quantum logic	267	8.6×10^{-18}
$^{88}\text{Sr}^+$	Ion quadrupole	674	1.2×10^{-17}
$^{199}\text{Hg}^+$	Ion quadrupole	282	1.9×10^{-17}
$^{40}\text{Ca}^+$	Ion quadrupole	729	3.4×10^{-17}
^{199}Hg	Lattice	266	7.2×10^{-17}
$^{171}\text{Yb}^+$	Ion quadrupole	436	1.1×10^{-16}
^{171}Yb	Lattice	578	3.4×10^{-16}
^1H	Cryogenic beam	243	4.2×10^{-15}

Table 1.3: Secondary representation of second: Systematic fractional uncertainty of various optical clock species.

Except for ^1H , ^{199}Hg and $^{40}\text{Ca}^+$, all the candidates mentioned in table- 1.3 have been accepted as the secondary representation of the second by the International Committee for Weights and Measures (CIPM) [87] with the mentioned fractional uncertainty. The long-term performance of these clocks is being established by regularly reporting the clock operational data from various research laboratories to the International Bureau of Weights and Measures (BIPM).

Radio telescopey

The possibility to use optical clocks to precisely synchronize data signals coming from different places is applied to radio astronomy to synchronize different radio telescopes placed in different places on earth, looking at the same star. This approach, called ‘Very Large Baseline Interferometry,’ allowed to reach an effective angular resolution equivalent to have a single telescope with an aperture diameter of the size of the Earth [88].

For geodetic applications

The transition frequency of an optical clock on the earth's surface is affected by the gravitational redshift. This effect can be used for high precision mapping of the geoid (hypothetical surface of constant gravitation potential) of earth. This can be done by the frequency comparison of terrestrial transportable clocks with a master clock [89, 90]. The sensitivity of space optical clock-based geodesy will make it possible to monitor the motion of the surface of the earth with such outstanding precision that a new level of understanding of geophysical effects may be obtained, including earthquakes and volcano eruptions.

For deep space navigation

For deep space missions, the position and velocity of a spacecraft are determined by measuring the time taken by the signal from earth to reach the spacecraft and receive it back on earth. This two-way process can be a severe problem in future interplanetary travels. It is proposed that this problem can be avoided by incorporating an atomic clock in the spacecraft itself. In such a scenario, the spacecraft needs a minimal signal from an earth-based station to calculate its position and speed [91]. The first deep space atomic clock is launched by NASA using SpaceX's Falcon Heavy rocket. It is a miniaturized and stable mercury ion atomic clock. Currently, the clock is inside the orbital testbed (OTB) revolving around the earth in the low earth orbit for testing its precision and accuracy in the extreme space environment.

Variations in the fundamental constants

Due to unprecedented precision, optical clocks are useful for investigating fundamental physics. One such example is the Hafele-Keating experiment [92], which used atomic clocks to test the predictions of general and special relativity. Another such area is in the theories beyond the standard model of physics that predicts the temporal variation of the constants of nature, such as topological defect dark matter [93–95]. Since these constants of nature affect the structure of atoms, changes in these constants would be manifested as the changes to the energy levels of atoms, thus the change in atomic clock transition, which is measurable with the current state-of-the-art atomic clocks.

Many experiments have been carried out to measure such deviations in the constants of nature [96–99].

1.7 Objective of the thesis

This thesis deals with the development of an experimental setup for the application towards the precision measurements and frequency metrology using the doubly forbidden singlet to triplet transition at 698 nm. Since this transition has an extremely low linewidth and is highly sensitive to external environmental perturbation, it can be considered as an ideal candidate for a precision sensor. This thesis describes the design and construction of an experimental setup that generates an ensemble of cold ^{88}Sr atoms in MOT and magnetic trap. During the development of this setup various novel designs have been developed such as a spectroscopy cell for performing the beam spectroscopy of Sr atoms, and developments of simple atomic beam oven for loading the MOT from Zeeman slowed atoms.

The developed system has been used for the measurement of the collision cross section between ^{88}Sr and N_2 in the MOT. This measurement is important as N_2 is one of the prominent species that remains in the vacuum chamber even after the bake-out and affect the ultimate achievable lifetime of the atomic sample. These background collisions induce shifts and broadening of the clock transition. This collision induced contribution towards the total error budget of the Sr based optical atomic clock can be determined by using the C_6 coefficients of the ground and excited clock state. We have used the loss rate of atoms from the MOT to determine the collision cross section and for the determination of C_6 of the ground state of clock transition. We have also studied various loss mechanisms of the atoms in the MOT. We characterize the effect of usually ignored channel, i.e., the loss induced by the escape of atoms out of the capture region. This loss rate is proportional to the temperature of the atoms. We show that for the atomic species that require two stages of laser cooling, this loss channel is the dominant one and must be considered for the complete description of the system.

Organization of the thesis

Chapter 2 presents the physics of laser cooling of dilute neutral gases. The explanation of light forces on the atoms, Doppler cooling, MOT and the temperature determination using the technique of release and recapture.

Chapter 3 describes the experimental setup used for the production of a cold sample of Sr atoms in MOT and a magnetic trap (MT). This includes the design and construction of the vacuum chamber with a pressure of less than 10^{-10} torr in the science chamber. This section also describes the design of an atomic oven for loading the MOT.

Chapter 4 describes the generation of lasers for cooling and repumping transitions. Theory and experimental realization of the second harmonic generation for the production of the laser at 461 nm have been explained. This chapter also discusses about the frequency stabilization of the first stage cooling laser by performing Doppler free spectroscopy, frequency schemes for various laser beams and production of magneto-optically trapped atomic cloud.

Chapter 5 reports the first experimental measurement of Sr–N₂ collision cross section in MOT. This chapter also describes the model to explain the various loss mechanisms of atoms in MOT and determination of C_6 of the ground state of the clock transition. We also show that for the atomic species which require two stages of cooling, the loss rate induced by the thermal escape of atoms from the trapping region can play a significant role in the total observed loss rate.

Chapter 6 summarizes and presents the future outlook for this work.

In the end, **Appendix** describes the mechanical designs of various components and electronic circuits diagrams of the devices used during the experiment.

Chapter 2

Theoretical background

This chapter describes the theoretical background required for laser cooling and trapping of neutral atoms. A semi-classical treatment is presented. The analysis is done by considering the atom as a two-level system in the presence of an external electromagnetic field. The principles of laser cooling and trapping of atoms using dissipative and conservative forces are discussed briefly.

2.1 Importance of cooling and trapping

The techniques of laser cooling and trapping have opened a new pathway to study matters at low and ultra-low temperatures. These samples at ultra-low temperatures find extensive use in experiments ranging from quantum degeneracy, quantum simulations to quantum information processing, and in building the most accurate atomic clock. Utilizing the atomic transition as a frequency reference depends entirely on the experimental capability of isolating the atoms from the environment and the accurate measurement of the transition frequency between the two selected atomic states. The discovery of using lasers for reducing the thermal motion of atoms has given experimentalists the necessary tool to cool the atomic sample to a very low temperature and eliminate the perturbing effects that cause frequency shifts and line broadening.

From an experimental point of view, the ideal situation would be to have a collection of atoms completely at rest in the laboratory frame of reference. This would correspond to a temperature of absolute zero which is impossible to achieve, as it violates the laws

of physics. The most realistic situation would be the one where a collection of atoms moves with a statistical distribution of velocities governed by the Maxwell-Boltzmann distribution law at some finite non-zero temperature. According to this, for a sample of atoms in thermal equilibrium at a temperature T , the number of atoms in the velocity class of v and $v + dv$ is given by:

$$f(v)dv = \left(\frac{m}{2\pi k_B T} \right)^{3/2} \exp\left(-\frac{mv^2}{2k_B T} \right) dv \quad (2.1)$$

At a temperature T , these atoms move with an average velocity of v_0 ,

$$v_0 = \sqrt{\frac{8k_B T}{m}} \quad (2.2)$$

Here, k_B is the Boltzmann constant and m is the mass of the particle under consideration.

This finite temperature and hence the finite velocity of the atoms in the laboratory frame of reference gives rise to several undesirable effects while observing the natural spectral features of an atomic ensemble. One such effect arises due to the motion of an atom with respect to the direction of an incoming interrogation light, leading to a shift in the measurement of the natural angular frequency $\omega_0 = 2\pi\nu_0$, called the Doppler shift. For the atomic motion that is much smaller than the speed of light, this shift is given by:

$$\omega'_0 = \omega_0 + \mathbf{k} \cdot \mathbf{v} \quad (2.3)$$

Here, ω'_0 is the natural angular frequency of the addressing laser in the laboratory frame of reference, \mathbf{v} is the velocity of atoms with respect to the interrogation light having a wave vector \mathbf{k} . In the atomic spectroscopy experiments, atoms act as a source of radiation, and the detector is the observer in the laboratory frame of reference. This leads to the observed broadening of the spectral lines. This is called the Doppler broadening. Eq. 2.1 can be modified as:

$$f(v)dv = \frac{1}{v_{mp}\sqrt{\pi}} \exp\left(-\frac{v^2}{v_{mp}^2} \right) dv \quad (2.4)$$

Here, v_{mp} is the most probable velocity, given by $v_{mp} = \sqrt{\frac{2k_B T}{m}}$. In the presence of an interrogation light, each velocity class of the atoms experiences a different Doppler shifts given by Eq. 2.3. The cumulative effect of these individual shifts due to all atoms of the ensemble leads to a Gaussian line shape in the total frequency response of an atomic ensemble.

$$\frac{\Delta\nu_D}{\nu_0} = 2\sqrt{\text{Ln}2}\frac{v_0}{c} \quad (2.5)$$

Besides, due to the finite velocity v , when these atoms transverse the probe laser beam with diameter d in the direction perpendicular to the wave vector \mathbf{k} , the interaction time between the light and the atoms is limited to τ . This limited interaction time induces transit-time broadening. This is a direct manifestation of the energy-time uncertainty relation and is given by:

$$\Delta_{tt} \approx \frac{1}{\tau} = \frac{v}{d} \quad (2.6)$$

This broadening can be more significant than the natural linewidth of a transition and thus hinder the capability to take the full advantage of its high Q value.

The above discussion shows that to access the natural transition properties of atoms and to reduce the shift and broadening in the transition frequency arising from their thermal motion, it is imperative to cool and trap them. Unlike charged particles, cooling and trapping of neutral atoms is technically complicated. However, developments in the field of lasers have provided the tool to manipulate the internal and external degrees of freedom in atoms by light-atom interaction. Since then, rapid progress in the field of laser cooling and trapping has enabled experimentalists to use the radiation force to cool atoms. These cold atoms are now the ideal candidates for the precision measurements and frequency metrology.

One of the key requirements for an atom to be cooled using the techniques of laser cooling is to have simple energy levels with a strong cyclic cooling transition. The second most important criteria is the availability of lasers to address individual energy levels. Conventionally, alkali atoms such as rubidium (Rb), sodium (Na), potassium (K), cesium (Cs) have been the elements of choice due to the above-mentioned reasons. The experiments with alkali metals led to the first observation of Bose-Einstein Condensation (BEC) in rubidium [100, 101] and sodium [102, 103] and the achievement of

first Degenerate Fermi Gas using potassium.

Alkaline earth elements are the elements from the neighboring group in the periodic table. These elements have relatively rich electronic levels, which can be used to study various physical phenomena. However, working with these elements is challenging due to demanding wavelength requirements for cooling and trapping stages. Nevertheless, the research using these elements is pursued because of the immense possibilities offered by them to study the diverse physical phenomenon. As mentioned in the previous chapter, these alkaline earth elements are the leading candidates for the optical frequency reference due to the existence of their uniquely addressable energy levels. Alkaline earth element, *strontium* is one such promising candidate for frequency reference. In the following sections, we present some relevant physical and chemical properties of *strontium*.

2.2 The strontium atom

Strontium is an element having an atomic number of 38. It is denoted by the symbol ‘Sr’ and belongs to the second group of the periodic table. The elements belonging to this group are called the alkaline earth elements or group-II elements. Sr is a soft silver-white metallic element that is chemically highly reactive. It occurs in the minerals celestine and strontianite. Some of the fundamental physical properties of Sr has been tabulated in table- 2.1.

Quantities	Value
Phase	solid
Melting point	1050 K
Boiling point	1650 K
Density	2.64 g/cm ³
Vapor pressure	1 Pa @ 796 K

Table 2.1: Physical properties of Sr atom

There are four naturally occurring stable isotopes of strontium atom. The list of these isotopes of strontium along with their relative abundance, atomic mass, and nuclear spin is given in table- 2.2.

Strontium has two valence electrons in the outer shell. The energy levels can be grouped into two separate classes similar to atomic helium, viz.

- with the anti-parallel arrangement of the electronic spins such that the total spin is $S = 0$, called the singlet state
- with electronic spins aligned parallelly, so the total electronic spin is $S = 1$, called the triplet state

There are strong transitions within the singlet and the triplet states. Most of these transitions lie in the visible region of the electromagnetic spectrum. The transitions between the singlet to triplet states are not allowed under the dipole approximation. However, the spin-orbit interaction, which breaks the spin symmetry, provides a small probability of such transitions to take place under the dipole approximation. These inter-combination lines are usually very narrow with the linewidths of the order of mHz to kHz and are suitable for the metrology applications and laser cooling with smaller Doppler limited temperature. Experiments reported in this thesis uses the most abundant even isotope ^{88}Sr .

Isotope	Nature	Nuclear spin	Relative atomic mass	Relative abundance
^{84}Sr	Boson	0	83.913 425(4)	0.56(1)
^{86}Sr	Boson	0	85.909 2624(24)	9.86(1)
^{87}Sr	Fermion	9/2	86.908 8793 (24)	7.00(1)
^{88}Sr	Boson	0	87.905 6143(24)	82.58(1)

Table 2.2: Isotopes of Sr atom: Naturally stable isotopes of Sr atom. Numbers are taken from NIST data.

The bosonic isotopes of Sr have zero nuclear spin; therefore, the states with $J = 0$ do not have hyperfine sub levels. This fact is crucial for precision spectroscopy as in the absence of nuclear spin, the state with $J = 0$ is insensitive to the stray magnetic field. This insensitivity to the magnetic field makes them an ideal candidate for the optical atomic clock. Some of the advantages offered by strontium are listed below:

- The existence of strong cooling transition for the first stage of cooling and trapping

- The existence of narrow inter-combination transition that can be used for the second stage of cooling the atomic sample
- The presence of ultra-narrow singlet to triplet transition that can be utilized for the experiments related to atomic clock and metrology
- The even isotope of Sr, particularly ^{88}Sr , has an extremely low collision cross section in its ground state. This makes them immune to collision-induced broadening
- The existence of the metastable state with a very large lifetime. This state is particularly crucial for trapping atoms in a magnetic reservoir and for the experiments which require trapping and manipulation of single atom

The other elements of choice for the frequency reference are magnesium [104], calcium and other two-electron elements such as ytterbium and mercury. All of them are collectively called the alkaline-earth-metal-like elements. Strontium is preferred due to the existence of energy levels lying in the visible or near-infrared range. These transitions are easily accessible using the existing technology of diode lasers.

Following the discussion about the unique properties of Sr atoms, we will focus on the atomic transitions used for laser cooling and trapping.

The low lying relevant energy level diagram of strontium is shown in Fig. 2.1. In this figure, the atomic states are labeled by using *Russel-Saunders (RS)* notation of $^{2S+1}L_J$, where S is the total electronic spin with values 0 or 1 corresponding to singlet and triplet states as mentioned earlier, L is the orbital angular momentum of electrons, and $J = L + S$ is the total angular momentum of the state under consideration. Much of the interest in strontium atoms relies upon the existence of narrow inter-combination lines, especially the $^1S_0 \rightarrow ^3P_0$. This transition is doubly forbidden under the selection rule $\Delta S = 0$ and $\Delta J \neq 0$ (if $J = 0$). For even isotopes, this transition has virtually zero linewidth in the absence of an external magnetic field. However, in case of an odd isotope, the hyperfine mixing of the states gives rise to a finite linewidth of the order of 1 mHz.

2.2.1 Cooling transitions

The first stage cooling transition:

The strong dipole allowed cyclic transition $5s^2\ ^1S_0 \longrightarrow 5s\ 5p\ ^1P_1$ is used for the first stage of cooling and trapping. It requires a laser having a wavelength of 460.8 nm. This transition has a very short lifetime of ~ 5 ns, which corresponds to the linewidth of 32 MHz. The broadness in this transition is reflected in the higher Doppler limited temperature of $\sim 770\ \mu\text{K}$. Also, the transition itself is not entirely closed. Atoms, when excited to 1P_1 state, decays to 1D_2 state with a branching ratio of $1 : 2 \times 10^{-5}$. These atoms can further decay to the triplet states $5s\ 5p\ ^3P_2$ and $5s\ 5p\ ^3P_1$ states with a branching ratio of $1 : 2$ respectively.

The second stage cooling transition:

One of the advantages of Sr atoms is the existence of an inter-combination line, which is suitable for second-stage cooling. Pre-cooled atoms after the first stage cooling utilizing the blue transition can be transferred to a MOT operating using a laser addressing the transition $5s^2\ ^1S_0 \longrightarrow 5s\ 5p\ ^3P_1$. This singlet to triplet transition has a wavelength of 689.4 nm. This transition has a relatively long lifetime of $21\ \mu\text{s}$ and linewidth of $2\pi \times 7.5$ kHz. It has an extremely low Doppler limited temperature of 180 nK. The parameters relevant for each of the cooling stages are summarized in table- 2.3.

2.2.2 Repumping transitions

As mentioned earlier, atoms in the excited state 1P_1 can decay to the intermediate state 1D_2 with a branching ratio of $1 : 2 \times 10^{-5}$. These atoms in intermediate state 1D_2 further decay to states 3P_2 and 3P_1 with a branching ratio $1 : 2$, respectively. The atoms in 3P_1 have a lifetime of $21\ \mu\text{s}$ and can decay directly to the ground state 1S_0 . However, atoms in the state 3P_2 can not directly decay into the ground state and require additional lasers to bring them back into the primary cooling cycle.

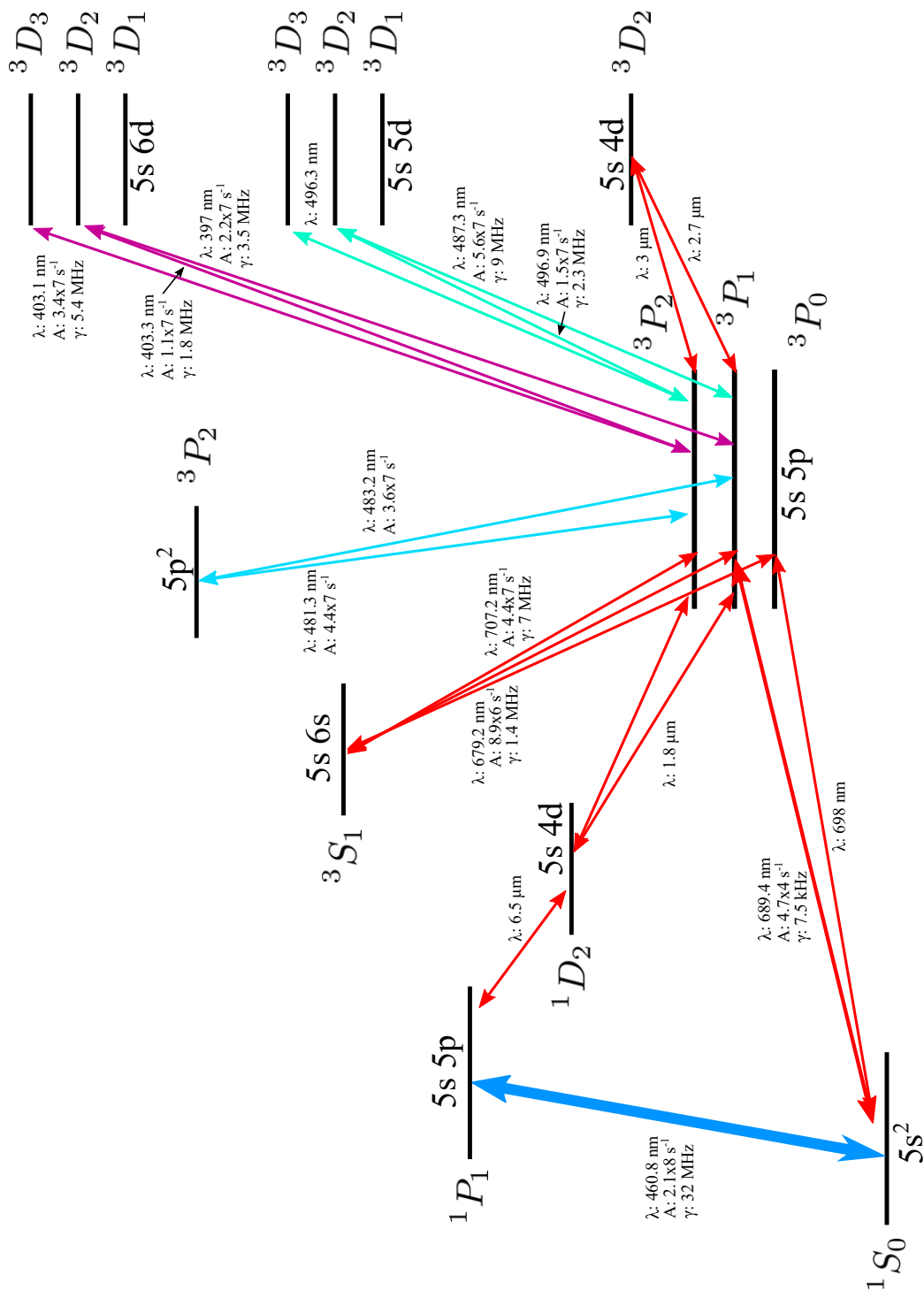


Figure 2.1: Schematic Grotrian diagram for strontium transitions: The low lying electronic energy levels of atomic strontium. The clock transition $1S_0 \rightarrow 3P_0$ and the transitions for laser cooling and repumping are indicated with their wavelength, linewidth and scattering rates.

Transition	λ (nm)	T_D	T_r	I_{sat}	a_{max} (m/s ²)
$^1S_0 \rightarrow ^1P_1$	461	770 μK	1.03 μK	43 mW/cm ²	$\sim 10^6$
$^1S_0 \rightarrow ^3P_1$	689	180 nK	460 nK	3 $\mu W/cm^2$	160

Table 2.3: Comparison of the two cooling transitions: Relevant parameters for laser cooling and trapping using the $^1S_0 \rightarrow ^1P_1$ and $^1S_0 \rightarrow ^3P_1$ in Sr atoms.

There are several repumping schemes to clear the atoms from the triplet state 3P_2 . However, depending on the availability of lasers some of the schemes are more popular than the other:

- $5s 5p \ ^3P_2 \rightarrow 5s 5d \ ^3D_2$:

This repumping scheme requires a single laser with a wavelength of 496.9 nm. This takes the atoms from the state 3P_2 to the excited state $5s 5d \ ^3D_2$. Atoms from this state decay back to state 3P_2 and 3P_1 . The atoms in 3P_1 decay back to ground state 1S_0 .

- $5s 5p \ ^3P_2 \rightarrow 5s 6d \ ^3D_2$:

Similar to the transition mentioned earlier, this scheme also requires a single laser with wavelength 403.3 nm. This laser pumps the atoms to a higher D manifold, i.e., to the atomic state $5s 6d \ ^3D_2$. The decay channel for the excited state atoms is similar to the scheme mentioned above. This repumping scheme is not widespread due to the difficulty in the availability of the laser.

- $5s 5p \ ^3P_2 \rightarrow 5s 6s \ ^3S_1$ and $5s 5p \ ^3P_0 \rightarrow 5s 6s \ ^3S_1$:

This repumping scheme requires two lasers operating at a wavelength of 707.2 nm and 679.2 nm. In this scheme, atoms in the state $5s 5p \ ^3P_2$ are excited to the state $5s 6s \ ^3S_1$ using a laser at wavelength 707.2 nm. These excited state atoms decay to 3P_2 , 3P_1 and 3P_0 . If they decay to 3P_2 , they are again pumped to $5s 6s \ ^3S_1$ state. Atoms decayed to 3P_1 can return to the ground state 1S_0 . However, the atoms that decay to the state 3P_0 are lost from the cooling cycle as the transition from this state to the ground state is forbidden by the spin selection rule. To revive these atoms, another laser at a wavelength of 679.3 nm is required. This laser pumps the atoms from 3P_0 to $5s 6s \ ^3S_1$ state. Since the laser diodes are easily available for both these wavelengths, this is the

most popular scheme to suppress the loss of atoms into the metastable states.

- $5s\ 5p\ ^3P_2 \longrightarrow 5s\ 4d\ ^3D_2$:

Similar to the above mentioned repumping transitions connecting the metastable state 3P_2 to the D state manifolds, this scheme also requires only one laser with a wavelength of $3\ \mu\text{m}$. This transition connects $5s\ 5p\ ^3P_2$ to $5s\ 4d\ ^3D_2$ states.

- $5s\ 5p\ ^3P_2 \longrightarrow 5p^2\ ^3P_2$:

Reviving the atoms from the metastable state 3P_2 can be done using a laser operating at the wavelength of 481.3 nm. This laser pumps the atoms to the excited state $5p^2\ ^3P_2$. These excited-state atoms can decay back to states 3P_2 and 3P_1 . The atoms in triplet state 3P_1 decay back to the ground state 1S_0 of the principal cooling transition.

2.2.3 The clock transition

The doubly forbidden singlet to triplet transition connecting $5s^2\ ^1S_0 \longrightarrow 5s\ 5p\ ^3P_0$ at a wavelength of 698 nm is the clock transition in Sr atom. This transition has a natural linewidth of 1 mHz for fermionic isotope ^{87}Sr and the measured frequency is 429,228,004,229,874.0 (1.1) Hz [105]. For the Bosonic isotope, this transition is forbidden under the spin selection rule. However, in the presence of a small external magnetic field, one can induce mixing between the two states of triplet manifold: 3P_0 and 3P_1 . This mixing gives a finite lifetime to this transition, that can be used as the clock transition.

2.3 Laser cooling and trapping

2.3.1 Light atom interaction

To understand the concept behind the laser cooling, a semi-classical model is sufficient. In this model, the energy levels of atoms are considered to be quantized, and the light is considered as a classical oscillating field. The light interacts with the atoms in various ways, such as in the presence of an oscillating electric field of the radiation, the population of atom oscillates between the ground state and the excited state with a characteristic frequency. This frequency is called the Rabi frequency, and the phenomenon

is known as Rabi oscillations. Here, it is assumed that the atoms have only two energy levels. On the other hand, there is a shift in energy that occurs in the presence of external electromagnetic radiation. This shift is known as the light shift or AC stark shift. This occurs due to the coupling of the electric field with the induced electric dipole moment of the atom.

Broadly, based on the nature of interaction, the force experienced by atoms in the presence of external electromagnetic radiation can be divided into two categories:

- 1) **Dissipative force:** Arises due to spontaneous emission
- 2) **Dipole force:** Arises due to intensity gradient seen by atoms

The concept of laser cooling and trapping is based on the fact that, like matter, a photon has both energy and momentum. According to Einstein's theory, each quanta of light, called the photon, carries an energy $E = h\nu$ and momentum of $p = \hbar k$. Here, ν is the frequency of radiation, and k is the wave vector and is given by $k = 2\pi/\lambda$. The laser cooling can be achieved by transferring the momentum to the atoms in an orderly way. When an atom is placed in a beam of light whose frequency is close to the atomic transition frequency, it absorbs a photon and goes to the excited state. Now, considering the velocity of the atom to be v , the momentum of the atom changes from $p_{atom} = mv$ to $p_{atom} = mv + \hbar k$. Thus, during an absorption process, atom experience a momentum kick in the direction of the light beam. On subsequent relaxation, the atom spontaneously emits a photon in a random direction and experiences a momentum kick in the direction opposite to that of the of emission of the photon. However, this emission is a random process and is isotropic in nature. Thus, averaging over many absorption and emission cycles, the momentum transfer due to the emission of photons is zero, and atom experience a net change of momentum or force due to the absorption process. This scattering force is directed along the direction of the laser beam and is given by:

$$\mathbf{F}_s = \hbar \mathbf{k} R_s \quad (2.7)$$

In the above equation, \mathbf{F}_s is the force experienced by the atoms by undergoing absorption and emission cycle in the presence of external electromagnetic radiation with wave vector \mathbf{k} , \hbar is the reduced Planck's constant and R_s is the scattering rate of the atom.

The scattering rate is given by:

$$R_s = \frac{\Gamma}{2} \frac{I/I_{sat}}{1 + I/I_{sat} + (2\Delta/\Gamma)^2} \quad (2.8)$$

In the above equation, I is the total intensity of the laser beam, and I_{sat} is the saturation intensity of the transition under consideration. Δ and Γ are the detuning and the linewidth of the transition, respectively. The saturation intensity is given by:

$$I_{sat} = \frac{h\nu}{2\tau(3\lambda^2/2\pi)} \quad (2.9)$$

Here, τ is the lifetime of the excited state, and ν is the frequency of the atomic transition under consideration.

2.3.2 Doppler cooling of atoms

The temperature of an ensemble is defined by the randomness of the motional degree of constituent particles. A sample where the particles are moving at a higher average speed is said to have a higher temperature. The law of equipartition of energy relates the temperature of a cloud of atoms to the average velocity of the particles. Thus the reduction of temperature implies that the average speed of constituent particles is being reduced. The idea behind the laser cooling is to use the scattering force by external electromagnetic radiation to reduce the velocity of atoms to the minimum possible value.

As mentioned at the beginning of this chapter, a collection of atoms at room temperature moves with a distribution of velocities governed by the Maxwell Boltzmann distribution. The frequency of the addressing laser seen by these moving atoms in their rest frame is different from the frequency of the laser in the laboratory frame of reference. This shift in frequency is given by a factor $\omega_D = \mathbf{k} \cdot \mathbf{v}$, called the Doppler shift. This relation holds only for the atoms that move with velocities much smaller than the speed of light. Let us consider the frequency of the laser is ω_L , and the resonant transition frequency of the atom is ω_0 . The detuning of the laser light is defined as;

$$\Delta = \omega_L - \omega_0 \quad (2.10)$$

If the value of Δ is positive, the laser is said to be blue-detuned, and if the value is negative, the laser is red-detuned.

In order to understand the concept of Doppler cooling, we consider a simplified case where the atom is moving in one dimension, in the presence of two counter-propagating laser beams. If both the beams are red-detuned with respect to the atomic transition frequency, the atoms moving opposite to the direction of propagation of light sees the frequency to be upshifted by a factor ω_D . The effective frequency of laser seen by the atoms is:

$$\omega'_L = \omega_L - \omega_D = \omega_0 + (\mathbf{k} \cdot \mathbf{v} + \Delta) \quad (2.11)$$

The above equation shows that the Doppler cooling technique is based on the velocity dependence of the scattering force. Only those atoms will absorb the photons for whom the Doppler shift is precisely equal to the detuning of the laser beam. In this case, the scattering rate is given by Eq. 2.8, and hence the force experienced by atoms is maximum.

Above analysis shows that the atoms are more likely to absorb photons from a laser beam opposite to its direction of motion, resulting in a cooling force. On each absorption of a photon, the atom experience a momentum kick of magnitude $\hbar k$ in the direction opposite to motion. The recoil momentum kick during the relaxation of atoms due to spontaneous emission is isotropic and averaged to zero, as mentioned earlier. For the case of low intensity ($I/I_{sat} \ll 1$) of counter-propagating laser beams, the net force experienced by an atom is $\mathbf{F}_{net} = \mathbf{F}_+ + \mathbf{F}_-$ and can be expressed as:

$$\mathbf{F}_{net} = \hbar \mathbf{k} \frac{\Gamma}{2} \frac{I/I_{sat}}{1 + I/I_{sat} + 4((\Delta - \omega_D)/\Gamma)^2} - \hbar \mathbf{k} \frac{\Gamma}{2} \frac{I/I_{sat}}{1 + I/I_{sat} + 4((\Delta + \omega_D)/\Gamma)^2} \quad (2.12)$$

The plot of force as a function of velocity is shown in Fig. 2.2. The graph shows that the force is always opposite to the velocity of atoms. For small velocities of atoms, i.e., $kv \ll \Delta$, the above equation can be modified as:

$$\mathbf{F}_{net} \approx -\beta \mathbf{v} \quad (2.13)$$

Here, the constant of proportionality β is called the damping constant and is given as:

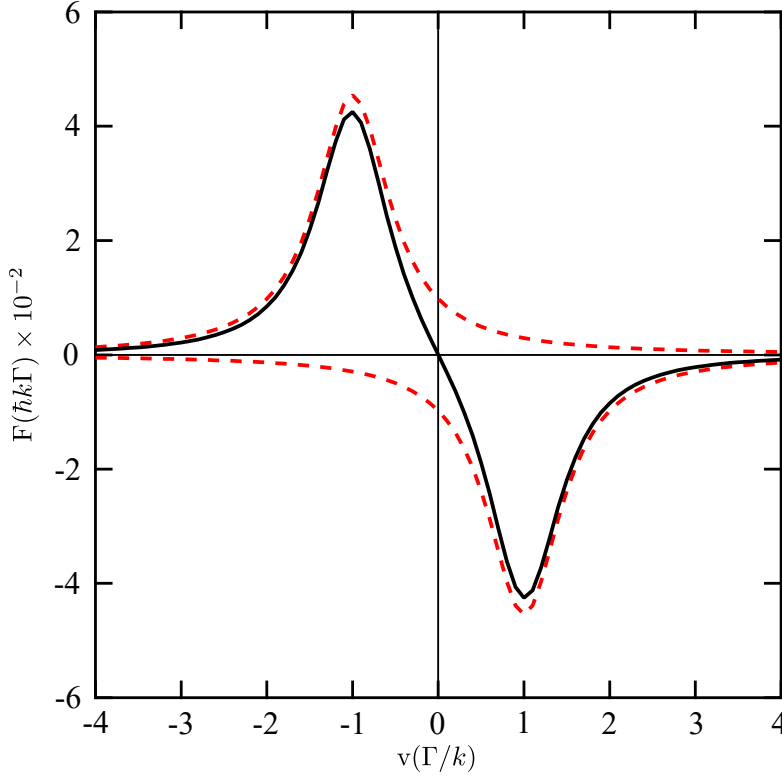


Figure 2.2: Doppler force: The force experienced by an atom in a counter-propagating laser beam as a function of atomic velocity. The parameters are taken to be $I/I_{sat} = 0.1$ and $\Delta = -\Gamma$. The dashed lines show the forces due to the individual laser beams, and the solid line represents the net force experienced by the atom. Note that this plot is true only for the broad transition used for the first stage cooling of Sr atoms. For the second stage of cooling, the situation becomes complicated due to the narrow linewidth of the transition.

$$\beta = -8\hbar k^2 \frac{\Delta}{\Gamma} \frac{I/I_{sat}}{[1 + I/I_{sat} + 4(\Delta/\Gamma)^2]^2} \quad (2.14)$$

For red-detuning of laser beams, β is positive, and the force is similar to the frictional force, which opposes the motion of atoms and proportional to its velocity. This is similar to the movement of a particle in a viscous medium and is called the “*optical molasses*”.

If there were no other influences on the atomic motion, the atoms would have cooled to the temperature close to absolute zero. However, this is not possible physically. Due to the discrete size of the momentum transfer during the absorption and random spontaneous emission of photons, the atoms also get heated. During each decay process, the momentum of atoms changes by $\hbar k$. At the steady-state, the rates of heating and the

cooling rate are in equilibrium, and it sets a lower bound on the temperature that can be achieved by Doppler cooling. The resulting temperature is known as Doppler limited temperature. For a low intensity $I/I_{sat} \ll 1$ and detuning $\Delta = -\Gamma/2$, this minimum temperature T_D [106, 107] is given by:

$$k_B T_D = \frac{\hbar\Gamma}{2} \quad (2.15)$$

The model described above considers a counter-propagating laser beam in only one direction. In a cloud of atoms, the atoms are free to move in all the directions; thus, it needs to be cooled in all three dimensions. This can be achieved by simply adding two extra pairs of mutually perpendicular counter-propagating laser beams. This three-dimensional version is called 3D optical molasses. The first optical molasses was demonstrated by Steven Chu in 1985 [108].

Atoms with degenerate sub-levels can be cooled to a temperature lower than the that set by the Doppler limit. The technique for doing so is called the Sisyphus cooling [109, 110]. The ultimate temperature achieved using laser cooling is limited by the recoil energy gained by the spontaneous emission. In the presence of a resonant light source, the atom will at least have the momentum due to last emitted photon; thus, the limiting recoil temperature is given by:

$$T_r = \frac{\hbar^2 k^2}{k_B m} \quad (2.16)$$

2.4 Magneto optical trap

The optical molasses technique described in the last section, cool the atoms to a certain extent. The minimum temperature reached in the optical molasses is of the order of a few recoil limit. Nevertheless, the most significant disadvantage is that it does not provide the atomic confinement in space. Atoms in the optical molasses are in a diffusive motion within the region where laser beams intersect and move with some minimum velocities and have the tendency to go out of the trapping region. In order to avoid this loss and provide the spatial confinement for the atoms, a position-dependent spring-like force is required that always tries to push the atoms towards the center of the rapping region.

The most widely used trap for neutral atoms uses both optical and magnetic fields and is known as the magneto-optical-trap (MOT). The MOT was first demonstrated in 1987 [111]. The operation of MOT depends on both the inhomogeneous magnetic field and the radiative selection rule for the atomic transitions. It is generated by superimposing an inhomogeneous magnetic field produced by a pair of anti-Helmholtz coil with three counter-propagating pairs of laser beams as in an optical molasses configuration to achieve confinement in three dimensions. In the presence of an external magnetic field, the Zeeman levels of the atoms shift, making the atomic transition frequency position-dependent with respect to the center of the external magnetic field. The field profile due to the quadrupole coil is linear near the center of the trap and is given by:

$$B(z) = bz \quad (2.17)$$

Here, $b (> 0)$ is the magnetic field gradient of the anti-Helmholtz coil. This gradient is determined by the geometry, the number of turns, and the number of layers of the coil. In presence of a magnetic field, the shift in Zeeman sub-level is given by;

$$\Delta E(z) = \mu m_J B(z) \implies \omega_0(z) = \omega_0 + m_J \alpha z \quad (2.18)$$

where, $\alpha = \mu b / \hbar$.

With the proper choice of polarization of the laser beams, the magnetic field provides the required restoring force. In order to understand the working of the MOT, let us consider a simple one-dimensional model with an atom having total angular momentum of the ground state (J) to be zero and that of the excited state to be $J= 1$. For simplicity, we are considering the atom to be in rest. Eq. 2.17 gives the one dimensional analog of the field profile of the spherical quadrupole field. In the presence of such a magnetic field, the Zeeman level of the excited state with $J= 1$ splits into sub-levels $m_j = -1, 0, 1$. The resulting modified energy level of the atom is shown in Fig. 2.3.

Now, if the atom is illuminated by two counter-propagating laser beam with opposite circular polarization and having the detuning to the red side of the atomic resonance, the opposite helicity of the circular polarization of radiation drives different transitions. For example, σ^+ drives $m_j = 0 \rightarrow m_j = 1$ and σ^- excites $m_j = 1 \rightarrow m_j = 0$. The

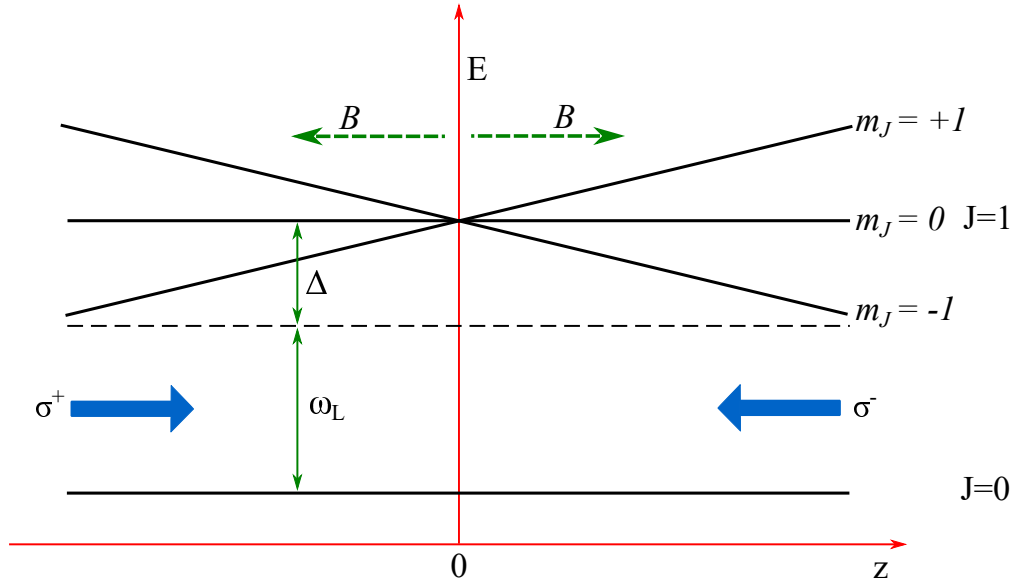


Figure 2.3: MOT Operation: Illustration of working of MOT in 1-dimension for an atomic system with $J = 0$ to $J = 1$ transition. Magnetic field along with the circularly polarized light provides the spatial confinement of the atoms.

allowed transition is governed by the selection rule $\Delta m_j = 0, \pm 1$. Now, if the atom moves towards the right from the center ($z > 0$), atom sees the light with polarization σ^- closer to resonance. This gives a scattering force that pushes the atom towards the center of the trap at $z = 0$. Similarly, if the atom moves towards the left of the center, the light with polarization σ^+ becomes closer to atomic resonance and pushes the atom back to the center. Thus, the force due to preferential absorption of photons gives rise to a force that opposes the motion of the atoms and is always directed towards the center of the trap. In this configuration, the net force experienced by the atom is the combination of dissipative force and the restoring force:

$$\mathbf{F}_{MOT} = -\beta\mathbf{v} - \kappa z \quad (2.19)$$

The first term in the above equation denotes the dissipative force in the presence of the counter-propagating laser beams given by Eq. 2.13. The second term represents the restoring force with a spring constant κ , such that:

$$\kappa = \frac{g_F \mu_B m_F}{\hbar k} \beta \frac{dB}{dz} z \quad (2.20)$$

where, g_F is the Landé g-factor, μ_B is the Bohr magneton, m_F is the magnetic sublevel of an atomic state with corresponding F level and dB/dz is the magnetic field gradient along the z -direction.

The model discussed above considers the force experienced by the atoms in one dimension only. The model can be easily extended to 3D by incorporating two additional pairs of laser beams with appropriate polarization. This gives the confinement along all the three directions for the atoms. Experimentally, the required field is generated using a pair of coils in the anti-Helmholtz configuration. The schematic diagram for the three dimensional MOT is shown in Fig.2.4.

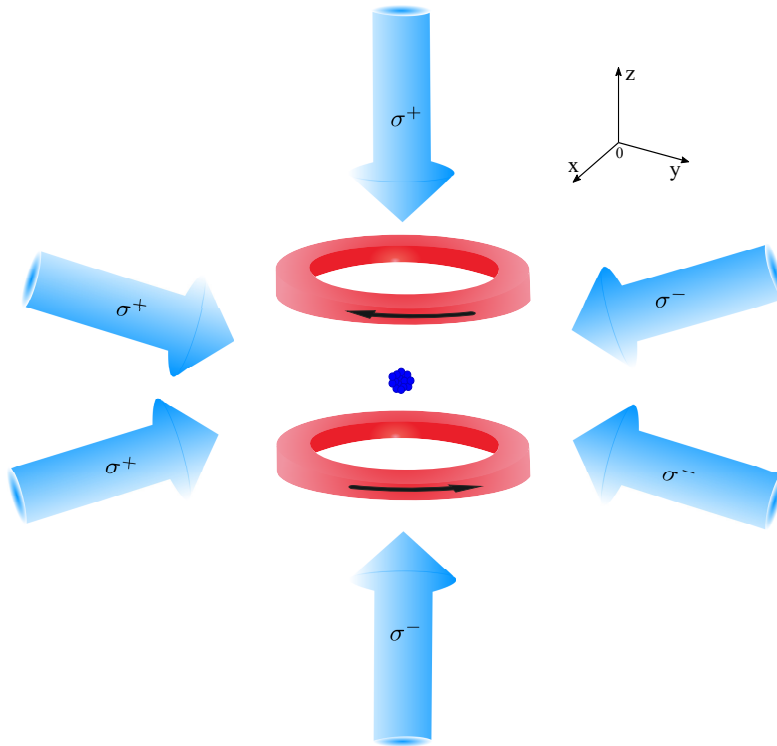


Figure 2.4: Magneto-Optical Trap: Illustration of working of MOT in 3-dimension. Magnetic field along with the circularly polarized light provides the spatial confinement of the atoms.

The MOT is an extremely robust trap. This is practically insensitive to the precise balance of the intensity of the laser beams or their degrees of polarization. The magnetic field gradient requirement is modest and can easily be achieved using a pair of air-cooled coils. This trap is easy to make as it can capture the atoms from room temperature vapor without the use of any particular technique. However, it has to be noted that the MOT

can not capture atoms at any temperature. Every MOT has a characteristic capture velocity v_c that can be expressed as [112]:

$$v_c^{MOT} = \sqrt{\frac{\hbar k_L \Gamma}{M} \frac{r}{4}} \quad (2.21)$$

The temperature of an atomic cloud in MOT is higher than that in the optical molasses due to the following two reasons: The first reason holds for the atomic species with degenerate energy levels. The sub-Doppler cooling mechanism is suppressed due to the presence of an external magnetic field as it breaks the degeneracy of the Zeeman sub-levels, which is crucial for the cooling mechanism to take place. Also, in the MOT at a high-density regime, there is a finite probability that an atom in MOT can absorb the resonant photon spontaneously emitted by the dense cloud of cold atoms.

The MOT is typically used to collect cold atoms from the slowed atomic beam or for loading directly from the background vapor. Such cold samples of atoms are then transferred into different trap geometries for further cooling and performing the experiments.

Strontium has two transitions that can be used for laser cooling. The detailed energy level diagram has been discussed earlier and is shown in Fig. 2.1. The $5s^2 \ ^1S_0 \rightarrow 5s \ 5p \ ^1P_1$ transition has a very small lifetime ~ 5 ns. The corresponding linewidth is 32 MHz. This transition is well suited for pre-cooling and trapping of atoms. The broad linewidth of this transition gives rise to a high cooling force to efficiently cool and trap the atoms. However, this wide linewidth can be disadvantageous too. As we have seen that the Doppler limited temperature is proportional to the linewidth of the transition, cooling using $5s^2 \ ^1S_0 \rightarrow 5s \ 5p \ ^1P_1$ have the Doppler temperature of $T_D = 770 \ \mu\text{K}$, with the typically achievable temperature of the order of few mK [113,114]. The second cooling transition connects the singlet state to triplet state $5s^2 \ ^1S_0 \rightarrow 5s \ 5p \ ^3P_1$. The linewidth of this transition is 7.6 kHz. Atoms can not be directly loaded into the MOT operated using this transition. Thus, the atoms are first cooled and trapped in the broad transition with linewidth 32 MHz called the blue MOT and then transferred to red MOT for additional cooling. This transition has a peculiar property of Doppler temperature to be lower than the recoil temperature. The typical temperatures achieved in red MOT

are of the order of a few μK [113, 115, 116].

2.5 Determination of number of atoms

In order to characterize the MOT, it is necessary to know the number of trapped atoms and their temperature. The number of atoms in MOT is determined by measuring the power of fluorescence emitted by the trapped atoms using a calibrated photodiode/photomultiplier tube. The relation between optical power and the number of atoms is given by the equation:

$$P = \frac{hc}{\lambda} \frac{\Omega}{4\pi} N \gamma_{sc} \quad (2.22)$$

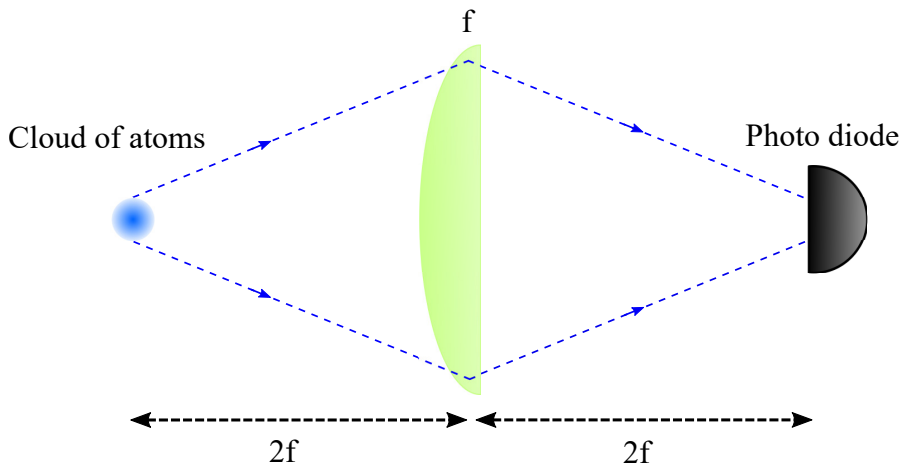


Figure 2.5: Atoms number measurement: Schematic to collect the fluorescence emitted by a cloud of atoms in MOT. A lens of focal length ‘f’ is used to image the atomic cloud onto the calibrated photodiode.

In the above equation, Ω is the solid angle subtended by the collection lens on an atomic cloud and γ_{sc} is the photon scattering rate, given by:

$$\gamma_{sc} = \frac{\Gamma}{2} \frac{I/I_{sat}}{1 + I/I_{sat} + (2\Delta/\Gamma)^2} \quad (2.23)$$

The above equation holds good only for a calibrated photodiode. Thus, for atom number determination, the first step is to calibrate the photodiode. This is done by sending the known amount of light on the photodiode and noting the corresponding generated voltage.

The number of trapped atoms can also be determined using the technique of absorption imaging. In this method, a laser beam in resonance with the atomic species under consideration is shown on the cloud of atoms. The atoms absorb light and form a shadow that is imaged using a CCD camera. This captured image is then processed to get some relevant information such as the temperature and the number of atoms in an atomic cloud. For a laser beam with zero detuning and intensity much less than the saturation intensity, the intensity distribution of the light transmitted through the atomic cloud is given by:

$$I(x, y) = I_0(x, y) \exp \left[-\sigma \int n(x, y, z) dz \right] \quad (2.24)$$

The intensity distribution given by the above equation is imaged on the CCD camera. In the above equation $n(x, y, z)$ is the column density, and σ is the resonant cross section. This is given by:

$$\sigma = \frac{3\lambda^2}{2\pi^2} \quad (2.25)$$

After this, another image with no atoms is taken. This image serves as a reference image for calculating $I_0(x, y)$. Using this, one can calculate the optical density of the trapped atoms. The expression is given by:

$$D_{opt}(x, y) = -\ln \left(\frac{I(x, y)}{I_0(x, y)} \right) = \left[-\sigma \int n(x, y, z) dz \right] \quad (2.26)$$

Using this, the number of atoms can be calculated as:

$$N = \int \int n(x, y) dx dy = \frac{1}{\sigma} \int \int D_{opt}(x, y) dx dy \quad (2.27)$$

Here, N is the total number of atoms. The technique of absorption imaging can further be used for the determination of atomic cloud temperature.

2.6 Magnetic trap

Magnetic trapping of neutral atoms has been used in various experiments such as collision study, creation of Bose-Einstein condensate, precision spectroscopy, etc. It is used

for the confinement of low energy atoms and is usually loaded from the MOT, which collects the thermal atoms and cools them to the temperature of ~ 1 mK. The working of this trap depends on the interaction of the magnetic moment of an atom with the inhomogeneous magnetic field. When an atom with magnetic moment μ is placed in an inhomogeneous magnetic field \mathbf{B} , the force experienced by the atom is given by:

$$\mathbf{F} = -\nabla(\mu \cdot \mathbf{B}) \quad (2.28)$$

Thus the corresponding potential is:

$$U = -g_F m_F \mu_B |\mathbf{B}| \quad (2.29)$$

Since magnetic traps do not require laser light for the confinement of atoms, the ultimate attainable temperature in such traps can be lower than the photon recoil limited temperature. On the other hand, the trap depth of this trap is not as high as MOT and can not be loaded directly from Zeeman slowed atom or from the background vapor.

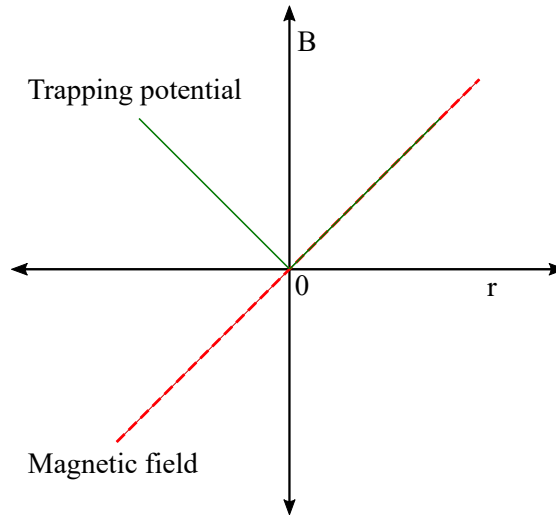


Figure 2.6: Quadrupole field: The field profile generated by the anti-Helmholtz coil along one direction (Red dotted curve) and the corresponding potential seen by the atom (Green solid line).

Although there are many magnetic traps with varying geometries that have been studied in some detail in the literature, it was soon realized that the quadrupole trap containing two coils in the anti-Helmholtz configuration is the simplest among them.

This trap was used during the first atom trapping experiment in NIST for laser cooling of sodium (Na) atoms. This trap provides a magnetic field which varies linearly with distance and increases in all the direction as given below:

$$B = A\sqrt{\rho^2 + 4z^2} \quad (2.30)$$

In the above equation, $\rho \equiv x^2 + y^2$ and A is the field gradient, which is a constant [117]. The field gradient is constant in a particular direction; however, it has different values for them. The field gradients are related as below:

$$B'_z = \frac{\partial B}{\partial z} = 2\frac{\partial B}{\partial r} \quad (2.31)$$

It should be noted that the magnetic force which confines the atoms is neither harmonic nor central.

As discussed in the earlier sections, the first stage cooling transition is not entirely closed, and atoms effectively decay to a metastable state 3P_2 . Atoms in this state ($m_J = 1, 2$) are magnetically trappable and have no direct decay channel to the ground state or the other metastable states. This state effectively works as a magnetic reservoir. It is used for collecting a large number of atoms with small natural abundance for the experiments towards the quantum degeneracy of ^{84}Sr [118]. These atoms can be recovered by applying appropriate repumping lasers. The loading and decay rate of this magnetic trap can be used as a pressure sensor for measuring the background gas level. It has been experimentally shown that one can trap atoms with the number $\sim 10^8$ [119]. The temperature of such a cloud of atoms is found to be ~ 1 mK. The loading into the magnetic trap can be enhanced by using a depumping laser, which effectively pumps the atoms from the triplet states to 3S_1 to 3P_2 [120]. It has to be noted that the ground state 1S_0 of the even isotopes of strontium atoms does not have a magnetic moment; thus, they can not be trapped in pure magnetic potential.

2.6.1 Majorana loss in magnetic trap

When an atom with a finite magnetic moment is placed in an external magnetic field, it experiences a torque. In such a scenario, the magnetic moment of atoms always tries to

follow the direction of the magnetic field to minimize its energy and precesses around it. This phenomenon is known as the Larmor precession. The frequency of precession called the ‘‘Larmor frequency’’ and is given by:

$$\omega_L = \frac{g_F m_F \mu_F}{\hbar} |\mathbf{B}| \quad (2.32)$$

Considering each atom as a magnetic dipole, if the direction of external magnetic field changes adiabatically such that:

$$\frac{d\theta}{dt} \ll \omega_L = \frac{g_F m_F \mu_F}{\hbar} |\mathbf{B}| \quad (2.33)$$

the atoms remain trapped in the magnetic potential. For the atoms to remain trapped, the quantum state of the atoms should remain unchanged; the adiabatic condition ensures this criterion.

In order to understand the origin of the Majorana spin-flip loss [121], it is vital to highlight the characteristics of the quadrupole magnetic trap. These features are:

- (1) the direction of magnetic field changes as the atom crosses the center of the trap
- (2) The magnitude of the magnetic field is more as one goes away from the center
- (3) the direction of magnetic field changes at the fastest rate near the origin.

According to the above mentioned adiabatic condition (Eq. 2.33), if the magnetic field changes its direction slowly in comparison to the Larmor frequency, the atoms are always aligned with the local magnetic field. In the opposite situation, the atoms will not follow the direction of the magnetic field and lose alignment with the local magnetic field. This leads to the flipping of the spin and loss from the trap. Considering the motion of the atoms inside a magnetic trap, as long as the atoms move in a region of the trap where the magnitude of the magnetic field is sufficiently large, the Larmor precession period will be short compared to the time scale in which atoms experience a significant change in the field direction. In such a scenario, the atoms remain in the same Zeeman sublevel and remain trapped. This condition is easily fulfilled by the atoms which are away from the center of the trap. Thus, the higher energy atoms will stay in a trapped state while the lower energy atoms will have a higher probability of undergoing spin flips [122]. This loss occurs when the Larmor frequency is lower than the rate of

change of the magnetic field direction, and this loss rate can be easily estimated [123].

This Majorana spin-flip transition from the trapped to untrapped magnetic levels near the zero of the quadrupole magnetic field limits the lifetime and the ultimately achievable density of atoms in the magnetic trap. Thus, in order to eliminate the Majorana spin-flip, an additional magnetic field is required to remove the zero-field crossing region of the quadrupole magnetic field. Alternatively, the atoms can be transferred into an entirely different trap called the optical dipole trap.

2.7 Temperature measurement of atoms

The measurement of temperature is one of the most crucial processes while study the ensemble of cold atoms. It helps to deduce the other quantities of interest, such as spring constant, diffusion coefficient, etc. It helps for the mapping of temperature and density regime of cold cloud and tells about the efficiency to which the cooling process has been carried out. There are many techniques of measuring the temperature of the atomic cloud, most of the techniques take advantage of the degree of expansion of the atomic cloud after the particular release time from a trap [124]. The most popular of them is called the time-of-flight (TOF) measurement. It uses the thermal expansion of the cloud in a given free evolution time to determine temperature. It must be noted that despite all the advantages offered by the TOF technique, it is a destructive way of measurement. The atomic cloud is destroyed after the measurement event.

For the experiments reported in this thesis, we have used a nondestructive way called the *Release and Recapture* technique [124, 125] for the determination of temperature. This technique relies on the measurement of a fraction of atoms that remained in the trap after some finite free-evolution release time. The cloud of atoms tends to expand due to its thermal energy and goes out of the trapping region. In order to understand this, let us consider a spherical cloud of atoms with the Maxwell-Boltzmann velocity distribution. If this sample is allowed to expand for time Δt homogeneously from an initial finite diameter, the fraction of atoms remaining in the trap after the given release time is given by:

$$f_r = \int_0^{\frac{v_c}{v_T}} e^{-u^2} u^2 du \cdot 4\pi \quad (2.34)$$

In the above equation, $u^2 du \cdot 4\pi$ is the spherical coordinate for atomic velocity. At temperature T , the thermal velocity of atoms in MOT is $v_T = \sqrt{\left(\frac{2k_B T}{m}\right)}$ and $v_c = \frac{R_c}{\Delta t}$ is the velocity for which an atom starting from the center of the trap just reaches the position R_c in time Δt . The capture region in the present case is determined by the radius of the MOT beams. Simplifying the above equation gives:

$$f_r = -\frac{2e^{-v_c^2/v_T^2} v_c}{\sqrt{\pi} v_T} + \text{Erf} \left[\frac{v_c}{v_T} \right] \quad (2.35)$$

This equation shows the relationship between f_r and Δt . This equation is fitted to the experimental data to determine the temperature of the atomic cloud.

2.8 Rate equation

With the ability to measure the number of atoms at any instant of time by collecting the fluorescence emitted by atoms in MOT, we can model the loading and loss of atoms from the trap. At room temperature, the untrapped background particles have sufficient kinetic energy to knock the atoms out of the trap. Since the probability of such collisions scales with the background pressure inside the vacuum chamber, this loss rate can be used for the measurement of pressure and determination of the collision cross section between the species of interest. The loading of atoms in a MOT is a dynamic process, and a steady-state population is achieved by attaining the equilibrium between the loading rate and the various loss rates. The rate equation for such a process can be written as:

$$\frac{dN}{dt} = R - \frac{N}{\tau} - \beta N^2 \quad (2.36)$$

In the above expression, N is the number of atoms at a given instant of time ' t ,' R is the loading rate, $1/\tau$ is the linear loss rate of atoms due to various factors, and β represents the non-linear loss rate due to light-assisted collisions between trapped atoms. Depending upon the density of atoms inside the trap, one can choose to work in the linear or non-linear regime. All the experiments reported in this thesis have been performed in the low-density regime. Thus the terms that are quadratic in N have been neglected [126] for all the treatments. In the low-density regime, the solution to Eq. 2.36 displays an exponential growth in the number of atoms in the MOT and be written

as:

$$N = N_s [1 - \exp(-t/\tau)] \quad (2.37)$$

where,

$$N_s = R\tau \quad (2.38)$$

For the atomic species under consideration, the linear loss rate can be attributed to several factors such as:

(a) Loss rate induced by the collision with the background species such as N_2 , untrapped Sr atoms which include all the isotopes weighted over their natural abundance and other background species

(b) The decay of atoms into the metastable states

(c) Escape of atoms out of the atom capture region

By combining the factors mentioned above, the total linear loss rate can be written as:

$$\frac{1}{\tau} = \frac{1}{\tau_{bg}} + \frac{1}{\tau_{power}} + \frac{1}{\tau_{temp}} \quad (2.39)$$

The first term in the above equation can be written as the combination of loss rate induced by the species introduced inside the vacuum chamber to measure the collision cross section and the that due to the inherent background atoms/molecules. The experiments described in section- 5.2 of this thesis have been used for the determination of the collision cross section between ^{88}Sr and N_2 . However, the choice of atomic species depends upon the aim of the experiment and can easily be replaced without much alteration in the experimental setup. The first term of Eq. 2.39 can be written as:

$$\frac{1}{\tau_{bg}} = n_{N_2} \sigma_{N_2} v_{N_2} + \Gamma_b \quad (2.40)$$

Here, n is the density of the background particle, σ is the collision cross section, and v is the average velocity of the particle under consideration. The subscript N_2 denotes the background species used for the experiments reported in thesis. The second term, Γ_b in the above equation, accounts for the loss induced by the background species other than N_2 . For analysis purposes, we can assume that the speed of trapped atoms is low compared to the velocity of background atoms, which is in thermal equilibrium

with the vacuum chamber. In such a scenario, one can use the Maxwell-Boltzmann distribution of velocity for the background particles and calculate the average velocity for the determination of the collision cross section.

Eq. 2.39 is the master equation for characterizing various loss channels in MOT. This can be modified for a specific experimental situation, as described in chapter - 5.

Chapter 3

Experimental apparatus and methods - I : Vacuum assembly

This chapter describes the design and construction of the experimental setup for production of a cold cloud of strontium atoms in a magneto-optical trap (MOT) and magnetic trap (MT). For the first phase of development of apparatus, we have decided to design a system that can be used for experiments such as those related to frequency metrology using the clock transition, precision measurements, and experiments related to quantum chaos using the architecture of an atom optics kicked rotor. The current system can be further modified for an experimental demonstration of quantum information processing using ultracold strontium atoms coupled to plasmonic nanostructures.

The experimental setup is built on a 1.5 m \times 3 m optical table. This table consists of both vacuum chamber and the laser systems for performing the cooling and trapping. The development of the entire experimental setup can be split into various parts viz. design and construction of vacuum assembly to provide a collision-free environment for cooling and trapping, generation of a high flux, high collimation atomic beam of Sr atoms for loading the MOTs.

We generate a cold cloud of ^{88}Sr atoms in a standard $\sigma^+ - \sigma^-$ MOT configuration, which is loaded from an atomic beam of strontium that is slowed by a zero-field-crossing Zeeman slower. Laser light at a wavelength of 461 nm for addressing the first stage cooling of strontium atoms is generated using a home-made cavity-enhanced optical

frequency doubler. This blue light is locked to the atomic transition by performing an atomic beam spectroscopy. Control electronics for the length stabilization of frequency doubling cavity and for the frequency stabilization of the seed laser operating at 922 nm are developed in laboratory. The entire experimental sequence is controlled with the help of the data acquisition cards and LabView interface.

3.1 The vacuum system

The principle of laser cooling is based on the directed momentum transfer from light to the atoms. This means that any additional random kicks due to particles/photons can adversely affect the cooling process. In such a scenario, collisions with background atoms/molecules that can impart random motion to the particles under consideration must be avoided to the maximum possible extent. This is ensured by performing the entire process of laser cooling and trapping inside an ultra-high vacuum (UHV) chamber (pressure $< 10^{-9}$ torr). This UHV environment also ensures a long background collision limited lifetime of atoms in a given trap. The required operational conditions are achieved by designing a vacuum chamber with a suitable pumping mechanism for creating and maintaining the desired pressure inside the vacuum assembly. This is one of the most crucial requirements for experiments with cold and ultracold atoms/molecules and requires careful design considerations.

For the experiments reported in this thesis, the vacuum chamber is carefully designed by using 3D CAD software to choose among different possible configurations and is assembled using standard vacuum components from MDC vacuum, Kurt J. Leskar, UHV Design, and Agilent technologies. Some of the components for the assembly are custom made by Fourvac Technologies, Pune.

The schematic diagram of the vacuum chamber is shown in Fig. 3.1. The vacuum chamber can be divided into two parts namely; (a) the UHV science chamber where cold atoms are collected, and all the experiments are performed and (b) the oven region where a high flux and highly collimated beam of hot Sr atoms is generated from an effusive atomic source. These two regions are connected by a Zeeman slower tube as shown in Fig. 3.1. In order to keep the science chamber at the desired lower pressure with respect to the relatively high-pressure oven region, a differential pumping tube has

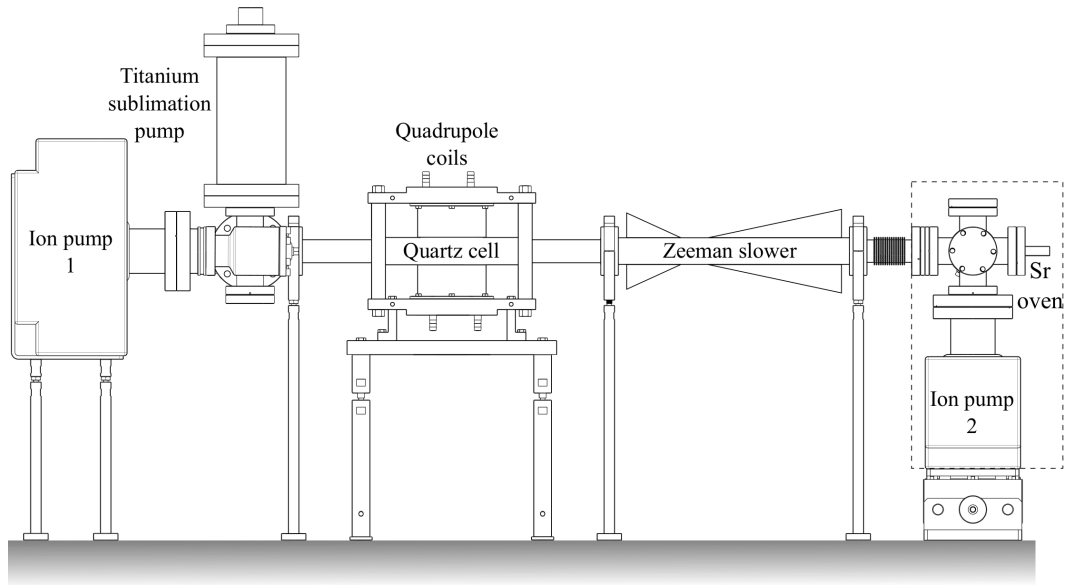


Figure 3.1: Vacuum chamber: Side view of the vacuum chamber used for the production of cold strontium atoms. The oven region is shown within the dashed rectangle.

been installed between them. A differential pumping tube is simply a narrow path connecting the two regions and limits the conductivity of the gases between them. The pressure difference maintained by such a tube depends on its dimensions. For our experimental setup, we choose a differential pumping tube of internal diameter (ID) 6.4 mm and length 113.6 mm. This maintains a pressure difference of ~ 2 order of magnitude between the two regions. The pressures inside the two regions are maintained with the help of two independent ion pumps with capacity 55 l s^{-1} (*Agilent*, Model: *VacIon Plus 55 Starcell*). Besides, we have connected a titanium sublimation pump (TSP) near the science chamber to provide additional pumping and to maintain the desired low pressure. With this setup, at normal operating conditions, we achieve a vacuum with pressure $< 10^{-10}$ torr in the science chamber. A rotary shutter (*UHV Design*, Model: *MD20RAIX000Z*) is placed between the two regions of the vacuum chamber to block the flow of atoms from the oven to the UHV region when experiment is not running.

A zero-field-crossing Zeeman slower is placed between the quartz cell and the oven region. This reduces the velocity of the beam of Sr atoms emanating from the effusive source and increases the loading efficiency of the MOT. The length of the Zeeman slower tube is ~ 38 cm. The Zeeman slower tube is connected to the oven region via

a flexible joint. This helps to perform small alignment of the oven with respect to the MOT capture region. Optical access for the Zeeman slower laser beam is provided with the help of a CF35 viewport (*MPF Products*, Model: A8007-2-CF), as shown in Fig. 3.1. Strontium is highly reactive with glass and forms a permanent coating that can eventually block the optical access. To avoid this, we have used a sapphire viewport facing the direct atomic beam. Sapphire is a crystalline material that shows different optical properties in different directions. Thus the crystal has to be with particular cut so that it does not affect the polarization property of the Zeeman slower laser beam. For our purpose, we have chosen a particular cut of the crystal called the “z-cutting”, with the crystal orientation parallel to the optical axis. In following sections, we will go through the various components of the vacuum system followed by the procedure of assembly and baking to achieve the desired low pressure.

3.2 Atomic oven for strontium atoms

This section has been published as:

“A simple atomic beam oven with a metal thermal break”

Chetan Vishwakarma, Jay Mangaonkar, Kushal Patel, Gunjan Verma, Sumit Sarkar, and Umakant D. Rapol

Review of Scientific Instruments, 90, 053106 (2019)

One of the fundamental requirements for the laser cooling experiments is to have a high flux atomic source capable of producing a highly collimated beam of atoms. Such an atomic beam then slowed down in a collision-free environment using Zeeman slower [127] and is used for loading into a MOT for further laser-cooling as described in the earlier chapter. Therefore, designing an efficient atomic oven for the atomic species under consideration [128] is the first crucial step towards the production of laser-cooled atomic samples. Atomic species with relatively low vapor pressure (e.g., 1 Pa at 796 K for Sr atoms) require the oven to be operated at a high temperature (e.g., greater than 700 K for Sr). For such systems, the isolation of the vacuum chamber from this high-temperature oven region is technically challenging. This problem is traditionally tackled by either of the following methods:

(1) by using a glass or a ceramic break between the oven and the vacuum chamber

(2) by incorporating the oven completely inside the UHV chamber [128, 129]

These measures are good enough for the problem under consideration, but they are relatively complex in terms of design, construction, and maintenance. The later solution is quite appealing; however, due to thermal cycling, the heating elements kept inside the vacuum chamber sometimes become fragile and need to be replaced by venting the UHV chamber, which can be time-consuming and tedious. Thus, it is advantageous to keep the heating elements completely outside the vacuum system.

To overcome the above-mentioned problems, we designed a simple and easy to machine oven for Sr atoms. Unlike the conventional micro-capillaries based atomic ovens, this oven does not require the individual heating of the reservoir and the collimating capillaries [130, 131] and can be easily implemented for other low vapor pressure atomic species. In the following sections, we describe a detailed design and construction of the oven followed by the steady-state thermal profile simulation of the system using the finite element analysis (FEM) by COMSOL Multiphysics software [132]. We have shown that the numerically computed thermal profile is in good agreement with that of experimentally measured values in our system. This detailed analysis of the thermal profile has enabled us to propose a minor change in the design of the existing oven. These modifications improve the thermal isolation between the reservoir and flange of the oven without compromising the physical strength.

3.2.1 Design and Construction

The oven consists of two sections. The first part is machined from a single block of UHV compatible stainless steel (SS304) and shaped into a CF35 vacuum flange, as shown in Fig. 3.2(a). The relevant dimensions of the different parts are shown in Fig. 3.2(b). The novelty of this design lies in choosing a geometry that reduces the thermal conductivity between the high-temperature oven and the rest of the vacuum system. For a given material, the thermal conductivity between two points can be reduced by decreasing its thickness and by increasing the distance between them. For the current design, in order to reduce the thermal conductivity, a narrow constriction of thickness 4.5 mm is made by scraping out the material along the radial direction. The length of this narrow neck

is limited by the geometry of the current design to 4.5 mm. A hole with diameter 7 mm and length 39 mm is made on this section, which serves as a reservoir for 99.9 % pure strontium atoms (*Sigma Aldrich: 460346-5G*).

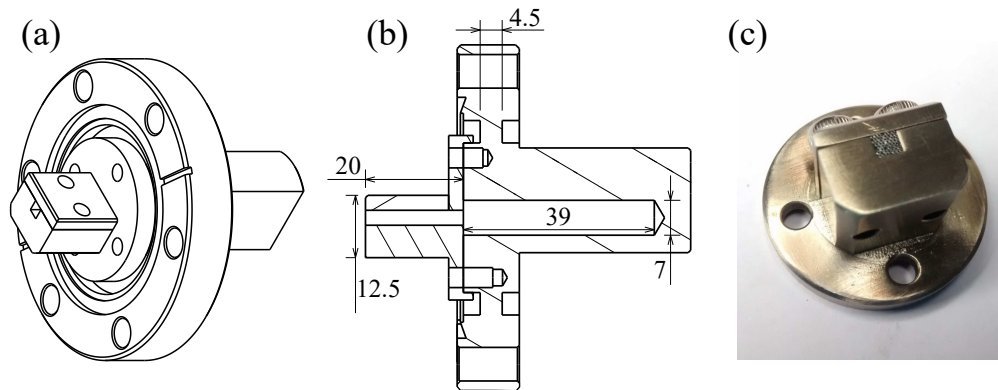


Figure 3.2: Strontium atomic beam source design: (a) Isometric view of the oven assembly; (b) Schematic diagram of Sr reservoir. All the dimensions are in mm; (c) Image of the needle holder carrying ~ 60 hypodermic needles.

The second part of the oven houses a bundle of narrow capillaries and is shown in Fig. 3.2(c). It has been shown that an array of microcapillary channels outperforms a single aperture collimation tube in terms of intensity and collimation ratio along the axial direction [133]. For a system in the molecular flow regime, the mean free path of the particle is larger than the dimension of the vacuum chamber. If the system is not in the molecular flow regime (Knudsen number < 0.5), the collimation is determined by the aspect ratio of the micro-capillary tube. As the aspect ratio is the key to the degree of collimation, for the current experiment, 27 gauge disposable hypodermic needles are used. These needles are made of stainless steel having an internal diameter (ID): $210 \mu\text{m}$ and external diameter (ED): $413 \mu\text{m}$, and are extensively used in medical applications. The needles are cut to a length of 15 mm and polished using a fine emery paper to get flat and smooth faces. The calculated collimation of each needle is ~ 14 mrad. Approximately 60 needles are bunched together with the help of a stack holder, as shown in Fig. 3.2(c). For the smooth operation of such a micro-channel-based oven, it is necessary to ensure that all the capillaries are aligned axially in the direction of the atom-capture region. One of the several ways to make a defect-free lattice of such tubes is to use a holder with a triangular cross section [130], which results in the hexagonal

packing of the needles. For the current experiment, we choose a design with square cross section for the needle holder. This is done due to the convenience of machining. The resulting defect in the alignment has not led to any observable problems. The needle holder and the reservoir are assembled with the help of four M4 screws, as shown in Fig. 3.2(a).

3.2.2 Heating of strontium reservoir

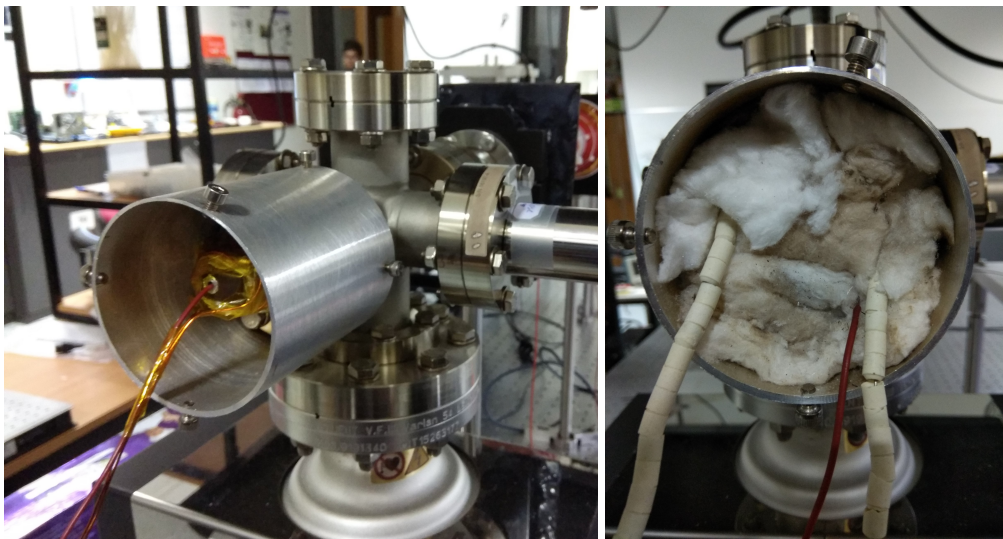


Figure 3.3: Thermal isolation of heating elements: Aluminum enclosure filled with glass wool is used for minimizing the heat loss to the environment.

As mentioned earlier, the vapor pressure of Sr is very low at room temperature. Thus for generating an intense beam of atoms, the oven has to be heated to a temperature more than 450°C . In our setup, we heat the oven to the temperature of $\sim 600^{\circ}\text{C}$. The oven is electrically heated using a 21 AWG (American Wire Gauge) nichrome wire. During the initial days of experiments, we used two layers of such nichrome wire wound on the reservoir for the heating purpose. Later we started following the configuration using a single layer of heating wire. This is done to avoid the local heatings at the spots where wires from two layers cross each other. We use a layer of seven turns wound on the reservoir. The electrical short is avoided by using a Mica sheet between the oven and the heating wire. For an externally heated system, the isolation of the hot region from the environment is very crucial. The absence of such isolation can drastically increase

the electrical power requirement for achieving the desired temperature. For isolating the oven region from the surrounding, a cylindrical enclosure (ID 70 mm, length 150 mm) made of aluminum is used. This cylinder is filled with glass wool and closed, as shown in Fig. 3.3. This ensured the reduction in heat loss directly to the environment by convection. The required temperature for operating the oven is achieved and maintained by using a switching module (*SELEC*, Model: TC533). It periodically turns the current “ON” to maintain a particular set temperature. During each “ON” time, it passes an alternating current of 8.3 A with a voltage drop of 22.5 V_{rms} controlled by a variac. By changing the duty cycle, it controls the power delivered to the oven and hence maintains the temperature of the oven. The power delivered to the system has been computed by measuring the duty cycle of the switching. The electrical power delivered as a function of oven temperature is shown in Fig. 3.4.

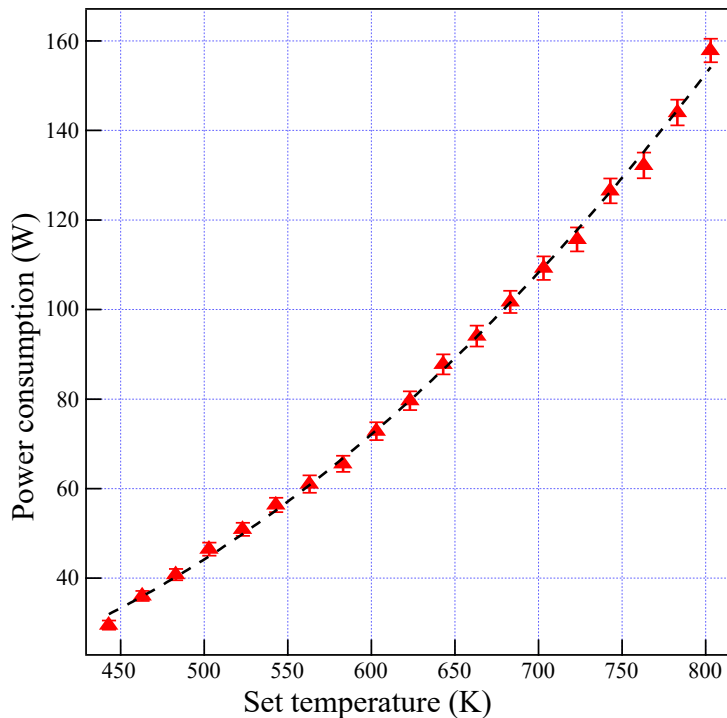


Figure 3.4: Power consumption of the Sr oven: Estimated electrical power as a function of the set temperature. Symbols represent the experimentally measured data point. The dashed line is a guide to eye. The error bars represent the uncertainty in the estimation of power due to an error in the measurement of the duty cycle.

3.2.3 Comsol simulation of the oven

In order to understand the temperature distribution of the oven and effects of modifications in geometry, we ran the heat simulations in COMSOL Multiphysics (version-5.2) software. COMSOL uses the finite element method (FEM) to calculate an approximate numerical solution of the required partial differential equation (PDE) for a given set of boundary conditions. The oven attains thermal equilibrium by dissipating heat to the surrounding ambient air via convection and radiation cooling mechanism.

To accommodate the above mentioned factors in the simulation of the temperature profile, we employ the “heat transfer in solid” module in COMSOL. This module allows one to simulate the steady-state/time-dependent solution of the temperature profile in presence of fluid and solid elements. It utilizes experimentally determined correlations between the temperature profile and fluid flow around a particular geometry to calculate the thermal profile of a given system. The geometry for implementing forced convection in our system is taken to be “planar”. To employ forced convection cooling on a surface, we take the characteristic length to be the largest relevant dimension in that region e.g., the characteristic length for the surfaces of the ion pump is taken to be 0.3 m. Solutions thus obtained under these conditions are found to converge to reasonable values.

Fig. 3.5 displays a numerically simulated thermal profile of the system. In our experimental setup, the oven is connected to a CF35 6-way cross, a 55 l/s ion pump, and a pneumatically operated rotary shutter (*UHV Design*, Model: MD20RAIX000Z) as shown in Fig. 3.1. A simplified model of the system has been considered for the numerical simulation using COMSOL Multiphysics. The temperature of Sr reservoir is varied from 500 K to 1300 K in the simulations. For forced convective cooling, the air speed is taken to be 1.5 m/s and the characteristic length at a surface to be the largest local dimension, as mentioned previously. Radiative cooling is taken into account by considering the surrounding temperature to be 20°C and the emissivity of stainless steel (grade SS304) to be 0.65 [134] at all the surfaces under consideration (outside as well as inside the vacuum). After each such simulation, the temperature was monitored at the periphery of the oven flange marked as point ‘P’ in Fig. 3.5. These simulation parameters give results comparable to the experimentally measured thermal profile at the flange within a reasonable error bound.

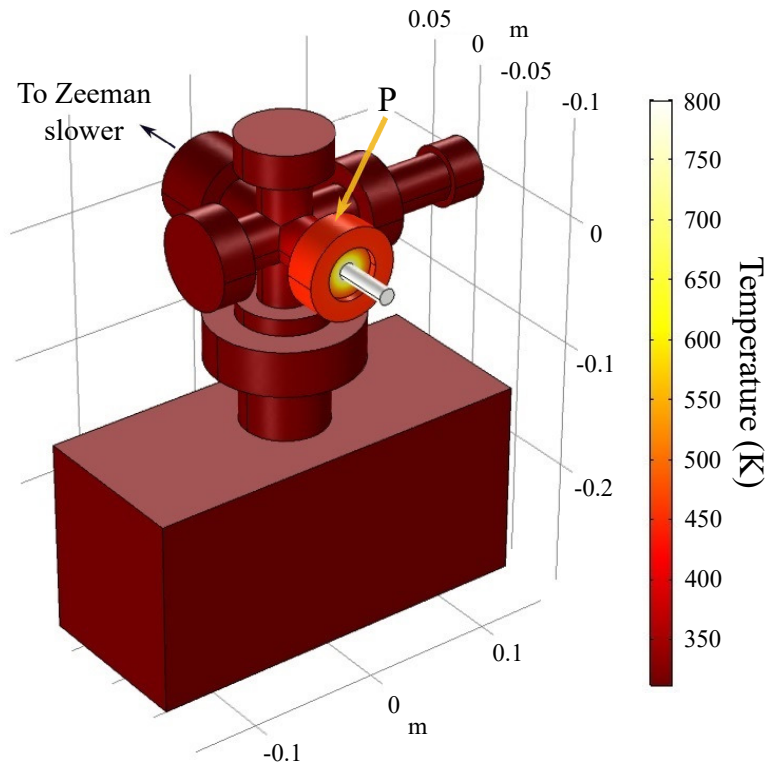


Figure 3.5: FEM analysis of the temperature profile: Numerically simulated thermal profile of the oven including a CF35 6-way cross, a 55 l/sec ion pump (bottom) and an atomic beam shutter (right). The reservoir is maintained at the constant temperature of 800 K. The temperature is monitored at the region connected to 6-way cross, shown by point ‘P’

As the heating elements are located at the reservoir, it is crucial to get the information about the thermal profile along the length of the needles. A separate simulation is run for the experimentally used oven geometry, including the needle holder assembly, and is shown in Fig. 3.6(a). Points ‘A’ and ‘B’ represent the two ends of the needle holder, and ‘C’ represents a point on the reservoir. The temperature distribution along the length of the oven is shown in Fig. 3.6(b). In the current setup, the simulated temperature difference between the two ends of the needles is found to be ~ 27 K. The small temperature difference between the two points reduces the probability of clogging of Sr in the needles. This statement is supported by extensive use of the oven over prolonged operation time without observable differences in the quality of the atomic beam.

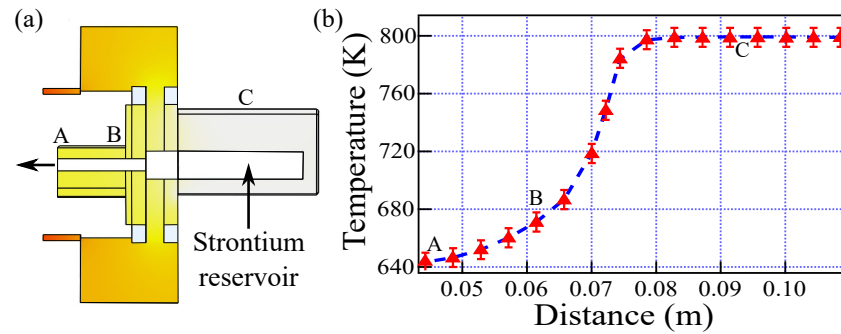


Figure 3.6: Thermal profile along the axis of oven: (a) cross-sectional view of the current design of the oven, including the assembly that holds the microcapillaries. Points ‘A’ and ‘B’ represent the two ends of the needle holder, and ‘C’ represents the point on the reservoir. The arrow at point ‘A’ shows the direction of the atomic beam, (b) temperature distribution along the length of the oven. The points under consideration are marked as ‘A,’ ‘B,’ and ‘C.’ The error bars represent the deviation of the simulated values considering uncertainty in the emissivity around 1 %. The dashed line is a guide to the eye.

3.2.4 Modification of oven design

The quality of thermal isolation without using any glass or ceramic break and a good agreement between the experimentally measured values and the simulation results motivated us to modify the geometry of the oven for enhanced performance in terms of thermal isolation. In order to see the effect of modification of geometry on the degree of thermal isolation between the reservoir and the connecting flange (shown as point ‘P’ in Fig. 3.5), we simulated the thermal profile for the various oven geometries.

The numerically simulated values of such temperature differences have been plotted as a function of oven temperature in Fig. 3.7. Simulations were repeated for different oven geometries; (a) without any constriction (diamond symbols), (b) with the current design of the oven [length and thickness of the constriction equal to 4.5 mm (circular symbols)], and finally (c) with the proposed design of the oven [length and thickness of the constriction equal to 13.5 mm and 1.5 mm respectively (triangular symbols)], mentioned later in the text.

The observed temperature difference between the reservoir and at point ‘P’ of the flange scales linearly with oven temperature at higher temperatures. A comparison between the experimental result and numerically simulated values for the current setup are

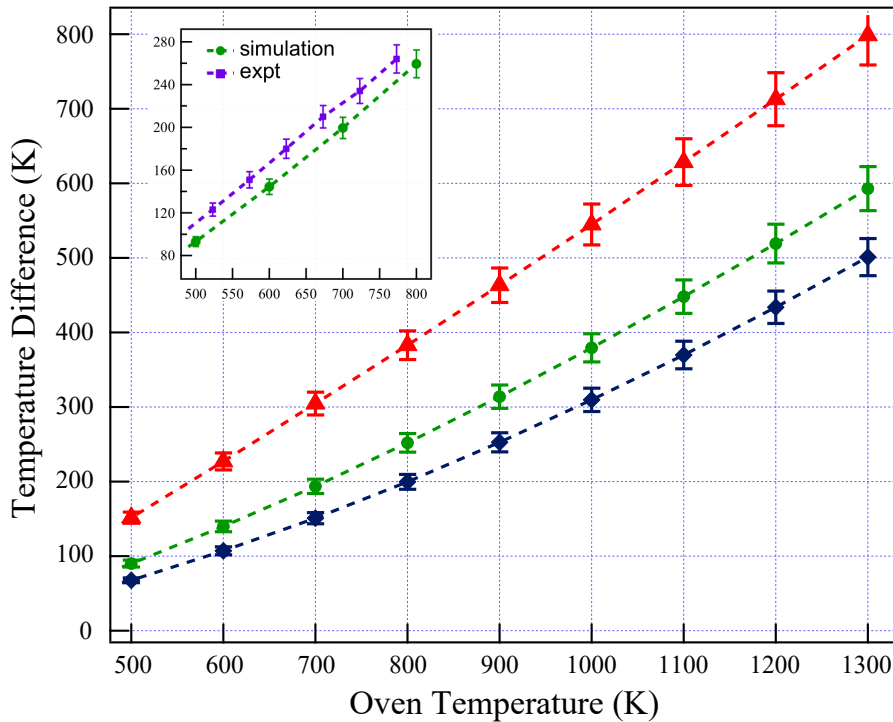


Figure 3.7: Effect of the geometry of the constriction on thermal isolation: The numerically simulated temperature difference as a function of oven temperature (a) without any constriction (diamond symbols), (b) with the current design of constriction (circular symbols), (c) with proposed design (triangular symbols). Inset shows a comparison between the numerically simulated (circular symbols) and experimentally measured (square symbols) temperature difference as a function of the oven temperature. Error bars represent the uncertainty in the values of the temperature difference between point ‘P’ and the reservoir as represented in figure 3.3.

displayed in the inset of Fig. 3.7. A $\pm 5\%$ error has been considered for both the cases to incorporate the uncertainty in the values of emissivity and air current. The experimentally measured thermal profile shows a promising agreement with the simulated one. The offset (~ 20 K) between these two curves can be attributed to the fact that the model used for the simulations is not an exact 3-D model of the experimental setup being used. The connections between various flanges in the real system are poorer as opposed to the simulated system since, in the simulated model, the six-way cross together with the flanges is taken as a homogeneous material. We have also omitted the Zeeman slower connected to the other side of the oven. In the actual system, the various flanges are connected with copper gaskets and stainless steel fasteners. Besides, the emissivity is

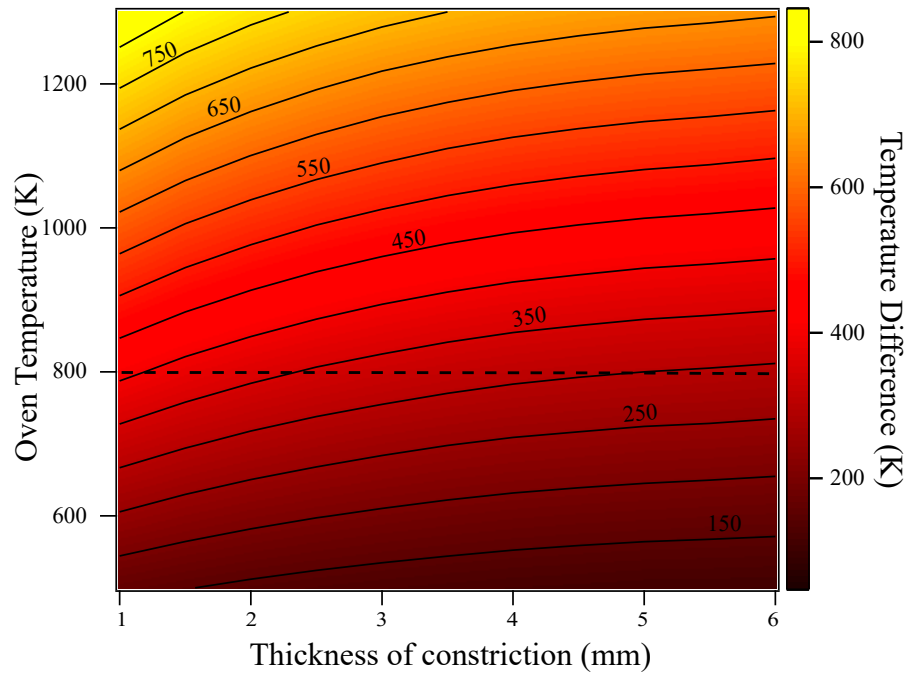


Figure 3.8: Contour plot of thermal profile: Contour plot of the difference in temperature as a function of oven temperature and thickness of the constriction (length of the constriction = 13.5 mm).

non-uniform since there are slightly different materials near the ion pump and the rotary shutter.

In order to understand the effect of the geometry on the thermal isolation, a series of simulations were performed by varying the thickness of the constriction (for a fixed length of 13.5 mm) and the oven temperature. The results of these simulations are summarized in Fig. 3.8 as a contour plot. To see the effect of the thickness, a plot of temperature difference as a function of the same is shown in Fig. 3.9 while keeping the operating temperature of the oven constant at 800 K. The variation of temperature shows power-law behavior with thickness. This leads us to propose a modified design of the oven. In this new design, the length of the narrow part is increased to 13.5 mm, and the thickness of constriction is reduced to 1.5 mm for better thermal resistance. The length of the “break” can be extended radially inwards and by modifying the dimensions of the reservoir appropriately without compromising on the size of the cavity that holds the collimation tubes.

In order to check the structural integrity of the system, we performed the stress pro-

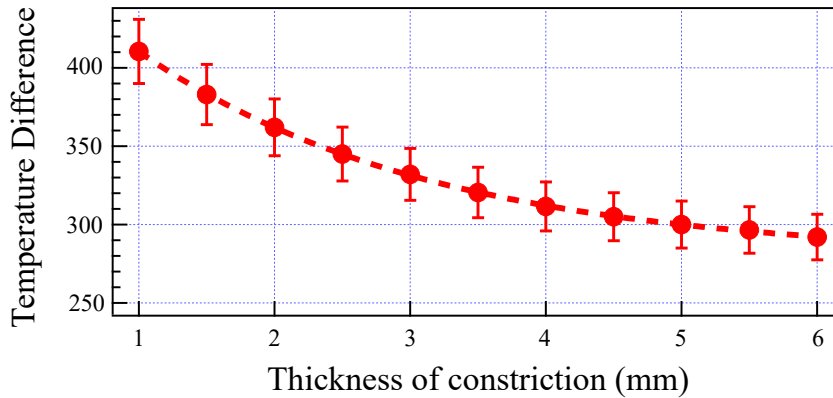


Figure 3.9: Cross section of Fig. 3.8: Variation of temperature difference as a function of thickness of the constriction for fixed oven temperature at 800 K (Cross section of the contour, shown in figure 3.8, along the dotted line). Dashed line is a guide to eye.

file simulation using the “structural analysis” module in Comsol Multiphysics software. For the simulation, relevant parameters for stainless steel (SS304) are taken from the *Handbook of Chemistry and Physics* (CRC Press, 89th Edition) [135]. FEM simulations of one such design have been shown in Fig. 3.10. According to the simulations, the maximum stress experienced is ~ 0.38 MPa as shown by the red color in figure. However, the ultimate tensile strength of SS304 is 550 MPa. Since, the maximum value of the simulated stress is orders of magnitude lower than the ultimate tensile strength of the material, we expect the structure to be mechanically stable under the operating condition. In the above case, we have considered the stress experienced by the structure due to its own weight. To incorporate the additional weight due to the heating elements, we have added an extra weight of 100 gm at the reservoir part. With this modification, the simulated profile gives the maximum value of stress ~ 0.65 MPa which remains acceptable. To compare this design of oven with the existing one, the simulation results for this oven design (triangular symbol) are also shown in Fig. 3.7 along with the other designs. This design, with minimal modification, outperforms the existing one by a significant factor making it more suitable for elements that have lower vapor pressure than Sr and need higher operating temperatures.

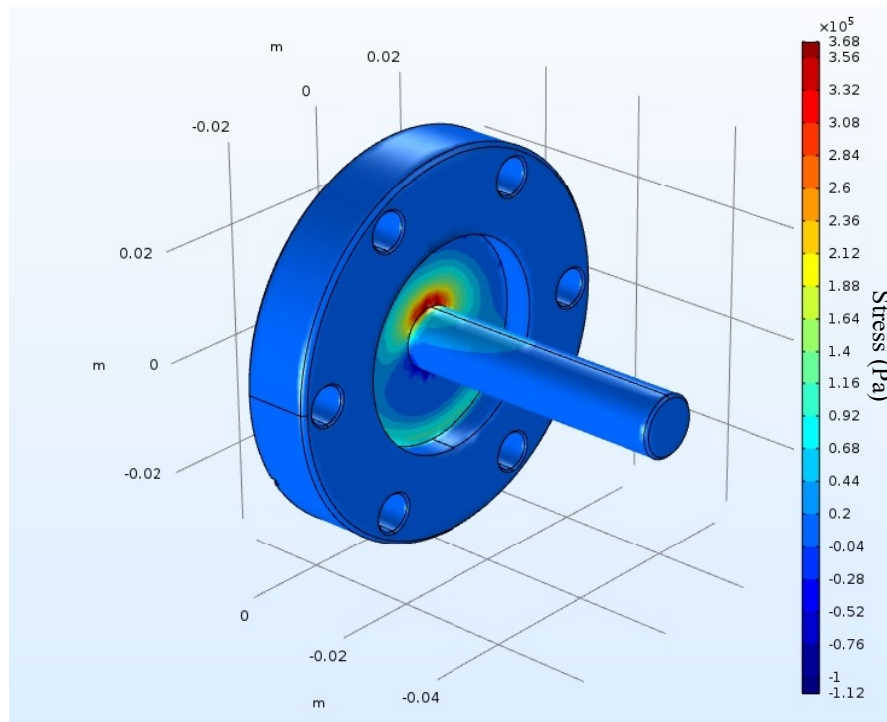


Figure 3.10: Stress profile: FEM simulations of the stress profile for the proposed design of oven. The maximum stress experienced is orders of magnitude smaller than the ultimate tensile strength of the material (~ 550 MPa).

3.2.5 Characterization of the oven

A critical criterion for the characterization of the atomic oven is the measure of flux generated by such a source. This is reflected in the loading rate of a MOT. However, since the MOT loading rate itself depends on several other factors such as parameters of Zeeman slower, presence of transverse cooling, alignment of MOT laser beams, etc. Thus, the measurement performed may lead to an unreliable estimate of the atomic flux. To avoid this, we directly measured the atomic flux at the MOT capture region by fluorescence detection using the technique mentioned in Ref. [129]. The measured flux at the oven at the operating temperature of 870 K is found to be approximately 6×10^9 atoms/sec. The incorporation of the transverse cooling beam just after the atomic oven is expected to increase the flux.

3.3 Zeeman slower

The atomic beam generated by Sr oven heated at $\sim 600^\circ \text{C}$, has very high most probable velocity $v = \sqrt{\frac{3k_B T}{m}}$. These atoms can not directly be used for loading the MOT with capture velocity $\sim 40 \text{ m/s}$. In order to increase the loading efficiency of the MOT, atoms need to be slowed down to a velocity that is smaller than the trap depth of MOT. This is done by placing a Zeeman slower between the capture region and the atomic beam source. In the region of Zeeman slower, the atoms are slowed down by using the radiation force due to a counter-propagating laser beam of fixed detuning. Since the atoms in the atomic beam have velocities opposite to the k -vector of light, the laser has to be red detuned with respect to the atomic resonance to increase the scattering rate. During the cooling process, the velocity of atoms continuously changes due to radiation pressure; in such a situation, the laser need to be always maintained at atomic resonance. This is ensured by applying a spatially varying magnetic field to modulate the Zeeman levels of atoms. The condition can summarized as:

$$\omega_0 + \frac{\mu B(z)}{\hbar} = \omega_L + k_L v(z) \quad (3.1)$$

Here, μ is the magnetic moment of the atom, and z represents the position along the direction of the atomic beam. Considering the constant deceleration a and the initial velocity to be v_i at $z = 0$, the velocity as a function of z can be written as:

$$v(z) = v_i \sqrt{1 - \frac{z}{L_0}} \quad (3.2)$$

where,

$$L_0 = v_i^2 / 2a \quad (3.3)$$

is the stopping distance. Thus, using Eq. 3.1 and Eq. 3.2, the desired spatial variation of the magnetic field can be written as:

$$B(z) = B_0 \sqrt{\left(1 - \frac{z}{L_0}\right)} + B_{bias} \quad (3.4)$$

here,

$$B_0 = \frac{\hbar k_L v_i}{\mu} \quad (3.5)$$

and,

$$B_{bias} = \frac{\hbar(\omega_L - \omega_0)}{\mu} \quad (3.6)$$

The use of light force along with an external varying magnetic field for slowing the atomic beam is known as the Zeeman slower. The Zeeman slower used for a beam of Sr atoms is shown in Fig. 3.11.

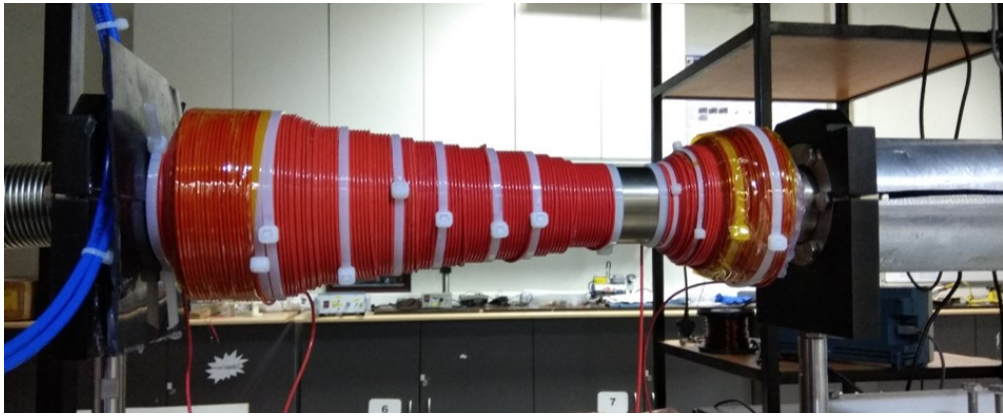


Figure 3.11: Zeeman slower: The Zeeman slower used in the experiment. The spatially modulated magnetic field is generated using layers of solenoids with different number of turns.

The magnetic field for compensating the varying Doppler shift seen by the atoms is generated using a series of solenoids having a different number of turns. The field profile is initially simulated using MATLAB before winding the Zeeman slower coils. The simulation for this was performed by *Gunjan Verma*, PhD student, IISER Pune. For the current experiment, we have chosen a configuration with a zero-crossing magnetic field profile. This configuration provides some experimental advantages, such as:

(1) The field has lower maximum value compared the non-zero crossing configuration, thus requires less current

(2) The magnetic field after the Zeeman slower tube tends to cancel each other due to the contributions of two coils, making the final exit velocity more definite compared to non-zero field crossing design

Layer	Positive Coil	Negative Coil
1	126	41
2	114	37
3	111	36
4	106	35
5	98	33
6	86	30
7	77	28
8	68	27
9	62	22
10	55	21
11	50	20
12	41	15
13	35	13
14	33	11
15	30	9
16	28	–
17	18	–

Table 3.1: Zeeman slower solenoids: Details of number of turns in each layer of the Zeeman slower.

To generate the field with opposite signs, two different coils were wound on a 35 cm long standard CF35 nipple, as shown in Fig. 3.11. We used Teflon coated copper wire of 18 gauge for winding. Teflon is chosen due to its high-temperature handling capacity. The details for the number of turns in each layer is given in table- 3.1. The Zeeman slower coils are air-cooled by using two CPU cooling fans. The high scattering rate of Sr atoms allows the use of smaller lengths for the Zeeman slower. Two separate DC power supplies were used for generating the required field profile. The measured resistance of positive and negative coils is 4.4Ω and 1.5Ω , respectively. The current in positive and negative coils are kept at 0.9 A and 3.5 A respectively for optimized operation of the Zeeman slower.

The thermal beam of Sr atoms generated from the oven is slowed by a counter-

propagating laser beam of wavelength 461 nm and with the polarization σ^+ . The detuning of the laser beam is kept at 420 MHz with respect to the atomic transition towards the red side with a power of ~ 30 mW.

3.4 MOT capture region

The atomic beam of slowed Sr atoms is trapped and cooled inside a quartz cell with a rectangular cross-section made by *Starna Scientific Ltd*. The quartz cell has an external cross section of 38 mm \times 38 mm, and the length is 15 cm. The wall thickness of this cell is ~ 4 mm. This cell provides the optical access for performing the first stage cooling using the laser at a wavelength of 461 nm. The second stage cooling will be performed at the same capture region by superimposing a laser beam at wavelength 689 nm. The quartz cell is connected to the vacuum chamber with the help of two cylindrical glass to metal seal connected to the CF35 flange at both ends, as shown in Fig. 3.12.



Figure 3.12: Quartz cell: The quartz cell provides the optical access for cooling and trapping laser beams.

One end of the quartz cell is connected to CF35 flange via a flexible joint for having the freedom of small manipulation during the assembly of vacuum system. The use of a quartz cell rather than a stainless steel vacuum chamber provides the advantage of maximizing optical access for trapping and cooling. One end of the cell is connected to the Zeeman slower tube towards the oven end of the vacuum chamber. The other end is connected to a CF35, 6-way cross that connects to an ion pump with capacity 55 l s^{-1} and an all-metal right angle valve for connecting the external pumping station as shown in Fig. 3.1.

3.5 Assembly of vacuum system

The above-mentioned components are assembled, as shown in Fig. 3.1. Proper assembly of vacuum components is the vital process to ensure the high quality of vacuum inside the chamber. This is ensured by performing extensive cleaning of the vacuum components before connecting them. All the components are cleaned using a probe ultrasonication. The components are cleaned by sonicating them in HPLC grade toluene, acetone, and then in isopropyl alcohol (IPA) or methanol for 30 minutes in each cleaning agent. It is essential to follow the sequence mentioned above for cleaning. The components are then rinsed with distilled water and dried and covered in clean aluminum foil.

During assembly, it is required to maintain absolute cleanliness. This is ensured by wearing powder-free latex gloves during cleaning and assembly process. Just before connecting the components, knife edges are wiped with HPLC grade acetone. It is important to use lint-free wipes for this purpose. One has to be extremely careful with knife edges, as the slight damage can adversely affect the quality of the vacuum inside the chamber. Various components are connected with the help of nuts and bolts with a copper gasket between them. We have used anti-seize (*Bostik NEVER-SEEZ*, Regular grade) compound on the bolts before tightening. This is done to avoid any possibility of bolt seizing during the baking of the chamber. The tightening of the bolts is done using “criss-cross pattern bolt tightening” for getting uniform torque on the bolts, which results in uniform tightening of the flanges. While doing so, we have ensured the “metal-to-metal” contact between the faces of flanges. This reduces the possibility of leaks at the joints. The connection of oven filled with Sr is one of the most critical part during the assembly of the vacuum system and needs careful handling. The highly reactive nature of Sr demands an inert environment during the assembly process. To avoid any contamination of Sr, the oven is connected after assembling the entire vacuum assembly. Once the chamber is ready except the Sr oven, we connect a gas cylinder containing high purity argon through one end of the chamber via an all-metal valve designed for connecting the external pumping station. The whole chamber is purged with dry argon by maintaining a positive pressure inside it. The reservoir of the oven is filled with



Figure 3.13: Strontium ampule: The ampule is broken inside a glove box and dendrite pieces are filled in the oven reservoir shown in Fig. 3.2(b).

dendrite pieces of pure Sr atoms. This is done by carefully breaking the ampule (shown in Fig. 3.13) inside a glove box maintained at the inert environment. The oven is then transferred in an air-tight zip-seal filled with dry argon and brought to the assembly point. This is then quickly connected to the vacuum chamber maintained at positive argon pressure.

Pumping down and baking of vacuum system

The requirement of a collision-free environment is a must for experiments with cold and ultra-cold atoms. This is achieved by pumping down the vacuum chamber with the help of a pumping station. Our pumping station consists of a scroll pump and a turbo-molecular pump (TMP). The scroll pump does the initial pumping upto a pressure of $\sim 10^{-4}$ torr and assists the TMP at a higher vacuum. The pumping station is connected to the main vacuum chamber with the help of a 1.5 m long bellow via an all-metal right angle valve near the titanium sublimation pump. Once the pressure reaches the value of $\sim 10^{-8}$ torr, we performed a helium leak test to check for the vacuum integrity of the system. An air blow gun is connected to an ultra-pure helium cylinder via a gas regulator pressure gauge. In order to locate the position of leak precisely, a micro-pipette tip is connected to the nozzle of a blowgun. The flow of helium is kept small, approximately 1-2 bubbles per second in water (~ 2 cm below the water surface). With this setup, we released a small amount of gas at all the joints and checked for the helium pressure inside the chamber using SRS residual gas analyzer (RGA). After checking for the possible leaks, we prepare the system for bakeout process.

Adsorption of various atmospheric gases and particularly water on the surface of the vacuum chamber limits the attainment of low pressure. At room temperature, the rate of desorption of these gases is very low. This rate can be increased by heating the surface of the vacuum chamber to a higher temperature. During heating, it is necessary to run the pumping station to pump out the released gases out of the chamber. To reduce the amount of water vapor inside the chamber, a minimum bakeout temperature of 120°C is recommended. However, a higher temperature is required for splitting up longer-chain molecules. It is usually difficult to have a unique bakeout temperature regarding hydrocarbons since it depends on the length of the compounds. The rule of thumb is, the more long-chained the compound, the higher the temperature required.

To prepare the system for the bakeout process, the whole system was wrapped with two layers of aluminum foil. Extra care has been taken at the region of the quartz cell to avoid temperature gradients across the cell before starting the baking. The quartz cell was wrapped with aluminum foil to avoid any accidental scratch. This is then covered with an aluminum enclosure, resting on the two CF35 flanges on both sides of the cell. Once the entire system is wrapped by aluminum foil, resistive heating tapes were wrapped over the foil. While wrapping the heating tape, it is ensured that they do not cross each other. This was done to avoid excess heating at the point of intersection. The heating tape can be operated using either a DC or AC source. For our experiment, we used a variable AC transformer (variac) to control the current and hence the heating of the system. We have placed thermocouples at different locations of the vacuum chamber for monitoring the temperature during the bakeout process. In the end, we wrapped another layer of aluminum foil on the entire system. The picture of the system after wrapping the heating tape and aluminum foil is given in Fig. 3.14. Temperature monitors give us the idea of the temperature gradients. Hence to avoid large temperature gradients that can damage the material of the vacuum system, the heating rate was kept relatively low. We gradually increase the temperature during the span of four days to the final baking temperature of ~ 200 °C. The system is kept at this temperature for one week. After this, we turned on both the ion pumps. The measured pressure at this point was 1×10^{-8} torr and 4.8×10^{-7} torr at the science chamber end and the oven region respectively. At this point, we also turned on the Ti-sublimation filament. The

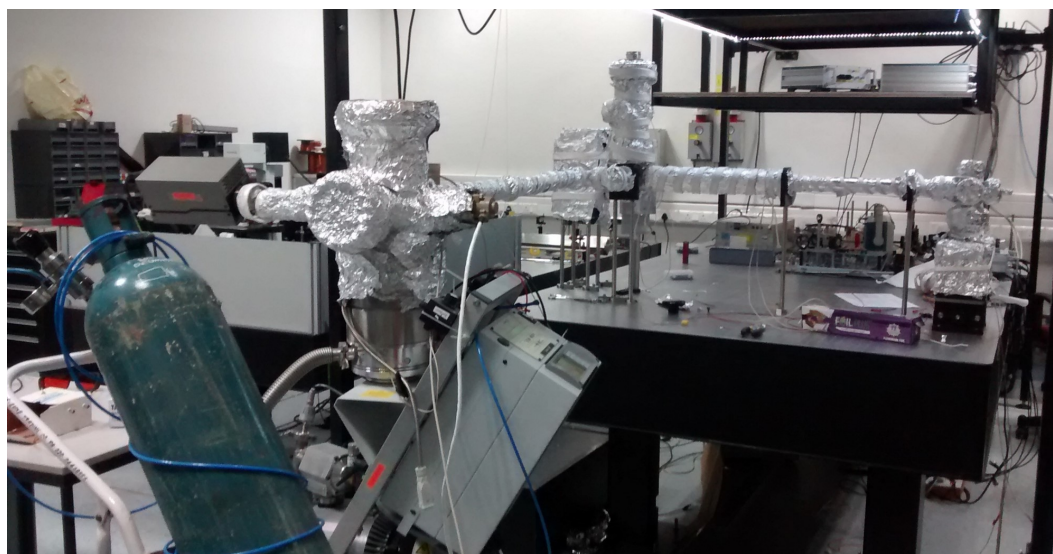


Figure 3.14: Bakeout: Vacuum chamber during the baking process.

Ti-sublimation pump consists of a filament that operates at a high current of ~ 46 A. At this current, the temperature reaches the sublimation temperature of Ti. Hence the inner wall of the surrounding chamber is coated with the thin layer of Ti. This freshly coated Ti is highly reactive to the residual gases present inside the vacuum chamber and thus chemically binds with them at the internal surface of the vacuum chamber, which results in a reduction of pressure.

In the ideal situation, it is preferable to have the provision of independent connection of the pumping station to the two regions separated by differential pumping tube. However, for the current setup, we avoided this due to the small volume of the oven region. This, however, results in a slightly longer pumping time during the baking process.

The system was cooled down by gradually reducing the voltage set by a variac. After the cooling the whole vacuum assembly, the achieved base pressure of the science chamber is found to be $< 10^{-10}$ torr. This pressure is estimated by measuring the ion pump current near the science chamber. The entire process of baking the assembly took nearly three weeks.

3.6 Magnetic field generating coils

This section describes the design and construction of the quadrupole trap for MOT and the 3D printed shim coil to nullify the effects of stray magnetic fields. The schematic of assembly used in the experiments is shown in Fig. 3.15. The whole assembly is made using Poly-oxymethylene plastic (Delrin) components.

3.6.1 Quadrupole coils

The magnetic field for the MOT is generated using a pair of coils in the anti-Helmholtz configuration. This quadrupole coil provides the required field for trapping atoms slowed by the Zeeman slower. Additionally, it also provides an advantage of transferring atoms from the MOT to a pure magnetic trap, provided the atoms are in a magnetically trap-pable state, e.g., atoms in 3P_2 state that can be trapped in a pure magnetic field. The quadrupole coils used in the experiment is shown in Fig. 3.15.

Each of the two coils of the quadrupole trap is made of 10 layers of 16 AWG enameled magnet wire. Each layer consists of 32 turns. In order to avoid local heating, 1 mm thick spacer is used between two layers while winding the coil, as can be seen in Fig. 3.15. After the assembly, the separation between the two coils is ~ 40 mm that is equal to the width of the quartz cell. To avoid heating at large operating currents, these coils are enclosed inside a water-tight Delrin assembly through which pressurized water at the temperature of $\sim 17^\circ\text{C}$ is passed. The magnetic field gradient generated by these coils is $\sim 11 \text{ G}\cdot\text{cm}^{-1}\cdot\text{A}^{-1}$ along the axial direction. During the MOT operation, the quadrupole coils are continuously water cooled.

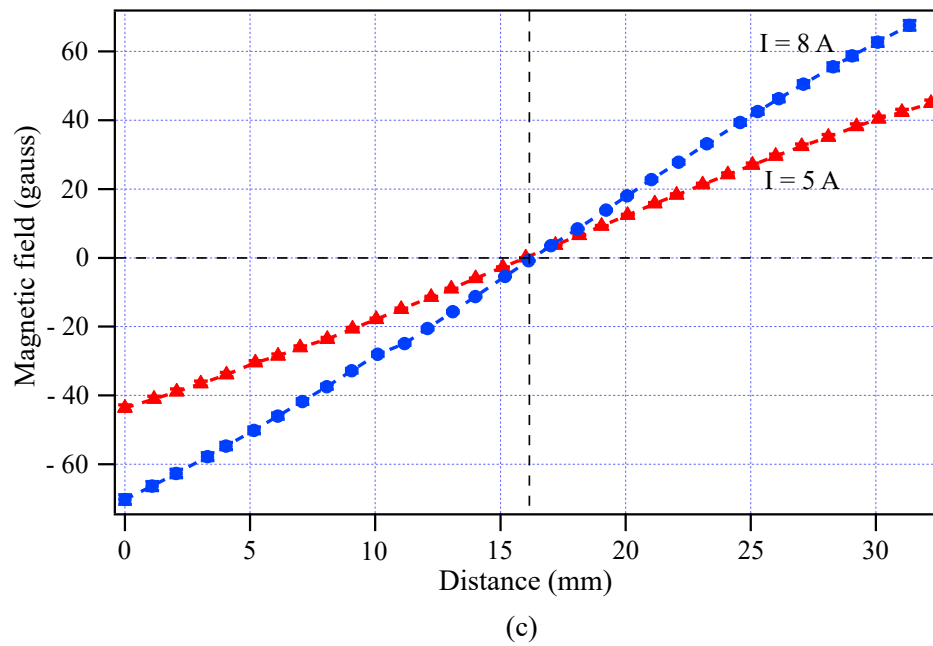
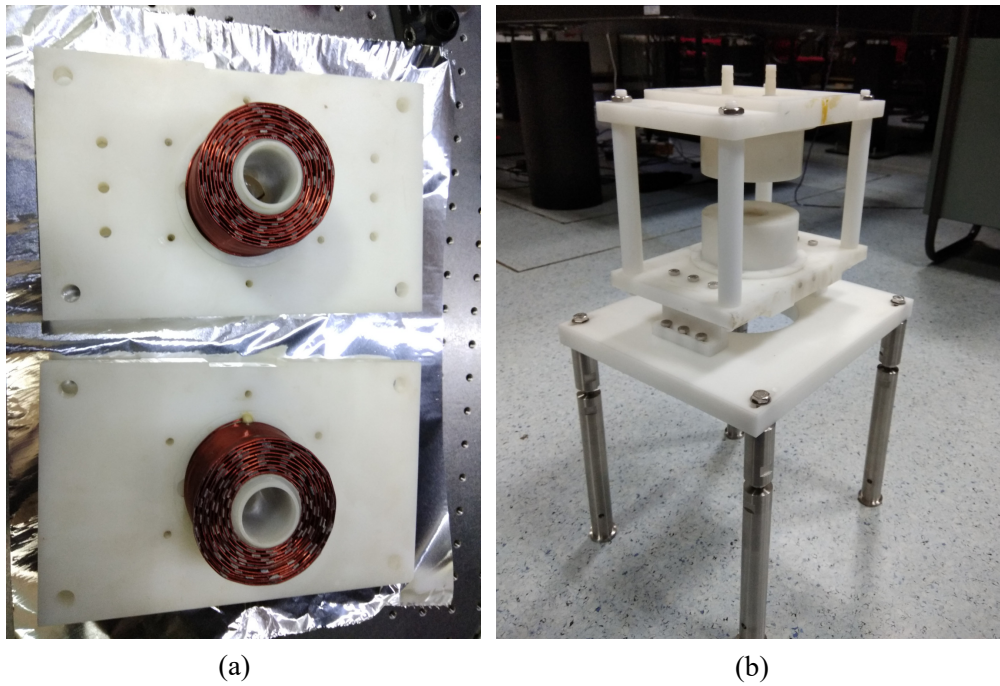


Figure 3.15: Quadrupole coil assembly: Pictures show the quadrupole coil assembly used in the experiment. (a) coil winding, (b) the coil mount, (c) profile of magnetic field generated by the coils at two different currents.

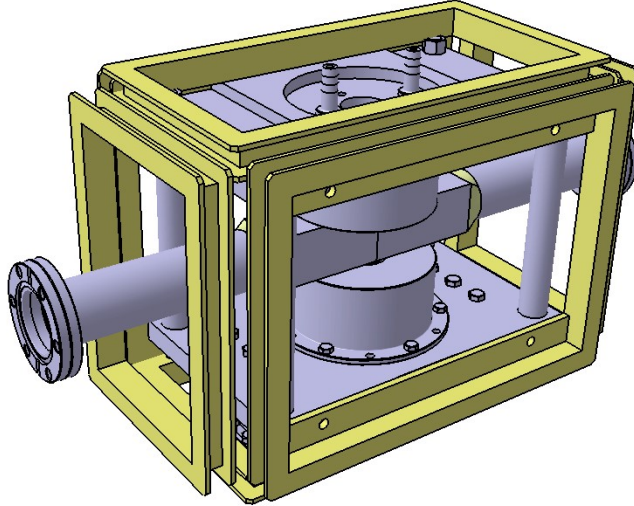


Figure 3.16: Shim coil assembly: Assembly of coils in Helmholtz configuration is used for the cancellation of stray magnetic field. The frames are made using a 3D printer.

3.6.2 Shim coils

Shimming coils have been used for cancellation of stray magnetic fields. This could be the residual field generated due to the Zeeman slower, earth's magnetic field, various magnetic components in the vicinity or due to nearby electronic circuitry. During the MOT operation, this cancellation is not very crucial but needs to be corrected during the transfer of atoms from the MOT to a pure magnetic trap. The spacer for shimming coil is made using a plastic 3D printer (MakerBot Replicator 2X). The material used for printing was ABS (Acrylonitrile Butadiene Styrene). Since the shimming coils are installed after the assembly of the vacuum chamber, we printed the frames in segments and later joined them using the industrial-grade super glue and screws. The schematic of the shim coils used in the experiment is shown as yellow color in Fig. 3.16. We later wind the coil on them to generate the fields required for the cancellation of the stray magnetic field. Each pair of coils are kept in the Helmholtz configuration and driven by three independent DC power supplies.

Chapter 4

Experimental apparatus and methods - II : Laser systems

One of the crucial requirements for laser cooling experiments is to have laser systems which are frequency stabilized with respect to a particular atomic transition. Much of the experimental effort goes into achieving this goal. This chapter describes the generation and frequency stabilization of lasers for various stages of cooling, trapping, probing and diagnostics of the most abundant isotope of Sr atoms.

The experiments reported in this thesis utilize lasers at wavelengths of 461 nm, 707 nm, and 481 nm. Apart from the 461 nm laser, the other two laser lights are generated using grating stabilized extended cavity diode lasers (ECDLs) in Littrow configuration. The laser at 461 nm is generated using the phenomenon of second harmonic generation (SHG) in a nonlinear crystal. In the following sections, we discuss the generation of light at the above-mentioned wavelengths and their frequency stabilization.

4.1 Generation of blue light for first stage cooling

The first stage cooling of Sr atoms requires a laser with a wavelength of 461 nm. Until the discovery of blue light-emitting diode, which fetched the Nobel prize in physics to Isamu Akasaki, Hiroshi Amano, and Shuji Nakamura [136–138], the lasers in the blue frequency regime were generated by using the phenomenon of SHG employing a nonlinear crystal. The method of SHG is still useful for generating laser lights at

the wavelengths which are not directly accessible using the current laser technologies such as the lasers for UV and deep UV. For our experiments, we have designed and constructed a cavity-enhanced optical frequency doubler for the generation of laser light at 461 nm. In the following sections, we will briefly go through the theory of nonlinear interaction of the light inside a material medium and also that of the SHG. The theory of nonlinear interaction and that of SHG has been taken from Ref. [139] and included here for the sake of completeness.

4.1.1 Theory of nonlinear interaction

The phenomenon of optical frequency doubling in a crystal is a nonlinear process. This nonlinearity is defined in terms of the type of response of a material with respect to the strength of an external field. The nonlinear interaction can be characterized by a coupling of two or more intersecting waves inside a material medium. Since the Maxwell's equations are linear in terms of electric and magnetic field variables, there is no coupling between two light waves intersecting in vacuum. In such a scenario, the superposition principle applies which implies that the sum of two independent solutions of the Maxwell's equation is also the solution to the wave equation.

In most scenarios, the interaction between light and matter is very weak. This can be understood by considering an example of the solar radiation that has an average electric field $E_l \sim 600$ V/m whereas the typical values of the same near the proximity of an atom are $E_a \sim 10^{11}$ V/m. Since $E_l \ll E_a$, the application of light polarises the electron cloud only slightly from its equilibrium position. Nonlinear effects are expected to become relevant only for very high optical intensities. The first experimental demonstration of the nonlinear effect “the second harmonic generation” was done by Franken and coworker in 1961 which followed immediately after the demonstration of a laser in the optical frequency regime in 1960 [140].

Fundamental mechanism

Although there are various mechanisms responsible for the nonlinear behavior of a material in the presence of an external intense electric field, the universal nonlinear optical mechanism can be explained by the distortion of electron cloud in the vicinity of atoms in a given medium. The mechanism can be understood by considering the effect of

light's electric field \mathbf{E} on the charge distribution of atoms. The applied electric field induces an electric dipole \mathbf{p} for each atom, which is in the same direction as that of \mathbf{E} . These induced dipoles oscillate at a frequency of incident wave similar to the driven harmonic oscillator. At low intensities, the polarization density \mathbf{P} can be written as:

$$\mathbf{P}(t) = \epsilon_0 \chi_{(1)} \mathbf{E}(t) \quad (4.1)$$

In the above equation, $\chi_{(1)}$ is the linear electric susceptibility of the medium. These oscillating dipoles radiate light with the same frequency and direction as the incident electric field. The re-radiated light is shifted in phase with respect to the incident light, similar to the driven damped harmonic oscillator. When this phase-shifted lights from the oscillating dipoles is added to the incident electromagnetic wave, the result is a single sinusoidal wave of the same frequency. This wave traverse through the medium with a phase velocity different than the speed of light in vacuum.

Second harmonic generation

The mechanism for SHG can be understood by considering an optical radiation with frequency ω propagating through a material medium. At a particular position, the variation in the electric field can be written as:

$$E(t) = A \cos \omega t \quad (4.2)$$

Here, A is the amplitude of the electric field. In the above equation, the phase is taken to be zero at $t = 0$. According to Eq. 4.1, this time-varying electric field creates a time-varying polarization density. Assuming the case of a medium which lacks inversion symmetry i.e., $\chi_2 \neq 0$, the polarization can be expressed as a power series in terms of the field strength:

$$P(t) = \epsilon_0 \chi_1 A \cos \omega t + \epsilon_0 \chi_2 A^2 \cos^2 \omega t \quad (4.3)$$

Using trigonometric identities, above equation can be written as:

$$P(t) = P_0 + P_\omega \cos \omega t + P_{2\omega} \cos 2\omega t \quad (4.4)$$

where,

$$P_0 = \epsilon_0 \chi_2 A^2 / 2 \quad (4.5)$$

$$P_\omega = \epsilon_0 \chi_1 A \quad (4.6)$$

$$P_{2\omega} = \epsilon_0 \chi_2 A^2 / 2 \quad (4.7)$$

Thus according to Eq. 4.4, the polarization density inside the material medium varies with time in three distinct ways. The first term P_0 corresponds to optical rectification. In this case, a static polarization is produced in response to the time varying electric field of the external radiation. This can be observed by placing the material between the plates of a capacitor. It is hardly ever used in practice. The second term, $P_\omega \cos \omega t$ causes the atoms to radiate at the same frequency as the incident light, corresponds to the linear response of the material medium. The third term, $P_{2\omega} \cos 2\omega t$ is of particular interest, as the induced dipoles oscillate at a frequency twice that of the incident light. This generates radiations that have a frequency of 2ω . The phenomenon thus referred to as the second harmonic generation or the frequency doubling. Its most important application is in the generation of light which can not be accessed directly using the current laser technologies such as light in ultraviolet wavelength regime.

Since the second harmonic generation requires $\chi_2 \neq 0$, it can only occur in the materials that lack the inversion symmetry. This requirement eliminates many materials which are isotropic in nature and hence have inversion symmetry, such as optical glass. Only crystals of certain type of symmetry are suitable for the phenomenon of optical frequency doubling.

The propagation constants for the fundamental and second harmonic generated waves, k_ω and $k_{2\omega}$ can be written as:

$$k_\omega = \frac{2\pi}{\lambda_\omega} = n_\omega \frac{\omega}{c} \quad (4.8)$$

$$k_{2\omega} = \frac{2\pi}{\lambda_{2\omega}} = n_{2\omega} \frac{\omega}{c} \quad (4.9)$$

where, λ_ω and $\lambda_{2\omega}$ are the wavelengths corresponding to two frequencies and n_ω and $n_{2\omega}$ are the corresponding index of refraction of the nonlinear medium. If $n_{2\omega} = n_\omega$, then the above equation gives $k_{2\omega} = k_\omega$ and $\lambda_{2\omega} = \lambda_\omega / 2$. In this case, the field maxima for the fundamental wave and the second harmonic wave occur at the same position z , as

shown in Fig. 4.1. Since the fundamental wave continuously create newly radiated light as it traverse through the medium, this would ensure that the frequency doubled wave radiated by atoms at one position z would be in phase with the light radiated by atoms at a different z . Thus, the condition $n_{2\omega} = n_{\omega}$, would result in constructive interference of the different radiated waves and hence the efficient SHG.

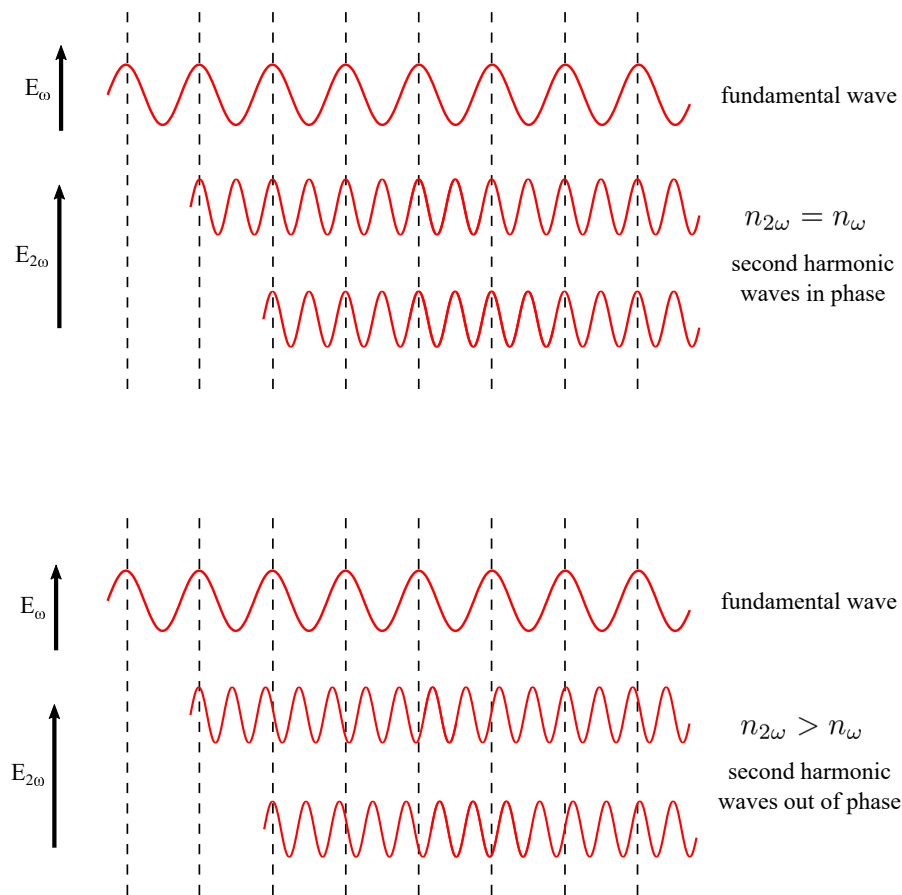


Figure 4.1: Phase matching of fundamental and second harmonic wave: (a) The upper wave is the fundamental wave, and lower waves are the second harmonic waves emitted by different atoms in a nonlinear medium. When the refractive indices for the two waves are same, constructive interference occurs as mentioned in the text, (b) When the refractive indices of the two waves are different, they tend to get out of phase and interfere destructively.

Unfortunately, dispersion results in the condition $n_{2\omega} > n_{\omega}$ thus $k_{2\omega} > k_{\omega}$ and $\lambda_{2\omega} < \lambda_{\omega}/2$. This leads to the second harmonic wave from different atoms that to be out of phase. For the atoms which are not too far apart, the phase of the second harmonic wave will still be sufficiently in phase to give efficient SHG. The efficiency

starts to decrease when the radiations from different atoms are out of phase by more than 180° . This occurs for a propagation distance of L_c , known as the coherence length, given by:

$$L_c(k_{2\omega} - 2k_\omega) \equiv L_c\Delta k = \pi \quad (4.10)$$

where, $\Delta k \equiv k_{2\omega} - 2k_\omega$ is the wave vector mismatch. Above equation can be modified as:

$$\Delta k = (n_{2\omega} - n_\omega) \frac{2\omega}{c} \quad (4.11)$$

Thus, the optimum SHG conversion efficiency is obtained by passing the fundamental wave through a crystal of length equal to L_c . In most of the cases, this length is very small, of the order of a few μm . This small length leads to the very inefficient conversion efficiency of the fundamental wave into the higher harmonics. To increase the SHG conversion efficiency, phase matching needs to be employed.

Phase matching

For crystals with certain symmetries, the refractive index not only varies with wavelength but also with the direction of polarization of the incident light wave. This birefringence provides a way to adjust the indices to be equal for ω and 2ω . As mentioned in last section, the condition for maximum conversion efficiency is:

$$n_\omega = n_{2\omega} \quad (4.12)$$

For a birefringent material, the refractive index varies with the direction of propagation of light with respect to the crystal axis. This variation of index of refraction with the propagation angle provides the mode for phase matching. Fig. 4.2 shows the variation of refractive index with frequency for a pure ordinary wave, pure extraordinary wave, and a mixture of two at some angle θ . If the fundamental wave is polarized along x and the second harmonic wave is polarized perpendicular to this, then the phase-matching occurs when θ is adjusted so that $n_\omega^0 = n_{2\omega}(\theta)$. This process is called the *critical phase matching*.

An alternative approach for achieving the phase matching condition is known as *quasi-phase matching*. In this method, no attempt is made to match the refractive index

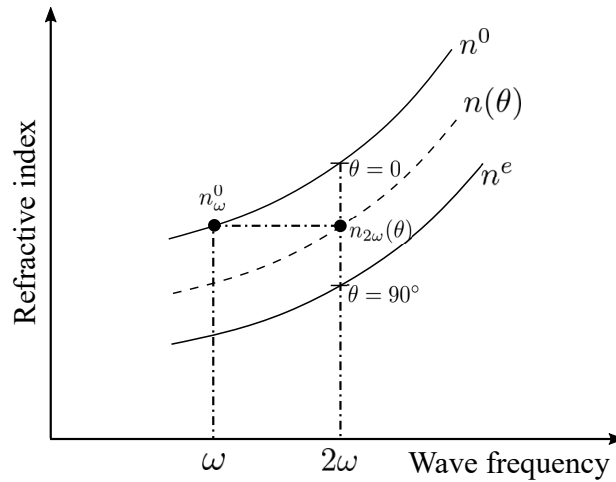


Figure 4.2: Critical phase matching: The variation of refractive index with the angle of propagation of light with respect to the crystal axis is used for achieving the phase matching condition. n^e and n^o represents the refractive index for extraordinary and ordinary ray respectively.

of the fundamental and the second harmonic wave, and they tend to get out of phase after traveling the distance of coherence length L_c . However, the direction of the crystalline axis of symmetry is made to alternate spatially with a period equal to the coherence length L_c as shown in Fig. 4.3. This reverses the sign of the nonlinear susceptibility periodically and brings the fundamental and second harmonic wave in phase. The most common material used for the quasi-phase-matching is lithium niobate, which is ferroelectric in nature. The alternating crystalline symmetry is created by poling the crystal. Poling is a process in which a high voltage is applied for a short time to the patterned electrodes which are deposited on the surface of the crystal. The resulting structure results in a periodically poled crystal.

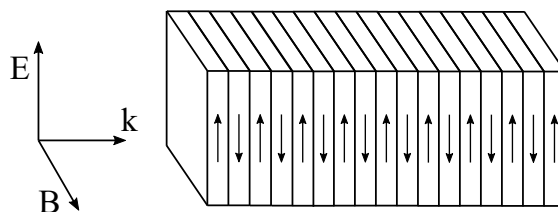


Figure 4.3: Periodically poled crystal: In quasi-phase-matching, a periodic variation in the crystalline axis of symmetry is produced by poling the nonlinear medium with the application of a high voltage. This periodically resets the phase relation between the fundamental and the second harmonic waves. Thus, on average they remain roughly in phase and interfere constructively.

A third way to achieve phase matching condition is through the temperature tuning of the crystal and is called the *non-critical phase matching*. Since the refractive index of the material changes differently with temperature for both, fundamental and second harmonic waves, the crystal temperature is adjusted to a point where the refractive index is the same for both the waves. For this process, the required temperature is of the order ~ 100 's $^{\circ}\text{C}$.

For our experiment, we use the phenomenon of quasi-phase matching for optimum SHG efficiency. We use a periodically-poled Potassium titanyl phosphate (PPKTP) crystal from *Raicol crystals* with the following specifications:

Parameter	Value
Aperture	2×1 mm
Length	20 mm
Transparency range	400 - 4000 nm
Flatness	$\lambda/10$ @ 922 nm
Scratch dig	10 - 5
Coating	AR for 461 nm and 922 nm
Poling period	$5.5 \mu\text{m}$

Table 4.1: Frequency doubling crystal specifications: The specification of the PPKTP crystal used for the SHG. The poling periode is decided by calculating the coherence length for the material.

4.1.2 Theory and analysis of a ring resonator for a Gaussian beam

As mentioned in the last section, the nonlinearity in a material medium can be induced by light with an electric field, which is comparable to the electric fields due to atoms. This fact is also supported by Eq. 4.7, which states that the second harmonic conversion efficiency depends quadratically on the fundamental power. Also, since most of the pump light is not converted to higher harmonic in a single pass, a mechanism to recycle the pump power through the nonlinear crystal is needed for achieving a better conversion efficiency. All the above-mentioned criteria can be fulfilled by using an optical resonator along with a frequency doubling nonlinear crystal inside it.

In the following sections, we discuss the theory of Gaussian beam optics, its prop-

agation through various optical elements, especially inside an optical resonator. The theory and analysis presented here have been taken from several textbooks and research articles [141, 142] and are included here for the sake of completeness. We first describe the various parameters used for the description of the Gaussian wave in paraxial approximation, followed by an introduction of the matrix method, also known as **ABCD** matrix for the analysis of bow-tie ring resonator. Finally, we describe the construction of an optical resonator for generating laser light at the wavelength of 461 nm using the SHG.

Gaussian beam

Lasers are a coherent and collimated source of light. In many respects, the laser light is similar to a plane wave, although the intensity distribution is not uniform at the constant phase wavefront but is concentrated near the axis of propagation, and also the phase fronts are slightly curved. The field component or the potential u of a coherent light source satisfies the scalar wave equation:

$$\nabla^2 u + k^2 u = 0 \quad (4.13)$$

here, $k = 2\pi/\lambda$ is the propagation constant in the medium under consideration, and λ is the wavelength of the laser. For a light beam propagating along the z direction, we can write:

$$u = \psi(x, y, z) \exp(-jkz) \quad (4.14)$$

where, ψ is a slowly varying complex function which represents the difference between a laser beam and a plane wave. The most important difference between them are: the non-uniform intensity distribution, expansion of the beam with a distance of propagation, and the curvature of the phase front. Using Eq. 4.13 and Eq. 4.14, we can write:

$$\frac{\partial^2 \psi}{\partial x^2} + \frac{\partial^2 \psi}{\partial y^2} - 2jk \frac{\partial \psi}{\partial z} = 0 \quad (4.15)$$

here, it is assumed that the variation of ψ is sufficiently slow with z and hence its second derivative $\frac{\partial^2 \psi}{\partial z^2}$ is neglected. The solution of above equation can be written as:

$$\psi = \exp \left[-j \left(P + \frac{k}{2q} r^2 \right) \right] \quad (4.16)$$

where,

$$r^2 = x^2 + y^2 \quad (4.17)$$

Here, the parameter $P(z)$ represents a complex phase shift associated with the propagation of the light beam and $q(z)$ is a complex beam parameter that describes the Gaussian variation in the beam intensity with distance r from the optic axis and the curvature of the phase front. On substituting ψ in the wave equation and comparing terms of the same orders in r , we obtain the relations:

$$\frac{dq}{dz} = 1 \quad (4.18)$$

and,

$$\frac{dP}{dz} = -\frac{j}{q} \quad (4.19)$$

Integration of Eq. 4.18 gives:

$$q_2 = q_1 + z \quad (4.20)$$

The above equation relates the beam parameters q_1 and q_2 of two different planes separated by the distance z .

Propagation of Gaussian mode

The coherent laser beam with Gaussian intensity distribution is one of the many solutions of the wave equation in free space or homogeneous media given by Eq. 4.13. This, however, is the most important among all of them and encountered most frequently in nature. This is also called the *fundamental mode*.

The fundamental Gaussian mode can be completely described using a complex beam parameter denoted by 'q':

$$\frac{1}{q} = \frac{1}{R} - j \frac{\lambda}{\pi \omega^2} \quad (4.21)$$

where, $R(z)$ is the radius of curvature of the wavefront that intersects the axis of propagation at some distance z and $\omega(z)$ is the radial extent of the laser at that point. For the fundamental Gaussian mode, $\omega(z)$ corresponds to the radial distance at which the amplitude falls to $1/e$ time the value at the axis of propagation and is called the *beam radius* or the *spot size*. The Gaussian beam contracts to a minimum diameter of $2\omega_0$ at the position where phase of the wavefront is planer i.e., $R = \infty$. The point of minimum spot size is called the *beam waist*. The complex beam parameter q at the beam waist is purely imaginary and is given by:

$$q_0 = j \frac{\pi\omega_0^2}{\lambda} \quad (4.22)$$

The q parameter at a distance z away from the beam waist is given by:

$$q = q_0 + z = j \frac{\pi\omega_0^2}{\lambda} + z \quad (4.23)$$

By combining the Eq. 4.21 and Eq. 4.23 and equating the real and imaginary parts separately, one gets:

$$\omega^2(z) = \omega_0^2 \left[1 + \left(\frac{\lambda z}{\pi\omega_0^2} \right)^2 \right] \quad (4.24)$$

and

$$R(z) = z \left[1 + \left(\frac{\pi\omega_0^2}{\lambda z} \right)^2 \right] \quad (4.25)$$

The above two parameters can completely specify the Gaussian beam. From the above equations, we can extract a common factor which is defined as the Rayleigh range. This is given by:

$$z_R = \frac{\pi\omega_0^2}{\lambda} \quad (4.26)$$

The Rayleigh range is defined as the axial distance from the beam waist at which the Gaussian beam diameter becomes $\sqrt{2}\omega_0$.

Propagation of ray through optical elements

Ray matrices, also known as “*ABCD*” matrices, have been widely used for the description of propagation of geometrical optical rays through the optical elements in the

paraxial approximation. These optical elements can be anything such as lenses, curved mirrors, or ducts. The ray matrices have been proved to be extremely useful for describing a large number of other optical beam and resonator problems, including those which involve the diffractive nature of light. In this section, we use the matrix method for the analysis of the optical resonator.

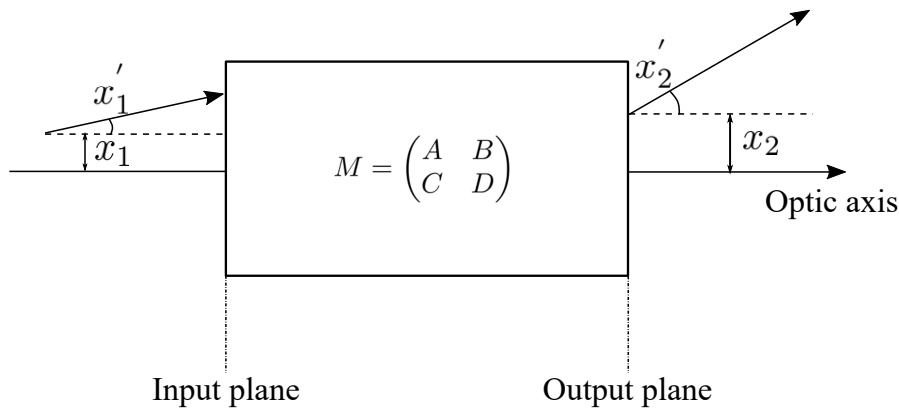


Figure 4.4: Example of ray matrix of method: An equivalent matrix is written corresponding to all the optical elements encountered by the ray from one reference plane to the final reference plane.

A ray of light traveling in the z direction can be characterized by its distance x from the optic axis (z) and by its slope, x' with respect to that axis. The above statement holds for the small angles with respect to the optic axis i.e., under the paraxial approximation. For a ray of light with the input parameters x_1 and slope x_1' passing through an optical element and having the output parameters x_2 and x_2' as shown in Fig. 4.4. Under the paraxial approximation, the output quantities are linearly dependent on the input parameters. This can be expressed in the matrix form:

$$\begin{pmatrix} x_2 \\ x_2' \end{pmatrix} = \begin{pmatrix} A & B \\ C & D \end{pmatrix} \begin{pmatrix} x_1 \\ x_1' \end{pmatrix} \quad (4.27)$$

where the slopes are measured positive, as shown in Fig. 4.4. The “**ABCD**” matrix is also known as the ray transfer matrix for the optical elements under consideration. A general property of all the basic optical elements is that the ray matrix determinant is unit:

$$AD - BC = 1 \quad (4.28)$$

The matrices for the optical elements used in the analysis of optical resonator is given in table - 4.2.

Optical element	Ray matrix
“Free space” region, refractive index n_0 , length L	$\begin{pmatrix} 1 & L/n_0 \\ 0 & 1 \end{pmatrix}$
Thin lens, focal length ‘ f ’	$\begin{pmatrix} 1 & 0 \\ -1/f & 1 \end{pmatrix}$
Curved mirror, radius ‘ R ’, normal incident	$\begin{pmatrix} 1 & 0 \\ -2/R & 1 \end{pmatrix}$
Curved mirror, arbitrary incident, $R_e = R \cos \theta$ in the plane of incident (“tangential”), $R_e = R/\cos \theta$ in the plane \perp to the plane of incident (“sagittal”)	$\begin{pmatrix} 1 & 0 \\ -2/R_e & 1 \end{pmatrix}$

Table 4.2: Ray matrices for paraxial optical elements: ABCD matrices for the optical elements used in the analysis of optical resonator.

If the equivalent “*ABCD*” matrix for the transfer of paraxial rays through the optical elements is known, the q parameters of the output and input beams are related as:

$$q_2 = \frac{Aq_1 + B}{Cq_1 + D} \quad (4.29)$$

here, q_2 and q_1 are the q parameters for the output and input beams respectively.

Analysis of bow-tie ring resonator

The matrix method described in the earlier section can be used for the description of the optical resonator used in the experiment for the second harmonic generation. The schematic of the bow-tie ring resonator is shown in Fig. 4.5. The optical cavity has two

plane mirrors denoted by M_1 and M_2 and two curved mirrors M_3 and M_4 . The folding angle of the mirrors is θ with respect to the optic axis. The path traversed by the optical beam is also shown in Fig. 4.5. The light is incident on the mirror M_1 , which is also the input coupling mirror to the resonator. The specifications of the mirrors used in the optical cavity are mentioned in the next section. The location of the beam waist inside the cavity depends on the radii of curvature of the resonator mirrors and the separation between them. In the present case, the resonator allows two beam waists inside the cavity: one between the plane mirrors M_1 and M_2 with a larger diameter and the other between the curved mirrors M_3 and M_4 with a smaller diameter. For the current cavity design, the beam waist between the plane mirrors has been used for mode matching of the light inside the cavity. This is done due to the relaxed mode matching criteria offered by it.

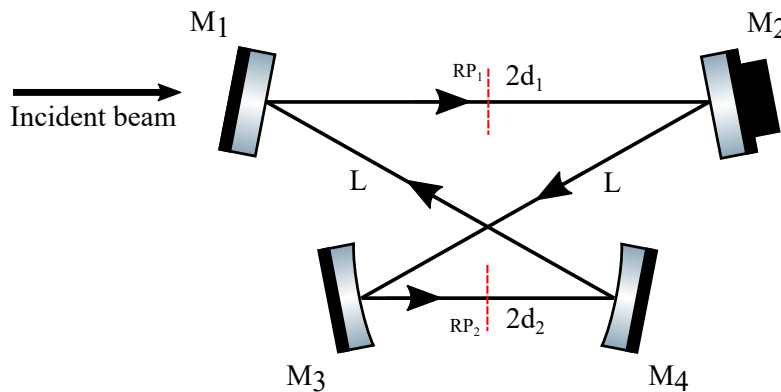


Figure 4.5: Cavity schematic: The ray diagram of the path traveled by the light inside the cavity.

We start the analysis of the cavity, assuming the cavity is in resonance and reached a steady-state condition. We consider a large beam waist ω_1 between the plane mirrors and a small beam waist ω_2 between the curved mirrors. We start with tracing the Gaussian beam from the waist ω_1 . As shown in Fig. 4.5, the optical path length between the plane mirrors is $2d_1$ and that between the curved mirrors is $2d_2$. Also, the diagonal distance between the plane and curved mirror is L . The beam path thus traveled during the round trip can be written as:

1. Propagation through free space from reference plane-1 (RP_1) to M_2
2. Reflection at M_2

3. Propagation through free space to M_3
4. Reflection at M_3
5. Propagation through free space to M_4
6. Reflection at M_4
7. Propagation through free space to M_1
8. Reflection at M_1
9. Propagation through free space to the starting point i.e. the location of beam waist

ω_1

The matrices for the optical elements encountered during the round trip can be taken from the table - 4.2. Due to the geometry of the optical resonator, the angle of an incident at the curved mirror is non-zero, this leads to the different ray matrices for the curved mirrors in the tangential and sagittal planes. The equivalent “**ABCD**” matrix in the present case can be written as:

$$\begin{pmatrix} A & B \\ C & D \end{pmatrix} = \begin{pmatrix} 1 & d_1 \\ 0 & 1 \end{pmatrix} \begin{pmatrix} 1 & L \\ 0 & 1 \end{pmatrix} \begin{pmatrix} 1 & 0 \\ -1/f & 1 \end{pmatrix} \begin{pmatrix} 1 & 2d_2 \\ 0 & 1 \end{pmatrix} \begin{pmatrix} 1 & 0 \\ -1/f & 1 \end{pmatrix} \begin{pmatrix} 1 & L \\ 0 & 1 \end{pmatrix} \begin{pmatrix} 1 & d_1 \\ 0 & 1 \end{pmatrix} \quad (4.30)$$

In the above equation, f is the focal length of the curved mirrors. As mentioned in the table for matrices, $f = f_{sag} = f/\cos\theta = R/(2\cos\theta)$ for the sagittal plane and similarly $f = f_{tan} = f\cos\theta = (R\cos\theta)/2$ for the tangential plane. In the above equations, R is the radius of curvature of the curved mirrors.

Thus if we start with the complex beam parameter q_{in} , and considering the beam parameter after the round trip is q_{out} . Then, the two parameters are related by:

$$q_{out} = \frac{q_{in}A + B}{q_{in}C + D} \quad (4.31)$$

In the above equation, A, B, C, D are the elements of matrix calculated from Eq. 4.30. Now, noting that the starting and the endpoints are the same and also since this point is the location of the beam waist between the plane mirrors, the beam parameter has to be purely imaginary. Thus, we can write:

$$q_{in} = q_{out} = jz_R \quad (4.32)$$

where, z_R is the Rayleigh range. The value for z_R in the sagittal and tangential planes can be obtained by replacing the focal length f with f_{sag} and f_{tan} respectively.

The above-mentioned steps can be repeated by considering the starting point between the curved mirrors M_3 and M_4 (RP_2). The solutions of the above equations give the parameters required for designing the resonator. For the fixed values of the focal lengths of the curved mirrors and the angle of incidence, one can achieve the stable operating region of the cavity by varying the distance between the plane mirrors $2d_1$ and that between the curved mirrors $2d_2$. It has to be noted that in order to reduce astigmatism (proportional to the difference of sagittal and tangential beam waists), it is advisable to minimize the folding angle of the cavity.

4.1.3 Cavity parameters

The method of optical resonator analysis can be used for designing the optical resonator for the harmonic generation. However, for our experiment, we followed the design reported by ‘‘R. Le Targat’’ in Ref. [143] with a reported mode matched conversion efficiency of 75%. The geometrical parameters of the optical cavity are given in table - 4.3

Parameter	Value
Distance between M_1 and M_2	149.5 mm
Distance between M_3 and M_4	140.4 mm
Folding angle	11°
Radius of curvature of curved mirrors	100 mm
Beam waist between the curved mirrors (ω_2)	$\sim 43 \mu\text{m}$
Free spectral range	537.8 MHz

Table 4.3: Cavity parameters: Geometrical parameters of the optical resonator in stable operating condition.

Mirrors specifications:

The mirrors for the optical resonator are custom made by ‘‘CVI Melles Griot’’. The specifications are chosen to increase the light coupling efficiency at 922 nm through the input coupling mirror M_1 and increase the circulation of the fundamental light by having the high reflectivity for it and at the same time enhancing the out-coupling of

the second harmonic light by having the high transmittivity for 461 nm. However, since the two wavelengths are related to each other by an integer, it is not easy to get the high reflection of one wavelength and, at the same time, high transmission for the other wavelength. The situation is shown in Fig. 4.6.

Mirror	Specifications
Input coupling mirror (M_1)	Material: UVFS SF: $\lambda/10$ at 633 nm SQ: 10-5 scratch-dig Side 1: 90% \pm 2% R @ 922 nm Side 2: < 1% R @ 922 and 461 nm
Mirror (M_2)	Material: UVFS SF: $\lambda/10$ at 633 nm SQ: 10-5 scratch-dig Side 1: >99.5% R @ 922 nm Side 2: uncoated, commercial polish
Dichroic spherical mirror (M_3 and M_4)	Material: UVFS Radius of curvature: 100 mm SF: $\lambda/10$ at 633 nm SQ: 10-5 scratch-dig Side 1: >99% R @ 922 nm and >70% T @ 461 nm Side 2: < 1% R @ 922 and 461 nm

Table 4.4: Cavity mirrors specifications: Specification of the mirrors used in the cavity-enhanced optical frequency doubler. Side 1 of each mirror faces inside of the frequency doubling cavity.

With the above mentioned limitations, we use the mirrors with 12.7 mm diameter and 6.35 mm thickness with the specifications mentioned in table - 4.4.

Construction of optical cavity

After finalizing the design parameters of the optical cavity and with the selection of mirrors, the next obvious step is the assembly of the components to make an operational

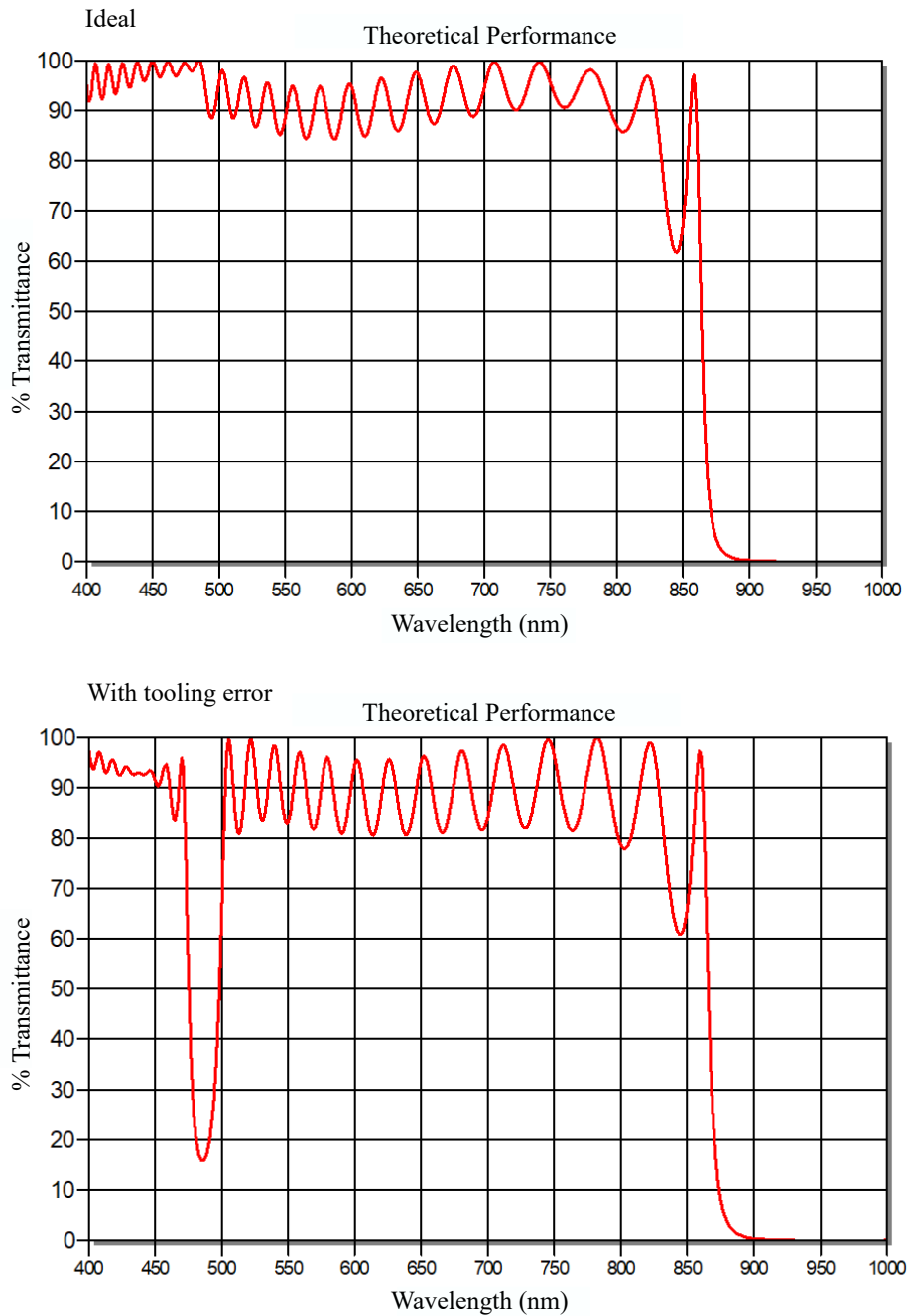


Figure 4.6: Cavity mirrors data from manufacturer: Transmission of the cavity mirror as a function of wavelength. In ideal condition, the reflectivity at 922 nm should be maximum and transmittivity at 461 nm should be maximum. However, in practice, it is extremely difficult to achieve. Source: *CVI Melles Griot*.

optical cavity. Considering the mechanical stability, we have used the mirrors with 12.7 mm diameter. Since the length of the cavity can change due to variation of room temperature and thus can go out of resonance, it is important to fix the mirrors on a thermally stable platform. This is ensured by making a base plate using aluminum (Grade: HE30), as shown in appendix - A.6. This optical resonator base consists of two sections. Two 55 W thermoelectric coolers connected in series and are sandwiched between them to maintain a fixed temperature of the top plate, as shown in Fig. A.6 of the appendix. The temperature of the top base plate is kept close to the room temperature in order to minimize the load on the Peltier cooler. The temperature of the base plate is actively monitored using a 10 k thermistor (*Thorlabs*: TH10K) and fed to a PID module by *Wavelength electronics* (Part No.: PTC10K-CH) to maintain the temperature at the fixed value. During the operation of the optical frequency doubler, air current can drift the cavity out of resonance, in order to avoid this, the whole setup is covered by an acrylic box. In order to lock the length of the cavity i.e., to keep the cavity on resonance to maximize the blue light conversion efficiency, mirror M_2 is attached to a tube piezoelectric transducer. This piezoelectric transducer receives a feedback from a separate PID module to compensate for the small drifts in the length of the optical cavity. All the four cavity mirrors are fixed on the top aluminum plate with the help of Newport 1/2" mirror mounts (Part No.: U50-A).

4.1.4 Master laser

Master laser is the laser operating at the wavelength of 922 nm and provides the seed light for the Tapered Amplifier (TA). This is a grating stabilized external cavity diode laser (ECDL) in Littrow configuration as shown in Fig. 4.7.

For generating the light at 922 nm, we used the *Toptica* DL100 module with a broad-band diode laser (*Toptica*: LD-0935-0100-AR-1) with a compatible grating with 1200 lines/mm from *Toptica*. This laser provides the maximum output power of ~ 45 mW at the operating current of 125 mA. For seeding the TA, we operate the laser at the current of ~ 110 mA, which generates ~ 24 mW of light at the wavelength of 922 nm. This light is then passed through an optical isolator with an isolation of 60 dB to suppress any standing waves competing with the cavity mode and causing instability in the laser op-

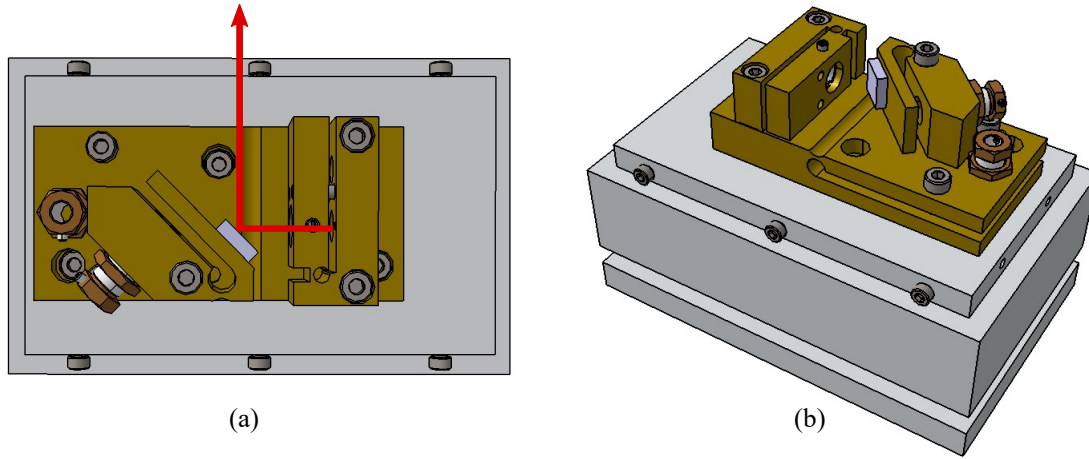


Figure 4.7: Seed laser for the generation of 922 nm light: (a) Schematic and (b) isometric view of ECDL in Littrow configuration for the generation of laser at 922 nm.

eration. The Littrow configuration uses a grating for wavelength selection and to form the laser resonator. The schematic diagram of the laser in this configuration is shown in Fig. 4.7. Depending on the angle of the grating, different wavelengths are reflected back into the laser diode via the “-1” order. The light is coupled out of the resonator via the zeroth order of the reflection and is used for the experiment. The angle of the grating can be shifted to achieve different wavelength operation by using a piezoelectric transducer.

Power amplification using Tapered amplifier

During the second harmonic generation using a non-linear crystal, the higher harmonic conversion efficiency is proportional to the fundamental power inside the cavity. The relation can be written as:

$$P_{2\omega} = \Gamma_{shg} P^2 \quad (4.33)$$

where, Γ_{shg} is the single pass conversion efficiency of the crystal and P is the fundamental power in the crystal.

The high power light for the frequency doubling cavity is generated using a Toptica tapered amplifier (TA) module (*BoosTA*). The light from the seed laser is coupled to the TA by using two mirrors. The TA produces a maximum output power of ~ 1.5 W of

922 nm light at the operating current of 2.5 A. The TA module's calibration curve as a function of TA chip current is shown in Fig. 4.8. The light thus amplified is sent to the optical resonator for the SHG with a proper mode-matching optics. As discussed in the earlier section, due to the geometry of the cavity, it has two different beam waists for the sagittal and tangential planes. In such a scenario, the mode matching can be achieved by using an anamorphic prism pair. However, since for the present cavity, the folding angle is very small $\sim 11^\circ$, the resulting astigmatism is very small and the mode-matching has been achieved simply by using a planoconvex lens of 2" diameter and 500 mm focal length. This lens has been mounted on a translation stage for achieving better control on the beam steering during the cavity alignment.

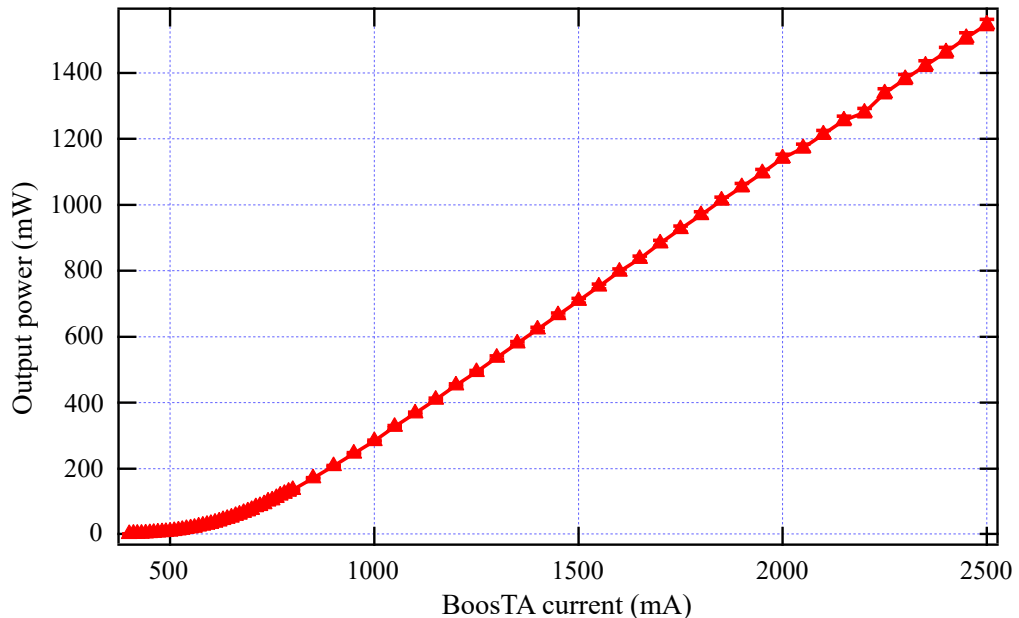


Figure 4.8: BoosTA output power as a function of TA chip current: The TA is seeded with a laser at 922 nm wavelength at the power of 22 mW.

Alignment of the optical cavity

Alignment of the optical cavity can be a tedious task for a first time user. Depending on the type of freedom offered by the cavity design, the process can vary. During the initial days of cavity operation, we tried to align the cavity without the crystal by monitoring the light reflected from the input coupling mirror M_1 . Nevertheless, this approach did not help us to optimize the alignment. Later, we started with the alignment of the cavity

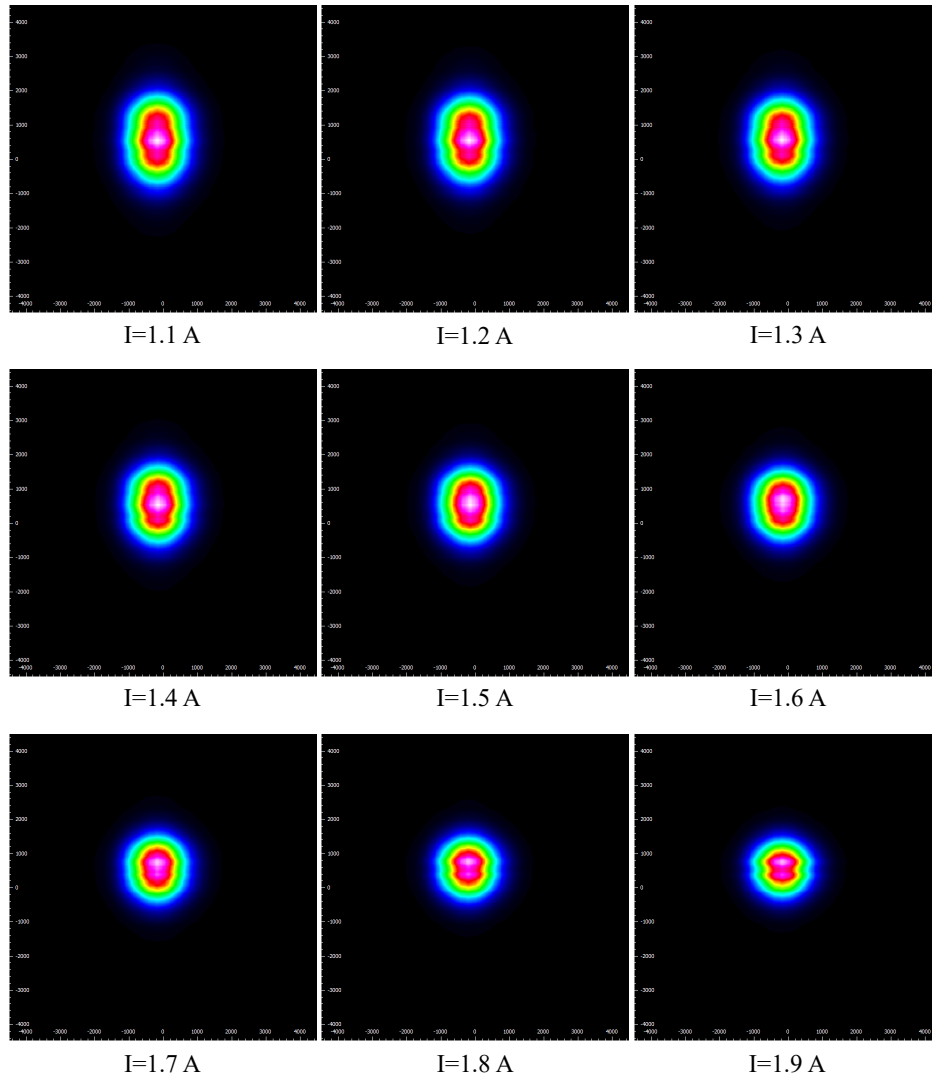


Figure 4.9: BoosTA output beam profile: BoosTA profile as a function of TA chip current.

after placing the non-linear crystal inside it and by monitoring the transmitted blue light through the out-coupling mirror M_4 . This approach proved to be helpful in our situation. Before starting the alignment procedure, we operate the BoosTA at low current while ensuring that the beam spot is clearly visible. We use the following steps to ensure the proper alignment of the cavity (see Fig. 4.5):

1. Remove the input coupling mirror
2. Trace the path of fundamental light to mirror M_2 . It should fall at the center of this mirror. The reflected light is then sent to mirror M_3 .

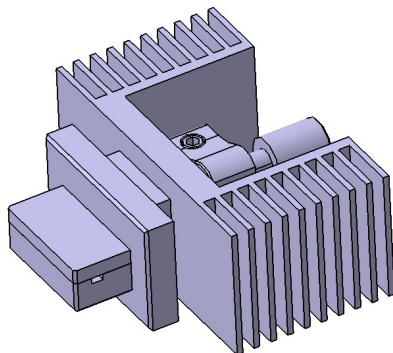
3. The light from mirror M_2 should fall at the center of mirror M_3 . The light reflected by this mirror should go through the center of the crystal and fall at the center of mirror M_4 .

4. The light reflected from mirror M_4 should coincide with the spot of the incoming light at the expected position of the inside facing surface of the input coupling mirror M_1 .

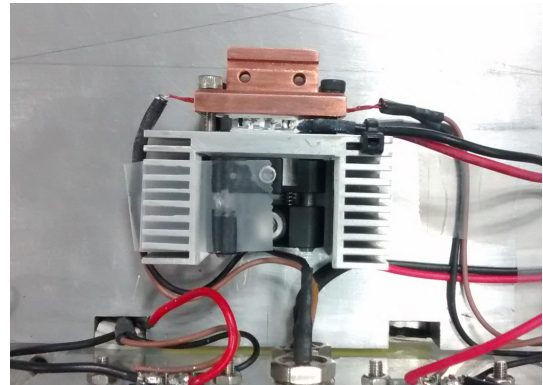
5. At this point, the input coupling mirror M_1 can be fixed with slight misalignment such that the light traversing one round trip falls near M_2 after the reflection from M_1 and can be seen on the IR detection card.

6. Now, the tilt-adjustment screws of M_1 are moved in such a way that the light reflected from M_1 and falling to M_2 and that transmitted directly to M_2 coincides.

7. At this point, the cavity scan is switched ON, and the transmitted blue light resonance peak is monitored on an oscilloscope using a photodiode. Note that the mirrors M_2 and M_3 ensure the alignment of the beam through the crystal, however, mirrors M_4 and M_1 is used for making the multiple reflected beams collinear through the direct incoming beam. Thus during the alignment, the mirrors are fine adjusted in the pair of $M_2 - M_3$ and $M_4 - M_1$.



(a)



(b)

Figure 4.10: Crystal holder: The crystal is kept in a specially designed mount to maintain the fixed operating temperature. The crystal holder is fixed with the help of Newport 12.7 mm mirror mount (Part No.: U50-A) for achieving the freedom of fine alignment of light through the crystal.

8. With the above-mentioned procedure, the output power (the height of the res-

onance peak) initially increases and then saturates. Once the saturation condition is achieved, the current of the BoosTA is increased gradually, and step-7 is repeated. This is done until the operating current is reached. This stepwise optimization of alignment with each increase in BoosTA current is mandatory, as the output beam profile of TA varies with the change in operating current, as shown in Fig. 4.9.

9. Once the height of the resonance peak saturates, one can play with the length of the cavity. This is done by rotating the three fine adjustment screws of a mirror mount by the same number of turns. For this, the pair of mirrors is selected such that the position of beam waist translates with respect to the mirror-plane of symmetry of the cavity. The mirror pairs for this purpose are $M_1 - M_2$ and $M_3 - M_4$.

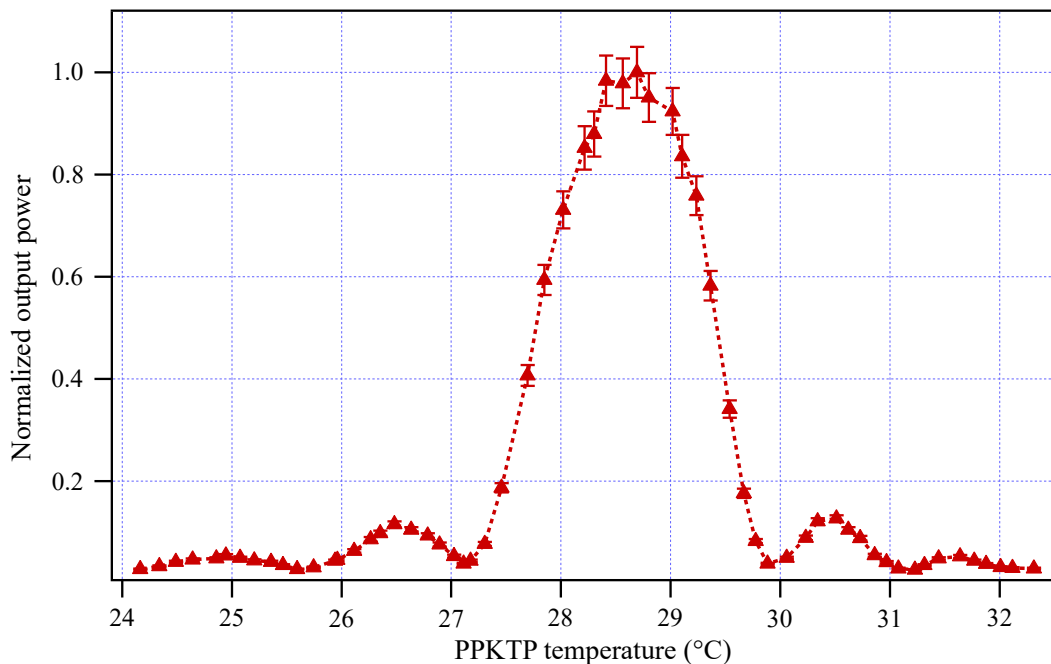


Figure 4.11: Temperature optimization of the nonlinear crystal: Frequency doubling efficiency of PPKTP crystal as a function of crystal temperature

Since the temperature of the crystal helps in achieving phase matching, the SHG efficiency is highly sensitive to the non-linear crystal temperature. In order to ensure the constant high power output from the cavity, it is crucial to actively stabilize the temperature of the crystal. In order to do so, the crystal is kept inside a specially designed holder, as shown in Fig. 4.10. The temperature of the crystal is stabilized with the help

of a thermoelectric cooler of capacity 12 W. The mechanical design of the crystal holder is given in appendix - A.5. The temperature is monitored using 10 k thermistor and fed to a wavelength electronics PID module similar to the one used for the temperature stabilization of the cavity base plate.

To find the optimum operating temperature of the non-linear crystal, we varied the temperature and monitored the power of output blue light. During the temperature variation, at some of the temperature, the SHG output is so low that the cavity can not be locked. To avoid the problem, we monitor the time-averaged output power at the scanning mode of the cavity operation. During this process, the offset is adjusted manually to keep the cavity length near resonance, and enough time is given to the crystal to reach the thermal equilibrium after each change of the temperature. The graph, thus obtained, is shown in Fig. 4.11.

4.1.5 Length stabilization of optical cavity

Length stabilization of the optical cavity is achieved using the standard Pound-Drever-Hall (PDH) locking scheme. The light from the seed laser operating at 922 nm is frequency modulated. This is done by modulating the current of the seed laser at the frequency of ~ 18 MHz using the Bias-T port of Toptica DL-100 laser. This frequency-modulated light passes through the Toptica BoostA and coupled into the cavity. Ideally, for a PDH scheme, the reflected light is monitored using a fast photodiode, in our case, we used the second harmonic generated light at 461 nm for monitoring purpose.

We have used a homemade fast photodiode amplifier for monitoring the cavity resonance. The circuit diagram of this amplifier is given in appendix - A.1. The input coupling mirror M_1 reflects a large fraction of the fundamental light, which is not mode matched into the cavity and at the same time, leaks out some of the harmonic generated blue light. The beam thus consists of lights at the wavelengths of 922 nm and 461 nm. We used a low pass optical filter to separate the two wavelengths. The reflected light at 922 nm is dumped into a beam dump. The transmitted beam consists of light at 461 nm. This light is reflected using a polarizing beam splitter to the fast photodiode. The photodiode signal is sent to the PDH module for demodulation. The PDH module is made using the standard RF components from *Mini-Circuits*. The block diagram is shown in

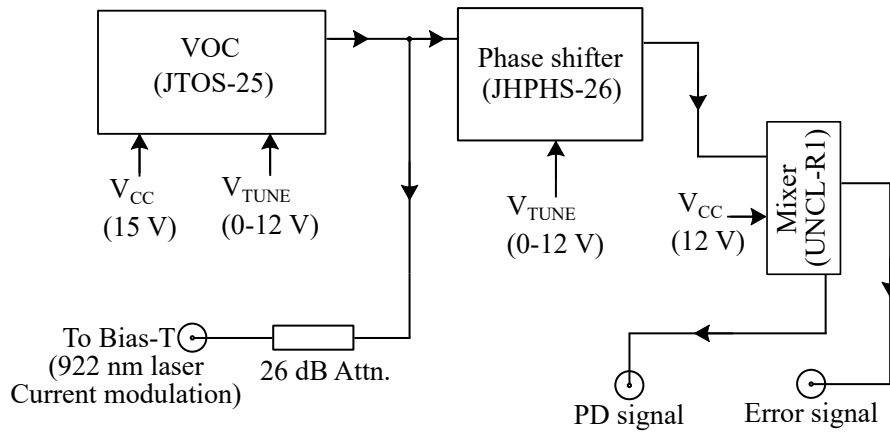


Figure 4.12: PDH module: Block diagram of the PDH module used for the length stabilization of the optical cavity. Standard RF components from Mini-Circuits have been used for making the module.

Fig. 4.12. The mixture output after the demodulation is the required error signal for the length stabilization. The error signal thus generated is fed into the Toptica PID module *PID110* to generate the correction voltage. The cavity resonance and the corresponding error signal is shown in Fig. 4.13. This voltage after the amplification goes to one of the mirrors, which is connected to the tube piezoelectric transducer, in our case M_2 , for length adjustment to keep the cavity on resonance. Fig. 4.14 shows the picture of the frequency doubler at the locked position. The SHG output of the optical frequency doubler as a function of fundamental pump power has been shown in Fig. 4.15.

The second harmonic generated blue light enables us to perform spectroscopy of the first stage cooling transition of Sr atoms. The obtained atomic spectrum has been used for the frequency stabilization of the seed laser. In the next sections, we will go through the development of spectroscopy cell for the Doppler-free spectroscopy of Sr atoms and techniques of laser locking.

4.2 Doppler free spectroscopy of the Sr atoms

This section has been published as:

“A compact atomic beam based system for Doppler free laser spectroscopy for Sr atoms”

*Gunjan Verma *, Chetan Vishwakarma *, C. V. Dharmadhikari and Umakant D. Rapol*

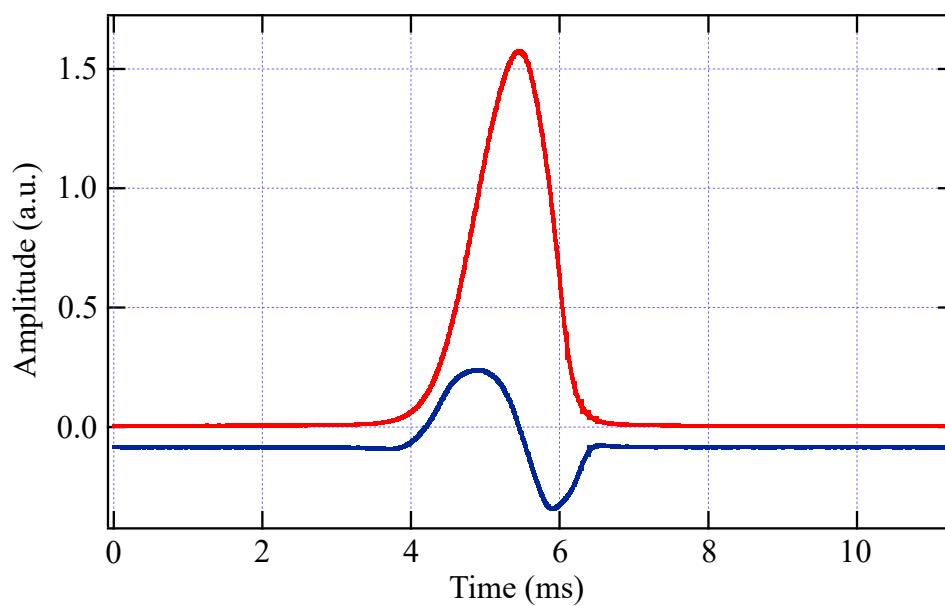


Figure 4.13: Optical cavity resonance: Cavity resonance (red curve) and the corresponding error signal (blue curve). The error signal is generated using the PDH scheme.

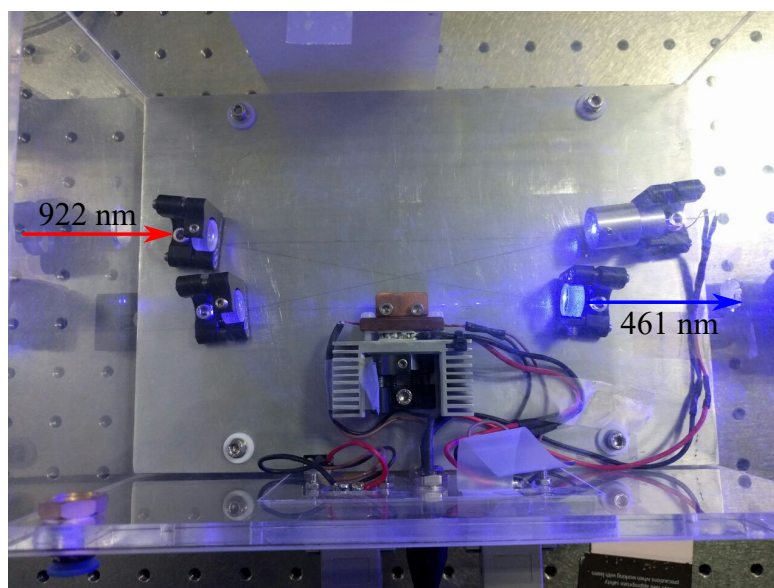


Figure 4.14: Optical frequency doubler: Picture of frequency doubler in the locked position.

Review of Scientific Instruments, **88**, 033103 (2017)

* Both the authors have contributed equally to the work.

This section describes the design and construction of a simple, lightweight, and com-

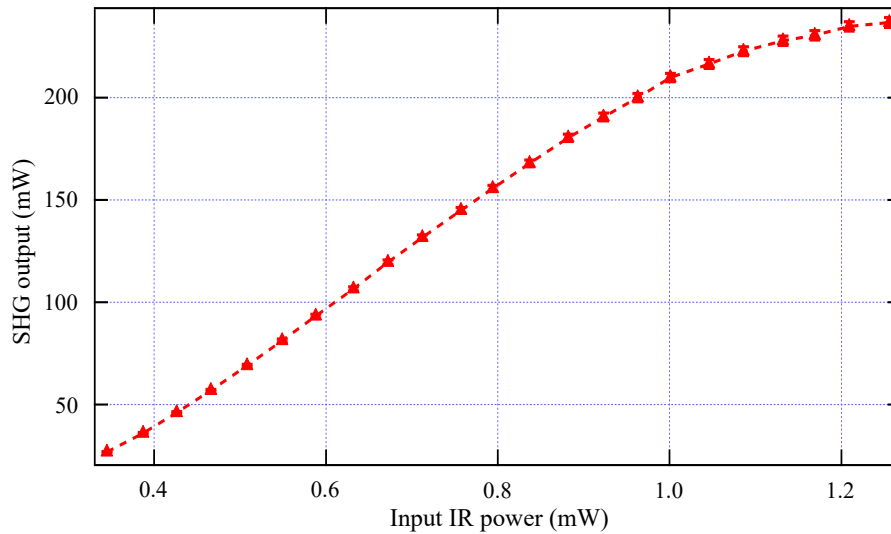


Figure 4.15: SHG output: SHG output as a function of input fundamental power. The crystal is maintained at the optimum temperature for the best harmonic conversion efficiency.

pact atomic beam spectroscopy cell for the Doppler-free spectroscopy of Sr atoms. The cell is built using the glass blowing technique and includes a simple home-made TSP for active pumping of residual background gases. A commercially available and electrically heated dispenser source is used to generate the beam of strontium atoms. The cell is characterized by comparing the obtained spectrum with the one acquired through the saturation absorption spectroscopy (SAS) and by checking the vacuum integrity by observing the spectrum for various operating currents and operation time.

In order to use the atomic transition as a frequency reference for locking the laser, one needs a Doppler-free spectrum of the atomic transition under consideration. There are two popular ways to generate a Doppler-free spectrum viz.:

- (1) saturation absorption spectroscopy (SAS) in a vapor cell [144]
- (2) the atomic beam spectroscopy, using an atomic beam derived from a high flux Sr oven used for loading the magneto-optical trap [129]

The SAS is one of the most popular techniques for generating a Doppler-free spectrum. It requires a combination of three laser beams to selectively target the atoms with zero group velocity. The details of the SAS is given in Ref. [145, 146]. However, the extremely low vapor pressure of alkaline earth metals (1 Pa at 796 K for Sr atoms) at room temperature requires special techniques to make spectroscopy cell. Most of the time,

samples need to be heated at very high temperatures, i.e., more than 650 K to get the appreciable amount of vapors for interrogation. The other hindrance is the highly reactive nature of Sr with glass. This forms an opaque coating on the glass surfaces [144, 147] and thus obstructs the optical access. In the earlier works on Sr spectroscopy, one of the above-mentioned methods were used for frequency stabilization. There are several limitations of using these designs. One of the disadvantages of using option (2) is that the system gets more complex and bulky if one is only interested in performing independent laser spectroscopy. The other disadvantage is that the atoms that are being interrogated are illuminated simultaneously by a Zeeman slowing laser beam, which leads to light-shift in the measured spectrum.

4.2.1 Design and construction

To counteract the problems as mentioned above, we constructed a simple, lightweight, and compact atomic beam spectroscopy cell for Sr atoms. The schematic diagram of the cell is shown in Fig. 4.16. The cell is fabricated using the glass-blowing technique. For the atomic beam spectroscopy, the observed Doppler broadening depends on the degree of collimation of the atomic beam for the transverse direction of interrogation. The Doppler shift along the transverse direction is given by:

$$\nu_0 = \frac{\nu_s}{\gamma(1 + \frac{v}{c}\cos\theta)} \quad (4.34)$$

In the above equation, ν_0 is the observed frequency in the laboratory frame of reference, ν_s is the source frequency, θ is the detection angle with respect to the atomic velocity and $\gamma = 1/\sqrt{1 + v^2/c^2}$. Therefore, by choosing the direction of interrogation to be perpendicular to the atomic beam's direction, one can obtain a spectrum that is free from the Doppler broadening.

To reduce the Doppler broadening as small as possible, we came up with a geometry of the cell that reduces the intrinsic divergence of the dispenser source (*Alvasource*: AS-5-Sr-500-V) ~ 120 mrad. For this, a long glass (Borosilicate type 3.3) tube with an outer diameter (OD) 19.2 mm and length 274 mm is chosen, which gives a divergence of ~ 95 mrad. An optical cross is created on the other end by fusing four glass tubes having an OD 28.5 mm and length 50 mm. Optical flats (windows) are fused on these tubes

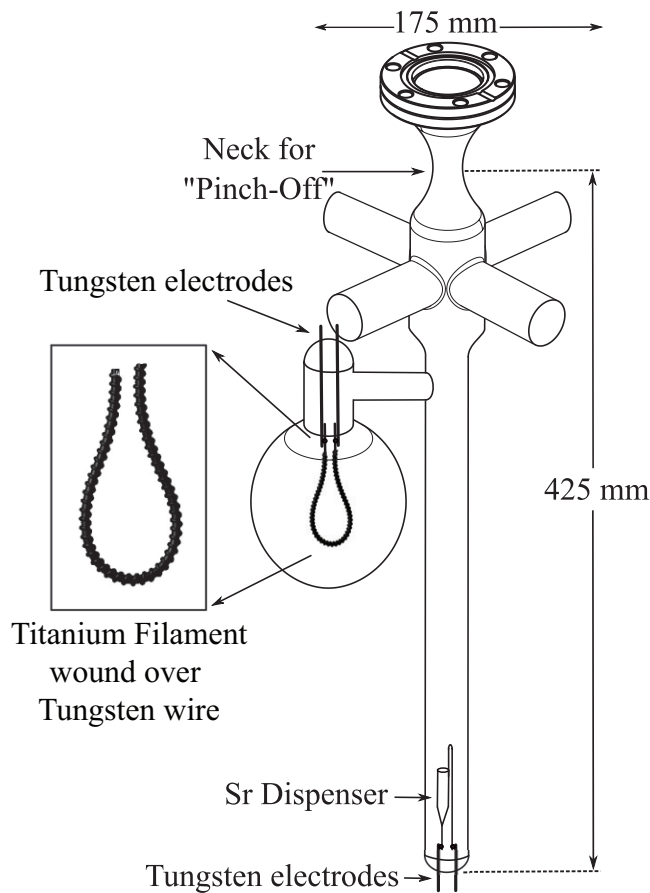


Figure 4.16: Schematic diagram of the spectroscopy cell: The atomic beam is generated by a Sr dispenser source at the bottom of the cell. The collimation provided by the tube of the cell is nearly 95 mrad. The crossed arms are used for excitation and collection of the fluorescence signal. TSP maintains the UHV inside the cell.

for optical access from orthogonal directions. These optical flats are 2 mm thick with a 25 mm diameter and optically polished on both sides. Excitation of the atomic beam and collection of fluorescence from atoms is done from these two orthogonal directions, as shown in Fig. 4.17. The cross eliminates the risk of forming dark coating by the deposition of Sr atoms on the glass windows that can block the optical access for the probe beam. We generate a well collimated atomic beam in the direction along the length of the long glass tube. In order to have a stand-alone spectroscopy solution, one needs an active pumping mechanism for the system. For this, we incorporated a homemade TSP in the system. This helps us to maintain a vacuum better than $< 10^{-8}$ mbar in the system. This whole system is connected to a CF35 glass-to-metal

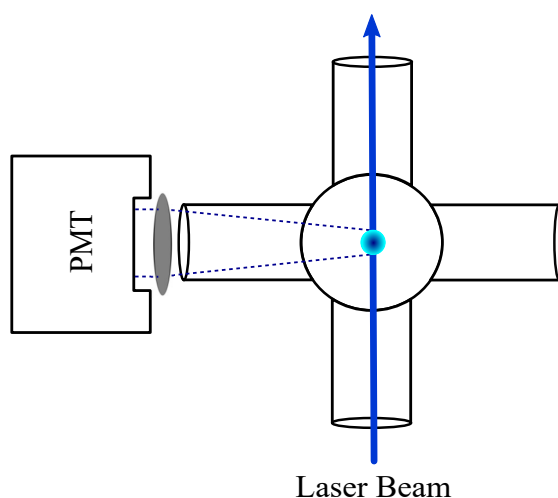


Figure 4.17: Top view of the spectroscopy cell: The fluorescence signal is collected along the transverse direction using a planoconvex lens of diameter 25.4 mm and focal length 75mm.

adapter through a narrow neck for connecting it to a pumping station based on the turbomolecular pump (TMP) depicted in Fig. 4.16.

The filament for TSP is made by winding a 0.25 mm diameter titanium wire onto a tungsten wire of 0.5 mm diameter and length ~ 90 mm in the form of a loop shown in the inset of Fig. 4.16. The tungsten loop provides physical support to titanium wire and also ensures electrical conductivity within the titanium wire. For electrical contacts, we used another pair of tungsten wires of diameter 1 mm, which is spot welded to the 0.5 mm wire. This TSP filament is enclosed in a spherical glass bulb of diameter ~ 79 mm. The pumping efficiency of TSP is directly proportional to the internal surface area of this bulb.



Figure 4.18: Sr dispenser: Sr dispenser is spot welded to the tungsten electrode. These electrodes provide the electrical connections for dispenser operation.

Tungsten electrodes cannot be fused directly to borosilicate glass as they have different coefficients of thermal expansion (3.3×10^{-6} m/m-K for glass and 4.3×10^{-6} m/m-K for tungsten) which can cause cracks and leaks in the vacuum system. We use the glass beads formed on the tungsten rods as graded seals to compensate for the difference between the thermal expansion coefficient of tungsten and borosilicate glass. The fusing is done independently before making the entire system. The flame used for this purpose causes the oxidation of tungsten and thus needs to be adequately cleaned before assembling the entire system using the glass blowing technique. This is one of the most crucial steps as it can degrade the quality of the vacuum and can affect the observed spectrum. We employ the standard electro-polishing technique for cleaning tungsten electrodes.

We use a commercial dispenser source from Alvatec (*Alvasource*: AS-5-Sr-500-V) for generating the atomic beam of Sr atoms similar to the one reported in Ref. [144] albeit of a smaller length. This dispenser is a small capsule made up of stainless steel of OD 3 mm and length 25 mm. The dispenser is gas-tight sealed by pressing an indium plug and filled with an isotopic mixture of strontium under a pure argon atmosphere. When used, the source is heated via conventional resistance heating. As a consequence, the indium sealing melts, and a small argon puff of gas is released in the vacuum system. During operation, the dispenser releases 99.95% pure Sr when the activation current is reached. The electrical connection to the dispenser is provided through a pair of Tungsten wires, which are spot welded with the legs of the dispenser and fused with the glass, as shown in Fig. 4.18.

4.2.2 Baking of the spectroscopy cell

To achieve UHV, the spectroscopy cell is initially connected to the TMP pumping station using CF35 flange. An all-metal in-line valve is placed between the spectroscopy cell and the pumping station. In order to avoid direct contact with the heating coil with the glass manifold, we made a cage-like enclosure around the cell. The heating coils are wrapped around the enclosure. The glass cell is then heated indirectly by the transfer of heat by the convective and radiative mechanism. The heat loss by radiative cooling is reduced by covering everything by an aluminum foil, as shown in Fig. 4.19.



Figure 4.19: Baking of spectroscopy cell: A cage-like enclosure is used for baking. A heating coils are wrapped around the enclosure. The cell is baked by the convective and radiative heating mechanism.

The system is initially soft baked at a temperature of 140°C for 36 hours while running the TMP continuously. The maximum baking temperature is limited by the melting point of the indium seal of the dispenser. During the bakeout cycle, the TSP filament and dispenser source are degassed by passing a current of 3 A and 2 A, respectively. The dispenser source is activated by melt the indium seal before detaching the cell from the pumping station. This is done by gradually increasing the current through the dispenser from 3.5 A to 8 A. During this process, we observe an increase in pressure of up to 1.2×10^{-3} mbar and then a quick drop to its original value (1.0×10^{-5} mbar), caused by the release of argon from the dispenser. The entire glass cell is gradually cooled down to

room temperature to get the pressure below 10^{-8} mbar. A helium leak test was carried out for checking the vacuum integrity at this point. The TSP filament is then flashed at a current of 4.5 A for a period of nearly 1 hour. This leads to the improvement of the vacuum by an order of magnitude. The spectroscopy cell is detached from TMP by closing the in-line valve and slowly heating the “neck” of the cell with a gas torch and then “pinching-off” at that point.

4.2.3 Characterization of spectroscopy cell

To characterize the spectroscopy cell, we excite the $5s^2\ ^1S_0 \rightarrow 5s\ 5p\ ^1P_1$ transition (saturation intensity, $I_s = 42.7\ \text{mW/cm}^2$) of Sr atoms using a linearly polarized probe beam of 0.82 mW with a $1/e^2$ diameter of $\phi = 2\ \text{mm}$ at wavelength 460.7 nm (saturation parameter = $I/I_s = 0.61$). An atomic beam is generated by passing a current of 8.0 A through the dispenser. Due to finite dimensions of the dispenser capsule, we get an intrinsic divergence of 120 mrad, as mentioned in the earlier section; this divergence is further reduced by the geometry of the cell to 95 mrad. We measure the longitudinal velocity of the atomic beam by having another probe beam at an angle of 4.7° with respect to the first probe beam and extract the most probable velocity to be 420 m/s. Fig. 4.20 shows the dependency of longitudinal velocity on source current. The probe light was generated from home-built frequency doubler, which was fed with an input light of 922 nm with 1.2 W power generated from a commercial Tapered amplifier, as mentioned in the earlier section.

The fluorescence of the atoms is collected through a rectangular slit by a plano-convex lens of focal length 75 mm on a photomultiplier tube (*Hamamatsu*: Model H9307-02) in the perpendicular direction to probe beam. The circuit diagram of the PMT control-box is given in appendix - A.4. We scan the probe beam frequency over a range of 700 MHz by applying a linear voltage ramp to the piezoelectric transducer of the seed laser (922 nm) to cover the spectrum of all isotopes of Sr. The obtained fluorescence signal is fitted with a sum of six Voigt profiles for three bosonic and three hyperfine components of fermionic ^{87}Sr isotope as shown in Fig. 4.21. The relative area under each peak of the fluorescence signal is proportional to the relative abundance of the corresponding isotopes.

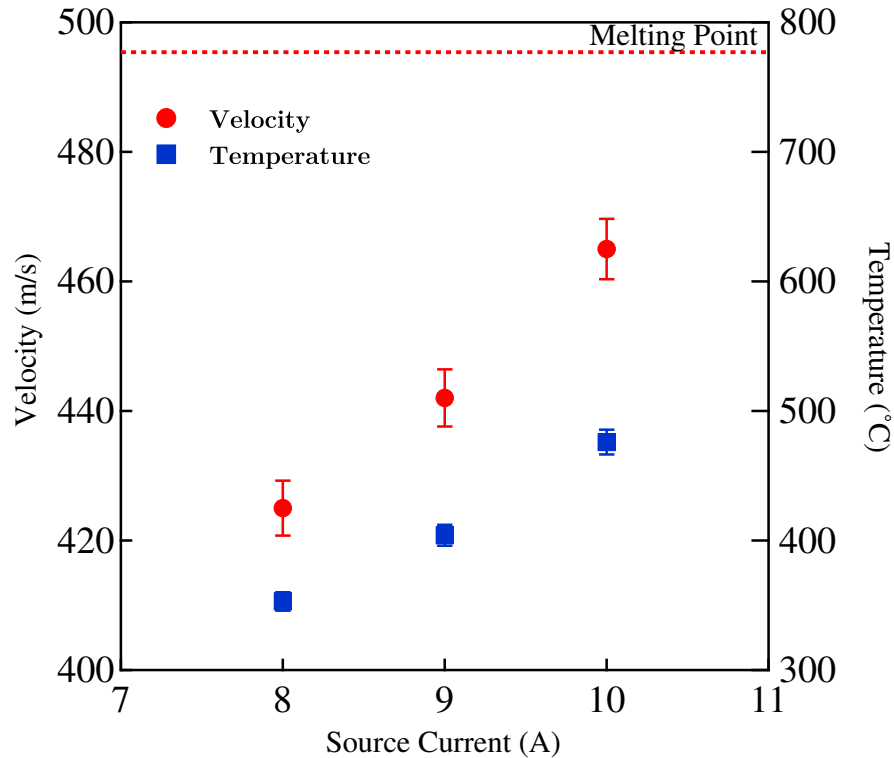


Figure 4.20: Dispenser characterization: Most probable velocity of atoms (red filled circles) and the estimated temperature (filled blue squares) of the dispenser vs. the current through the dispenser: A laser beam crossing the atomic beam at an angle 4.7° is used to probe the velocity distribution of the atomic beam. The broken horizontal line indicates the melting point of Sr.

By using the known values of the isotope shifts, hyperfine splitting, relative abundances [148], and considering a power and pressure broadened Lorentzian width ($\Gamma = 42$ MHz), we perform a multiple Voigt fitting to the measured signal (similar to Ref. [144]). We estimate the transverse Doppler line broadening of each component, offset, and center. We use the relative peak positions of the various spectral lines for frequency scaling, and alternately, we also cross-check the frequency calibration against the known Free Spectral Range (FSR) of the frequency doubling optical cavity.

The estimated width of the transverse velocity profile is determined by fitting the fluorescence peaks recorded for a dispenser source current of 8A. The estimated ^{88}Sr Full Width at Half Maximum (FWHM) and corresponding velocity spread are found to be 33.3 ± 1.7 MHz, 6.5 ± 0.3 m/s respectively. The width is less compared to the

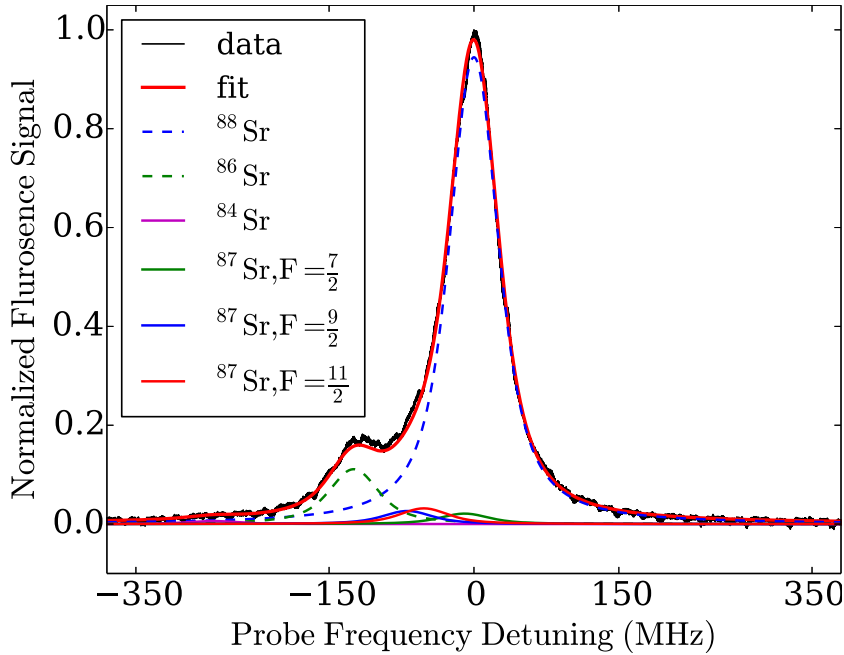


Figure 4.21: Strontium spectrum: Fluorescence spectrum of $5s^2\ ^1S_0 \rightarrow 5s\ 5p\ ^1P_1$ transition of Sr atoms. The spectrum is fitted with a sum of six voigt profiles for the individual isotopes of Sr.

reported values in previous studies. The transverse Doppler width is found to be very close to natural linewidth ($\Gamma = 32$ MHz) which is essentially equivalent to a Doppler-free spectrum.

Continuous operation of Strontium source for 6-7 hours at higher currents (> 9 A) during the experiment increases the background pressure in the spectroscopy cell, which broadens the spectral lines. To maintain a high vacuum in the cell, we implemented a TSP shown in the inset of Fig. 4.16. We tested the performance of the TSP in maintaining the pressure by monitoring the FWHM of ^{88}Sr peak over time while keeping the dispenser source continuously ON for 5-6 hours on three consecutive days. We then operated the source at 10 A current and kept it ON continuously for over 6 hours. We observe that the FWHM continuously increases from 34.2 MHz for the initial 3 hrs and then saturates at 54.8 MHz, while the overall flux remains almost constant. This velocity broadening can be attributed to increased background pressure. After 6 hours, we turned OFF the source and switched ON the TSP for half an hour by passing 5 A current through it. Next day we repeated the measurement to observe the similar behavior of

FWHM, i.e., we saw that the FWHM dropped to the initial value (35.6 MHz) which indicates the recovery of vacuum inside the cell and also a quick saturation of FWHM to a lower value (44.2 MHz) over 5.3 hours run compared to the previous day. Similar behavior was seen on the third day, where we see FWHM going from 35.2 MHz to 36.5 MHz. This exercise not only indicates the reasonably good performance of TSP but also an active pumping of TSP during the continuous operation of the source. We have been using this source continuously for over three years without any degradation in the observed spectral qualities. Since the optical cross used in this setup is out of line-of-sight of the atomic beam, there is no opaque coating by the deposition of Sr atoms on the glass windows. After a repeated operation of the cell over several months, we do not see any coating on the windows; however, Sr gets coated on the walls of the long tube near the source and the neck used for “Pinch-off” (as shown in Fig. 4.16) that does not affect the performance of this spectroscopy cell.

4.3 Frequency stabilization of laser systems

4.3.1 Frequency stabilization of seed laser

The spectrum obtained by performing atomic beam spectroscopy is used to generate the feedback signal for compensating the drift of the seed laser operating at 922 nm. The error signal for locking the seed laser is generated using standard lock-in-detection technique [149]. For this, the laser frequency needs to be modulated. In our system, this modulation is added by an acousto-optic modulator (AOM), which is also used for adding a constant frequency shift of 168 MHz in the spectroscopy beam with respect to the frequency doubler output. The complete optical layout, along with the frequency detuning scheme, is given in later sections. The frequency of modulation is chosen to be ~ 34 kHz. The signal for frequency modulation is generated by the SRS lock-in amplifier (*Stanford Research System*, Model: SR830) and combined with the DC voltage sent to the voltage controlled oscillator of the AOM driver using an OP amp based adder circuit. Schematic of the setup used for generating the error signal for locking the laser is shown in Fig. 4.22. The frequency modulated laser beam at the wavelength of 461 nm is then used for probing the first stage cooling transition $5s^2 \ ^1S_0 \longrightarrow 5s \ 5p \ ^1P_1$

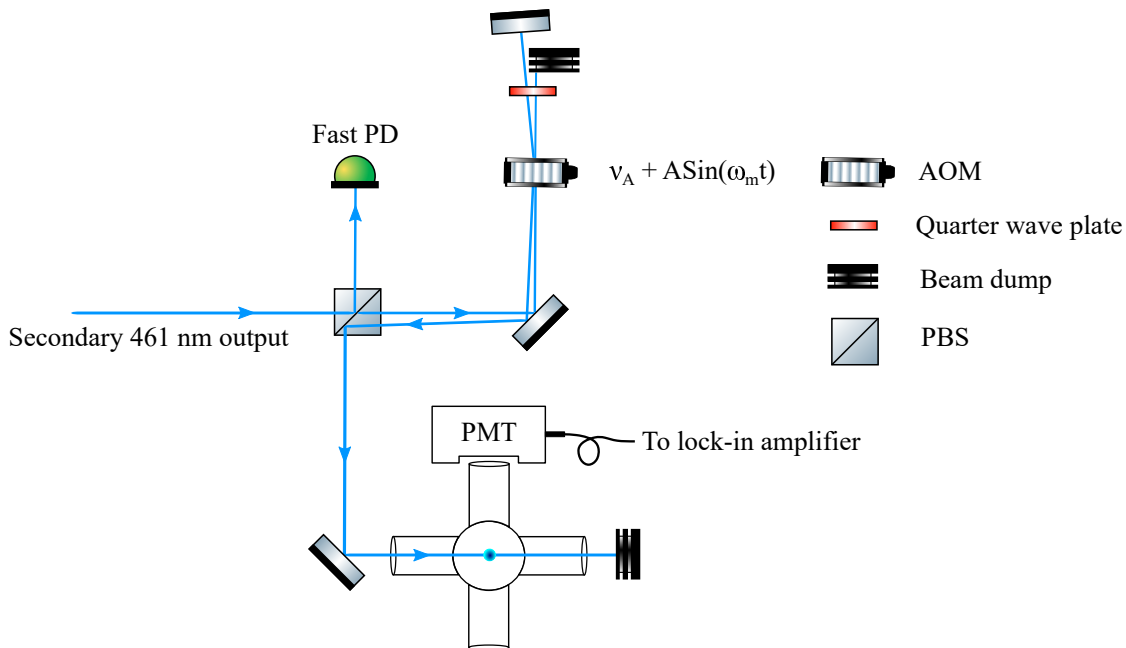


Figure 4.22: Error signal generation for locking seed laser: The secondary output of the SHG cavity at 461 nm is frequency modulated using an AOM. This modulated light is used for probing the first stage cooling transition $5s^2 \ ^1S_0 \longrightarrow 5s \ 5p \ ^1P_1$.

by passing it through the atomic beam generated in the spectroscopy cell as mentioned in the last section. The atomic fluorescence thus produced is detected by the PMT in the direction orthogonal to both the atomic and the laser beam, as shown in Fig. 4.22. The signal detected by the PMT is demodulated at the same frequency to generate the corresponding error signal. This is done using the above-mentioned lock-in amplifier.

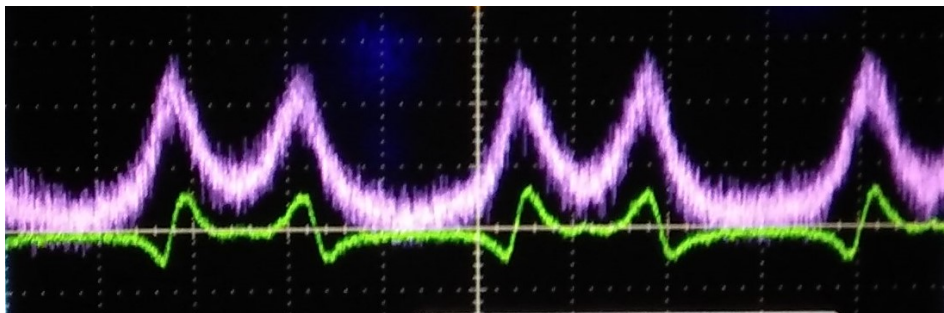


Figure 4.23: Sr spectrum: Spectrum of Sr atoms (pink curve) along with the corresponding error signal (green curve). The error signal is generated using standard lock-in detection.

The obtained atomic spectrum and the corresponding error signal is shown in Fig. 4.23.

Since the seed laser operating at 922 nm drifts slowly at the rate of few MHz/min, a slow feedback to the laser's piezoelectric transducer is sufficient to compensate for the drift. Therefore, we fed the error signal to PZT via a PID controller and a voltage amplifier. The circuit diagrams for both the circuits are given in appendix - A.2 and A.3.

4.3.2 Frequency stabilization of repumping lasers

The atoms, when excited to the state 1P_1 , decay to 1D_2 state with a branching ratio of $1: 2 \times 10^{-5}$. Atoms in 1D_2 connect to the triplet states 3P_2 and 3P_1 with a branching ratio of 1: 2, respectively. The transition to the ground state $^3P_2 \rightarrow ^1S_0$ is doubly forbidden; thus, the atoms once decayed to 3P_2 are lost from the cooling cycle. There are several repumping schemes to revive this loss [113, 150–153]. The most popular among them employs two lasers operating at 707.2 nm and 679.3 nm. In the experimental setup, we have utilized two repumping schemes using lasers with wavelength 707.2 nm addressing the transition $5s\ 5p\ ^3P_2 \rightarrow 5s\ 6s\ ^3S_1$ and the laser operating at wavelength 481.3 nm targeting the atomic transition $5s\ 5p\ ^3P_2 \rightarrow 5p^2\ ^3P_2$ (Fig. 2.1).

For the atomic transition between the ground state 1S_0 and the excited states 3P_1 and 1P_1 , a heat pipe can be used for generating the sufficient vapor pressure to perform the spectroscopy [154]. However, due to the high excitation energy involved, for the frequency stabilization to the transition between the metastable state and the higher excited states, the thermal occupation of the metastable state does not provide the sufficient optical depth for the spectroscopy purpose. The problem, however, can be solved by using a hollow-cathode lamp in which the collisions generate a sufficient population in the metastable state 3P_2 for spectroscopy and frequency stabilization of laser operating at the wavelength 707.2 nm [155]. Although hollow-cathode lamps are a compact solution for spectroscopy, they suffer from the drawback of short lifetimes and large pressure broadening [155, 156]. The alternative solution is to employ the spectra of molecules such as iodine, tellurium for frequency stabilization. However, the utility of such a system depends on the existence of a molecular line near the atomic transition under consideration.

An alternative approach is to use a commercially available, high accuracy wavemeter for measuring the frequency of laser light. The difference of laser frequency with respect

to the set frequency gives the error signal, which can be fed back to the piezoelectric transducer of the laser for wavelength correction. The wavemeter usually requires only a small amount of light for measurement, typically of the order of a few 10's of μW and can be used over a broad frequency range, typically of the order of 100's of nanometers. These schemes of using the wavemeter for laser locking have been used extensively [157–160].

Similar to the above-mentioned scheme, for our experiments, the frequencies of both the repumping lasers are locked using a LabView interfaced digital PID controller, which receives feedback of the laser frequency via a commercial wavemeter (*High Finesse*, model: WSU-30). An analog voltage is generated using a National Instruments data acquisition card, which is proportional to the difference of laser frequency and the set frequency. This voltage is fed into Toptica scan controller module SC110, which gives the feedback to the PZT of the laser for stabilizing the frequency.

4.3.3 Frequency control of laser

The laser beams for various stages of cooling and trapping are generated by splitting the frequency doubling cavity output. The laser is frequency stabilized to the atomic transition by performing the Doppler-free atomic beam spectroscopy, as mentioned in the earlier sections. These laser beams need to be kept at different frequency detunings for various purposes and have to be changed during the different stages of the experimental sequence. These frequency shifts are achieved using acousto-optic modulators (AOMs). The AOM uses the acousto-optic effect to diffract and shift the frequency of the light by the applied radio frequency (RF). In an AOM, a piezoelectric transducer is attached to a crystal. On the application of an RF signal, the transducer induces and couples the acoustic wave in the crystal. The process can be thought of as a moving periodic plane of expansion and compression that changes the refractive index of the material. The incoming light scatters off the resulting periodic index of modulation and results in interference similar to the Bragg diffraction. The AOMs have been utilized for generating the frequency shifts and for making high-speed optical switches.

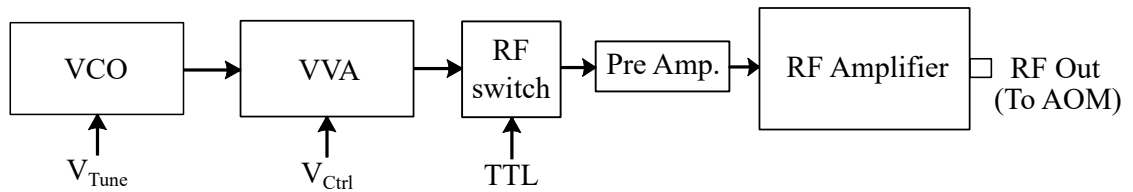


Figure 4.24: AOM driver block diagram: Block diagram of the AOM controller. This is made using the standard RF components from Mini-Circuits.

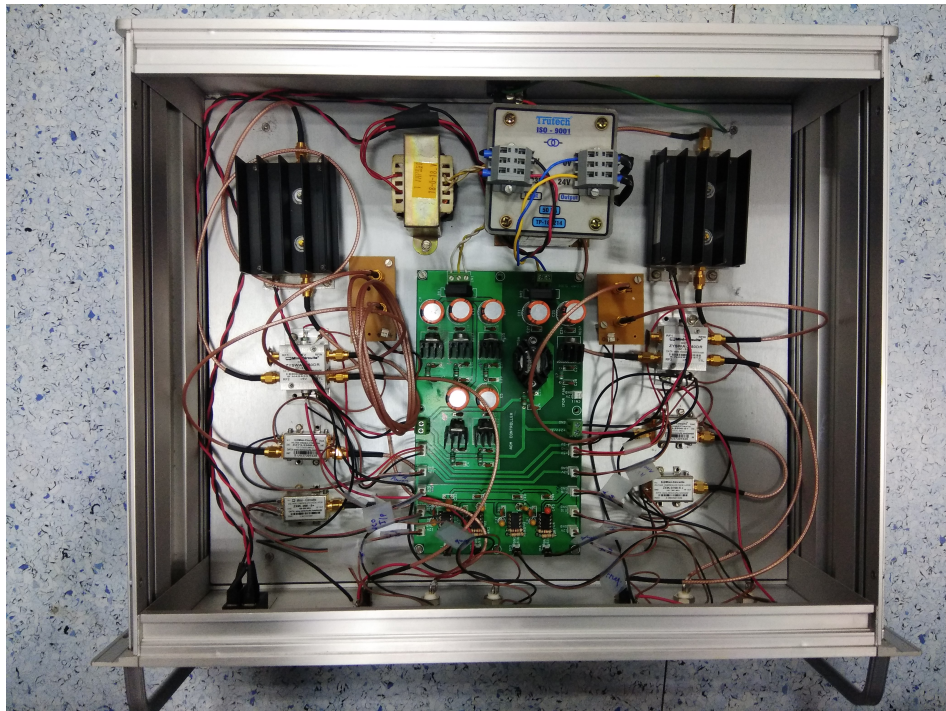


Figure 4.25: AOM driver box: Dual channel AOM controller, for controlling the frequency shifts of the different laser beams, showing all the necessary RF components in it.

In our experimental setup we have used AOMs from *IntraAction Corp.* (Model:ATM-801A1, ATM-110A1 and ATM-200A1). These AOMs use TeO_2 (Tellurium dioxide) crystal as a diffraction material. These are coated for the wavelength range of 400-700 nm and have a maximum diffraction efficiency of $\sim 85\%$. In order to drive these AOMs, high power RF signals of the order of few watts are required. These high power RF signals are generated using homemade AOM drivers using the commercially available components from Mini-Circuits. The block diagram and the picture of one such AOM driver box are shown in Fig. 4.24 and Fig. 4.25 respectively.

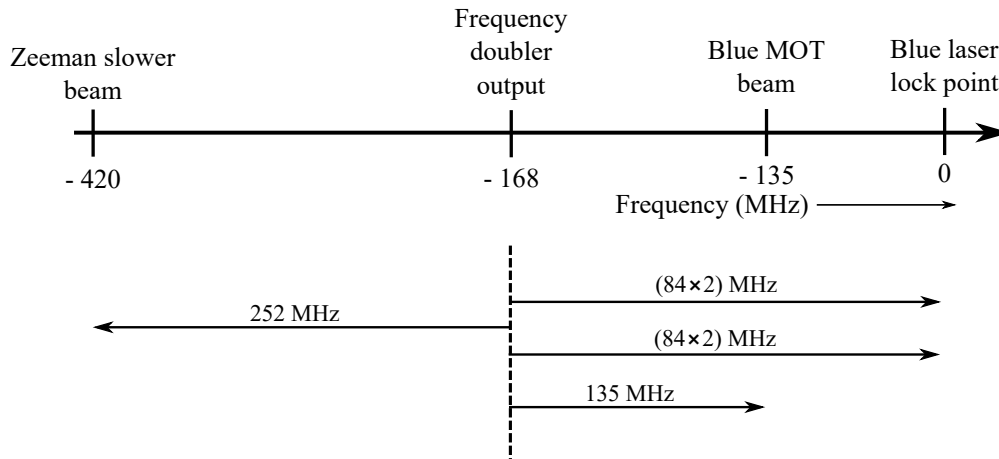


Figure 4.26: Laser frequency scheme for first stage cooling: The light coming out of optical frequency doubler is shifted by 168 MHz using acousto-optical modulator (AOM) in double pass configuration. All other beams are derived with respect this frequency-shifted laser beam.

Fig. 4.26 shows the detuning of the 461 nm laser beams with respect to the first stage cooling transition for the spectroscopy, Zeeman slower, MOT, and the probe beams. The frequencies in the individual beams are red detuned with respect to the first stage cooling transition frequency. As the frequency detuning requirement for the Zeeman slower beam is high ~ 420 MHz, we used the AOM at frequency 84 MHz in the double-pass configuration to probe the atoms for locking the laser. This way, the main frequency doubler output is 168 MHz red detuned with respect to the atomic transition. This blue light is then used for generating the rest of the laser beams for various purposes.

4.4 Optical layout

The schematic diagram of the laser systems used for the generation of cold atoms in the magneto-optical trap is shown in Fig. 4.27. The laser systems are set up on a $1.5 \text{ m} \times 3 \text{ m}$ optical table that also host the vacuum assembly. The optical table is pneumatically isolated using four legs. For the experiments reported in this thesis, we have used laser operating at 461 nm wavelength and two different repumping schemes utilizing the lasers operating at wavelengths 707.2 nm and 481.3 nm. The blue light is generated using a cavity-enhanced SHG. The seed light for the frequency doubler is generated using a diode laser in Littrow configuration. The light from this laser is passed through a Faraday isolator before going into a TA module by Toptica. The amplified light is

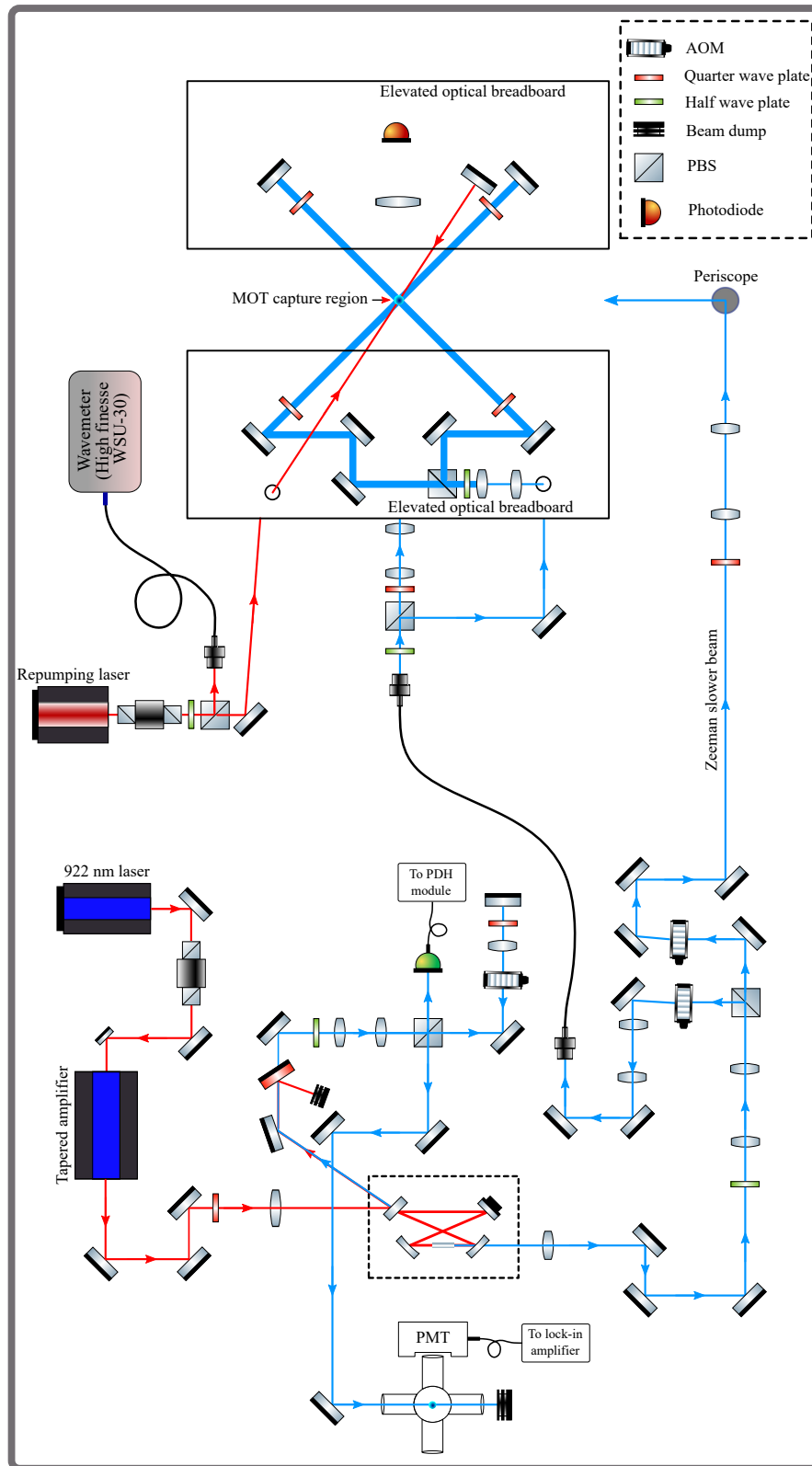


Figure 4.27: Optical table layout: Schematic of optical table layout showing all the necessary optical components used in the experiment.

mode matched into the optical cavity using a 500 mm plano-convex lens of 50.8 mm diameter. The main output of the cavity from the output coupling mirror M_4 is used for generating the beams for Zeeman slower, MOT, and probe beams. The secondary output of the cavity from mirror M_1 is used for locking the cavity using PDH locking scheme and for locking the seed laser to the atomic transition after double pass configuration through an AOM.

Similarly, both the repumping lasers used for the experiments are in standard Littrow configuration using home-built mechanical mounts, as shown in Fig. 4.7. For controlling temperature and current of the laser diodes and the voltage to the piezoelectric transducer, we use the commercially available Toptica controllers.

The diffraction efficiency through the AOMs is highly dependent on the spot size of the laser beam. To achieve the diffraction efficiency of $>75\%$, we used telescope assemblies to reduce the beam size by 3–4 times as shown in the schematic diagram.

During the first phase of the experiment, we used the repumping laser operating at a wavelength of 707.2 nm. During this time, the laser beams for the MOT were free-standing and had a beam diameter of 10 mm at the atom capture region. This repumping laser was later replaced by a laser operating at the wavelength of 481.3 nm. We used optical fiber to ensure the unchanged alignment of the MOT laser beams through the atom capture region. The main output from the frequency doubler is split into two parts for Zeeman slower and for the MOT beams. The laser beam for the MOT is then coupled into an optical fiber. The output of the optical fiber is then collimated using a plano-convex lens of focal length 25 mm. The collimated light is then split onto two parts for the horizontal and vertical MOT beams, as shown in the schematic diagram. In this case, the size of each MOT beams has been increased to 15 mm at the atoms capture region.

4.5 Loading and characterization of MOT

The MOT has been used for the studies reported in this thesis. Our MOT is loaded from a thermal beam of atoms generated by an effusive atomic source operated at the temperature of 600°C and slowed down by a zero-field crossing Zeeman slower. The light for the first stage laser cooling ($5s^2\ ^1S_0 \longrightarrow 5s\ 5p\ ^1P_1$, $I_s = 42.7\ \text{mW/cm}^2$) is generated

using a homemade cavity-enhanced optical frequency doubler as mentioned in section-4.1. The cavity is injected with an input laser ($\lambda = 922$ nm, power = 700 mW) light from a commercial tapered amplifier and generates ~ 200 mW of blue light. This light is split into different parts for various applications. The MOT laser beams are prepared following the standard $\sigma^+ - \sigma^-$ configuration with retro-reflection geometry. To generate the circularly polarized laser beams for MOT, the output of the frequency doubler is split into three beams using a polarizing beam splitter cube and half-wave plates ($\lambda/2$). These lights are then sent through the quarter-wave plate ($\lambda/4$) to set the required circular polarization by monitoring the polarization using a polarimeter. The MOT beam diameter was kept at ~ 10 mm ($1/e^2$) during the first phase of the experiments. These beams were free-standing from the beam splitting region to the MOT capture region. However, we found that after each alignment of the optical cavity (once in a week), the position of the main output beam of the cavity changes slightly. To ensure the same beam path as that of before tweaking the alignment of the cavity, a series of irises are placed along the path of the optical beam. This helped in the coarse alignment of the laser beams, which was later found to be insufficient for the reliable MOT operation. A slight change in the beam alignment or a change in the profile of the beams resulted in a change in temperature of the atomic cloud after the MOT cooling stage. To overcome

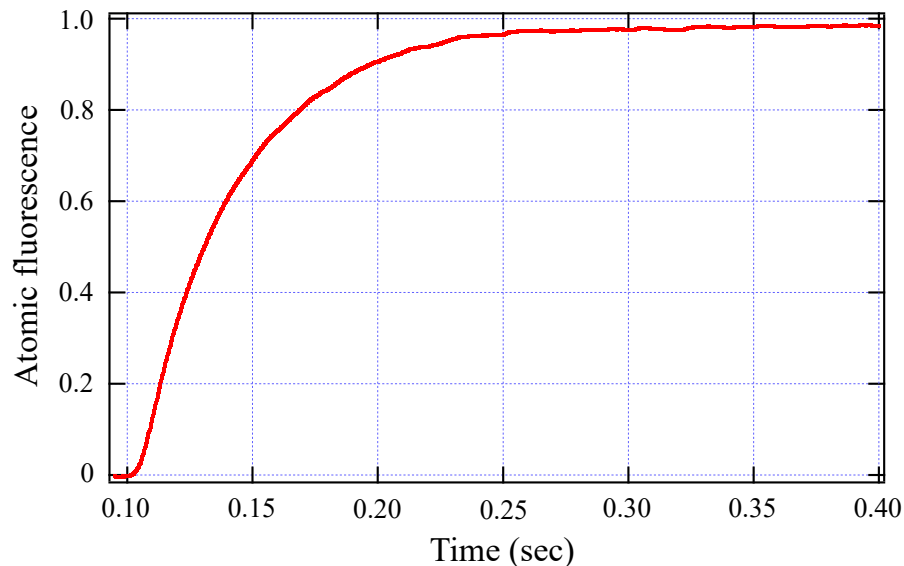


Figure 4.28: MOT loading: Loading curve of Sr atoms in blue MOT. The repumping laser operates at the wavelength of 707.2 nm.

the above-mentioned problem, we later incorporated an optical fiber in the path of the MOT laser beam. The frequency doubler output is split into two parts for the MOT and the Zeeman slower. The MOT beam is then coupled to an optical fiber which is 1 m in length. The light beam coming out of optical fiber is collimated using a plano-convex lens of 25.4 mm diameter and then split into three parts of equal power for the MOT, as shown in Fig. 4.27. The $1/e^2$ diameter of the MOT beams in this configuration is kept at ~ 15 mm. The high scattering rate of the first stage cooling transition of Sr atoms allows the use of laser beams of small diameter (~ 10 mm) for the MOT operation. Each beam in MOT has ~ 10 mW power and the detuning is kept at -33 MHz ($\sim 1\Gamma/2\pi$, where Γ is the natural linewidth of the cooling transition) with respect to $5s^2\ ^1S_0 \rightarrow 5s\ 5p\ ^1P_1$ transition. The repumping laser beam is sent directly to the MOT capture region, as shown in Fig. 4.27.

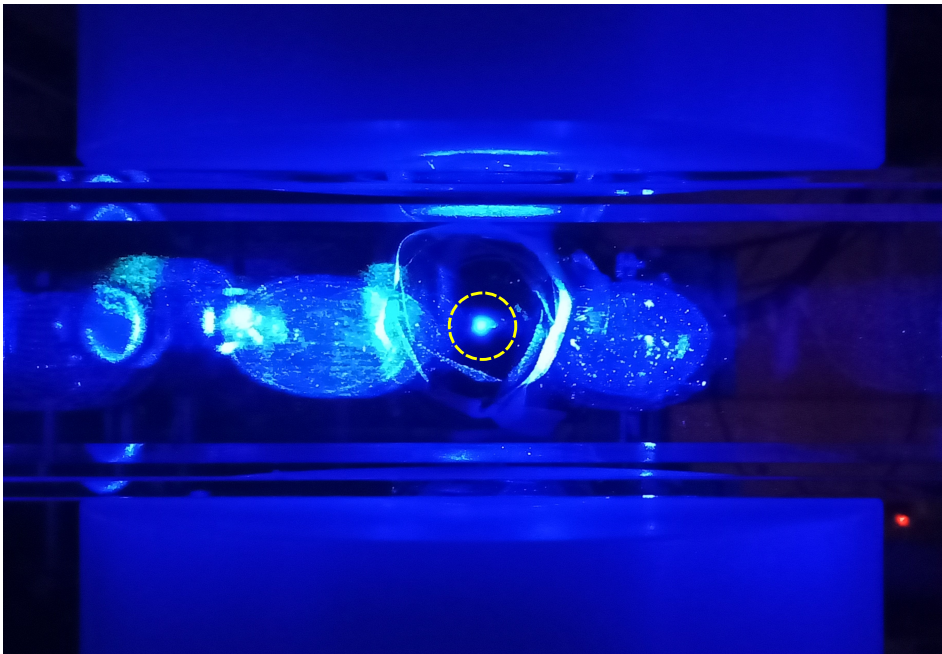


Figure 4.29: Atoms in MOT: Fluorescence of atoms trapped in MOT. The cloud of atoms is shown within the yellow circle

The Zeeman slower beam is also derived from the main output of the optical frequency doubler. The light with the desired detuning and polarization is sent inside the vacuum chamber using a periscope towards the atomic beam oven. In order to cover the divergence of the atomic beam emanating from the oven, the Zeeman slower beam is

focused on the surface of the collimating capillaries. The power in this beam is kept at ~ 30 mW during the experiment.

The field gradient of the quadrupole coils is kept at ~ 48 Gauss/cm along the axial direction. The loading curve of the MOT is obtained by collecting the fluorescence of the trapped atoms onto a Hamamatsu photo-multiplier tube (H9307-02) using a lens subtending a solid angle of 0.2 sr at the center of the trap as mentioned in section - 2.5. The loading curve of atoms in the presence of repumping laser operating at 707.2 nm is shown in Fig. 4.28. We load $\sim 1 \times 10^6$ atoms in MOT in the presence of repumping laser operating at 707.2 nm. This number has been improved by an order of magnitude by a using second repumping scheme utilizing a laser operating at 481.3 nm.

4.5.1 MOT alignment procedure

MOT is a very robust way of trapping the atoms from a thermal beam. It is not very sensitive to the alignment of the laser beams, its polarization, and the power of the trapping beam. It is relatively easy to trap the atoms in a MOT. However, to get the maximum number of atoms in this trap with the minimum allowed temperature, it is necessary to perform the alignment process properly. We followed the following steps for optimizing the MOT alignment:

1. The mutually perpendicular MOT laser beams are aligned to intersect at the center of the quartz cell. The counter-propagating beams are then overlapped with the corresponding incoming light. This is done with the maximum possible beam diameter of the MOT beams.
2. The size of the beam is reduced slightly by using two 50.8 mm irises in the path of horizontal and vertical MOT beams. After the reduction in size, the step-1 is repeated.
3. The diameter of the MOT beams is further reduced, and the above-mentioned steps are repeated. This is done until the beam diameter becomes almost 3 mm.
4. Now, the field gradient is increased to make the cloud smaller. At this point, the individual beams are finely adjusted in pairs to optimize the number of atoms in the trap. This is done by monitoring the fluorescence of the trapped atoms.
5. The alignment quality has been determined by turning off the quadrupole field and monitoring the movement of the atomic cloud. After switching off the field, the atoms

should not experience any push in a particular direction. This can be further ensured by monitoring the cloud's movement by changing the field gradient of the quadrupole field.

4.5.2 Temperature measurement

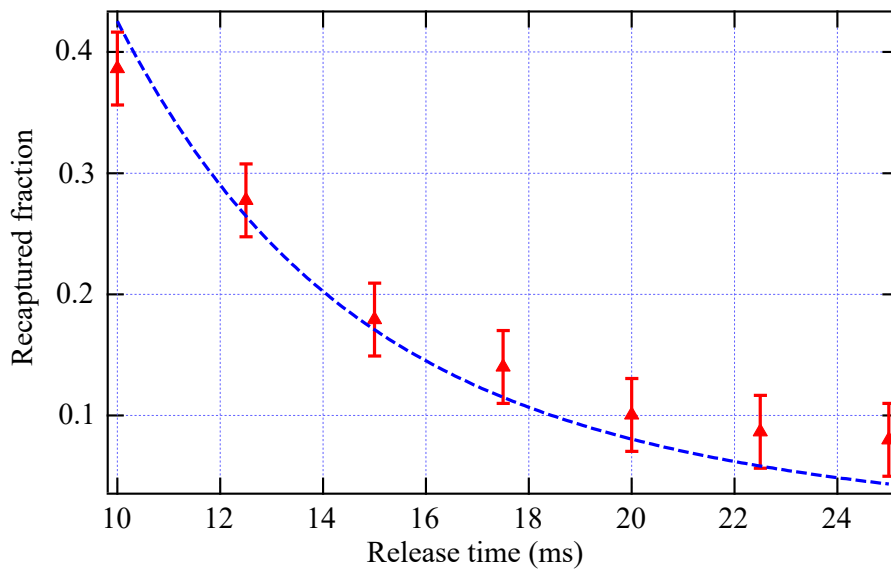


Figure 4.30: MOT temperature measurement: Fraction of recaptured atoms as a function of release time. Error bars of $\pm 5\%$ is added to incorporate the uncertainty in the measurement of recaptured fraction of atoms.

The temperature is one of the most important parameters for characterizing the atomic cloud. This is required for the study of the loss dynamics of atoms from a given trap. In our experiment, we employed the standard release and recapture technique for the determination of the atomic cloud's temperature, as mentioned in section - 2.7. In this technique, the fraction of atoms recaptured in the trap is measured as a function of release time. The recaptured fraction is inversely proportional to the rate of expansion of the atomic cloud and is used to determine temperature. The release time has been varied from 1 ms to 25 ms during the experiment. Fig. 4.30 shows one such measurement. The measured temperature is found to be $\sim 3.6(3)$ mK.

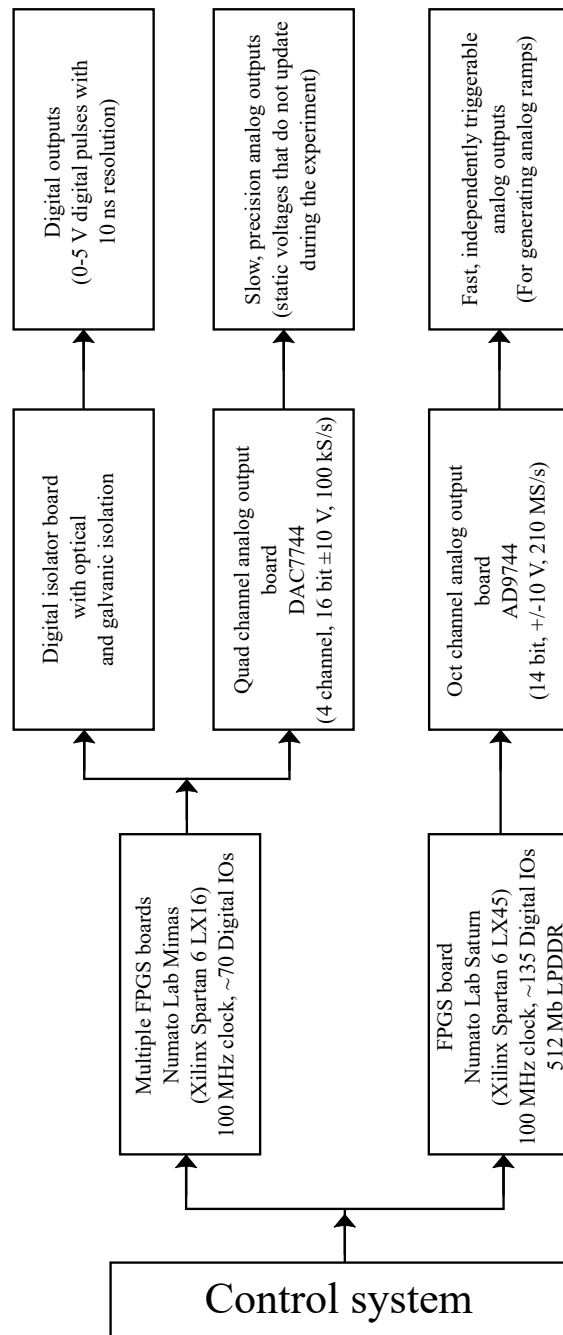


Figure 4.31: Control system: Block diagram of the FPGA based control system.

4.6 Computer control

The entire experimental sequence requires computer control. For example, the AOM drivers require DC voltages for setting the operating frequency and the amplitude of

the RF voltage. Various laser beams need to turn on and off during the entire sequence of the experiment at the timing accuracy of $\sim\mu\text{sec}$. These DC voltages and the TTL pulses are generated using a homemade Field Programmable Gate Array (FPGA) based modules. The systems have been developed by *M. Sainath*, project student IISER Pune.



Figure 4.32: Digital sequencer: Front panel of the digital sequencer used for the generation of TTL pulses for the experiment.

The digital sequencer uses multiple FPGA boards (*Numato Lab Mimas Model No.: Xilinx Spartan 6 LX16*) with the clock speed of 100 MHz and ~ 70 digital IOs. The pulses thus generated are sent through a digital isolator board with optical and galvanic isolation for the experiment's use. This results in the generation of digital pulses with the timing resolution of ~ 10 ns. The block diagram of the complete control system is shown in Fig. 4.29 and the front panel of the digital sequencer is shown in Fig. 4.28

Similarly, the static analog voltages are generated using the above-mentioned FPGA board (*Numato Lab Mimas Model No.: Xilinx Spartan 6 LX16*). The digital output is then converted to the analog voltage using a digital to analog (DAC) converter. On the other hand, the fast independently trigger-able analog voltage is generated using an FPGA board (*Numato Lab Mimas Model No.: Xilinx Spartan 6 LX45*) with again 100 MHz clock and ~ 135 digital IOs. The front panel of analog voltage generators is



Figure 4.33: Analog voltage generator: Front panel of the FPGA based analog voltage generator.

shown in Fig. 4.30. These boards are controlled by LabVIEW (National Instruments) interface.

Chapter 5

Study of loss dynamics of strontium in a magneto-optical trap

This chapter describes the experiments performed with Sr atoms in the magneto-optical trap operating on the 461 nm cooling transition. The first section describes the problem under consideration, followed by the theoretical background required for the description of the system. We later describe the experimental setup and the parameters used for performing the study of loss dynamics of atoms. All these experiments are performed in the presence of controllable background N_2 pressure. The loss rate of Sr atoms from the MOT is studied with different background pressures, and has been used in the determination of collision cross section between Sr and N_2 . We compare the experimentally measured collision cross section with the values reported for the alkali metals.

5.1 Definition of the problem

As described in the section - 1.4, the invention of optical frequency comb [161] has boosted efforts towards using optical transitions as a universal time standard. Among various architectures [162], neutral atom based platforms have become popular in realizing the next generation optical clocks which hold promise to revolutionize global time-keeping, precision sensing, and probing the stability of fundamental constants [162–164]. From an experimental point of view, it is impossible to isolate the atoms from the external perturbations completely. In such a case, the clock accuracy depends on

accurately quantifying various systematic shifts in the clock transition frequency.

Among all the factors, the frequency shifts due to background gas collisions (BGCs) are currently one of the largest sources of uncertainties in many of the best atomic clocks of various types [68, 165–172]. However, it has to be noted that the individual contribution is not very large compared to other factors affecting the clock performance. There have been many theoretical [173–177] and experimental [166, 178] studies performed to estimate the value of this small but highly uncertain factor. In particular, a model is developed by Kurt Gibble [173] relating the shifts to dispersion coefficients (and thus to collisional cross sections), facilitating the estimation of shifts without directly probing the clock transitions.

One of the leading candidates in neutral-atom based clocks is the Sr optical lattice clock, with the current performance of $2.0\text{--}2.1 \times 10^{-18}$ uncertainty in the two most-accurate clocks [68, 165] around the world. In these, BGC-induced shifts are the third largest uncertainty, contributing $4\text{--}6 \times 10^{-19}$ to the uncertainty budget. Recent work [178] had enabled a reduction in this contribution in the former clock [165] by a measurement of the frequency shift due to collisions with H_2 , with ongoing studies to investigate the effect of other species present in the background gas. A theoretical estimate for the shift due to Sr– H_2 collisions was also recently made [174].

While previous studies on BGC-induced shifts have mainly focused on H_2 since it is typically the dominant species present in the vacuum chamber, it is anticipated that as the clock uncertainties continue to improve, it may become necessary to account for the contribution of other background gas species. Dispersion coefficients have been estimated for collisions of N_2 with alkali, noble, and various molecular gases and collisional cross sections have been reported for Rb– N_2 [30, 179], $\text{Ne}^*\text{--N}_2$ [27, 180], Na– N_2 [181] and Ar– N_2 [182], but so far Sr– N_2 collisional properties have not been investigated.

The traditional way to determine the collision cross section is to employ crossed beam technique [183, 184] where two collimated atomic/molecular beams are generated and made to intersect in a well-defined interaction region. Uncertainties in the number of target atoms and the intersection region volume are the two major sources of errors in the measurement. Since the invention of the laser cooling technique, an alternative

way is developed to measure the collision cross section of the atomic species under consideration. This is done by monitoring the atomic loss rate from the MOT, magnetic trap (MT), or the Optical Dipole Trap (ODT). Collision cross sections determined in this manner have been shown to be more accurate than the beam-based method [27]. There have been extensive experimental studies performed in the same spirit using Rubidium [28–30], Ytterbium [31], Cesium [32], Neon [27, 33] etc.

In this chapter, we study the dynamics of a Sr MOT, by observing the loading and the loss rate under various experimental conditions and for two different repumping schemes. The loss rate measurement is used for the first experimental determination of $^{88}\text{Sr}-\text{N}_2$ collision cross section of the 1S_0 ground state by measuring the loss rate of atoms from ^{88}Sr MOT operating with the first stage cooling transition. The collision cross section is determined by injecting nitrogen (N_2) inside the vacuum chamber in a controlled manner and studying the atomic loss rate at different background pressures. These measurements are helpful in the evaluation of a systematic shift in the fractional frequency uncertainty in the clock operation. For Sr atoms, the presence of intermediate metastable states to which the atoms in the excited state (1P_1) of the cooling transition can decay into, complicates the loss rate dynamics. To study this, we identified the various loss mechanisms in the MOT and evaluated their contributions. In our experiment, the total atomic loss rate depends on various factors, as mentioned in section - 2.8. These are:

- (i) The collision with untrapped background atoms/molecules
- (ii) The decay of atoms into the triplet state 3P_0
- (iii) The temperature of the atomic cloud.

We present a model to accommodate for the above loss channels. In order to check the consistency of the model for loss rate determination, we have performed the entire experiment in the presence of two different repumping schemes utilizing (a) 707.2 nm laser connecting $5s\ 5p\ ^3P_2 \rightarrow 5s\ 6s\ ^3S_1$ and (b) with 481.3 nm laser addressing $5s\ 5p\ ^3P_2 \rightarrow 5p^2\ ^3P'_2$ transition. For even isotopes, the transition from 3P_0 to the ground state 1S_0 is forbidden under spin selection rule and contributes to the total atomic loss rate. Due to the existence of multiple decay channels from the excited state, the atoms spend a significant amount of time in the states unresponsive to the first

stage cooling laser. These atoms contribute to the total loss rate if the collective lifetime of these states is larger than the time required for the atoms to escape the capture region. This loss channel is proportional to the temperature of the atomic cloud and is the dominant channel for the atomic species under consideration. It is essential to consider this loss channel for the atomic species which have a level structure similar to Sr. The contribution of this term, along with losses induced by decay into the triplet state, is determined by studying the loss rate as a function of the MOT beam intensity.

5.2 Theoretical background

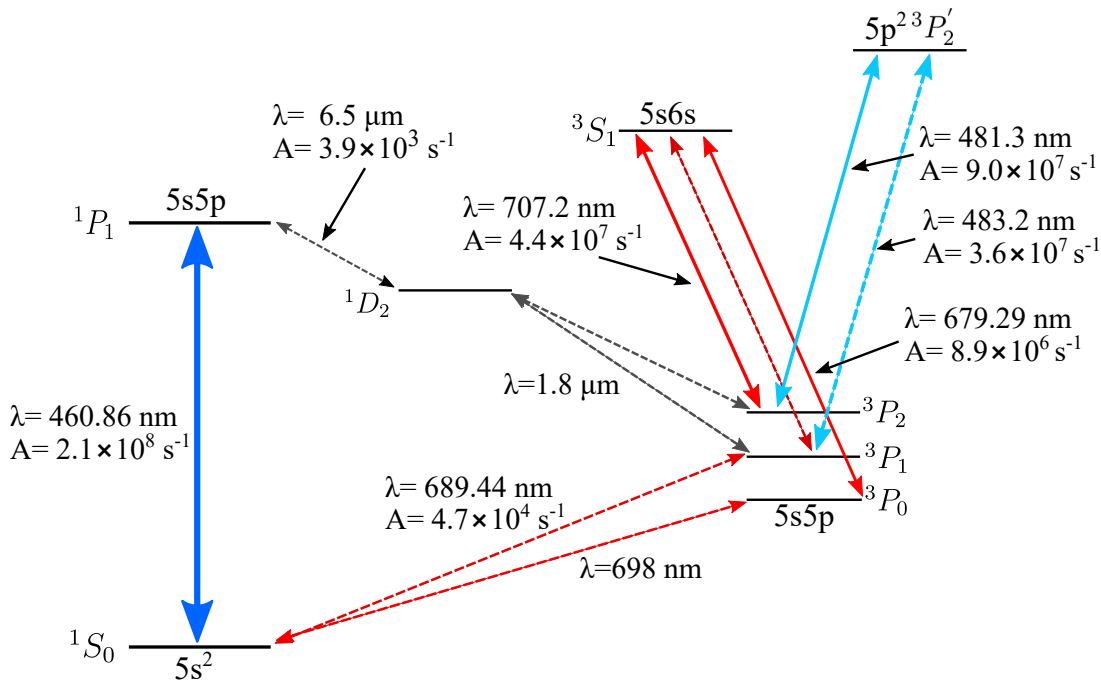


Figure 5.1: Strontium energy level diagram: The relevant low-lying energy level diagram of strontium (^{88}Sr) atoms. The wavelength (λ) and the decay rate (A) has been shown along with the transition.

The experiment is performed with the most abundant even isotope of strontium (^{88}Sr). Fig. 5.1, shows the low-lying energy level diagram of ^{88}Sr atom. For the sake of continuity, we will briefly go through the energy level diagram relevant to the studies mentioned in this chapter. Strontium has two cooling transitions $5s^2 \ ^1S_0 \rightarrow 5s \ 5p \ ^1P_1$ and $5s^2 \ ^1S_0 \rightarrow 5s \ 5p \ ^3P_1$ of wavelengths 460.8 nm and 689.4 nm respectively. The singlet to triplet transition ($^1S_0 \rightarrow ^3P_1$) has a long lifetime of 21 μs and linewidth of

$2\pi \times 7.5$ kHz. This transition has been used by others for the second stage cooling and has extremely low Doppler limited temperature of ~ 180 nK. The other cooling transition connects $^1S_0 \rightarrow ^1P_1$. This transition has a short lifetime of ~ 5 ns ($\Gamma = 2\pi \times 32$ MHz) and is well suited for the first stage of cooling and trapping. All the studies mentioned in this chapter have been performed utilizing this broad transition. The larger linewidth results in a higher Doppler limited temperature of ~ 770 μ K; further, the transition itself is not completely closed. The atoms in the excited state 1P_1 decays to 1D_2 state with a branching ratio of $1 : 2 \times 10^{-5}$. Atoms in 1D_2 further decay to 3P_2 and 3P_1 states with a branching ratio of $1 : 2$, respectively. The transition $^3P_2 \rightarrow ^1S_0$ state is doubly forbidden; thus, the atoms once decayed to 3P_2 are lost from the cooling cycle. There are several repumping schemes to revive this loss [113, 150–153]. The most popular of them employ two lasers operating at 707.2 nm and 679.3 nm. The decay rates and wavelengths of the transitions relevant for the present study are shown in Fig. 5.1.

The rate equation

The studies reported in this chapter are based on the change in the decay rate of atoms from the MOT as a function of background gas density and the trapping beam intensity. At room temperature, the untrapped background particles have sufficient kinetic energy to knock the atoms out of the trap. A pictorial representation of the collision events has been shown in Fig. 5.2. These collisions limit the atomic lifetime in the trap and are directly proportional to the background pressure inside the vacuum chamber. The loading of atoms in the MOT is a dynamic process, and a steady-state population is achieved on attaining equilibrium between the loading and the loss rate. The rate equation can be written as:

$$\frac{dN}{dt} = R - \frac{N}{\tau} - \beta N^2 \quad (5.1)$$

In the above expression, N is the number of atoms at a given instant of time ' t ,' R is the loading rate, $1/\tau$ is the linear loss rate of atoms, and β represents the non-linear loss rate due to intra-trap collisions. At lower atomic density, the non-linear loss can be ignored. The experiments reported in this chapter have been performed in the linear regime, and thus the term which is quadratic in N is neglected [126] for further analysis. In the low-density regime, the solution to Eq. 5.1 displays an exponential growth in the

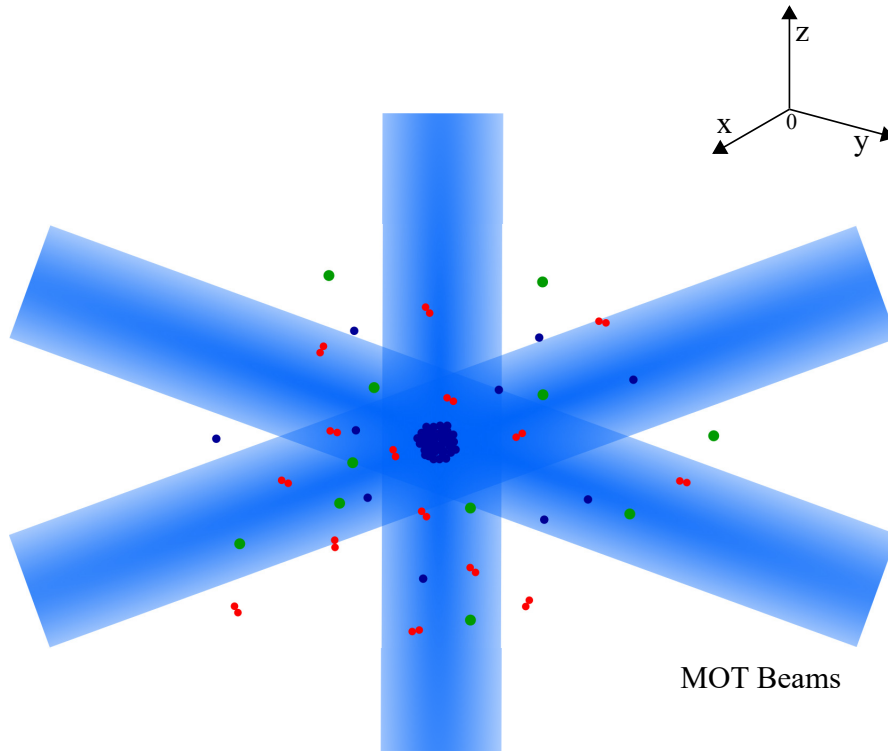


Figure 5.2: Representation of collisional process: Strontium atoms with velocities less than the capture velocity are trapped inside the MOT. Various gas species such as nitrogen (red circle), untrapped Sr (blue), and other species (green) remain in the background of the chamber. The collision between them and the trapped atoms limits the lifetime of the MOT.

number of atoms in MOT and can be written as:

$$N = N_s [1 - \exp(-t/\tau)] \tag{5.2}$$

where,

$$N_s = R\tau \tag{5.3}$$

As mentioned in section - 5.1, the linear loss rate in Eq. 5.1 can be attributed to several factors, namely:

- (i) collision with the background N_2
- (ii) collision with background species other than N_2
- (iii) the decay of atoms into the metastable states
- (iv) escape of atoms out of the capture region

By combining the factors mentioned above, the total linear loss rate can be written as:

$$\frac{1}{\tau} = n_{N_2} \sigma_{N_2} v_{N_2} + \Gamma_b + \alpha_0 f + \epsilon \gamma_t \frac{A_{^1P_1 \rightarrow ^1D_2} f}{A_{^1D_2 \rightarrow ^3P_2} + A_{^1D_2 \rightarrow ^3P_1}} \quad (5.4)$$

Note that the above equation is merely the expansion of Eq. 2.39 with the specific details of the current experimental situation. In the above equation, n is the density of the background particle, σ is the collision cross section, and v is the average velocity of the particle under consideration. The subscript N_2 denotes the background species used for the current experiment. Now, we will go through each of the linear factors contributing towards their loss of atoms from MOT.

The first term ($n_{N_2} \sigma_{N_2} v_{N_2}$):

The first term in Eq. 5.4 denotes the loss induced by the background N_2 . In the current experiment, we have control over the background N_2 pressure inside the vacuum chamber.

The second term (Γ_b):

The second term, Γ_b in Eq. 5.4, accounts for the loss induced by the background species other than N_2 . During the experiment, we do not have full control over the amount or the type of background species. It is usually hydrogen, helium, and an isotopic mixture of untrapped Sr, etc. The collective contribution towards the decay rate due to all these species has been denoted by Γ_b .

The third term ($\alpha_0 f$):

The term $\alpha_0 f$ in the above equation represents the loss of atoms due to branching into the metastable state. In our experiment (considering the cooling laser at 460.8 nm and repumping lasers at 707.2 nm and 481.3 nm for two different schemes), such a loss corresponds to the effective decay of atoms into the long-lived state 3P_0 and is denoted by $\alpha_0 f$. This loss channel can be explained in the following way. The atoms in excited state 1P_1 decay to the intermediate state 1D_2 with the rate $A_{^1P_1 \rightarrow ^1D_2}$. These 1D_2 atoms can further decay to 3P_2 state with the branching ratio $B_{^1D_2 \rightarrow ^3P_2}$. A fraction of atoms is excited into the $5s\ 6s\ ^3S_1$ ($5p^2\ ^3P'_2$) state by using the repumping laser at $\lambda = 707.2$

nm ($\lambda = 481.3$ nm). These atoms can make a transition from 3S_1 ($^3P'_2$) to 3P_0 state with the branching ratio $B_{^3S_1(^3P'_2) \rightarrow ^3P_0}$. For the isotope under consideration, the transition from the triplet state 3P_0 to the ground state 1S_0 is forbidden under the spin selection rule. Consequently, the process of populating the 3P_0 state is a loss channel. As the fraction of atoms in the excited state 1P_1 depends on the power of MOT beams, this loss rate is denoted by $1/\tau_{power}$. Thus, the third term of Eq. 5.4 can be expanded as [185]:

$$\frac{1}{\tau_{power}} = \alpha_0 f = (f A_{^1P_1 \rightarrow ^1D_2}) \times (B_{^1D_2 \rightarrow ^3P_2}) \times (f' B_{^3S_1(^3P'_2) \rightarrow ^3P_0}) \quad (5.5)$$

Here, f and f' are the fraction of atoms in the excited state 1P_1 and 3S_1 ($^3P'_2$) respectively. The general expression for these fractions is be given as:

$$f = \frac{1}{2} \frac{I/I_0}{1 + I/I_0 + (2\Delta/\Gamma)^2} \quad (5.6)$$

where, I is the total intensity, I_0 is the saturation intensity of the transition, Δ is detuning of the laser beam, and Γ is natural linewidth of the transition under consideration.

The fourth term $\left(\epsilon \gamma_t \frac{A_{^1P_1 \rightarrow ^1D_2} f}{A_{^1D_2 \rightarrow ^3P_2} + A_{^1D_2 \rightarrow ^3P_1}} \right)$:

The last term in Eq. 5.4 represents the atomic loss due to escape from the capture region and will be denoted by $1/\tau_{temp}$ for further analysis in this chapter. The detailed methodology for the calculation of this loss channel is taken from Ref. [186]. The term $A_{^1D_2 \rightarrow ^3P_2(^3P_1)}$ denotes the decay rate from the intermediate state 1D_2 to the triplet state 3P_2 (3P_1). This loss channel can be understood as follows. A fraction of atoms from the excited state 1P_1 decay to the intermediate state 1D_2 , which further connects to two triplet states 3P_2 and 3P_1 as shown in Fig. 5.1. The atoms in 3P_1 state decay to the ground state in $21 \mu\text{s}$. On the other hand, the atoms that have decayed to 3P_2 state can be brought back to the main cooling transition by using repumping lasers. Considering all the cascade channels, it takes ~ 1 ms ($\equiv \gamma_t^{-1}$) for the atoms in 1D_2 to return to the ground state via 3P_2 and 3P_1 state. During this process, the atoms are not responsive to the main cooling laser operating at 460.8 nm and therefore have a finite non-zero probability of escaping from the capture region of MOT. This probability (ϵ)

is determined by the diameter of the MOT beams and the average temperature of the atomic ensemble [186]:

$$\epsilon \sim \int_0^\infty \left(\frac{1}{2\pi v_0^2} \right)^{\frac{3}{2}} 4\pi v^2 \exp\left(\frac{-v^2}{2v_0^2}\right) \exp\left(\frac{-R\gamma t}{v}\right) dv \quad (5.7)$$

Here, v_0 and R denote the root mean square velocity of the atoms and the radius of the trapping beam, respectively.

After the identification of various loss mechanisms, the individual contributions have been evaluated by operating the MOT at different experimental conditions. The measurement of the total loss rate as a function of power in the trapping beams and the density of the background N_2 gas provides relevant information regarding the collision cross section and losses due to branching into the long-lived state 3P_0 .

5.3 Experimental Details

The experiments are performed using the blue MOT of ^{88}Sr atoms. The detailed description of the experimental setup is given in section - 4.5. The magnetic field for the MOT is generated using a pair of anti-Helmholtz coils with an axial field gradient of ~ 48 Gauss/cm. During the loading process, detuning of the MOT beams is kept at -33 MHz. The entire experiments have been conducted in two different configurations. In the first set, each of the MOT beams has $1/e^2$ diameter of 10 mm and maximum intensity of ~ 16 mW/cm². The decay of atoms into the metastable state 3P_2 is suppressed using a repumping laser of wavelength 707.2 nm operating on the $5s\ 5p\ ^3P_2 \rightarrow 5s\ 6s\ ^3S_1$ transition. This transition has a saturation intensity $I_s = 3.4$ mW/cm². For the second set of experiments, the $1/e^2$ diameter of the MOT beams has been increased to 15 mm. The maximum intensity of each beam in this configuration is ~ 8 mW/cm². For this set, we used the second repumping scheme with wavelength 481.3 nm ($I_s = 0.028$ mW/cm²) [153]. This laser connects the transition $5s\ 5p\ ^3P_2 \rightarrow 5p^2\ ^3P'_2$ as shown in Fig. 5.1. The frequency of both the repumping lasers is locked using a digital PID controller, which receives feedback of the laser frequency via a commercial wave-meter (*High Finesse*, model: WSU-30) [157]. The number of trapped atoms in MOT is estimated by collecting the fluorescence of the

atoms on a calibrated photomultiplier tube (*Hamamatsu*, model H9307-02).

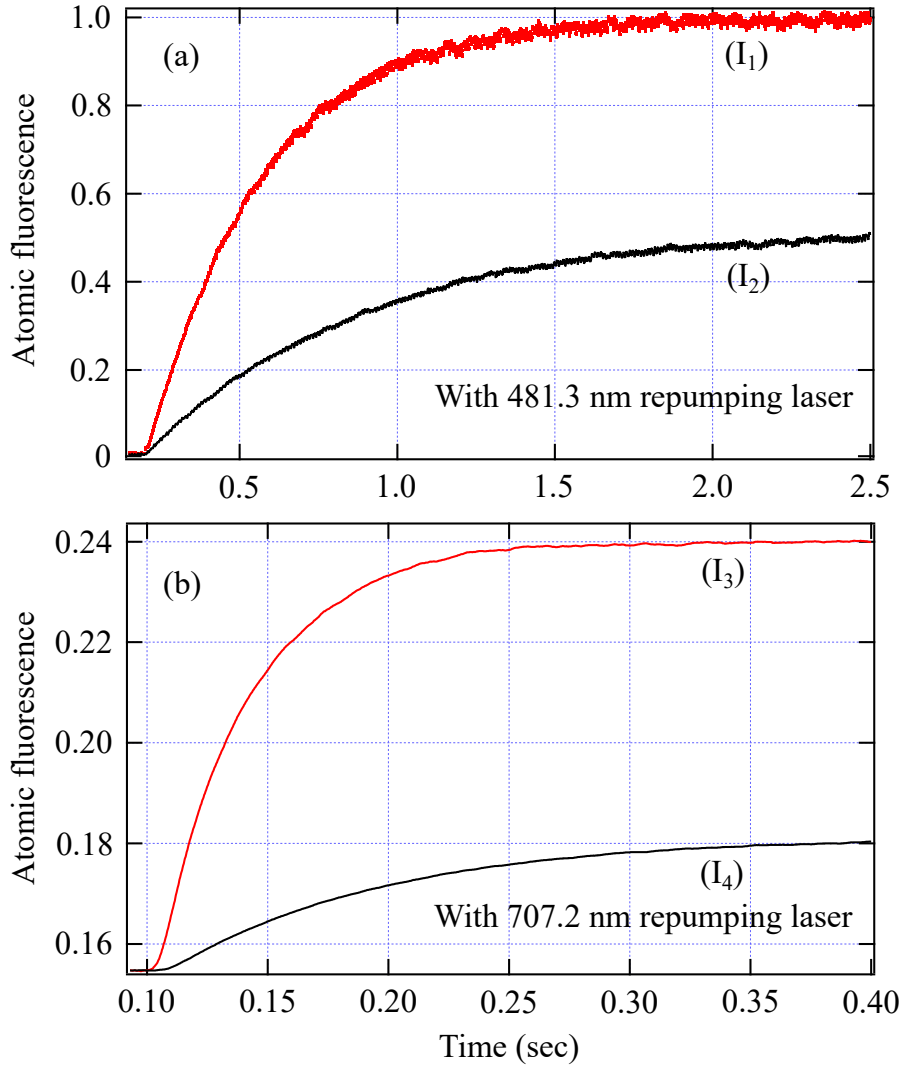


Figure 5.3: MOT loading in presence of two repumping schemes: Normalized fluorescence of ^{88}Sr MOT in the presence of repumping laser operating at (a) 481.3 nm and (b) 707.2 nm for different trapping intensities, $I_1 = 46.4 \text{ mW/cm}^2$, $I_2 = 26.4 \text{ mW/cm}^2$, $I_3 = 96.8 \text{ mW/cm}^2$ and $I_4 = 31 \text{ mW/cm}^2$. All other parameters are kept constant. Note that the loading rates of the MOT for the two repumping schemes is significantly different.

The determination of the collision cross section is based on the change in the MOT loading rate on the introduction of gas species inside the vacuum chamber. The design and construction of the vacuum system for the current experiment have been described in chapter - 3 of this thesis. Nevertheless, for the sake of continuity, it has been mentioned again. The vacuum system consists of two sections; the oven region and the

quartz cell connected to the Zeeman slower tube. These two regions are separated by a differential pumping tube. The pressure in these sections is maintained by two independent ion pumps (capacity $\sim 55 \text{ l s}^{-1}$). Also, a Titanium Sublimation Pump (TSP) is connected to the science chamber (near the quartz cell) for maintaining the desired low pressure. The base pressure inside the quartz cell is less than 1×10^{-10} torr. In the current experiment, the MOT loading curves at different background pressures are used to determine the collision cross section between the species of our interest. A leak valve (*Granville-Phillips*, 203 Series) is connected to the quartz cell via an all-metal right angle valve for releasing the background species in a controlled manner. The other end of the leak valve is connected to a gas cylinder containing high purity (99.999%) N_2 gas, which is used as the background species in our experiment. Since the vacuum pumps connected to the system continuously pump out the background gas, specific leak rates of N_2 gas is used to achieve desired values of equilibrium pressure of N_2 in the chamber. This equilibrium pressure is determined by the ion pump current (*Agilent*, Model: VacIon Plus 55 Starcell).

In order to study the dependence of the loss rate on the power of the trapping laser beams, the MOT is operated at different powers while keeping all other experimental parameters unchanged. The loss of atoms due to escape from the capture region is characterized by measuring the temperature of the atomic cloud. We use the release and recapture technique [125] to determine the temperature of the atomic cloud. The release time has been varied from 1 ms to 25 ms for the determination of MOT temperature.

5.4 Results and Discussion

To measure the $^{88}\text{Sr}-\text{N}_2$ collision cross section and study the various loss channels, we have used the formulation represented in Eq. 5.4. The validity of Eq. 5.4 demands the MOT to be operated in the low-density regime, which is manifested by the exponential growth of the number of atoms in the MOT [31, 126, 187]. Fig. 5.3 displays four MOT loading curves utilizing the two repumping schemes, as mentioned in the earlier section. These loading curves are recorded in the presence of two repumping lasers operating at (a) 481.3 and (b) 707.2 nm at the respective extreme powers ($I_1 = 46.4 \text{ mW/cm}^2$, $I_2 = 26.4 \text{ mW/cm}^2$, $I_3 = 96.8 \text{ mW/cm}^2$ and $I_4 = 31 \text{ mW/cm}^2$) of the trapping laser beams.

5.4.1 Determination of collision cross section

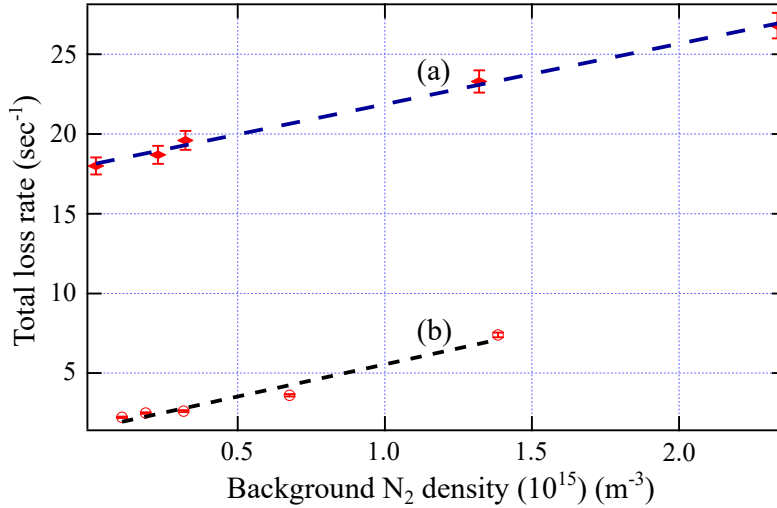


Figure 5.4: Loss rate measurement: Loss rate of atoms in Sr MOT as a function of background N₂ density. The two curves show the loss rate observed in the presence of two repumping schemes. (a) in the presence of repumper laser operating at the wavelength 707.2 nm and (b) with a repumping laser at 481.3 nm.

To determine the ⁸⁸Sr–N₂ collision cross section, the loading curves are recorded at different background pressures. Fig. 5.4 represents the total loss rate of atoms as a function of the density of N₂ gas. Considering the loss rate for two different background pressures and using Eq. 5.4:

$$\frac{1}{\tau_h} - \frac{1}{\tau_l} = (n_{N_2}^h - n_{N_2}^l) \sigma_{N_2} v_{N_2} \quad (5.8)$$

Here, the superscripts *h* and *l* denote the two different background pressures. On increasing the pressure of N₂, the total loss rate exhibits a linear increase with a slope of $\sigma_{N_2} v_{N_2}$ (as predicted by Eq. 5.8) and is shown in Fig. 5.4. The knowledge of the values of the background densities ($n_{N_2}^h$ and $n_{N_2}^l$) and the average velocity (v_{N_2}) of N₂ molecules at room temperature enables us to calculate the value of ⁸⁸Sr–N₂ collision cross section. For the laser-cooled sample of atoms, the average velocity of trapped atoms is negligible with respect to the hot background species, thus for the purpose of calculation, we use the absolute average velocity of background N₂ instead of the relative velocity. Since N₂ gas is in thermal equilibrium with the vacuum system, we

have used $v_{N_2} = 470 \text{ ms}^{-1}$ as calculated at room temperature (20°C). We found the average value of $^{88}\text{Sr}-\text{N}_2$ collision cross section to be $\sigma_{N_2} = 8.1(4) \times 10^{-18} \text{ m}^2$. This result is comparable to similar experiments performed with Rb and Na using the same background species (N_2) Ref. [30].

5.4.2 Determination of C_6 of the ground state

The obtained value of collision cross section for the ground state 1S_0 can be used to estimate the frequency shift in Sr clock transition due to background N_2 collisions by using the formulation given by Gibble [173]. These collisions, apart from limiting the trap lifetime, it affects the coherent superposition between the ground 1S_0 and the metastable excited state 3P_0 of the clock transition [173]. This is manifested as a shift in the clock transition frequency. The interaction potential between a trapped Sr atom in the ground state and a colliding N_2 molecule can be represented by the Lennard-Jones potential of the form:

$$V(r) = \frac{C_{12}}{r^{12}} - \frac{C_6}{r^6} \quad (5.9)$$

The fractional shift in clock transition frequency, introduced by the collisions with background gases is related to C_6 by:

$$\frac{\Delta C_6}{C_6} \propto \frac{\Delta\nu}{\nu} \quad (5.10)$$

where ΔC_6 is the difference between the C_6 values for the ground and the excited state of the clock transition [173] and $\Delta\nu/\nu$ is the fractional frequency shift in the clock transition.

The C_6 for atoms in 1S_0 state, undergoing collisions with the background N_2 , can be calculated using the experimentally determined collision cross section. For the long-range potential of the form $V(r) = -C_n/r^n$, where $n > 2$, the cross section is related to the coefficients in the expansion of the potential as follows [188]:

$$\sigma(v) \approx A(n) \left(\frac{C_n}{\hbar v} \right)^{2/(n-1)} \quad (5.11)$$

Here, $A(n)$ is a constant and v is the relative velocity of colliding particles. Using

the experimentally measured value of σ_{N_2} , the calculated value of C_6 is found to be $535(68) E_H a_B^6$ (at $v_{N_2} = 470 \text{ ms}^{-1}$, $A(6) = 8$ [27]). This formula assumes that there is no trapping force present for the atoms undergoing collisions and hence provide a lower bound for the C_6 .

For the loss rate measurements performed with cold atoms, there is always a trapping potential present. For such measurements using atoms in the MOT, the trap depth is high enough for an atom to stay trapped in spite of undergoing a collision. In such scenarios, it is appropriate to use the formula incorporating the trap depth [28] for deriving C_6 from the loss rate. However, the C_6 calculated by using this formula gives a value, which is an order of magnitude away from the expected value. A similar discrepancy is also observed in the C_6 's calculated from the other loss rates measured in MOT [27, 30, 181]. The reasons for this inconsistency are not yet known.

The C_6 for Sr–N₂ collisions can also be estimated using the Slater-Kirkwood formula [28]:

$$C_6 = \frac{3}{2} \frac{\hbar e}{(4\pi\epsilon_0)^2 m_e^{1/2}} \frac{\alpha_{Sr} \alpha_{N_2}}{(\alpha_{Sr}/\rho_{Sr})^{1/2} + (\alpha_{N_2}/\rho_{N_2})^{1/2}} \quad (5.12)$$

Here, m_e is the electron mass, α , and ρ is the static electric polarizability and the number of valence electrons, respectively, of the colliding species. The estimated C_6 value from this formula is found to be $310 E_H a_B^6$. The values of static polarizabilities for the calculation are taken from Refs. [189, 190]. The experimentally obtained C_6 value for the ground state can be used along with the C_6 for the excited state of the clock transition to determine the contribution of Sr–N₂ collisions to the clock shift and its error budget. A comparison of C_6 and collision cross section for rubidium (Rb) and strontium (Sr) is given in table - 5.1

Species	C_6 (a.u)	Loss rate ($\text{torr}^{-1}\text{s}^{-1}$)	Collision cross section (m^2)	Ref.
Rb	302	2.6×10^7	–	[28]
Rb	–	–	$3.5(4) \times 10^{-18}$	[30]
Sr	535	–	$8.1(4) \times 10^{-18}$	*

Table 5.1: Comparison with literature values: Comparison of literature values for collision cross sections and C_6 of N₂ with Rb and Sr. * indicates the values obtained for this work.

5.4.3 Determination of power and temperature-dependent loss rates

In this section, we proceed with the estimation of τ_{power}^{-1} and τ_{temp}^{-1} in Eq. 5.4. The presence of repumping laser at 707.2 nm, brings the atoms from 3P_2 state back to the triplet states 3P_1 via excited state 3S_1 . The branching ratios for 3P_2 , 3P_1 , and 3P_0 are 5/9, 3/9, and 1/9, respectively [60]. In the absence of 679.3 nm repumping light, the atoms eventually decay into the state 3P_0 and go out of the cooling cycle. For the second repumping laser operating at 481.3 nm, the branching ratio from the excited state $5p^2\ ^3P'_2$ to the triplet states 3P_2 and 3P_1 are 0.714 and 0.286 respectively. The transition $5p^2\ ^3P'_2 \rightarrow ^3P_0$ is electric-dipole forbidden.

On the other hand, temperature-dependent loss (τ_{temp}^{-1}) denoted by the fourth term in Eq. 5.4, occurs due to the transfer of atoms into states which are insensitive to the laser used for the first stage cooling transition. Since the atoms in these states do not experience any radiative force, they are free to go out of the MOT capture region. The decay probability into such states is proportional to the fraction of atoms in the excited state 1P_1 .

Since both the terms mentioned above are a function of the fraction of atoms in the excited state, the separation of these effects is beyond the scope of this experimental technique. Therefore we can only observe their cumulative effect.

We operated the MOT at different intensities of trapping beams to determine the combined contribution of power and temperature-dependent losses. For analysis, we have assumed that σ_{N_2} and Γ_b are independent of the power of laser beams ($\lambda = 460.8$ nm) [27]. Considering the probability of atoms to escape the capture region of MOT (ϵ) independent of the trapping beam power, the following relationship can be written using Eq. 5.4:

$$\frac{1}{\tau_1} - \frac{1}{\tau_2} = (f_1 - f_2) \alpha \quad (5.13)$$

Here, the subscripts 1, 2 denotes two different MOT beam powers, and α is the proportionality constant for the combined losses of atoms due to decay into 3P_0 and due to escape from the trapping region. Thus, α can be written as:

$$\alpha = \alpha_0 + \epsilon \gamma_t \frac{A_{^1P_1 \rightarrow ^1D_2}}{A_{^1D_2 \rightarrow ^3P_2} + A_{^1D_2 \rightarrow ^3P_1}} \quad (5.14)$$

In the above equation, the second term is τ_{temp}^{-1} . While writing Eq. 5.14, we have assumed that the escape probability (ϵ) is independent of the trapping beam intensity. To check the validity of the above equation, we measured the temperature of the atomic cloud with different intensities of the MOT beams. The variation in measured temperature with different MOT intensities was found to be ~ 0.3 mK, which is within the error of our experimental data. This allows us to use Eq. 5.13 for the calculation of power and temperature-dependent loss rate. The value of α is extracted by fitting:

$$1/\tau = \alpha f + c \tag{5.15}$$

to the plot of the total loss rate as a function of intensities of the MOT beams, as shown in Fig. 5.5. Employing the two different repumping schemes pumps a different fraction of atoms into 3P_0 state. The fitting to two different curves gives the value of $\alpha_{707} = 167(4) \text{ s}^{-1}$ and $\alpha_{481} = 18(1) \text{ s}^{-1}$. In the above equation, ‘ c ’ is the intercept on the vertical axis and signifies the loss rate limited solely by the pressure inside the vacuum chamber. The intercept of these curves in both the cases is $1.2(4) \text{ s}^{-1}$ showing the background limited lifetime is independent of the repumping schemes. To get the individual contributions

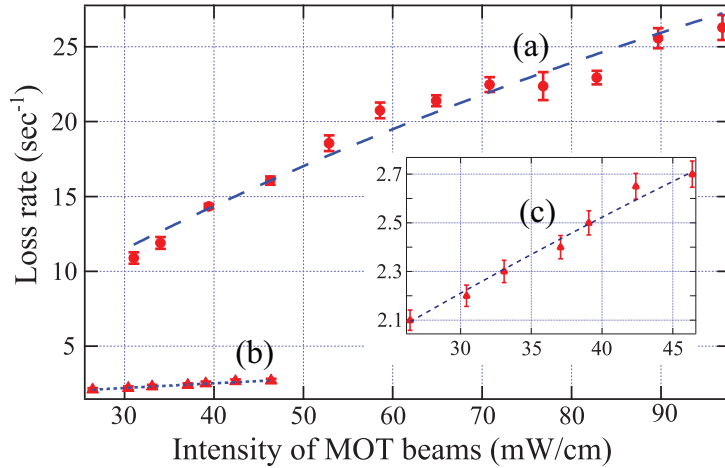


Figure 5.5: Loss rate of atoms in Sr MOT as a function of trapping beam intensity: The data is taken for two different configurations of repumping laser, (a) in the presence of repumping laser operating at 707.2 nm, (b) with repumper operating at 481.3 nm. The detuning and axial field gradient for the MOT is kept at -33 MHz and 48 gauss/cm respectively. Inset (c) is the expanded view of (b).

of both the terms in Eq. 5.14, we theoretically calculate the value of τ_{power}^{-1} using Eq.

5.5. Decay rates for the various energy levels used for the calculations have been taken from Fig. 5.1. The calculation yields a value of $\alpha_0 \sim 33 \text{ s}^{-1}$ for 707.2 nm laser and $\alpha_0 \sim 6.8 \text{ s}^{-1}$ for 481.3 nm. The contribution due to temperature-dependent loss channel τ_{temp}^{-1}/f , is obtained by subtracting the value of α_0 from α and is found to be $134(4) \text{ s}^{-1}$ and $11.2(1) \text{ s}^{-1}$ for the repumping schemes using 707.2 nm and 481.3 nm respectively.

Experimental determination of the thermal loss channel requires the knowledge of escape probability of the atoms from the capture region, which is proportional to the temperature of the atomic cloud. Temperature is measured using the standard release and recapture technique, as mentioned in section - 2.7. In this technique, the fraction of atoms recaptured in the trap is measured as a function of release time. This recaptured fraction is inversely proportional to the rate of expansion of the atomic cloud and is used for the determination of temperature.

In the first set of experiments with the MOT beam diameter 10 mm and with a repumping laser operating at the wavelength of 707.2 nm, we get an average temperature of $3.6(3) \text{ mK}$. Eq. 5.7 is used for the calculation of ϵ , and the value is found to be ~ 0.06 . This value is used to calculate τ_{temp}^{-1}/f , and the resulting loss rate is found to be $120(15) \text{ s}^{-1}$. Incorporating the temperature-dependent losses with the calculated power-dependent losses (α_0), we get $\alpha = 153(15) \text{ s}^{-1}$, which agrees with the experimental measurement ($\alpha = 167(4) \text{ s}^{-1}$) within error.

For the second set of experiments, we employed a repumping laser with wavelength 481.3 nm, and the diameter of the MOT beams was kept at 15 mm, as mentioned in the earlier section. In this configuration, the temperature is measured to be $3.0(1) \text{ mK}$. For this temperature of the atomic cloud, the calculated value of ϵ and τ_{temp}^{-1}/f is found to be 0.0047 and $9.3(8) \text{ s}^{-1}$, respectively. On combining the value of τ_{temp}^{-1}/f and α_0 , we obtain $\alpha = 16.1 \text{ s}^{-1}$, which is comparable to experimentally obtained value.

λ (nm)	α (s^{-1})	α_0 (s^{-1})	$\sigma_{^{88}\text{Sr}-\text{N}_2}$ (m^2)
707.2	167(4)	33	$8.1(4) \times 10^{-18}$
481.3	18(1)	6.8	$8.5(8) \times 10^{-18}$

Table 5.2: Summary of power dependent loss rate: Comparison of experimentally obtained values of α , α_0 and collision cross section between ^{88}Sr and N_2 in the presence of two different repumping schemes employing the lasers operating at 707.2 nm and 481.3 nm

After knowing the loss rate contribution due to background N_2 , the power dependent term ($1/\tau_{power}$) and the temperature dependent loss channel ($1/\tau_{temp}$), we can calculate the losses induced by the background species other than N_2 . This is represented by Γ_b in Eq. 5.4. This background mostly contains the isotopic mixture of untrapped Sr, H_2 , CO, CO_2 , etc. Using Eq. 5.4, the value of Γ_b is found to be $\sim 0.5 \text{ s}^{-1}$.

5.5 Conclusion

In conclusion, we have studied the loss dynamics of ^{88}Sr atoms in the blue MOT in two different configurations with repumping lasers operating at the wavelengths 707.2 nm and 481.3 nm. The effect of background N_2 gas on the total loss rate is studied and is used for the determination of collision cross section between $^{88}\text{Sr}-N_2$. The measured value is found to be $8.1(4) \times 10^{-18} \text{ m}^2$. This value of the collision cross section is utilized for the calculation of C_6 of ground state Sr atoms and is found to be $535(68) E_H a_B^6$. We also characterize the various loss channels and determine their contributions toward the total loss rate. We show that the dominant loss channel is from the combined effect of time taken by the atoms to return to the primary cooling cycle via the intermediate states and the thermal escape of atoms from the trapping region during this period. The other contributing loss channel is the decay of atoms into the long-lived state 3P_0 . For the current experimental setup, their collective contribution (α) is estimated by operating the MOT at different intensities of trapping beams. The combined decay rate is found to be $167(4) \text{ s}^{-1}$ and $18(1) \text{ s}^{-1}$ for 707.2 nm and 481.3 nm, respectively.

Chapter 6

Conclusion and Outlook

6.1 Summary

The ultimate goal of the thesis work was to develop an experimental platform to perform precision measurements and frequency metrology with ultracold Sr atoms. The existence of a narrow inter-combination line in Sr makes it an ideal candidate for an optical atomic clock. Optical clock based on neutral strontium atoms has reached the total uncertainty of 2.1×10^{-18} . Such precise clocks are useful for various applications such as fundamental physics, geophysics, and astronomical application. The work reported in this thesis is being used in developing a system that can be used for the frequency metrology using the clock transition. Towards this goal, an experimental setup is built which produces cold strontium atoms in the MOT.

In the current setup, an atomic beam is generated and slowed down using a zero-field crossing Zeeman slower to load the MOT. We load $\sim 10^7$, ^{88}Sr atoms in MOT operating in standard $\sigma^+ - \sigma^-$ configuration with the magnetic field gradient of ~ 48 Gauss/cm in the quadrupole coils. During the development of the experimental setup, we have given special emphasis on making the system simple and robust. To ensure this, we have implemented some novel techniques to overcome and simplify some technical issues in the existing systems. For example, in order to generate a beam of atoms for loading MOT, we have designed and constructed an effusive oven that provides the thermal isolation between the high-temperature oven region and the rest of the vacuum chamber. The above goal is achieved without using glass/ceramic break or without incorporating

the heated part of the oven inside the vacuum chamber. The advantage of our design lies in the existence of the heating element outside the vacuum chamber, which makes the maintenance of the oven easy. We have done extensive thermal profile simulation of the oven using Comsol Multiphysics to understand the temperature distribution along the vacuum chamber. Based on such simulation, we have proposed a new design of the oven with a small modification in the existing design. This modified design of the oven can provide the thermal isolation of ~ 400 K [191] without compromising on the physical strength. For our experimental setup, the measured atomic flux and MOT loading rate are found to be 6×10^9 atoms/sec and 2×10^7 atoms/sec respectively.

One of the basic requirements for the experiments using laser cooling and trapping is to have laser systems which are frequency stabilized with respect to particular atomic transitions. The most popular technique to do so is to perform Doppler-free saturated absorption spectroscopy (SAS) in a specially constructed vapor cell. However, unlike alkali atoms, the vapor pressure of Sr is very low at room temperature; also, it is highly reactive to glass, which hinders the construction of vapor cells for spectroscopic purposes. In order to overcome the limitations mentioned above, we designed and constructed a spectroscopy cell using glass blowing techniques for performing the atomic beam spectroscopy of Sr atoms [192]. This spectroscopy cell also incorporates a home-made TSP for maintaining the UHV inside the cell. The Full-Width Half Maximum (FWHM) of the first stage cooling transition, $5s^2 \ ^1S_0 \longrightarrow 5s \ 5p \ ^1P_1$, of Sr is found to be 33.3 ± 1.7 MHz. The measured value is comparable to the natural linewidth ($\Gamma = 32$ MHz) of this transition. The obtained spectrum is used for the frequency stabilization of the seed laser operating at 922 nm.

The designed system has been used to study the dynamics of Sr MOT, by observing the loading and loss rates under various conditions and repumping schemes. We have identified and characterized various loss mechanisms for the atoms in MOT. In our experiment, the total loss rate depends on (1) the collision with untrapped background atoms/molecules, (2) the decay of atoms into the triplet state 3P_0 , and (3) the temperature of the atomic cloud. The individual contribution due to the channels, as mentioned above, has been determined in the presence of two repumping schemes utilizing the lasers operating at 707.2 nm and 481.3 nm. We have also measured the collision cross

section between the ground state ^{88}Sr and background N_2 . The collision cross section is determined by injecting nitrogen (N_2) inside the vacuum chamber in a controlled manner and studying the atomic loss rate at different background pressures. The obtained value of the collision cross section has been used for the determination of C_6 of the ground state of ^{88}Sr . The obtained value of C_6 , along with the C_6 of the excited clock state, can be used for the determination of a systematic shift in the fractional frequency uncertainty in the clock operation. The measured value of the collision cross section is found to be $8.1(4) \times 10^{-18} \text{ m}^2$. The calculated value of C_6 using the above-mentioned value of the collision cross section is found to be $535(68) E_H a_B^6$ [193].

6.2 Future work

The current system generates $\sim 10^7$, ^{88}Sr atoms in MOT operating at the first stage cooling transition addressing $5s^2 \ ^1S_0 \longrightarrow 5s \ 5p \ ^1P_1$. This cooling process allows the maximum force to be exerted on the thermal atomic beam generated by the hot oven and cools them to the temperature of the order of a few mK. In our experimental setup, the temperature is measured to be ~ 3 mK. However, as mentioned in the introduction chapter, in order to take full advantage of the narrow linewidth of the clock transition, it is necessary to further cool the atoms to the minimum possible temperature. The final goal of performing the clock spectroscopy with the narrow inter-combination line of Sr atoms can be accomplished by going through the various steps, as mentioned below:

6.2.1 Second stage cooling: Red MOT

One of the advantages of Sr atoms is the existence of an inter-combination line, which is suitable for the second stage cooling. The pre-cooled atoms after the first stage cooling can be transferred to the MOT operating using the laser addressing the transition $5s^2 \ ^1S_0 \longrightarrow 5s \ 5p \ ^3P_1$ [194–196]. This singlet to triplet transition has a wavelength of 689.4 nm. This transition has a long lifetime of $21 \ \mu\text{s}$ and linewidth of $2\pi \times 7.5$ kHz. The linewidth is comparable to the single-photon recoil frequency shift:

$$\nu_r = E_r/h = 4.8 \text{ kHz} \quad (6.1)$$

Here, E_r is the single-photon recoil energy, and h is the Planck's constant. The above equation shows that the absorption/emission of photon kicks the atom out of resonance. In this case, the Doppler theory described in section- 2.3 can not be used for the description of laser cooling, and fully quantum mechanical treatment is required. It has to be noted that since the atoms are transferred from blue MOT, the Doppler profile of the Sr atoms is still above 1 MHz. In such a scenario, the spectral coverage of all the atoms is ensured by frequency modulating the laser at 689 nm to broaden the laser spectrum to a few MHz before switching to the single-frequency operation of the laser. Using the red MOT stage, the temperature of the atomic cloud can be reduced to $\sim 1 \mu\text{K}$ with a transfer efficiency of 50 %. It should be noted that the atom transfer efficiency going from a blue MOT to a red MOT depends strongly on the modulation parameters [197].

6.2.2 Trapping of atoms in magic wavelength optical dipole trap

Any radiation field that couples to the atomic states shifts their energies. This shift of the energy level is known as the light-shift or the AC stark shift. The optical dipole trapping utilizes the AC stark shifts to locally and temporally modify the energy level of the given atom to provide the necessary trapping potential. However, the differential AC stark shift is usually a nuisance during the experiments designed for precision measurements and needs to be avoided. This is accomplished by employing a special wavelength for which the AC stark shifts of the two involved atomic states are equal in magnitude and sign. This wavelength is called the 'magic wavelength'. Similarly, the wavelength, for which the stark shift is equal in magnitude but opposite in sign, is called the anti-magic wavelength. For strontium atoms, the two transitions for which the light shift plays an important role are $^1S_0 \rightarrow ^3P_0$, the clock transition, and the $^1S_0 \rightarrow ^3P_1$. The magic wavelengths for these transitions are $\sim 813 \text{ nm}$ [86] and $\sim 915 \text{ nm}$ respectively. The magic wavelength for the clock transition has to be determined with the highest possible precision to avoid any residual light-induced shifts. Apart from the externally applied laser field, another radiation field which induces a differential shift in the clock states is the background black-body radiation of the environment [198, 199]. Tremendous efforts have been put to quantify and reduce the magnitude of this shift accurately.

6.2.3 Magnetic field-induced spectroscopy of the clock transition

As mentioned in chapter - 2, the clock transition $5s^2 \ ^1S_0 \longrightarrow 5s \ 5p \ ^3P_0$ is forbidden under the dipole selection rule for the even isotope of strontium atoms. To induce finite transition probability between the states mentioned above, an external interaction has to be introduced to engineer the atomic-level structure. This is done by coupling the metastable state 3P_0 to the nearby electronic state for which the atomic transition is allowed under the dipole approximation. Two such ways to achieve the goal are (1) use multiple near-resonant laser fields [200, 201] or (2) by introducing a small static magnetic field [202]. Using the latter scheme [203], it is possible to reach the clock accuracy level of 10^{-17} [204]. In the case of strontium atoms, it is achieved by placing the atoms in the right magnetic field that couples the states 3P_0 and 3P_1 such that:

$$\langle ^3P_0 | \mu \cdot \mathbf{B} | ^3P_1 \rangle = \hbar \Omega_B \quad (6.2)$$

Here, μ is the magnetic-dipole operator. Now, according to the first-order perturbation theory with the condition $|\hbar \Omega_B / \Delta E| \ll 1$, the state 3P_0 acquires a small admixture of the state 3P_1 in the presence of the external static magnetic field. The new state can be written as:

$$|^3P'_0\rangle = |^3P_0\rangle + \frac{\hbar \Omega_B}{\Delta E} |^3P_1\rangle \quad (6.3)$$

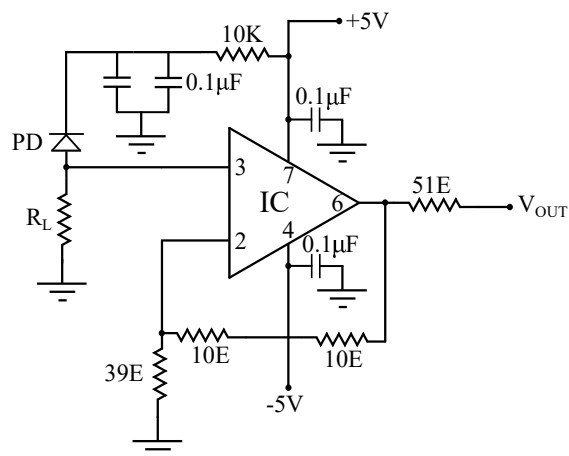
The result is that the clock transition between the unperturbed ground state 1S_0 and the effective excited state $^3P'_0$ become partially allowed.

With small modifications in the setup described in this thesis, one can study systematic shifts in the clock states. For example, for the determination of background hydrogen (H_2) induced shift and broadening of the clock transition. The experimental sequence would be similar to the one which is used for performing the experiments with background nitrogen. In this case, pure H_2 has to be introduced in the vacuum chamber in a controlled manner, and the resulting loss rate of the atoms has to be monitored as a function of time. The data thus obtained can be used for the calculation of Sr– H_2 collision cross section and corresponding C_6 coefficient for the ground state of Sr.

Appendix A

Appendix

A.1 Fast photodiode amplifier circuit



PD: S5972 (Hamamatsu)

IC: AD8001

Figure A.1: Circuit diagram of fast photodiode amplifier.

A.2 Lock box circuit diagram

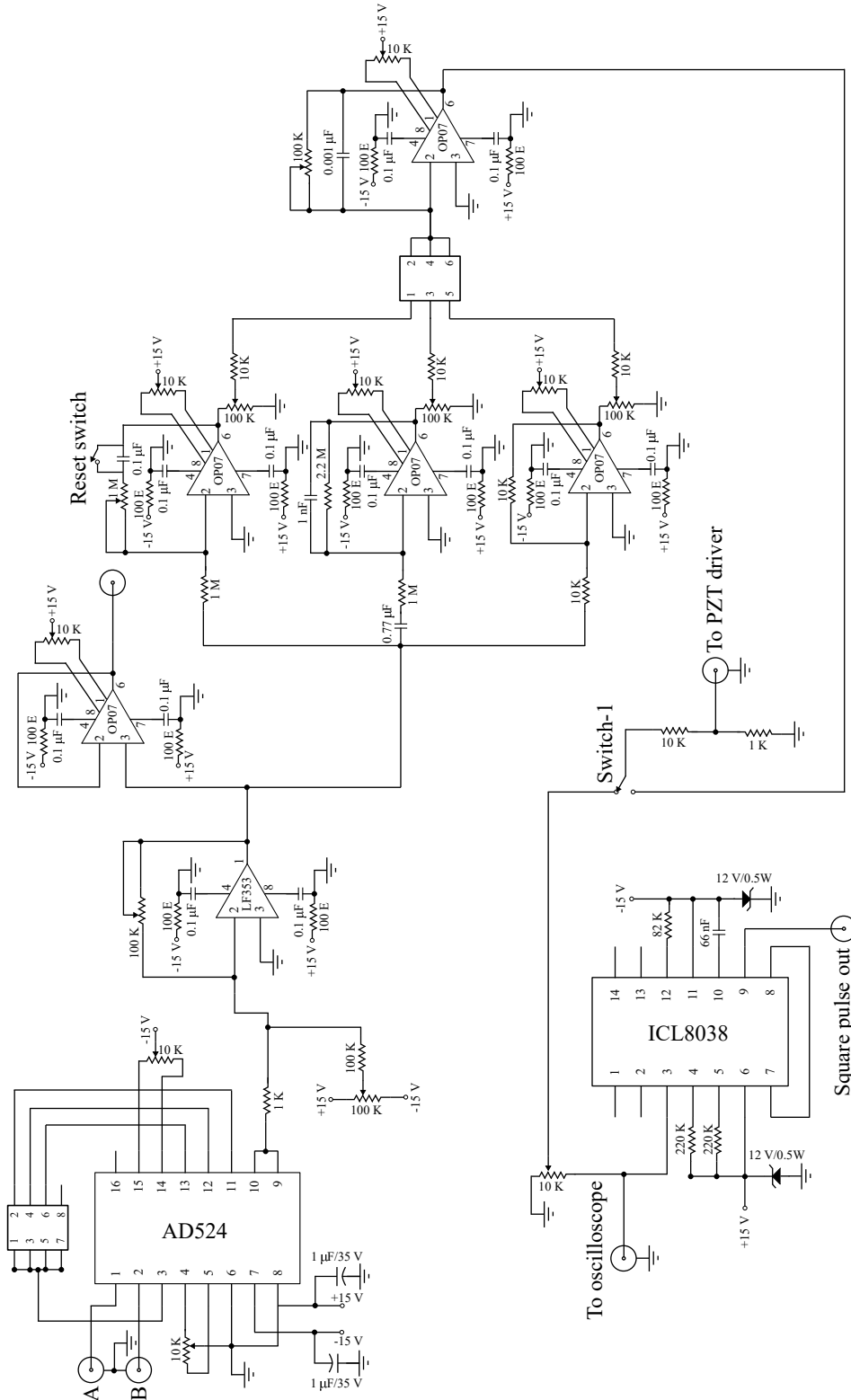


Figure A.2: Circuit diagram of lock box used for scanning and locking the seed laser: The circuit diagram is adopted from PhD Thesis, Umakant D. Rapol, IISc, Bangalore, with appropriate modifications.

A.3 High voltage amplifier circuit

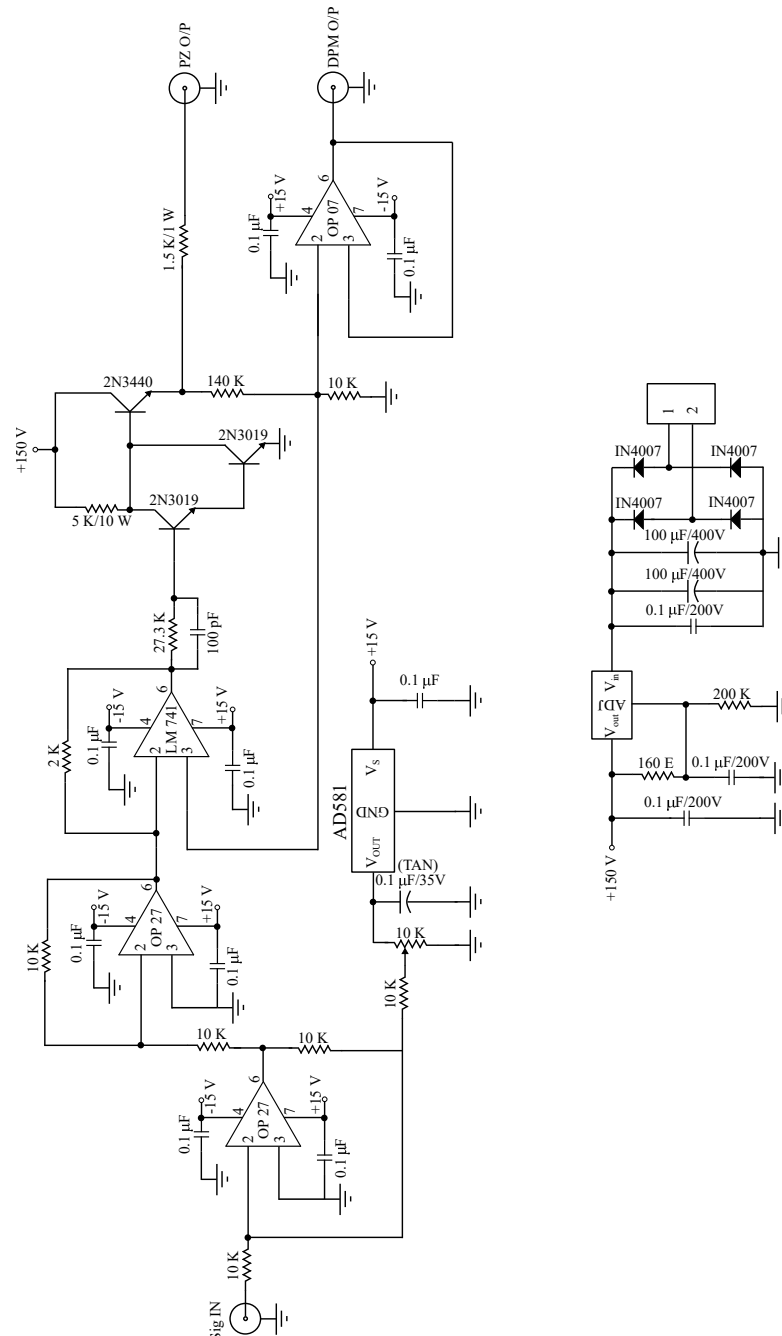


Figure A.3: Circuit diagram of high voltage amplifier: The gain of this amplifier is 15 and it produces the maximum output voltage of 150 V. The circuit diagram is adopted from PhD Thesis, Umakant D. Rapol, IISc, Bangalore.

A.4 Photo-multiplier tube controller

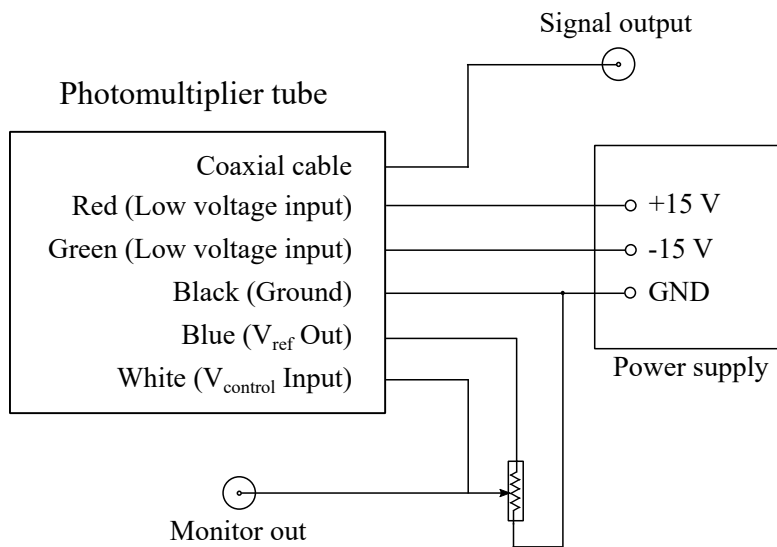
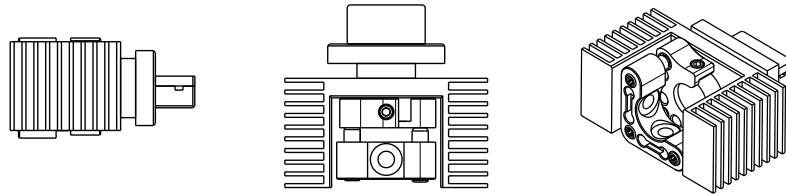


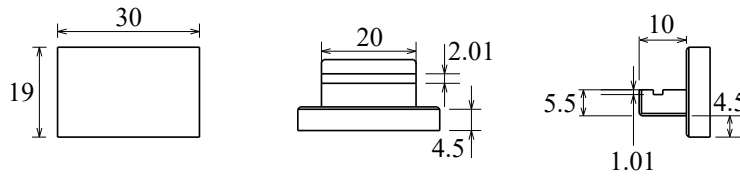
Figure A.4: Hamamatsu PMT (H9307-02) controller: The circuit diagram is taken from H9306/H9307 photosensor module datasheet.

A.5 Crystal holder design

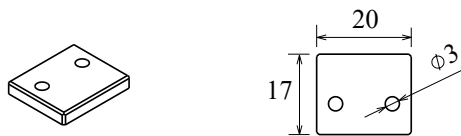
Assembled crystal holder



Crystal holder



Cover design



Heat sink

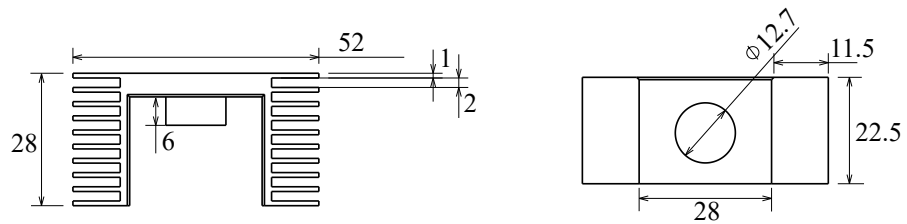


Figure A.5: Mechanical design of the crystal holder

A.6 Frequency doubler mechanical drawing

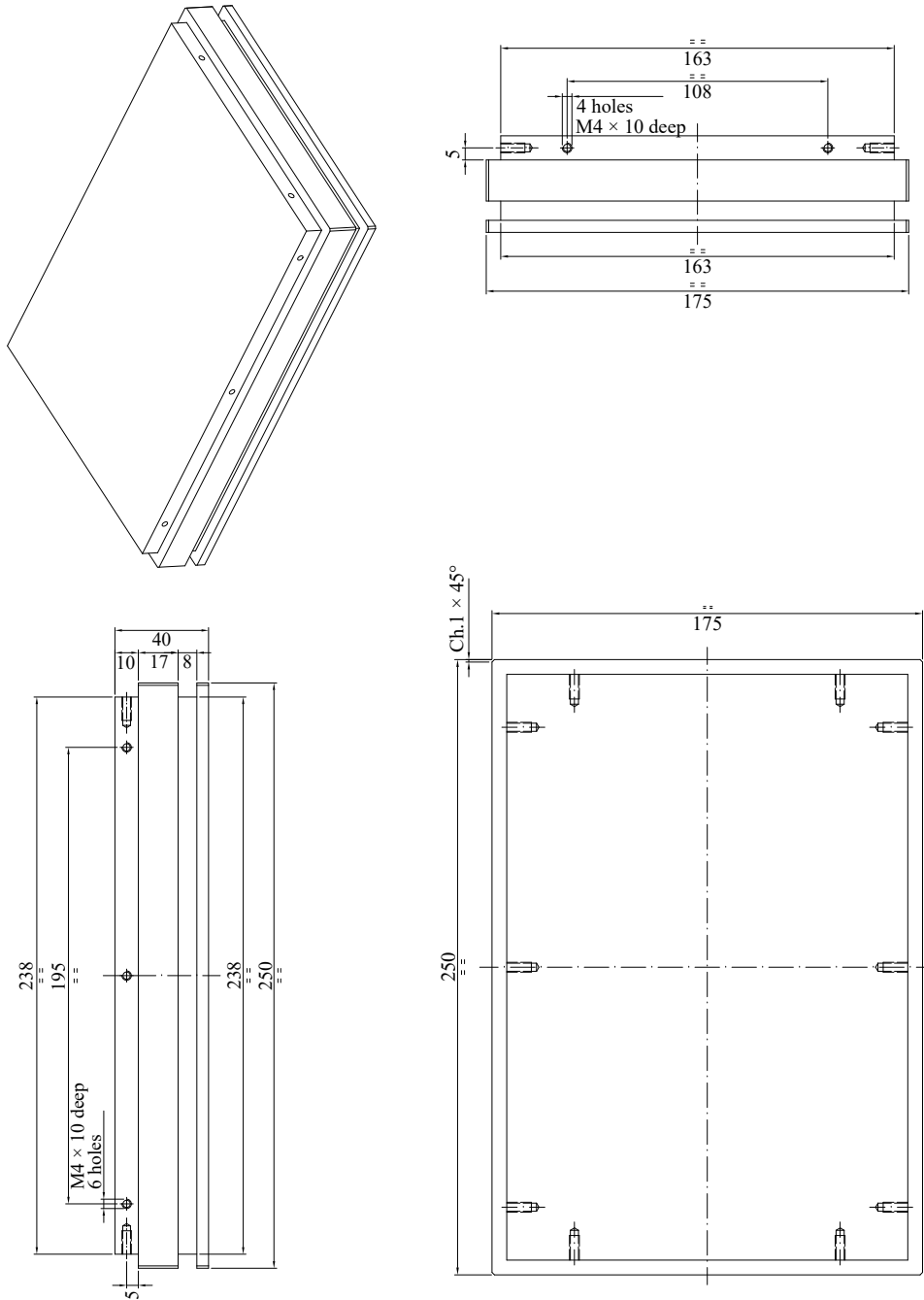


Figure A.6: Frequency doubler mount: Base plate

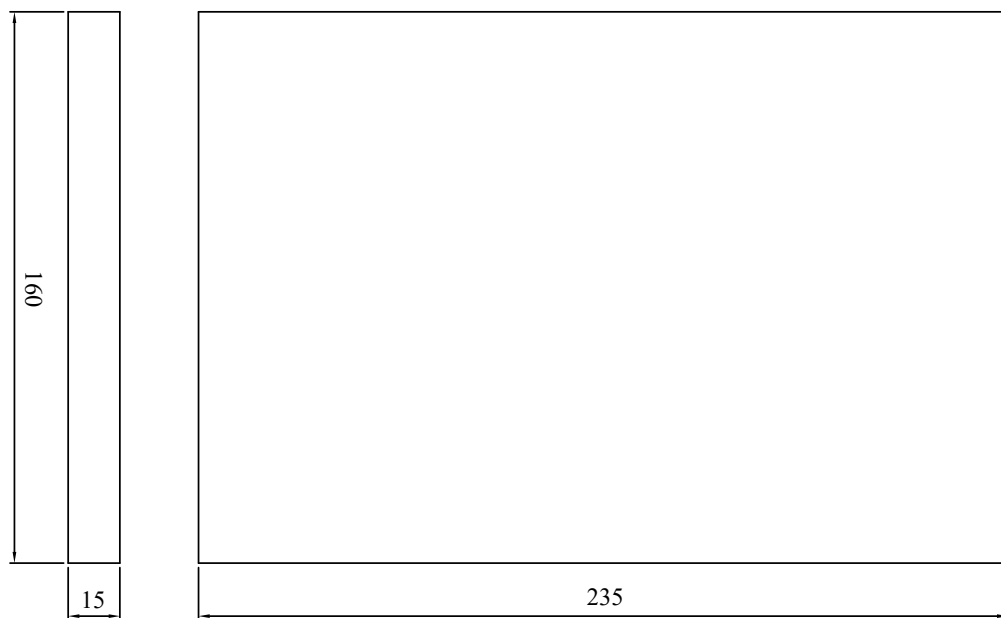


Figure A.7: Frequency doubler mount: Top platform for fixing mirrors. The distance between mirrors and folding angle is given in table - 4.3.

Bibliography

- [1] Mesures BIdPe. SI brochure: “The international system of units (SI)”. *ed. https://www.bipm.org*, (2014).
- [2] Ernst O Göbel and Uwe Siegener. “The New International System of Units (SI): Quantum Metrology and Quantum Standards”. *John Wiley & Sons*, (2019).
- [3] Richard Davis. “The SI unit of mass”. *Metrologia*, **40**(6), 299–305, (2003).
- [4] Ian A Robinson and Stephan Schlamminger. “The watt or Kibble balance: A technique for implementing the new SI definition of the unit of mass”. *Metrologia*, **53**(5), A46–A74, (2016).
- [5] A. A. Michelson and E. W. Morley. “On the relative motion of the earth and the luminiferous ether”. *Am. J. Sci.*, Series 3, **34**(203), 333–345, (1887).
- [6] Willis E. Lamb and Robert C. Retherford. “Fine structure of the hydrogen atom by a microwave method”. *Phys. Rev.*, **72**, 241–243, (1947).
- [7] Alexander D. Cronin, Jörg Schmiedmayer, and David E. Pritchard. “Optics and interferometry with atoms and molecules”. *Rev. Mod. Phys.*, **81**, 1051–1129, (2009).
- [8] Alan Lenef, Troy D. Hammond, Edward T. Smith, Michael S. Chapman, Richard A. Rubenstein, and David E. Pritchard. “Rotation sensing with an atom interferometer”. *Phys. Rev. Lett.*, **78**, 760–763, (1997).

- [9] T. L. Gustavson, P. Bouyer, and M. A. Kasevich. “Precision rotation measurements with an atom interferometer gyroscope”. *Phys. Rev. Lett.*, **78**, 2046–2049, (1997).
- [10] Alex Sugarbaker, Susannah M. Dickerson, Jason M. Hogan, David M. S. Johnson, and Mark A. Kasevich. “Enhanced atom interferometer readout through the application of phase shear”. *Phys. Rev. Lett.*, **111**, 113002, (2013).
- [11] S. Gupta, K. Dieckmann, Z. Hadzibabic, and D. E. Pritchard. “Contrast interferometry using Bose-Einstein condensates to measure h/m and α ”. *Phys. Rev. Lett.*, **89**, 140401, (2002).
- [12] Rym Bouchendira, Pierre Cladé, Saïda Guellati-Khélifa, François Nez, and François Biraben. “New determination of the fine structure constant and test of the quantum electrodynamics”. *Phys. Rev. Lett.*, **106**, 080801, (2011).
- [13] Andreas Wicht, Joel M. Hensley, Edina Sarajlic, and Steven Chu. “A preliminary measurement of the fine structure constant based on atom interferometry”. *Phys. Scripta*, **T102**(1), 82, (2002).
- [14] Christopher R. Ekstrom, Jörg Schmiedmayer, Michael S. Chapman, Troy D. Hammond, and David E. Pritchard. “Measurement of the electric polarizability of sodium with an atom interferometer”. *Phys. Rev. A*, **51**, 3883–3888, (1995).
- [15] M. Kasevich and S. Chu. “Measurement of the gravitational acceleration of an atom with a light-pulse atom interferometer”. *Appl. Phys. B*, **54**(5), 321–332, (1992).
- [16] Achim Peters, Keng Yeow Chung, and Steven Chu. “Measurement of gravitational acceleration by dropping atoms”. *Nature*, **400**(6747), 849, (1999).
- [17] Remi Geiger, Vincent Ménotet, Guillaume Stern, Nassim Zahzam, Patrick Cheinet, Baptiste Battelier, André Villing, Frédéric Moron, Michel Lours, Yannick Bidet, et al. “Detecting inertial effects with airborne matter-wave interferometry”. *Nat. Commun.*, **2**, 474, (2011).

- [18] G. Lamporesi, A. Bertoldi, L. Cacciapuoti, M. Prevedelli, and G. M. Tino. “Determination of the newtonian gravitational constant using atom interferometry”. *Phys. Rev. Lett.*, **100**, 050801, (2008).
- [19] J. B. Fixler, G. T. Foster, J. M. McGuirk, and M. A. Kasevich. “Atom interferometer measurement of the newtonian constant of gravity”. *Science*, **315**(5808), 74–77, (2007).
- [20] M. J. Snadden, J. M. McGuirk, P. Bouyer, K. G. Haritos, and M. A. Kasevich. “Measurement of the earth’s gravity gradient with an atom interferometer-based gravity gradiometer”. *Phys. Rev. Lett.*, **81**, 971–974, (1998).
- [21] J. M. McGuirk, G. T. Foster, J. B. Fixler, M. J. Snadden, and M. A. Kasevich. “Sensitive absolute-gravity gradiometry using atom interferometry”. *Phys. Rev. A*, **65**, 033608, (2002).
- [22] Savas Dimopoulos, Peter W. Graham, Jason M. Hogan, Mark A. Kasevich, and Surjeet Rajendran. “Atomic gravitational wave interferometric sensor”. *Phys. Rev. D*, **78**, 122002, (2008).
- [23] Peter W. Graham, Jason M. Hogan, Mark A. Kasevich, and Surjeet Rajendran. “New method for gravitational wave detection with atomic sensors”. *Phys. Rev. Lett.*, **110**, 171102, (2013).
- [24] Julia Scherschligt, James A Fedchak, Daniel S Barker, Stephen Eckel, Nikolai Klimov, Constantinos Makrides, and Eite Tiesinga. “Development of a new UHV/XHV pressure standard (cold atom vacuum standard)”. *Metrologia*, **54**(6), S125–S132, (2017).
- [25] V B Makhlov, K A Martiyanov, and A V Turlapov. “Primary vacuumeter based on an ultracold gas in a shallow optical dipole trap”. *Metrologia*, **53**(6), 1287–1294, (2016).
- [26] Stephen Eckel, Daniel S Barker, James A Fedchak, Nikolai N Klimov, Eric Norrgard, Julia Scherschligt, Constantinos Makrides, and Eite Tiesinga. “Chal-

- allenges to miniaturizing cold atom technology for deployable vacuum metrology”. *Metrologia*, **55**(5), S182–S193, (2018).
- [27] K. J. Matherson, R. D. Glover, D. E. Laban, and R. T. Sang. “Measurement of low-energy total absolute atomic collision cross sections with the metastable 3P_2 state of neon using a magneto-optical trap”. *Phys. Rev. A*, **78**, 042712, (2008).
- [28] T. Arpornthip, C. A. Sackett, and K. J. Hughes. “Vacuum-pressure measurement using a magneto-optical trap”. *Phys. Rev. A*, **85**, 033420, (2012).
- [29] Rowan W. G. Moore, Lucie A. Lee, Elizabeth A. Findlay, Lara Torralbo-Campo, Graham D. Bruce, and Donatella Cassettari. “Measurement of vacuum pressure with a magneto-optical trap: A pressure-rise method”. *Rev. Sci. Instrum.*, **86**(9), 093108, (2015).
- [30] Umakant D. Rapol, Ajay Wasan, and Vasant Natarajan. “Loading of a Rb magneto-optic trap from a getter source”. *Phys. Rev. A*, **64**, 023402, (2001).
- [31] U. D. Rapol, A. Krishna, A. Wasan, and V. Natarajan. “Laser cooling and trapping of Yb from a thermal source”. *Eur. Phys. J. D - Atomic, Molecular, Optical and Plasma Physics*, **29**(3), 409–414, (2004).
- [32] Jin-Peng Yuan, Zhong-Hua Ji, Yan-Ting Zhao, Xue-Fang Chang, Lian-Tuan Xiao, and Suo-Tang Jia. “Simple, reliable, and nondestructive method for the measurement of vacuum pressure without specialized equipment”. *Appl. Optics*, **52**(25), 6195–6200, (2013).
- [33] K. J. Matherson, R. D. Glover, D. E. Laban, and R. T. Sang. “Absolute metastable atom-atom collision cross section measurements using a magneto-optical trap”. *Rev. Sci. Instrum.*, **78**(7), 073102, (2007).
- [34] B. J. Claessens, J. P. Ashmore, R. T. Sang, W. R. MacGillivray, H. C. W. Beijerinck, and E. J. D. Vredenburg. “Measurement of the photoionization cross section of the $(2p)^5(3p) ^3D_3$ state of neon”. *Phys. Rev. A*, **73**, 012706, (2006).

- [35] Timothy P. Dinneen, Christopher D. Wallace, Kit-Yan N. Tan, and Phillip L. Gould. “Use of trapped atoms to measure absolute photoionization cross sections”. *Opt. Lett.*, **17**(23), 1706–1708, (1992).
- [36] R. S. Schappe, T. Walker, L. W. Anderson, and Chun C. Lin. “Absolute electron-impact ionization cross section measurements using a magneto-optical trap”. *Phys. Rev. Lett.*, **76**, 4328–4331, (1996).
- [37] Theodor W. Hänsch. “Nobel lecture: Passion for precision”. *Rev. Mod. Phys.*, **78**, 1297–1309, (2006).
- [38] John L. Hall. “Nobel lecture: Defining and measuring optical frequencies”. *Rev. Mod. Phys.*, **78**, 1279–1295, (2006).
- [39] Matthew Bennett, Michael F Schatz, Heidi Rockwood, and Kurt Wiesenfeld. Huygens’s clocks. *P. Roy. Soc. Lond. A Mat*, **458**(2019), 563–579, (2002).
- [40] William Thomson Baron Kelvin and Peter Guthrie Tait. *Treatise on natural philosophy*, volume 1. Clarendon Press, (1867).
- [41] Harold Lyons. “Microwave spectroscopy frequency and time standards”. *Elec. Eng.*, **68**, 251, (1949).
- [42] RD Huntoon and U Fano. “Atomic definition of primary standards”. *Nature*, **166**(4213), 167, (1950).
- [43] Louis Essen and Jack VL Parry. “An atomic standard of frequency and time interval: a caesium resonator”. *Nature*, **176**(4476), 280–282, (1955).
- [44] V Gerginov, N Nemitz, D Griebisch, M Kazda, R Li, Kurt Gibble, R Wynands, and S Weyers. “Recent improvements and current uncertainty budget of PTB fountain clock CsF2”. *EFTF-2010 24th European Frequency and Time Forum*, 1–7. IEEE, (2010).
- [45] Hans G Dehmelt. “Monoion oscillator as potential ultimate laser frequency standard”. *IEEE T. Instrum. Meas.*, **2**, 83–87, (1982).

- [46] A. L. Schawlow and C. H. Townes. “Infrared and optical masers”. *Phys. Rev.*, **112**, 1940–1949, (1958).
- [47] Steven Chu. “Nobel lecture: The manipulation of neutral particles”. *Rev. Mod. Phys.*, **70**, 685–706, (1998).
- [48] Claude N. Cohen-Tannoudji. “Nobel lecture: Manipulating atoms with photons”. *Rev. Mod. Phys.*, **70**, 707–719, (1998).
- [49] William D. Phillips. “Nobel lecture: Laser cooling and trapping of neutral atoms”. *Rev. Mod. Phys.*, **70**, 721–741, (1998).
- [50] L Hollberg, S Diddams, A Bartels, T Fortier, and K Kim. “The measurement of optical frequencies”. *Metrologia*, **42**(3), S105–S124, (2005).
- [51] H. Schnatz, B. Lipphardt, J. Helmcke, F. Riehle, and G. Zinner. “First phase-coherent frequency measurement of visible radiation”. *Phys. Rev. Lett.*, **76**, 18–21, (1996).
- [52] R. Holzwarth, Th. Udem, T. W. Hänsch, J. C. Knight, W. J. Wadsworth, and P. St. J. Russell. “Optical frequency synthesizer for precision spectroscopy”. *Phys. Rev. Lett.*, **85**, 2264–2267, (2000).
- [53] Scott A. Diddams, David J. Jones, Jun Ye, Steven T. Cundiff, John L. Hall, Jindendra K. Ranka, Robert S. Windeler, Ronald Holzwarth, Thomas Udem, and T. W. Hänsch. “Direct link between microwave and optical frequencies with a 300 THz femtosecond laser comb”. *Phys. Rev. Lett.*, **84**, 5102–5105, (2000).
- [54] Th. Udem, S. A. Diddams, K. R. Vogel, C. W. Oates, E. A. Curtis, W. D. Lee, W. M. Itano, R. E. Drullinger, J. C. Bergquist, and L. Hollberg. “Absolute frequency measurements of the Hg^+ and Ca optical clock transitions with a femtosecond laser”. *Phys. Rev. Lett.*, **86**, 4996–4999, (2001).
- [55] Scott A Diddams, Thomas Udem, Kurt R Vogel, Chris W Oates, EA Curtis, Robert S Windeler, A Bartels, James C Bergquist, and Leo W Hollberg. “Com-

- pact femtosecond-laser-based optical clockwork". *P. Soc. Photo-Opt Ins.*, 4269: 77–83, (2001).
- [56] David W Allan. "Statistics of atomic frequency standards". *P. IEEE*, **54**(2), 221–230, (1966).
- [57] BJ Bloom, TL son, JR Williams, SL Campbell, M Bishof, X Zhang, W Zhang, SL Bromley, and J Ye. "An optical lattice clock with accuracy and stability at the 10^{-18} level". *Nature*, **506**(7486), 71, (2014).
- [58] W. M. Itano, J. C. Bergquist, J. J. Bollinger, J. M. Gilligan, D. J. Heinzen, F. L. Moore, M. G. Raizen, and D. J. Wineland. "Quantum projection noise: Population fluctuations in two-level systems". *Phys. Rev. A*, **47**, 3554–3570, (1993).
- [59] Masao Takamoto, Tetsushi Takano, and Hidetoshi Katori. "Frequency comparison of optical lattice clocks beyond the dick limit". *Nat. Photonics*, **5**(5), 288, (2011).
- [60] Tetsuya Ido and Hidetoshi Katori. "Recoil-free spectroscopy of neutral Sr atoms in the lamb-dicke regime". *Phys. Rev. Lett.*, **91**, 053001, (2003).
- [61] Hidetoshi Katori. "Optical lattice clocks and quantum metrology". *Nat. Photonics*, **5**(4), 203, (2011).
- [62] P. G. Westergaard, J. Lodewyck, L. Lorini, A. Lecallier, E. A. Burt, M. Zawada, J. Millo, and P. Lemonde. "Lattice-induced frequency shifts in Sr optical lattice clocks at the 10^{-17} level". *Phys. Rev. Lett.*, **106**, 210801, (2011).
- [63] Matthew D Swallows, Michael Bishof, Yige Lin, Sebastian Blatt, Michael J Martin, Ana Maria Rey, and Jun Ye. "Suppression of collisional shifts in a strongly interacting lattice clock". *Science*, **331**(6020), 1043–1046, (2011).
- [64] K. Beloy. "Lattice-induced nonadiabatic frequency shifts in optical lattice clocks". *Phys. Rev. A*, **82**, 031402, (2010).
- [65] Tomoya Akatsuka, Masao Takamoto, and Hidetoshi Katori. "Three-dimensional optical lattice clock with bosonic ^{88}Sr atoms". *Phys. Rev. A*, **81**, 023402, (2010).

- [66] Ch. Lisdat, J. S. R. Vellore Winfred, T. Middelmann, F. Riehle, and U. Sterr. “Collisional losses, decoherence, and frequency shifts in optical lattice clocks with bosons”. *Phys. Rev. Lett.*, **103**, 090801, (2009).
- [67] Masao Takamoto, Feng-Lei Hong, Ryoichi Higashi, and Hidetoshi Katori. “An optical lattice clock”. *Nature*, **435**(7040), 321, (2005).
- [68] TL Nicholson, SL Campbell, RB Hutson, GE Marti, BJ Bloom, RL McNally, Wei Zhang, MD Barrett, MS Safronova, GF Strouse, et al. “Systematic evaluation of an atomic clock at 2×10^{-18} total uncertainty”. *Nat. Commun.*, **6**, 6896, (2015).
- [69] Ichiro Ushijima, Masao Takamoto, Manoj Das, Takuya Ohkubo, and Hidetoshi Katori. “Cryogenic optical lattice clocks”. *Nature Photonics*, **9**(3), 185, (2015).
- [70] Sara L Campbell, RB Hutson, GE Marti, A Goban, N Darkwah Oppong, RL McNally, L Sonderhouse, JM Robinson, W Zhang, BJ Bloom, et al. “A fermi-degenerate three-dimensional optical lattice clock”. *Science*, **358**(6359), 90–94, (2017).
- [71] Till Rosenband, DB Hume, PO Schmidt, Chin-Wen Chou, Anders Brusch, Luca Lorini, WH Oskay, Robert E Drullinger, Tara M Fortier, Jason E Stalnaker, et al. “Frequency ratio of Al^+ and Hg^+ single-ion optical clocks; metrology at the 17th decimal place”. *Science*, **319**(5871), 1808–1812, (2008).
- [72] Caroline Champenois, Marie Houssin, Caroline Lisowski, Martina Knoop, Gaetan Hagel, Michel Vedel, and Fernande Vedel. “Evaluation of the ultimate performances of a Ca^+ single-ion frequency standard”. *Phys. Lett. A*, **331**(5), 298–311, (2004).
- [73] Kensuke Matsubara, Kazuhiro Hayasaka, Ying Li, Hiroyuki Ito, Shigeo Nagano, Masatoshi Kajita, and Mizuhiko Hosokawa. “Frequency measurement of the optical clock transition of $^{40}\text{Ca}^+$ ions with an uncertainty of 10^{-14} level”. *Appl. Phys. Express*, **1**(6), 067011, (2008).
- [74] M Chwalla, J Benhelm, K Kim, G Kirchmair, T Monz, M Riebe, P Schindler, AS Villar, W Hänsel, CF Roos, et al. “Absolute frequency measurement of the

- $^{40}\text{Ca}^+$ $4\text{ s }^2S_{1/2} - 3d^2D_{5/2}$ clock transition”. *Phys. Rev. Lett.*, **102**(2), 023002, (2009).
- [75] WH Oskay, Scott A Diddams, Elizabeth A Donley, Tara M Fortier, Thomas P Heavner, L Hollberg, Wayne M Itano, Steven R Jefferts, MJ Delaney, Kyoungsik Kim, et al. “Single-atom optical clock with high accuracy”. *Phys. Rev. Lett.*, **97**(2), 020801, (2006).
- [76] Chr Tamm, Burghard Lipphardt, Harald Schnatz, Robert Wynands, Stefan Weyers, Tobias Schneider, and Ekkehard Peik. “ $^{171}\text{Yb}^+$ single-ion optical frequency standard at 688 THz”. *P. IEEE Int. Freq. Cont.*, 457–461. IEEE, (2006).
- [77] Kazumoto Hosaka, Stephen A Webster, Peter J Blythe, Adrian Stannard, David Beaton, Helen S Margolis, Stephen N Lea, and Patrick Gill. “An optical frequency standard based on the electric octupole transition in/sup $^{171}\text{Yb}^+$ ”. *IEEE T. Instrum. Meas.*, **54**(2), 759–762, (2005).
- [78] J Von Zanthier, Th Becker, M Eichenseer, A Yu Nevsky, Ch Schwedes, E Peik, H Walther, R Holzwarth, J Reichert, Th Udem, et al. “Absolute frequency measurement of the In^+ clock transition with a mode-locked laser”. *Opt. Lett.*, **25**(23), 1729–1731, (2000).
- [79] HS Margolis, GP Barwood, G Huang, HA Klein, SN Lea, K Szymaniec, and P Gill. “Hertz-level measurement of the optical clock frequency in a single $^{88}\text{Sr}^+$ ion”. *Science*, **306**(5700), 1355–1358, (2004).
- [80] P Dubé, AA Madej, JE Bernard, L Marmet, J-S Boulanger, and S Cundy. “Electric quadrupole shift cancellation in single-ion optical frequency standards”. *Phys. Rev. Lett.*, **95**(3), 033001, (2005).
- [81] HS Margolis. “Frequency metrology and clocks”. *J. Phys. B - At. Mol. Opt.*, **42**(15), 154017, (2009).
- [82] Jason T Burke. “One tick closer to a nuclear clock” *Nature Publishing Group*, (2019).

- [83] Benedict Seiferle, Lars von der Wense, Pavlo V. Bilous, Ines Amersdorfer, Christoph Lemell, Florian Libisch, Simon Stellmer, Thorsten Schumm, Christoph E. Düllmann, Adriana Pálffy, and Peter G. Thirolf. “Energy of the ^{229}Th nuclear clock transition”. *Nature*, **573**, 243–246, (2019).
- [84] Takahiko Masuda, Akihiro Yoshimi, Akira Fujieda, Hiroyuki Fujimoto, Hiromitsu Haba, Hideaki Hara, Takahiro Hiraki, Hiroyuki Kaino, Yoshitaka Kasamatsu, Shinji Kitao, et al. “X-ray pumping of the ^{229}Th nuclear clock isomer”. *arXiv:1902.04823*, (2019).
- [85] C. J. Campbell, A. G. Radnaev, A. Kuzmich, V. A. Dzuba, V. V. Flambaum, and A. Derevianko. “Single-ion nuclear clock for metrology at the 19th decimal place”. *Phys. Rev. Lett.*, **108**, 120802, (2012).
- [86] Kai Guo, Guangfu Wang, and Anpei Ye. “Dipole polarizabilities and magic wavelengths for a Sr and Yb atomic optical lattice clock”. *J. Phys. B - At. Mol. Opt.*, **43**(13), 135004, (2010).
- [87] Patrick Gill. “Is the time right for a redefinition of the second by optical atomic clocks?” *J. Phys. Conf. Ser.*, **723**, 012053, (2016).
- [88] H Hirabayashi, H Hirosawa, H Kobayashi, Y Murata, PG Edwards, EB Fomalont, K Fujisawa, T Ichikawa, T Kii, J E Lovell, et al. “Overview and initial results of the very long baseline interferometry space observatory programme”. *Science*, **281**(5384), 1825–1829, (1998).
- [89] Tetsushi Takano, Masao Takamoto, Ichiro Ushijima, Noriaki Ohmae, Tomoya Akatsuka, Atsushi Yamaguchi, Yuki Kuroishi, Hiroshi Munekane, Basara Miyahara, and Hidetoshi Katori. “Geopotential measurements with synchronously linked optical lattice clocks”. *Nat. Photonics*, **10**(10), 662, (2016).
- [90] Jacopo Grotti, Silvio Koller, Stefan Vogt, Sebastian Häfner, Uwe Sterr, Christian Lisdat, Heiner Denker, Christian Voigt, Ludger Timmen, Antoine Rolland, et al. “Geodesy and metrology with a transportable optical clock”. *Nat. Phys.*, **14**(5), 437–441, (2018).

- [91] Todd A Ely, David Murphy, Jill Seubert, Julia Bell, and Da Kuang. “Expected performance of the deep space atomic clock mission”. *AAS/AIAA Space Flight Mechanics Meeting*, (2014).
- [92] J Hafele and R Keating. “Around-the-world atomic clocks: Observed relativistic time gains”. *Science*, **177**, 168–170, (1972).
- [93] Jean-Philippe Uzan. “The fundamental constants and their variation: observational and theoretical status”. *Rev. Mod. Phys.*, **75**(2), 403, (2003).
- [94] William J. Marciano. “Time variation of the fundamental ‘constants’ and kaluza-klein theories”. *Phys. Rev. Lett.*, **52**, 489–491, (1984).
- [95] Thibault Damour, Federico Piazza, and Gabriele Veneziano. “Runaway dilaton and equivalence principle violations”. *Phys. Rev. Lett.*, **89**, 081601, (2002).
- [96] V. A. Dzuba and V. V. Flambaum. Relativistic corrections to transition frequencies of Ag I, Dy I, Ho I, Yb II, Yb III, Au I, and Hg II and search for variation of the fine-structure constant. *Phys. Rev. A*, **77**, 012515, (2008).
- [97] V. A. Dzuba, V. V. Flambaum, and M. V. Marchenko. “Relativistic effects in Sr, Dy, Yb II, and Yb III and search for variation of the fine-structure constant”. *Phys. Rev. A*, **68**, 022506, (2003).
- [98] E. J. Angstmann, V. A. Dzuba, and V. V. Flambaum. “Relativistic effects in two valence-electron atoms and ions and the search for variation of the fine-structure constant”. *Phys. Rev. A*, **70**, 014102, (2004).
- [99] SN Lea. “Limits to time variation of fundamental constants from comparisons of atomic frequency standards”. *Rep. Prog. Phys.*, **70**(9), 1473, (2007).
- [100] M. H. Anderson, J. R. Ensher, M. R. Matthews, C. E. Wieman, and E. A. Cornell. “Observation of Bose-Einstein condensation in a dilute atomic vapor”. *Science*, **269**(5221), 198–201, (1995).

- [101] E. A. Cornell and C. E. Wieman. “Nobel lecture: Bose-Einstein condensation in a dilute gas, the first 70 years and some recent experiments”. *Rev. Mod. Phys.*, **74**, 875–893, (2002).
- [102] W Ketterle, M R Andrews, K B, D S Durfee, D M Kurn, M O Mewes, and N J van Druten. “Bose–Einstein condensation of ultracold atomic gases”. *Phys. Scripta*, **T66**, 31–37, (1996).
- [103] Wolfgang Ketterle. “Nobel lecture: When atoms behave as waves: Bose-Einstein condensation and the atom laser”. *Rev. Mod. Phys.*, **74**, 1131–1151, (2002).
- [104] Jan Friebe, André Pape, Matthias Riedmann, Karsten Moldenhauer, Tanja Mehlstäubler, Nils Rehbein, Christian Lisdat, Ernst M. Rasel, Wolfgang Ertmer, Harald Schnatz, Burghard Lipphardt, and Gesine Grosche. “Absolute frequency measurement of the magnesium intercombination transition $^1S_0 \rightarrow ^3P_1$ ”. *Phys. Rev. A*, **78**, 033830, (2008).
- [105] Martin M. Boyd, Andrew D. Ludlow, Sebastian Blatt, Seth M. Foreman, Tetsuya Ido, Tanya Zelevinsky, and Jun Ye. ^{87}Sr lattice clock with inaccuracy below 10^{-15} . *Phys. Rev. Lett.*, **98**, 083002, (2007).
- [106] C J FOOT. “Atomic physics”. *Oxford University Press*, (2004).
- [107] Harold J Metcalf and Peter Van der Straten. “Laser cooling and trapping of neutral atoms”. *The Optics Encyclopedia: Basic Foundations and Practical Applications*, (2007).
- [108] Steven Chu, L. Hollberg, J. E. Bjorkholm, Alex Cable, and A. Ashkin. “Three-dimensional viscous confinement and cooling of atoms by resonance radiation pressure”. *Phys. Rev. Lett.*, **55**, 48–51, (1985).
- [109] Xinye Xu, Thomas H. Loftus, Josh W. Dunn, Chris H. Greene, John L. Hall, Alan Gallagher, and Jun Ye. “Single-stage sub-doppler cooling of alkaline earth atoms”. *Phys. Rev. Lett.*, **90**, 193002, (2003).

- [110] J. Dalibard and C. Cohen-Tannoudji. “Laser cooling below the doppler limit by polarization gradients: simple theoretical models”. *J. Opt. Soc. Am. B*, **6**(11), 2023–2045, (1989).
- [111] E. L. Raab, M. Prentiss, Alex Cable, Steven Chu, and D. E. Pritchard. “Trapping of neutral sodium atoms with radiation pressure”. *Phys. Rev. Lett.*, **59**, 2631–2634, (1987).
- [112] Marco Schioppo. “Development of transportable optical clock”. *PhD thesis*, Università Degli Studi Di Firenze, (2010).
- [113] N. Poli, R. E. Drullinger, G. Ferrari, J. Léonard, F. Sorrentino, and G. M. Tino. “Cooling and trapping of ultracold strontium isotopic mixtures”. *Phys. Rev. A*, **71**, 061403, (2005).
- [114] T. Legero, J. S. R. V. Winfred, F. Riehle, and U. Sterr. “Ultracold ^{88}Sr atoms for an optical lattice clock”. *IEEE International Frequency Control Symposium Joint with the 21st European Frequency and Time Forum*, 119–122, (2007).
- [115] Takashi Mukaiyama, Hidetoshi Katori, Tetsuya Ido, Ying Li, and Makoto Kuwata-Gonokami. “Recoil-limited laser cooling of ^{87}Sr atoms near the fermi temperature”. *Phys. Rev. Lett.*, **90**, 113002, (2003).
- [116] M. Chalony, A. Kastberg, B. Klappauf, and D. Wilkowski. “Doppler cooling to the quantum limit”. *Phys. Rev. Lett.*, **107**, 243002, (2011).
- [117] T. Bergeman, Gidon Erez, and Harold J. Metcalf. “Magnetostatic trapping fields for neutral atoms”. *Phys. Rev. A*, **35**, 1535–1546, (1987).
- [118] Simon Stellmer, Meng Khoon Tey, Bo Huang, Rudolf Grimm, and Florian Schreck. “Bose-Einstein condensation of strontium”. *Phys. Rev. Lett.*, **103**, 200401, (2009).
- [119] S. B. Nagel, C. E. Simien, S. Laha, P. Gupta, V. S. Ashoka, and T. C. Killian. “Magnetic trapping of metastable 3P_2 atomic strontium”. *Phys. Rev. A*, **67**, 011401, (2003).

- [120] D. S. Barker, B. J. Reschovsky, N. C. Pienti, and G. K. Campbell. “Enhanced magnetic trap loading for atomic strontium”. *Phys. Rev. A*, **92**, 043418, (2015).
- [121] Alan L. Migdall, John V. Prodan, William D. Phillips, Thomas H. Bergeman, and Harold J. Metcalf. “First observation of magnetically trapped neutral atoms”. *Phys. Rev. Lett.*, **54**, 2596–2599, (1985).
- [122] T. H. Bergeman, Patrick McNicholl, Jan Kycia, Harold Metcalf, and N. L. Balazs. “Quantized motion of atoms in a quadrupole magnetostatic trap”. *J. Opt. Soc. Am. B*, **6**(11):2249–2256, (1989).
- [123] Wolfgang Petrich, Michael H. Anderson, Jason R. Ensher, and Eric A. Cornell. “Stable, tightly confining magnetic trap for evaporative cooling of neutral atoms”. *Phys. Rev. Lett.*, **74**, 3352–3355, (1995).
- [124] Paul D. Lett, Richard N. Watts, Christoph I. Westbrook, William D. Phillips, Phillip L. Gould, and Harold J. Metcalf. “Observation of atoms laser cooled below the doppler limit”. *Phys. Rev. Lett.*, **61**, 169–172, (1988).
- [125] L Russell, R Kumar, VB Tiwari, and S Nic Chormaic. “Measurements on release–recapture of cold ^{85}Rb atoms using an optical nanofibre in a magneto-optical trap”. *Opt. Commun.*, **309**, 313–317, (2013).
- [126] Timothy P. Dinneen, Kurt R. Vogel, Ennio Arimondo, John L. Hall, and Alan Gallagher. “Cold collisions of $\text{Sr}^* - \text{Sr}$ in a magneto-optical trap”. *Phys. Rev. A*, **59**, 1216–1222, (1999).
- [127] Y.-J. Lin, A. R. Perry, R. L. Compton, I. B. Spielman, and J. V. Porto. “Rapid production of ^{87}Rb Bose-Einstein condensates in a combined magnetic and optical potential”. *Phys. Rev. A*, **79**, 063631, (2009).
- [128] K. J. Ross and B. Sonntag. “High temperature metal atom beam sources”. *Rev. Sci. Instrum.*, **66**(9), 4409–4433, (1995).

- [129] M. Schioppo, N. Poli, M. Prevedelli, St. Falke, Ch. Lisdat, U. Sterr, and G. M. Tino. “A compact and efficient strontium oven for laser-cooling experiments”. *Rev. Sci. Instrum.*, **83**(10), 103101, (2012).
- [130] Ruwan Senaratne, Shankari V. Rajagopal, Zachary A. Geiger, Kurt M. Fujiwara, Vyacheslav Lebedev, and David M. Weld. “Effusive atomic oven nozzle design using an aligned microcapillary array”. *Rev. Sci. Instrum.*, **86**(2), 023105, (2015).
- [131] Bo Song, Yueyang Zou, Shanchao Zhang, Chang-woo Cho, and Gyu-Boong Jo. “A cost-effective high-flux source of cold ytterbium atoms”. *Appl. Phys. B*, **122**(10), 250, (2016).
- [132] “Comsol Multiphysics Reference Manual”. *Version 5.3a*.
- [133] G. R. Hanes. “Multiple tube collimator for gas beams”. *J. Appl. Phys.*, **31**(12), 2171–2175, (1960).
- [134] Wenjie Zhu, Deheng Shi, Zunlue Zhu, and Jinfeng Sun. “Normal spectral emissivity models of steel 304 at 800–1100 k with an oxide layer on the specimen surface”. *T. Indian I. Metals*, **70**(4), 1083–1090, (2017).
- [135] DR Lide. “Handbook of Chemistry and Physics”, 89th (internet version), (2008).
- [136] Shuji Nakamura. “Nobel lecture: Background story of the invention of efficient blue ingan light emitting diodes”. *Rev. Mod. Phys.*, **87**, 1139–1151, (2015).
- [137] Hiroshi Amano. “Nobel lecture: Growth of GaN on sapphire via low-temperature deposited buffer layer and realization of *p*-type GaN by Mg doping followed by low-energy electron beam irradiation”. *Rev. Mod. Phys.*, **87**, 1133–1138, (2015).
- [138] Isamu Akasaki. “Nobel lecture: Fascinated journeys into blue light”. *Rev. Mod. Phys.*, **87**, 1119–1131, (2015).
- [139] Richard S Quimby. *Photonics and lasers: an introduction*. John Wiley & Sons, (2006).

- [140] P. A. Franken, A. E. Hill, C. W. Peters, and G. Weinreich. “Generation of optical harmonics”. *Phys. Rev. Lett.*, **7**, 118–119, (1961).
- [141] Anthony E Siegman and AE Siegman. *An introduction to lasers and masers*, Volume 122. McGraw-Hill New York, (1971).
- [142] H. Kogelnik and T. Li. “Laser beams and resonators”. *Appl. Opt.*, **5**(10), 1550–1567, (1966).
- [143] R. Le Targat, J.-J. Zondy, and P. Lemonde. “75% - efficiency blue generation from an intracavity PPKTP frequency doubler”. *Opt. Commun.*, **247**(4), 471–481, (2005).
- [144] E. M. Bridge, J Millen, C. S. Adams, and MPA Jones. “A vapor cell based on dispensers for laser spectroscopy”. *Rev. Sci. Instrum.*, **80**(1), 013101, (2009).
- [145] J. L. Hall, C. J. Bordé, and K. Uehara. “Direct optical resolution of the recoil effect using saturated absorption spectroscopy”. *Phys. Rev. Lett.*, **37**, 1339–1342, (1976).
- [146] Daryl W Preston. “Doppler-free saturated absorption: Laser spectroscopy”. *Am. J. Phys.*, **64**(11), 1432–1436, (1996).
- [147] G. M. Tino, M. Barsanti, M. de Angelis, L. Gianfrani, and M. Inguscio. “Spectroscopy of the 689 nm intercombination line of strontium using an extended-cavity ingap/ingaaip diode laser”. *Appl. Phys. B*, **55**(4), 397–400, (1992).
- [148] S Mauger, J Millen, and M P A Jones. “Spectroscopy of strontium Rydberg states using electromagnetically induced transparency”. *J. Phys. B*, **40**(22), F319, (2007).
- [149] M Weel and A Kumarakrishnan. “Laser-frequency stabilization using a lock-in amplifier”. *Can. J. Phys.*, **80**(12), 1449–1458, (2002).
- [150] Simon Stellmer and Florian Schreck. “Reservoir spectroscopy of $5s5p\ ^3P_2 - 5snd\ ^3D_{1,2,3}$ transitions in strontium”. *Phys. Rev. A*, **90**, 022512, (2014).

- [151] P H Moriya, M O Araújo, F Todão, M Hemmerling, H Keßler, R F Shiozaki, R Celistrino Teixeira, and Ph W Courteille. “Comparison between 403 nm and 497 nm repumping schemes for strontium magneto-optical traps”. *J. Phys. Commun.*, **2**(12), 125008, (2018).
- [152] P G Mickelson, Y N Martinez de Escobar, P Anzel, B J DeSalvo, S B Nagel, A J Traverso, M Yan, and T C Killian. “Repumping and spectroscopy of laser-cooled Sr atoms using the $(5s5p)^3P_2 - (5s4d)^3D_2$ transition”. *J. Phys. B: At. Mol. Opt. Phys.*, **42**(23), 235001, (2009).
- [153] Fachao Hu, Ingo Nosske, Luc Couturier, Canzhu Tan, Chang Qiao, Peng Chen, Y. H. Jiang, Bing Zhu, and Matthias Weidemüller. “Analyzing a single-laser repumping scheme for efficient loading of a strontium magneto-optical trap”. *Phys. Rev. A*, **99**, 033422, (2019).
- [154] Y Li, T Ido, T Eichler, and H Katori. “Narrow-line diode laser system for laser cooling of strontium atoms on the intercombination transition”. *Appl. Phys. B*, **78**(3-4), 315–320, (2004).
- [155] Matthew A. Norcia and James K. Thompson. “Simple laser stabilization to the strontium ^{88}Sr transition at 707 nm”. *Rev. Sci. Instrum.*, **87**(2), 023110, (2016).
- [156] Michael W Lee, Marie Claire Jarratt, Christian Marciniak, and Michael J Biercuk. “Frequency stabilization of a 369 nm diode laser by nonlinear spectroscopy of ytterbium ions in a discharge”. *Opt. Express*, **22**(6), 7210–7221, (2014).
- [157] Luc Couturier, Ingo Nosske, Fachao Hu, Canzhu Tan, Chang Qiao, Y. H. Jiang, Peng Chen, and Matthias Weidemüller. “Laser frequency stabilization using a commercial wavelength meter”. *Rev. Sci. Instrum.*, **89**(4), 043103, (2018).
- [158] Sergey Kobtsev, Stepan Kandrushin, and Andrey Potekhin. “Long-term frequency stabilization of a continuous-wave tunable laser with the help of a precision wavelengthmeter”. *Appl. Optics*, **46**(23), 5840–5843, (2007).

- [159] Khaldoun Saleh, Jacques Millo, Alexandre Didier, Yann Kersalé, and Clément Lacroûte. “Frequency stability of a wavelength meter and applications to laser frequency stabilization”. *Appl. Optics*, **54**(32), 9446–9449, (2015).
- [160] Sergei Aramovich Saakyan, Vladimir Alekseevich Sautenkov, Evgenia Vladimirovna Vilshanskaya, VV Vasiliev, Boris Borisovich Zelener, and Boris Vigdorovich Zelener. “Frequency control of tunable lasers using a frequency-calibrated λ -meter in an experiment on preparation of rydberg atoms in a magneto-optical trap”. *Quantum Electron.*, **45**(9), 828, (2015).
- [161] Steven T. Cundiff and Jun Ye. “Colloquium: Femtosecond optical frequency combs”. *Rev. Mod. Phys.*, **75**, 325–342, (2003).
- [162] Andrew D. Ludlow, Martin M. Boyd, Jun Ye, E. Peik, and P. O. Schmidt. “Optical atomic clocks”. *Rev. Mod. Phys.*, **87**, 637–701, (2015).
- [163] G.M. Tino, L. Cacciapuoti, K. Bongs, Ch.J. Bordè, P. Bouyer, H. Dittus, W. Ertmer, A. Görlitz, M. Inguscio, A. Landragin, P. Lemonde, C. Lammerzahl, A. Peters, E. Rasel, J. Reichel, C. Salomon, S. Schiller, W. Schleich, K. Sengstock, U. Sterr, and M. Wilkens. “Atom interferometers and optical atomic clocks: New quantum sensors for fundamental physics experiments in space”. *Nucl. Phys. B - Proc. Sup.*, **166**, 159–165, (2007)
- [164] S N Lea. “Limits to time variation of fundamental constants from comparisons of atomic frequency standards”. *Rep. Prog. Phys.*, **70**(9), 1473–1523, (2007).
- [165] Tobias Bothwell, Dhruv Kedar, Eric Oelker, John M. Robinson, Sarah L. Bromley, Weston L. Tew, Jun Ye, and Colin J. Kennedy. “JILA Sr I optical lattice clock with uncertainty of 2.0×10^{-18} ”. *arXiv: 1906.06004*, (2019).
- [166] W. F. McGrew, X. Zhang, R. J. Fasano, S. A. Schäffer, K. Beloy, D. Nicolodi, R. C. Brown, N. Hinkley, G. Milani, M. Schioppo, T. H. Yoon, and A. D. Ludlow. “Atomic clock performance enabling geodesy below the centimetre level”. *Nature*, **564**(7734), 87–90, (2018).

- [167] S. M. Brewer, J.-S. Chen, A. M. Hankin, E. R. Clements, C. W. Chou, D. J. Wineland, D. B. Hume, and D. R. Leibbrandt. “ $^{27}\text{Al}^+$ quantum-logic clock with a systematic uncertainty below 10^{-18} ”. *Phys. Rev. Lett.*, **123**, 033201, (2019).
- [168] Amar C. Vutha, Tom Kirchner, and Pierre Dubé. “Collisional frequency shift of a trapped-ion optical clock”. *Phys. Rev. A*, **96**, 022704, (2017).
- [169] N. Huntemann, C. Sanner, B. Lipphardt, Chr. Tamm, and E. Peik. “Single-ion atomic clock with 3×10^{-18} systematic uncertainty”. *Phys. Rev. Lett.*, **116**, 063001, (2016).
- [170] Pierre Dubé, Alan A. Madej, Zichao Zhou, and John E. Bernard. “Evaluation of systematic shifts of the $^{88}\text{Sr}^+$ single-ion optical frequency standard at the 10^{-17} level”. *Phys. Rev. A*, **87**, 023806, (2013).
- [171] C. W. Chou, D. B. Hume, J. C. J. Koelemeij, D. J. Wineland, and T. Rosenband. “Frequency comparison of two high-accuracy Al^+ optical clocks”. *Phys. Rev. Lett.*, **104**, 070802, (2010).
- [172] J Cao, P Zhang, J Shang, K Cui, J Yuan, S Chao, S Wang, H Shu, and X Huang. “A compact, transportable single-ion optical clock with 7.8×10^{-17} systematic uncertainty”. *Applied Physics B*, **123**(4), 112, (2017).
- [173] Kurt Gibble. “Scattering of cold-atom coherences by hot atoms: Frequency shifts from background-gas collisions”. *Phys. Rev. Lett.*, **110**, 180802, (2013).
- [174] Hubert Cybulski. “Ab initio studies of the ground and first excited states of the $\text{Sr} - \text{H}_2$ and $\text{Yb} - \text{H}_2$ complexes”. *J. Chem. Phys.*, **150**(6), 064316, (2019).
- [175] Jack Davis, Pierre Dubé, and Amar C. Vutha. “Improved estimate of the collisional frequency shift in Al^+ optical clocks”. *arXiv: 1901.06443*, (2019).
- [176] Amar Vutha, Tom Kirchner, and Pierre Dubé. “Doppler and collisional frequency shifts in trapped-atom clocks”. *arXiv: 1812.00973*, (2018).

- [177] A. M. Hankin, E. R. Clements, Y. Huang, S. M. Brewer, J.-S. Chen, C. W. Chou, D. B. Hume, and D. R. Leibbrandt. “Systematic uncertainty due to background-gas collisions in trapped-ion optical clocks”. *Phys. Rev. A*, **100**, 033419, (2019).
- [178] B. X. R. Alves, Y. Foucault, G. Vallet, and J. Lodewyck. “Background gas collision frequency shift on lattice-trapped strontium atoms”. *Joint Conf. IEEE Int.*, (2019).
- [179] James L Booth, Pinrui Shen, Roman V Krems, and Kirk W Madison. “Universality of quantum diffractive collisions and the quantum pressure standard”. *New J. Phys.*, **21**(10), 102001, (2019).
- [180] R D Glover, D E Laban, K J Matherson, W Wallace, and R T Sang. “Experimental investigation of atomic collisions in time scales varying from nanosecond to microseconds”. *J. Phys. Conf. Ser.*, **212**, 012013, (2010).
- [181] M. Prentiss, A. Cable, J. E. Bjorkholm, Steven Chu, E. L. Raab, and D. E. Pritchard. “Atomic-density-dependent losses in an optical trap”. *Opt. Lett.*, **13**(6), 452–454, (1988).
- [182] B. Brunetti, G. Liuti, E. Luzzatti, F. Pirani, and G. G. Volpi. “The interaction of atomic and molecular nitrogen with argon by scattering measurements”. *J. Chem. Phys.*, **79**(1), 273–277, (1983).
- [183] Dawn Rickey and John Krenos. “Molecular beam study of the collisions of state-monitored, metastable noble gas atoms with O₂ ($X^3\Sigma_g^-$)”. *J. Chem. Phys.*, **106**(8), 3135–3145, (1997).
- [184] R Kau, I D Petrov, V L Sukhorukov, and H Hotop. “Experimental and theoretical cross sections for photoionization of metastable atoms near threshold”. *J. Phys. B: At. Mol. Opt. Phys.*, **29**(23), 5673–5698, (1996).
- [185] Xinye Xu, Thomas H. Loftus, John L. Hall, Alan Gallagher, and Jun Ye. “Cooling and trapping of atomic strontium”. *J. Opt. Soc. Am. B*, **20**(5), 968–976, (2003).

- [186] Takayuki Kurosu and Fujio Shimizu. “Laser cooling and trapping of alkaline earth atoms”. *Jpn. J. Appl. Phys.*, **31**, 908–912, (1992).
- [187] T. Loftus, J. R. Bochinski, R. Shivitz, and T. W. Mossberg. “Power-dependent loss from an ytterbium magneto-optic trap”. *Phys. Rev. A*, **61**, 051401, (2000).
- [188] David E. Fagnan, Jicheng Wang, Chenchong Zhu, Pavle Djuricanin, Bruce G. Klappauf, James L. Booth, and Kirk W. Madison. “Observation of quantum diffractive collisions using shallow atomic traps”. *Phys. Rev. A*, **80**, 022712, (2009).
- [189] Dirk Spelsberg and Wilfried Meyer. “Static dipole polarizabilities of N₂, O₂, F₂, and H₂O”. *J. Chem. Phys.*, **101**(2), 1282–1288, (1994).
- [190] Peter Schwerdtfeger and Jeffrey K. Nagle. “2018 table of static dipole polarizabilities of the neutral elements in the periodic table”. *Mol. Phys.*, **117**(9-12), 1200–1225, (2019).
- [191] Chetan Vishwakarma, Jay Mangaonkar, Kushal Patel, Gunjan Verma, Sumit Sarkar, and Umakant D. Rapol. “A simple atomic beam oven with a metal thermal break”. *Rev. Sci. Instrum.*, **90**(5), 053106, (2019).
- [192] Gunjan Verma, Chetan Vishwakarma, C. V. Dharmadhikari, and Umakant D. Rapol. “A compact atomic beam based system for doppler-free laser spectroscopy of strontium atoms”. *Rev. Sci. Instrum.*, **88**(3), 033103, (2017).
- [193] Chetan Vishwakarma, Kushal Patel, Jay Mangaonkar, Jamie L. MacLennan, Korak Biswas, and Umakant D. Rapol. “Study of loss dynamics of strontium in a magneto-optical trap”. *arXiv: 1905.03202*, (2019).
- [194] Hidetoshi Katori, Tetsuya Ido, Yoshitomo Isoya, and Makoto Kuwata-Gonokami. “Magneto-optical trapping and cooling of strontium atoms down to the photon recoil temperature”. *Phys. Rev. Lett.*, **82**, 1116–1119, (1999).

- [195] Thomas H. Loftus, Tetsuya Ido, Andrew D. Ludlow, Martin M. Boyd, and Jun Ye. “Narrow line cooling: Finite photon recoil dynamics”. *Phys. Rev. Lett.*, **93**, 073003, (2004).
- [196] Thierry Chaneliere, Ling He, Robin Kaiser, and David Wilkowsky. “Three dimensional cooling and trapping with a narrow line”. *Eur. Phys. J. D*, **46**(3), 507–515, (2008).
- [197] Thomas H. Loftus, Tetsuya Ido, Martin M. Boyd, Andrew D. Ludlow, and Jun Ye. “Narrow line cooling and momentum-space crystals”. *Phys. Rev. A*, **70**, 063413, (2004).
- [198] J. A. Sherman, N. D. Lemke, N. Hinkley, M. Pizzocaro, R. W. Fox, A. D. Ludlow, and C. W. Oates. “High-accuracy measurement of atomic polarizability in an optical lattice clock”. *Phys. Rev. Lett.*, **108**, 153002, (2012).
- [199] Thomas Middelmann, Stephan Falke, Christian Lisdat, and Uwe Sterr. “High accuracy correction of blackbody radiation shift in an optical lattice clock”. *Phys. Rev. Lett.*, **109**, 263004, (2012).
- [200] Tao Hong, Claire Cramer, Warren Nagourney, and E. N. Fortson. “Optical clocks based on ultranarrow three-photon resonances in alkaline earth atoms”. *Phys. Rev. Lett.*, **94**, 050801, (2005).
- [201] Robin Santra, Ennio Arimondo, Tetsuya Ido, Chris H. Greene, and Jun Ye. “High-accuracy optical clock via three-level coherence in neutral bosonic ^{88}Sr ”. *Phys. Rev. Lett.*, **94**, 173002, (2005).
- [202] A. V. Taichenachev, V. I. Yudin, C. W. Oates, C. W. Hoyt, Z. W. Barber, and L. Hollberg. “Magnetic field-induced spectroscopy of forbidden optical transitions with application to lattice-based optical atomic clocks”. *Phys. Rev. Lett.*, **96**, 083001, (2006).
- [203] Z. W. Barber, C. W. Hoyt, C. W. Oates, L. Hollberg, A. V. Taichenachev, and V. I. Yudin. “Direct excitation of the forbidden clock transition in neutral ^{174}Yb atoms confined to an optical lattice”. *Phys. Rev. Lett.*, **96**, 083002, (2006).

- [204] N. Poli, Z. W. Barber, N. D. Lemke, C. W. Oates, L. S. Ma, J. E. Stalnaker, T. M. Fortier, S. A. Diddams, L. Hollberg, J. C. Bergquist, A. Bruschi, S. Jefferts, T. Heavner, and T. Parker. “Frequency evaluation of the doubly forbidden $^1S_0 \rightarrow ^3P_0$ transition in bosonic ^{174}Yb ”. *Phys. Rev. A*, **77**, 050501, (2008).